FRONTIERS IN NEUROANATOMY – EDITOR'S PICK 2021

EDITED BY: Javier DeFelipe
PUBLISHED IN: Frontiers in Neuroanatomy

frontiers Research Topics

ISSN 1664-8714
ISBN 978-2-88971-109-3
DOI 10.3389/978-2-88971-109-3

About Frontiers

Frontiers is more than just an open-access publisher of scholarly articles: it is a pioneering approach to the world of academia, radically improving the way scholarly research is managed. The grand vision of Frontiers is a world where all people have an equal opportunity to seek, share and generate knowledge. Frontiers provides immediate and permanent online open access to all its publications, but this alone is not enough to realize our grand goals.

Frontiers Journal Series

The Frontiers Journal Series is a multi-tier and interdisciplinary set of open-access, online journals, promising a paradigm shift from the current review, selection and dissemination processes in academic publishing. All Frontiers journals are driven by researchers for researchers; therefore, they constitute a service to the scholarly community. At the same time, the Frontiers Journal Series operates on a revolutionary invention, the tiered publishing system, initially addressing specific communities of scholars, and gradually climbing up to broader public understanding, thus serving the interests of the lay society, too.

Dedication to Quality

Each Frontiers article is a landmark of the highest quality, thanks to genuinely collaborative interactions between authors and review editors, who include some of the world's best academicians. Research must be certified by peers before entering a stream of knowledge that may eventually reach the public - and shape society; therefore, Frontiers only applies the most rigorous and unbiased reviews.
Frontiers revolutionizes research publishing by freely delivering the most outstanding research, evaluated with no bias from both the academic and social point of view. By applying the most advanced information technologies, Frontiers is catapulting scholarly publishing into a new generation.

What are Frontiers Research Topics?

Frontiers Research Topics are very popular trademarks of the Frontiers Journals Series: they are collections of at least ten articles, all centered on a particular subject. With their unique mix of varied contributions from Original Research to Review Articles, Frontiers Research Topics unify the most influential researchers, the latest key findings and historical advances in a hot research area! Find out more on how to host your own Frontiers Research Topic or contribute to one as an author by contacting the Frontiers Editorial Office: frontiersin.org/about/contact

FRONTIERS IN NEUROANATOMY – EDITOR'S PICK 2021

Topic Editor:
Javier DeFelipe, Cajal Institute (CSIC), Spain

Citation: DeFelipe, J., ed. (2021). Frontiers in Neuroanatomy – Editor's Pick 2021. Lausanne: Frontiers Media SA. doi: 10.3389/978-2-88971-109-3

Table of Contents

frontiers in Neuroanatomy

ORIGINAL RESEARCH
published: 07 January 2019
doi: 10.3389/fnana.2018.00115

Centrifugal Inputs to the Main Olfactory Bulb Revealed Through Whole Brain Circuit-Mapping

Krishnan Padmanabhan[1,2,3]*, *Fumitaka Osakada*[4,5], *Anna Tarabrina*[6], *Erin Kizer*[6], *Edward M. Callaway*[1,4], *Fred H. Gage*[6] *and Terrence J. Sejnowski*[1,2,7]

[1] Crick-Jacobs Center for Theoretical and Computational Biology, Salk Institute for Biological Studies, La Jolla, CA, United States, [2] Computational Neurobiology Laboratory, Salk Institute for Biological Studies, La Jolla, CA, United States, [3] Department of Neuroscience, University of Rochester School of Medicine and Dentistry, Rochester, NY, United States, [4] Systems Neurobiology Laboratories, Salk Institute for Biological Studies, La Jolla, CA, United States, [5] Laboratory of Cellular Pharmacology, Graduate School of Pharmaceutical Sciences, Nagoya University, Nagoya, Japan, [6] Laboratory of Genetics, Salk Institute for Biological Studies, La Jolla, CA, United States, [7] Howard Hughes Medical Institute, Salk Institute for Biological Studies, La Jolla, CA, United States

Neuronal activity in sensory regions can be modulated by attention, behavioral state, motor output, learning, and memory. This is often done through direct feedback or centrifugal projections originating from higher processing areas. Though, functionally important, the identity and organization of these feedback connections remain poorly characterized. Using a retrograde monosynaptic g-deleted rabies virus and whole-brain reconstructions, we identified the organization of feedback projecting neurons to the main olfactory bulb of the mouse. In addition to previously described projections from regions such as the Anterior Olfactory Nucleus (AON) and the piriform cortex, we characterized direct projections from pyramidal cells in the ventral CA1 region of hippocampus and the entorhinal cortex to the granule cell layer (GCL) of the main olfactory bulb (MOB). These data suggest that areas involved in stress, anxiety, learning and memory are all tethered to olfactory coding, two synapses away from where chemical compounds are first detected. Consequently, we hypothesize that understanding olfactory perception, even at the earliest stages, may require studying memory and behavior in addition to studying the physiochemical features of odors.

Keywords: olfactory bulb, feedback, olfaction, retrograde tracer, circuits

OPEN ACCESS

Edited by:
Ricardo Insausti, University of Castilla La Mancha, Spain

Reviewed by:
Jorge A. Larriva-Sahd, National Autonomous University of Mexico, Mexico
Hirac Gurden, INSERM U1133 Physiologie de l'Axe Gonadotrope (Unité de Biologie Fonctionnelle et Adaptative), France

***Correspondence:**
Krishnan Padmanabhan
krishnan_padmanabhan@urmc.rochester.edu

Received: *21 August 2018*
Accepted: *04 December 2018*
Published: *07 January 2019*

Citation:
Padmanabhan K, Osakada F, Tarabrina A, Kizer E, Callaway EM, Gage FH and Sejnowski TJ (2019) Centrifugal Inputs to the Main Olfactory Bulb Revealed Through Whole Brain Circuit-Mapping. Front. Neuroanat. 12:115. doi: 10.3389/fnana.2018.00115

INTRODUCTION

Understanding the neural basis of olfactory perception remains one of the key challenges of sensory neuroscience. Part of the challenge arises from the inherently high dimensional nature of chemical structure (Secundo et al., 2014). For instance, mapping olfactory percepts onto any single feature of chemical structure such as carbon chain length, remains difficult. A parallel approach has focused on anatomy and physiology. In rodents, the neuronal representations of odors have been investigated by tracking neural activity from the olfactory receptor neurons (ORNs), where components of smell are first detected , to the piriform cortex (Stettler and Axel, 2009; Davison and Ehlers, 2011), where they are assembled combinatorially (Babadi and Sompolinsky, 2014) into odor percepts. However, such a feedforward model of olfactory coding, wherein neuronal responses are sequentially marshaled into more complex representations by progressively higher cortical areas glosses over the major feedback or centrifugal projections present in olfaction. As a result,

comparatively less is known about the origin, identity, and organization of feedback projecting cells (Price and Powell, 1970; Shipley and Adamek, 1984).

To address this, we used a modified g-deleted rabies virus (Wickersham et al., 2007; Osakada and Callaway, 2013) and whole-brain imaging methods (Padmanabhan et al., 2010), to describe the organization and identity of centrifugal projections to the main olfactory bulb (MOB). In addition to confirming centrifugal inputs in the mouse that have been previously identified in the rat (Price and Powell, 1970), we also identified monosynaptic feedback from CA1 pyramidal cells in the hippocampus and from cells in the entorhinal cortex to the bulb. Our results provide a feedback-wiring diagram for the olfactory system of the mouse.

METHODS

Some of the data used in this manuscript has been previously published (Padmanabhan et al., 2016). In this pervious work, the focus was exclusively on projections from the AON and the piriform cortex, with the goal being to understand the organization of feedback circuits from these two olfactory regions. Here we provide a quantitative assessment of the organization of the feedback projections from the entire mouse brain. Additionally, this work uses analysis and provides information about the relative distribution of feedback projections that were not previously reported or quantified.

Rabies Virus

GFP, mCherry, or BFP was cloned in pSADΔG-F3 as described previously (Wickersham et al., 2007; Osakada et al., 2011; Osakada and Callaway, 2013). SADΔG-GFP, SADΔG-mCherry, and SADΔG-BFP were recovered in B7GG cells with transfection with the corresponding genomic plasmid, pcDNA-SADB19N, pcDNA-SADB19P, pcDNA-SADB19L, and pcDNA-SADB19G. Viruses were amplified in B7GG cells in a humidified atmosphere of 3% CO_2 and 97% air at 35°C and concentrated by two rounds of ultracentrifuge. The concentrated rabies viruses were titrated in HEK293t cells. The titers of the rabies viruses used in the present study were 5.0×10^8 – 3.0×10^9 infectious units/ml.

Adeno-associated viruses (AAV) were generated by the GT3 Core facility at the Salk Institute. AAV1-CMV-eGFP and AAV2-CMV-eGFP was generated at titers of 1.20×10^{11} – 5.13×10^{12} infectious units/ml. The viruses were stored at −80°C until use.

Animals

This study was carried out in accordance with the accordance with the guidelines for care and use of animals by the Institutional Animal Care and Use Committee (IACUC) of the Salk Institute for Salk Institute for Biological Studies. The protocol was approved by the Institutional Animal Care and Use Committee (IACUC) of the Salk Institute for Biological Studies. Twenty mice (male and female) aged 3–4 months were used each having 1 to 2 injections ($N = 23$ injections total). The GCL was target with stereotaxic coordinates (Bregma +4.25 mm rostral/caudal, +1 mm medial/lateral, −0.6 mm to −1.5 mm dorsal/ventral) using a digital micromanipulator (Kopf, CA, USA). Stereotactic injections to the CA1 region were made relative to bregma (−3.25 mm rostral/caudal, + 3.25 mm medial/lateral, −4 mm dorsal-ventral). Borosilicate micropipettes were pulled on a Sutter P200 and 40–200 nl of virus were delivered to each bulb via pulsed injection from a picospritzer (Parker, OH, USA). Three different fluorescent reporters (GFP, MCherry, and BFP) in the G-deleted rabies virus were used for the experiments and all 3 labeled neurons extensively, including labeling of dendritic processes. For AAV viral vectors, either eGFP or dsRed were used as fluorescent reporters. Additionally, we used a Cholera-Toxin-β subunit tracer for some anterograde experiments.

Histology

Three to 10 days after the viral or fluorescent reporter injection, animals were sacrificed and perfused with 4% paraformaldehyde (PFA) and brains were extracted and transferred to a solution of 4% PFA/30% sucrose (Padmanabhan et al., 2010). Coronal sections, 100 μm in thickness, were made of the mouse brain from the bulb to approximately Bregma −4.25 mm, allowing us to characterize inputs to the bulb. In 3 of the animals, damage while extracting the brain resulted in incomplete reconstructions of some regions such as hippocampus and occipital cortex. In 2 additional animals, tissue warped during perfusion, and though these were qualitatively to determine properties such as injection site size, number of labeled neurons etc., they were not used in calculating the relative distribution of feedback projecting cells from different brain regions.

Imaging and Data Management

Images were acquired with an Olympus VS110 slide scanner (Tokyo, Japan). Complete scans of all coronal sections were done at 5 virtual Z-planes for each section. Each coronal section produced a stack of 5 ∼30,000 × 50,000 pixel 16-bit images, which were then collapsed into a single maximum intensity projection. Each whole brain scan resulted in ∼1 TB of data. For analysis and viewing, each individual section was sorted in a pyramid representation. For each representation

$$G(x,y) = I(x,y) \text{ for level, } l = 0 \quad (1)$$

$$G_l(x,y) = \frac{1}{M^*N} \sum_{m=-2}^{M} \sum_{n=-2}^{N} G_{l-1}(x+m,\ y+n) \quad (2)$$

Such that G is the pyramid representation and I the original image where $M = 2$ and $N = 2$. Our resolution resulted in representations for l = 0–3.

Image Dilation and Correlation

Individual coronal sections were aligned and alignment validated by correlation analysis (using custom functions in MATLAB (MathWorks, MA, USA). First, images were thresholded at different image places using previously described methods (Padmanabhan et al., 2010). This method simply finds an optimal threshold for binary images, or a series of binary image planes corresponding to individual objects of interest. To extent this to identify the boundaries of cells and tissues, we performed additional image processing. First, the Moore-Neighbor tracing algorithm was used to isolate tissue boundaries for each section

as well as boundaries for individual neurons (Gonzalez et al., 2004). Boundaries where then convolved with a 2-dimensional Gaussian to minimize alignment sensitivity to pixel noise, and then a correlation coefficient between all pairs of sections was used to validate the alignment.

Cell Finding

For each fluorescent image section, regions of interest were manually identified. Only label within these identified areas was used for analysis, thereby excluding background fluorescence. To identify neurons in an automated way, we defined an image X as a where x_n corresponds to the nth pixel:

$$\boldsymbol{x} = x_1, x_2, x_3, \ldots x_n \tag{3}$$

We defined another vector y where y_n corresponding to the *n*th pixel:

$$\boldsymbol{y} = y_1, y_2, y_3, \ldots y_n \tag{4}$$

such that

$$y_n \begin{cases} = \mathbf{1} \ \ \boldsymbol{if} \ \ \boldsymbol{x_n} > i \\ = \mathbf{0} \ \ \boldsymbol{else} \ \boldsymbol{x_n} \ \ \leq i \end{cases} \tag{5}$$

where *i* was a value selected manually for thresholding. Individual sections were thresholded using either a manually selected threshold value, or alternatively, using an optimal image thresholding method (Padmanabhan et al., 2010).

$$\mathrm{corr}\left(\mathrm{x}, \mathrm{y(i)}\right) = \frac{\sum_{\mathrm{j=i}}^{\mathrm{m}} \mathrm{n_j} * (\mathrm{j} - \overline{\mathrm{x}})}{\sqrt{\left(\sum_{\mathrm{j}}^{\mathrm{m}} (\mathrm{j} - \overline{\mathrm{x}})^2 * \mathrm{n_j}\right) * \left(\frac{(\mathrm{N_m} - \mathrm{N_i}) * \mathrm{N_i}}{\mathrm{N_m}}\right)}} \tag{6}$$

where x is the original image and the thresholded image y at the threshold value (i-1) with j as the bit-depth of the image (for example, between 0 and 255 for an 8-bit image), n_j as the number of pixels with the value j and $\overline{x}$ as the mean pixel value of the image. In addition, N_m was the total number of pixels in the image and N_i was the number of pixels above the threshold value (i-1). We rewrote our correlation where x was the original image and y(i) was the image thresholded at a value of i. The optimal correlation:

$$\mathrm{argmax\ t\ (m)} = \mathrm{corr}\left(\mathrm{x}, \mathrm{y(m)}\right) \tag{7}$$

Thresholded images were then run through a series of image processing functions to identify retrogradely labeled neurons. To take thresholded images and segment individual neurons (which constitute multiple pixels), we first, performed a nearest-neighbor pixel grouping to assign contiguous pixels into neurons. Following this step, groups of pixels were sorted based on morphological properties, including the shape (how round to the neurons look, which was biased by the median filtering step) and the number of pixels within each group (which eliminated small pixels that corresponded to either processes or large groups of cells that are clumped together and cannot be easily segmented).

Data Analysis

All analysis described in this manuscript, including tissue identification, was done with custom functions written in MATLAB. Unless otherwise noted, error bars are standard deviations.

RESULTS

A g-deleted rabies virus expressing a fluorescent reporter was injected into the granule cell layer (GCL) (Haberly and Price, 1978) of the MOB in adult mice (3–6 months of age, $N = 20$, **Figure 1A**). Retrogradely labeled cells infected with the virus did not express the rabies glycoprotein, thus fluorescence was confined only to neurons at the injection site (**Figure 1B**) and to those cells whose axonal buttons terminated at the site of the injection (Wickersham et al., 2007; Osakada and Callaway, 2013; Callaway and Luo, 2015). As feedback input to the glomerular layer (Petzold et al., 2009) and the mitral cell layer (Yan et al., 2008; Markopoulos et al., 2012) have been previously studied, we focused our analysis on the GCL. Following 3–10 days of viral infection ($N = 4$ at 3 days, $N = 17$ at 5–10 days), animals were sacrificed and coronal sections of the whole mouse brain were made. To characterize the spatial organization of centrifugal projections to the GCL, we established a whole-brain imaging and analysis method (**Figure 1C**). First, we collected data from ∼160 to 180 100 μm sections constituting the mouse brain (**Figure 1D**, we did not section regions of the cerebellum and the most caudal regions of the brainstem).

In order to identify all retrogradely labeled neurons throughout the brain, we needed to perform two segmentation and identification tasks: isolate the tissue to delineate brain areas and identify the location of individual cell bodies (**Figure 2A**). To do this, we first median filtered the raw images (**Figure 2B**) to eliminate shot noise in our imaging, as well as to smoothen out the edges of the cell bodies (**Figure 2Bi**). Although this did reduce the ability to reconstruct individual dendrites (**Figure 2Bi**), it allowed us to rapidly segment individual neurons and the regions of the brain they inhabited. Next, we used the Maximum Correlation Thresholding (MCT) algorithm (Padmanabhan et al., 2010) which thresholds the image at each single gray-scale value and then calculates the correlation of the thresholded image to the original (**Figure 2C**, top). The curve represented the correlation of the thresholded image to the original image for each gray-scale value, and had distinct transitions points that were clear when we visualized the derivative of the correlation curve (**Figure 2C**, bottom). Changes in the correlation corresponding to the edge of the tissue (**Figure 2C**, red line) and the labeled cells (**Figure 2C**, purple line) were apparent in both the correlation curve and the derivative curve. While the MCT algorithm provides thresholded images corresponding to various objects (tissue edge, individual neurons, etc.), it does not identify which feature are important, nor does it segment these individual images into objects (such as the various boundaries of tissues, or neurons) that are defined by multiple contiguous pixels in an imaging plane. To address these issues, we first chose thresholding at these two different gray-scale values

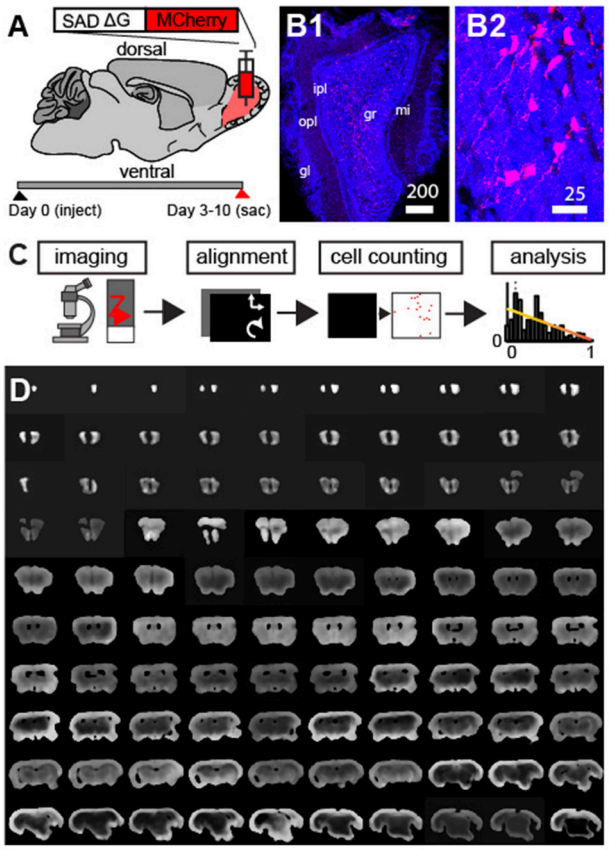

FIGURE 1 | Modified g-deleted rabies tracing to identify feedback projection to the olfactory bulb. **(A)** Schematic outlining experimental design. **(B1)** Neurons labeled with mCherry rabies (red) and DAPI nuclear counter-stain (blue) at the injection site. Scale bar = 200 um. mi, mitral cell layer; opl, outer plexiform layer; ipl, inner plexiform layer; gl, glomerular layer; gcl, granule cell layer. **(B2)** Enlargement of neurons in **(B1)** shows clearly labeled neurons in the GCL. **(C)** Outline of approach involves automated fluorescence microscopy, coronal section alignment, automated cell counting, and subsequent analysis. **(D)** Example of coronal sections used for whole brain reconstructions.

(**Figure 2D**), and using existing image segmentation algorithms (Padmanabhan et al., 2016) allowed us to define the tissue shape for each section (**Figures 2D–E**) as well as identify the individual cell bodies (**Figures 2Di–Ei**). As different traces have different levels of fluorescence corresponding to different objects (due to experimental variability like injection size, viral titer, cell type, and image parameters) we confirmed that the MCT algorithm produced different correlation curves (**Figure 2F**, left, red) reflecting differences in fluorescent pixel intensity across the various sections in a single mouse. The approach was robust to differences in pixel intensity across multiple fluorophores including GFP, RFP and, in this example Blue Fluorescent Protein (BFP, **Figure 2F**, right, blue curves). While the bit-depth for the maximum correlation was different across different experiments (**Figure 2G**), the shape of the correlation coefficient curve varied smoothly along the rostral caudal axis (**Figure 2H**), reflecting the overall decrease in mean fluorescence from the injection site in the bulb (where the density of labeled cells was high) to the caudal regions of the mouse brain.

Next, we wished to align the tissue and validate the image segmentation of cell bodies to assess the utility of the method. Using the thresholded images in 2D, we align section edges along the rostro-caudal axis (**Figure 3A**), which provided a 3D representation of the entire mouse brain. To determine the fidelity of this alignment, we calculated the correlation of each section to all adjacent sections (**Figure 3B**), with varying degrees of tolerance (as represented by the thickness of the edges of each section = gray lines). Correlation values were high in adjacent sections, but fell of dramatically, confirming that alignment of individual sections was tight (**Figure 3B**).

Following segmentation of the tissue, a segmentation was performed on the threshold images corresponding to labeled neurons which included shape analysis and cell size identification (See methods). The result of the algorithm appeared to be well-identified neurons. To determine the fidelity of the automated cell finder, in a subset of coronal sections from multiple animals, an expert used identified individual neurons manually and these were compared to the algorithm. Two representative examples of the olfactory bulb (**Figure 3C**, top) and the piriform cortex (**Figure 3C**, bottom) show neurons that were identified by the human user manually (red dots), and by the MCT algorithm (blue dots). In both examples, the automated cell finder identified the neurons that an expert human also identified in two distinct regions, with different fluorescent intensities, different neuronal morphologies, and different densities. When we quantified the accuracy of the MCT algorithm to the manual count, we found that across all comparisons, there was an $R^2 = 0.84$, and this was significantly different from chance (**Figure 3D**, black line is the unit line, gray line is the best-fit for the data). When we examined the correlation between the manual expert and the MCT algorithm further, we found that underestimates occurred when the density of neurons being counted was high (**Figure 3E**, red area). These corresponded to regions at or near the injection site, where multiple neurons overlapped one-another and the algorithm had difficulty parsing them into individual cells. Despite this limitation, the 0.84 correlation of the algorithm to neurons identified by an expert human, allowed us to study the organization of feedback projecting cells to the bulb.

We first analyzed the precision of our injections to the GCL of the bulb (**Figures 4A,B**). Boundaries were manually drawn in the tissue (light gray) between the inner plexiform layer (IPL) and the GCL (**Figures 4A,B**, dark gray) with the asterisk corresponding to the center of mass of the injection site (taken as the average of the Euclidian position of all the labeled neurons within the bulb). A 3D reconstruction of the bulb from this experiment revealed that although the injection site was confined to the GCL (**Figure 4C**, asterisk, red points correspond to labeled neurons within the GCL, gray lines correspond to the boundaries of the GCL for each coronal section), a small subset of neurons were also labeled outside the GCL (**Figure 4C**, magenta cells), likely due to label being taken up by neurites passing through the injection site and corresponding to mitral/tufted cells (Hovis et al., 2010; Padmanabhan and Urban, 2010). We assessed the ratio of labeled cells inside (**Figure 4D**, red cells) to cells outside

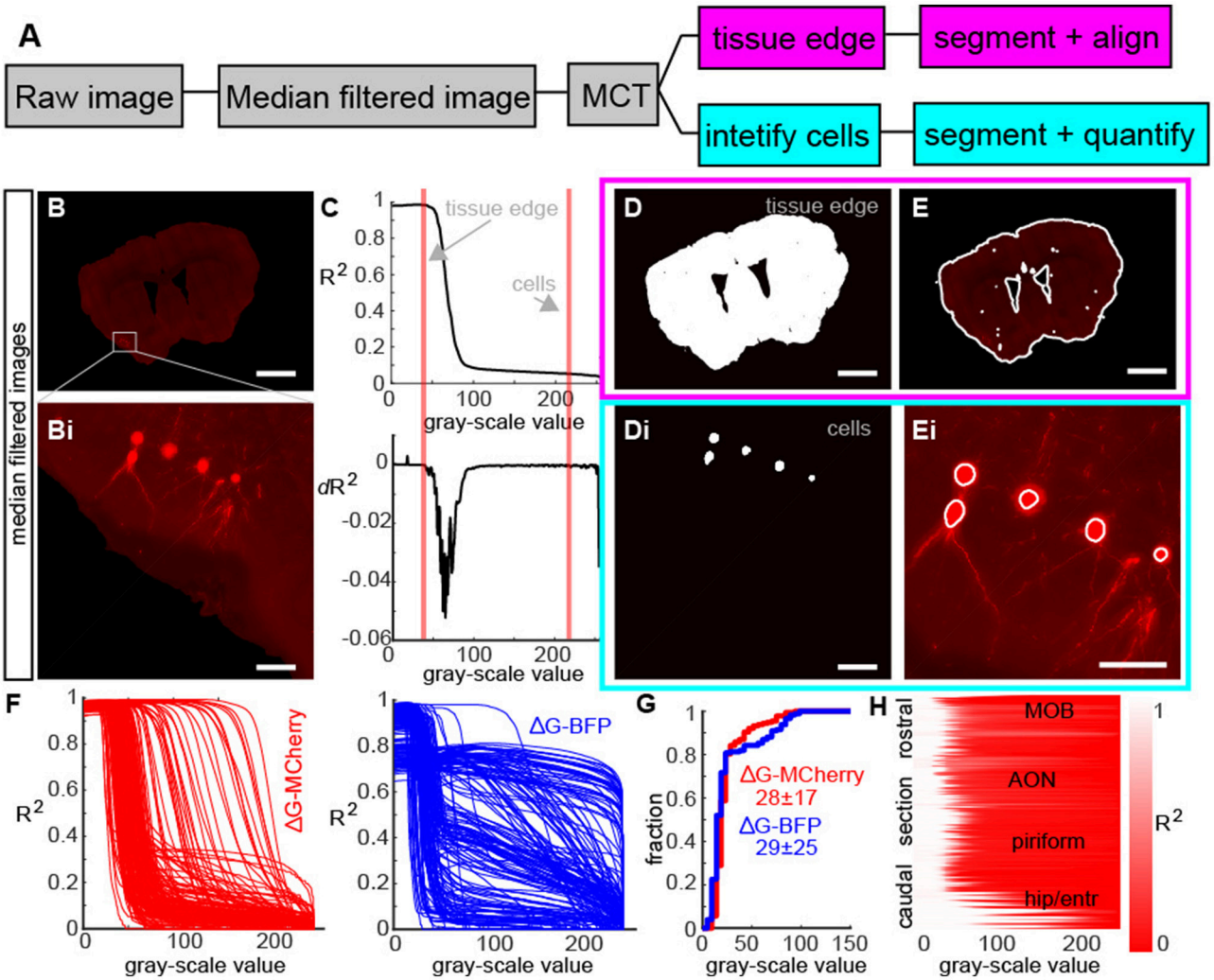

FIGURE 2 | Image processing steps for whole brain reconstructions. **(A)** Flow diagram of image processing for identifying tissue structure and neurons. **(B)** Representative example of a median filtered fluorescence image section and **(Bi)** enlargement of retrogradely labeled neurons showing blurring of cell bodies due to filtering. (**C**, top) Correlation of a thresholded image to the median filtered image as a function of threshold value and (**C**, bottom) derivate of correlation curve. Red lines show transitions in the image statistics that correspond to the tissue edge which identifies the section boundaries and labeled cells. **(D)** Example of thresholded images from A at the values corresponding to the tissue edge and **(Di)** to retrogradely labeled neurons. **(E)** Outline of tissue edge and **(Ei)** individual cells shows that the algorithm identifies both the sections in the imaging and individual neurons. **(F)** Correlation curve (as described in **C**) for all sections in an experiment using G-MCherry (left) and G-BFP show the diversity of threshold functions across different sections and different viral constructs. **(G)** Cumulative histogram of threshold values selected for each section in **(F)** for G-MCherry and G-BFP highlight this diversity. **(H)** Correlation curves as a function of rostral-caudal axis shows a systematic variation from the olfactory bulb to the hippocampus and entorhinal cortex, reflecting the ability of the algorithm to segment sections and identify cells across the systematic differences in fluorescence associated with different sections.

the GCL but still within the bulb (**Figure 4D**, magenta cells) to determine the precision of our targeting (**Figure 4D**, black line in each corresponds to the GCL boundary). In this example, 84% of fluorescently labeled neurons were inside the GCL, similar to the percentage of neurons inside the GCL across all experiments, (80 $\pm$ 19%, $N = 9$).

When we examined the distribution of neurons within the injection site, we found that they were confined to the GCL (**Figure 4E**), with asymmetries in the density of label corresponding to the non-spherical shape of the GCL along the medial-lateral axis (**Figure 4E**, left). Additionally, our injections were slightly biased to the dorsal and caudal domains of the GCL as evidenced by the skewed distribution of the labeled cells along the dorsal-ventral axis (**Figure 4E**, middle) and the rostral-caudal axis (**Figure 4E**, right). While the representative example in **Figure 4C** shows a dorsal biased injection, additional injections labeled various regions of the GCL (**Figure 4E**). Although we observed no significant/systematic differences in the label density across position (**Figure 4E**), this does not rule out the possibility that such differences could exist. Importantly however, these

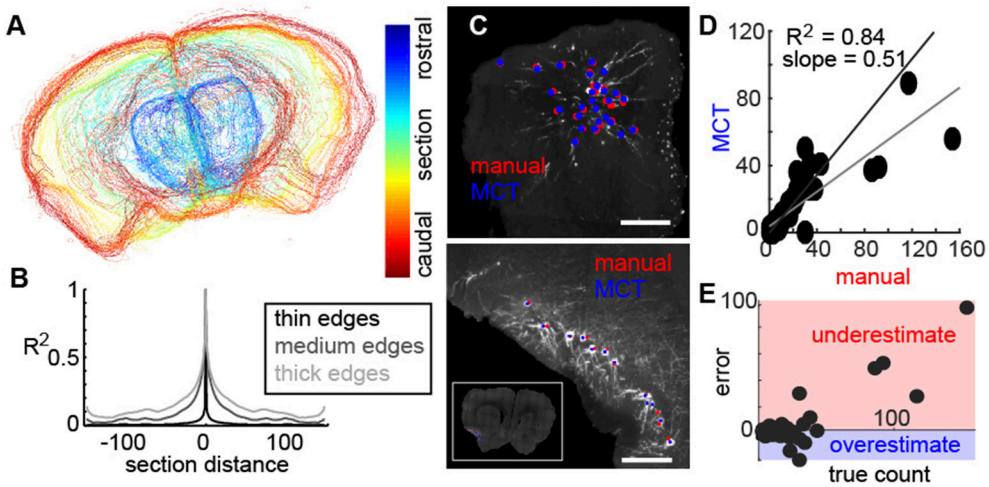

FIGURE 3 | Fidelity of aligned tissue and identified neurons. **(A)** Representative example of sequential sections of the mouse brain identified using MCT. **(B)** Correlation of each section to the sections in front and behind with varying degrees of precision (as controlled by edge thickness) shows a tight alignment of individual coronal sections in the reconstruction. **(C)** Representative examples of neurons manually identified (red) and using the MCT algorithm (blue) near the injection site (top) and in a section with retrogradely labeled neurons. **(D)** Correlation of neurons identified by the MCT algorithm to the number of neurons identified by an expert human shows a high agreement ($R^2 = 0.84$). **(E)** Error of MCT algorithm in identifying neurons as a function of neurons labeled in the section shows that the MCT. consistently underestimates the number of labeled cells when the label density is high, likely due to poor segmentation of neurons near the injection site and when cell clusters are densely packed.

distributions corresponded to the 3D volume of the GCL in our reconstructions (**Figure 4C**), further confirming the precision of our targeting. To determine the regions projecting to the GCL, we next examined the distribution of retrogradely labeled neurons throughout the mouse brain. A density map from the injection site in 4C (**Figure 4F**), and the distribution of label across 10 experiments for which we had reconstructions (**Figure 4G**, left), revealed that feedback-projecting neurons were almost entirely from ventral regions of the mouse brain (**Figure 4G**, right), predominantly archicortical in origin (piriform cortex, CA1, etc.) or neuromodulatory (HDB). As we saw label across these regions in an array of experiments (**Figure 4G**), feedback projections are likely to target both dorsal and ventral bulb.

To provide a more detailed description of the origins of the feedback projections, we aligned all of the brain sections to a mouse brain atlas (Paxinos and Franklin, 2004) and identified the areas corresponding to retrogradely labeled neurons (**Figure 5A**). We found labeled neurons in the both the ipsilateral (58%) and contralateral (5%) anterior olfactory nucleus (AON), the piriform cortex and the nucleus of the lateral olfactory tract (nLOT, 27.9%), the horizontal limb of the Diagonal Band (HDB, 3.5%), amygdala regions (1.4%), zona inserta (0.001%), the piriform-entorhinal cortex (0.001%) transition and in various nuclei of the hypothalamus (0.08%), consistent with previous reports (**Figure 2F**, Shipley and Adamek, 1984) as well as projections to the GCL directly from the entorhinal cortex (**Figure 5A**, light blue cells, 0.3%) and direct centrifugal input from the CA1 region of the hippocampus (**Figure 5A**, green, 0.75%) as had been hypothesized to exist previously in other species (de Olmos et al., 1978). We quantified the density of these projections from various regions (**Figure 5B**), and found that while the largest density of retrograde labeled cells came from major olfactory cortical areas (ipsilateral AON, contralateral AON = 63%), 10% of the retrogradely labeled neurons in the brain originated from areas that are not thought of as part of olfactory cortex.

Perhaps most unexpected were the retrogradely labeled neurons we found in the hippocampus and the entorhinal cortex [**Figure 5A**, light blue cells, and green cells (Leitner et al., 2016)]. Although some recent work has suggested that pyramidal cells in the CA1 region of hippocampus send axons directly to the bulb (Okuyama et al., 2016), it remains unclear if these are projections directly to the MOB or if these target the accessory olfactory bulb (AOB)(de Olmos et al., 1978; Shipley and Adamek, 1984).

To address this, we determined the spatial location of the neurons projecting from CA1. First, we mapped the location of cells onto a 3D model of the CA region of hippocampus (**Figures 6A,B**) and found retrogradely labeled cells were confined largely to the ventral-lateral region (**Figure 6C**, $N = 6$), and could be identified as pyramidal based on their morphology (**Figures 6D1, D2**). As the rabies label filled dendritic processed, we were able to reconstruct multiple neurons, all of which had soma in the *stratum pyramidale*, apical dendrites projecting into the *stratum radiatum* and basal dendritic arbors in the *stratum oriens* (**Figure 6D2**). To the best of our knowledge, these are the only direct projections from the CA1 to a primary sensory area (Oh et al., 2014), and they are all the more interesting because they target neurons 2 synapses downstream from olfactory receptors in the sensory epithelium where odors are first detected. To ensure that these vCA1 pyramidal neurons were not retrogradely labeled because our injections accidently spilled over into the AOB, we examined in detail the injection site in the bulb for the experiments (**Figure 6E**, $N = 6$) where

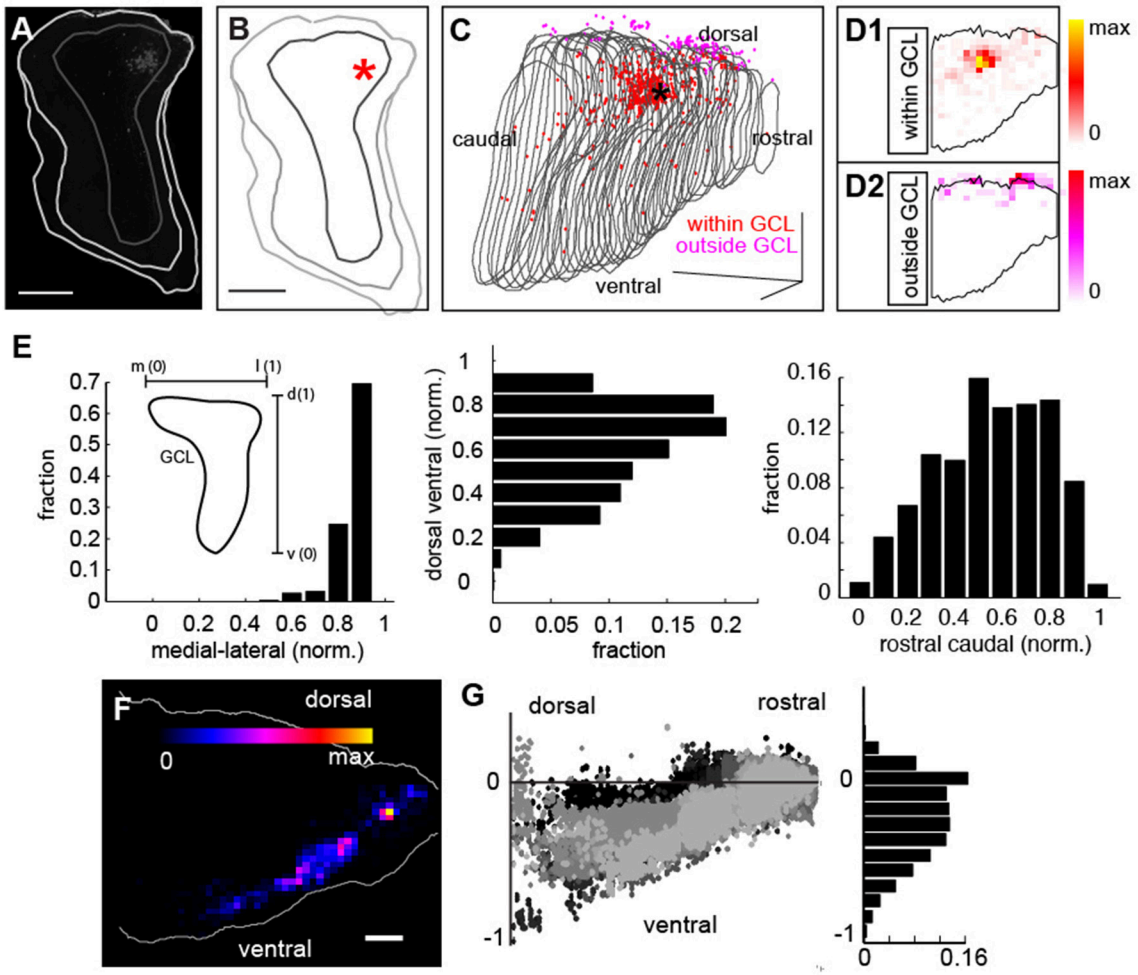

FIGURE 4 | Distribution of injection sites and retrograde label throughout the mouse brain. **(A)** Coronal section of injection site with GCL border in dark gray and tissue border in light gray. Scale bar = 500 um. **(B)** Reconstruction of coronal section in **(B)** with injection site in asterisk. Scale bar = 500 um. **(C)** 3D reconstruction of GCL (gray lines correspond to each coronal section) viewed from a sagittal perspective within neurons at the injection site within the GCL in red and fluorescently labeled neurons outside the GCL in magenta. Scale bar = 500 um. **(D1)** Density of neurons at the injection site within the GCL (black outline) and **(D2)** density of neurons outside the injection site (black outline) but within the bulb. **(E)** Distribution of labeled neurons in the GCL for all experiments along the medial-lateral axis (left), and the dorsal-ventral axis (middle) and the rostral-caudal axis (right). The insert in **(E)** shows that the skew in the distribution is due to the skew in the morphology of the GCL. **(F)** Dorsal ventral density distribution of labeled neurons from 1 example experiment. **(G)** Dorsal-ventral scatter (normalized to injection site) for 10 experiments, (left) reveals that retrograde labeled cells are confined largely to the ventral regions of the mouse brain (right) corresponding to regions who trace their origins to archicortex.

vCA1 cells were densely labeled. In these experiments, the MOB (**Figure 6F1**) was demarcated from the AOB (**Figure 6F2**). Neurons labeled in the injection site (**Figure 6G**, MOB cells in black, AOB cells in red) revealed that less that 1% of the fluorescent labeled neurons in the injection site (99.3% = MOB, 0.07% = AOB, **Figure 6H**) were in the granule layer of the AOB, further suggesting that projections from vCA1 did project directly to the GCL of the MOB. We further confirmed this direct projection by making injections of the anterograde tracer Cholera Toxin-β subunit conjugated to an Alexa 488/555 dye (**Figure 6J**) into the CA1 region (**Figures 6J,K**). Clear axonal projections in the GCL of the bulb (**Figures 6L1, L2**), providing complementary evidence of the link between CA1 and the olfactory bulb.

DISCUSSION

By combining a retrograde virus-labeling strategy with whole-brain 3D reconstruction methods, we describe the structure of centrifugal projections to the GCL of the bulb. First, from a methodological perspective, we provide an approach to segmentation of tissue and neurons that could be used more generally in a number of imaging applications. For instance, in light sheet microscopy application where voxel based approaches have been used (Ahrens et al., 2013), the strategy described here could afford additional insight into the dynamics of single neurons. Additionally, this method may be combined with brain clearing approaches (Liebmann et al., 2016) to reveal the spatial distributions of neurons within and across brain areas. Second,

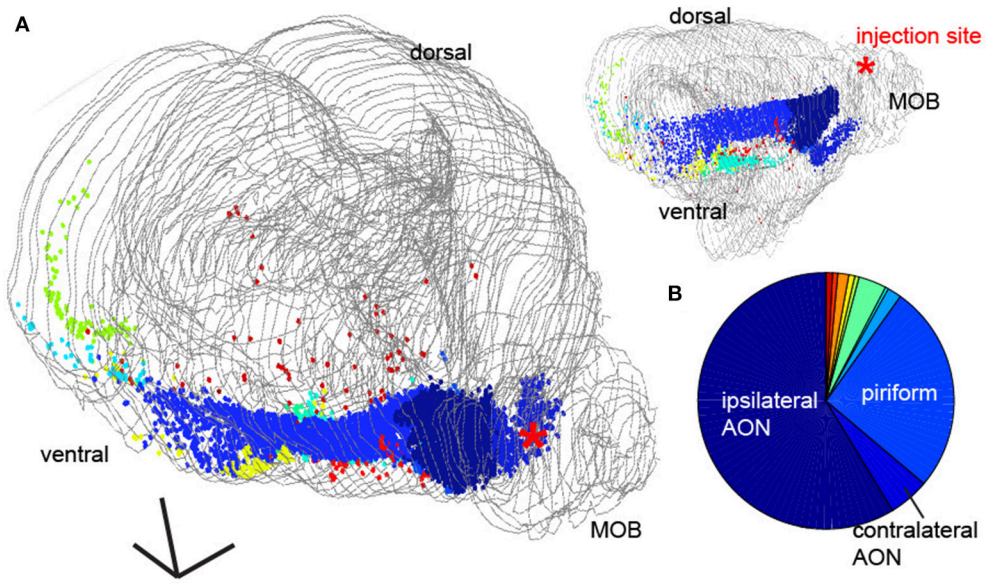

FIGURE 5 | Area identity of feedback projections to the main olfactory bulb. **(A)** Whole brain 3D reconstruction (gray lines correspond to tissue edge for each coronal section) from 2 perspectives with fluorescently labeled neurons in different brain regions represented as points. Scale bar = 500 um. **(B)** Pie chart of the distribution of cells in different brain areas from the 3D reconstruction The three largest sources of feedback are highlighted.

in addition to known projections from olfactory areas such as the AON and the piriform cortex and neuromodulatory areas such as the HDB, we identified direct CA1 pyramidal cell projections from the ventral/lateral region of the hippocampus and the entorhinal cortex directly to the bulb. Although these tracing methods cannot identify the cell types targeted by centrifugal projections to the GCL, which include granule cells, short axon cells, and the lateral dendrites of mitral/tufted (M/T) cells, they do suggest a diverse group of areas all send centrifugal projections to the bulb and could ultimately influence the neuronal activity of M/T cells in response to incoming stimuli. While this feedback and reciprocal connectivity has been identified previous in other species (Shipley and Adamek, 1984; Van Groen and Wyss, 1990) including the mouse (Mohedano-Moriano et al., 2012), and the findings of this study are in line with these previous descriptions, recent studies have overlooked these projections in detailing hippocampal connectivity in the mouse (Bienkowski et al., 2018). Additionally, our imaging method allowed us to identify the spatial pattern of cells across the brain (**Figures 3**–**5**) as well as provide a quantitative description of the relative density of cell projections from all of these feedback regions (**Figure 5**). Notably, we quantified that nearly 10% of projections come from regions other than olfactory cortex and piriform (**Figure 5**). Furthermore, that feedback from regions such as vCA1 and EC are pronounced across multiple experiments (**Figures 5**, **6**) suggests that these circuits could play important roles in shaping odor representations. Although these regions constitute ∼1% of the feedback projections we identified, they number of cells corresponds to the ratios observed in amygdala (1.3%) and ∼1/3 of the cell density of feedback from HDB (3%). Other previous work has shown the role that cholinergic neurons from the basal forebrain play in shaping mitral cells responses (Rothermel et al., 2014), suggesting that even small number of connections, such as those from vCA1 and entorhinal cortex may have a functional role. Furthermore, as vCA1 also projects to piriform cortex, both monosynaptic and disynaptic feedback projections may pay direct and indirect roles across multiple timescales to influence the firing of mitral and tufted cells. Finally, while our method examines the feedback to the GCL, distinctions in between dorsal and ventral bulb (Kobayakawa et al., 2007) may emerge functionally based on asymmetries in the feedback. The functional role of these projections shall be an important focus of future experiments.

While M/T cells, the principal neurons of the bulb are responsive to odor stimulation, their activity can be modulated by other sources (Kay and Laurent, 1999), including centrifugal input, both from olfactory regions (Wesson et al., 2008; Boyd et al., 2012; Markopoulos et al., 2012) and from neuromodulatory centers (Rothermel et al., 2014). In addition to these known projections, we characterized additional feedback from the ventral region of CA1 hippocampus, whose spatial location may provide a hint of their functional role (Moser and Moser, 1998; van Strien et al., 2009; Fanselow and Dong, 2010). Coherence in the electrical activity of Local Field Potentials (LFPs) between the MOB and the hippocampus has been previously described (Martin et al., 2007), including oscillatory coupling in the beta (15–35 Hz) frequencies (Gourévitch et al., 2010), suggesting that these feedback circuits could play a role in LFP coherence between the two regions. Furthermore, ventral/lateral regions of CA1 are important for encoding stress responses (Henke, 1990) and, accordingly, feedback could carry this behaviorally relevant information to gate odor processing at the level of the bulb.

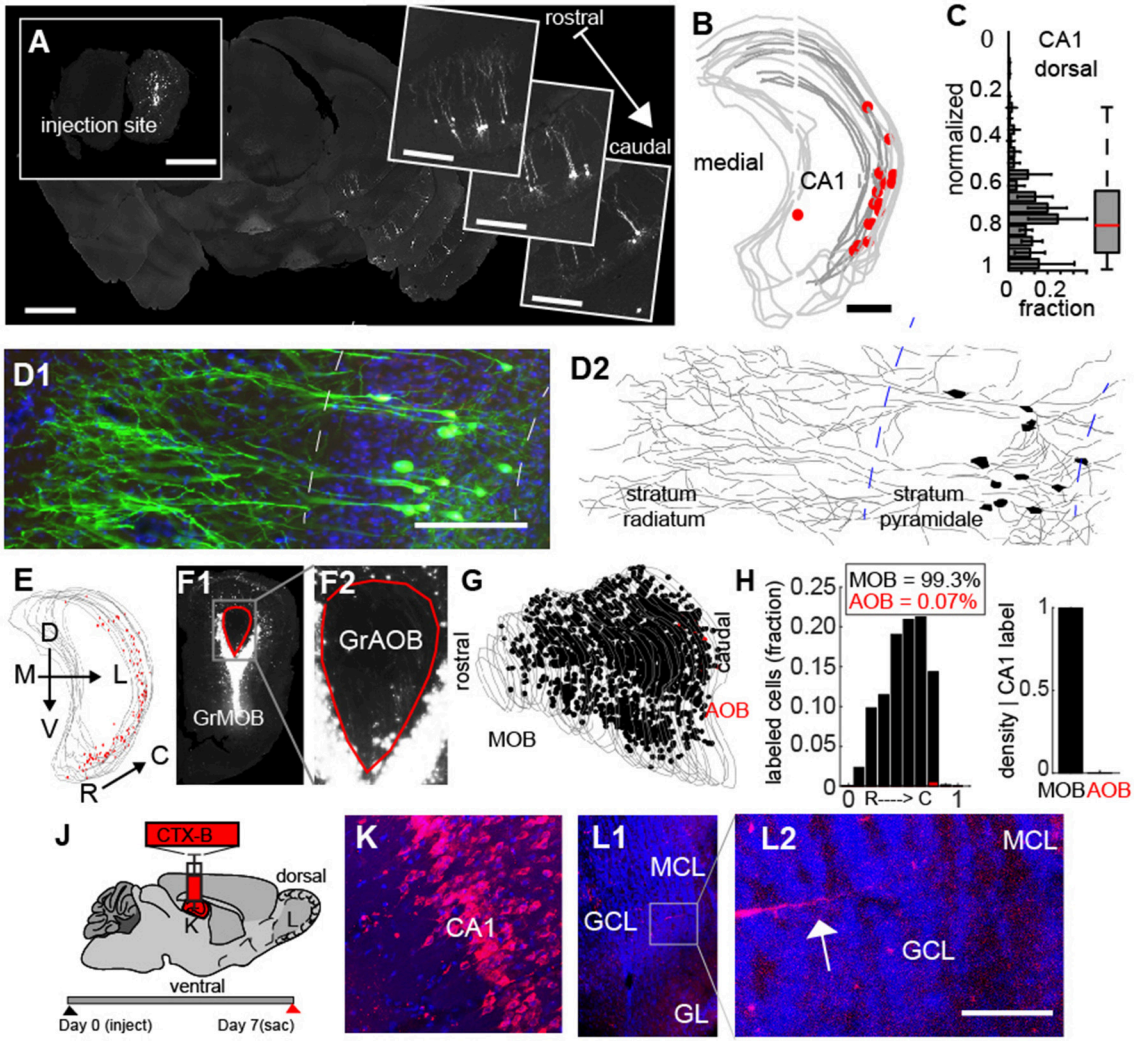

FIGURE 6 | Monosynatic feedback projections from CA1 hippocampus to the main olfactory bulb. **(A)** Widefield fluorescent image of an example of feedback projecting neurons from CA 1 to granule cells in the olfactory bulb (insert). Scale bar = 500 um. **(B)** 3D-reconstruction of hippocampus/CA 1 boundaries with retrogradely labeled neurons (red). Scale bar = 500 um **(C)** Normalized dorsal-ventral distribution of retrogradely labeled neurons in CA 1. **(D1)** Confocal image of CA 1 neurons. **(D2)** Reconstruction of neuronal morphology from cells in **D1**. Scale bar = 200 μm. **(E)** Example of densly labeled neurons in vCA 1. Gray lines = CA 1 boundary. Red dots = retrograde labeled neurons. **(F1)** Injection site in the bulb corresponding to CA 1 reconstruction in **(E)**. GrMOB = Granule cells in main olfactory bulb (MOB). Red line corresponds to the accessory olfactory bulb (AOB) boundary. **(E2)** Enlargement of AOB from **E1**. GrAOB = Granule cells of AOB. **(G)** Reconstruction of all sections of the MOB injection from **(E1)**. Black dots=labeled neurons in MOB. Red dots = labeled neurons in AOB. Gray lines = granule cell layer boundary. **(H)** Distribution of labeled cells along the rostral-caudal axis (normalized) for MOB (black) and AOB (red) in left and ratio of MOB to AOB cells for densly labeled injection sites (right). CTX-B = cholera toxin B subunit. **(K,L)** Correspond to subsequent panels. **(J)** Schematic for anterograde label of axons projecting to the MOB from vCA 1. **(K)** CTX-B injection into CA 1. **(L1)** MOB with axonal arbors from CA 1 injection. **(L2)** Enlargement of G2 shows feedback processes from CA 1. Scale bar = 50 μm.

The limitations of adducing function from structure alone notwithstanding, our description of centrifugal projections suggests unique features of olfactory system. First, unlike other sensory systems, olfactory circuits are highly compact. They target the amygdala and cortex without a thalamic way point and receive direct feedback at the earliest processing stages from a variety of brain regions. Second, circuits tasked with encoding chemical sensation are tethered to evolutionarily old circuits such as those of the hippocampus. Finally, centrifugal feedback to the bulb is diverse.

Unlike other sensory modalities, like vision or audition, where stimulus features have clear equivalents in perceptual space, the link between chemical structure and odor perception remains an open question (Secundo et al., 2014). We propose that one reason for this difference is that the olfactory system has privileged access to the information about prior olfactory representations, the animal's behavioral state, and input from learning and memory systems at the level of the mitral and tufted cells in the bulb via direct centrifugal innervation (Restrepo et al., 2009; Gire et al., 2013). Consequently, coding at the bulb may be far less of a

purely sensory operation and more about the interplay between chemical sensation and memory (Wilson and Stevenson, 2003).

AUTHOR CONTRIBUTIONS

KP conceived the project, designed, carried out the experiments and performed the analysis, and wrote the manuscript. FO provided reagents and assisted with experiments. AT and EK performed histology and imaging. FO, AT, and EK provided feedback on the manuscript. EC, FG, and TS provided assistance with project development and experiment design and contributed feedback to the manuscript writing and editing.

FUNDING

KP is supported by a NIMH K99 MH101634, R01 MH113924, a NSF CAREER Award, a NARSAD Young Investigator Award, the Lieber Foundation, and a Crick-Jacobs Junior Fellowship. FO was supported by the Japan Society for the Promotion of Science, the Japan Science and Technology Agency, the Japan Agency for Medical Research and Development, the Kanae Foundation for the Promotion of Medical Science, the Uehara Memorial Foundation, the Naito Foundation and the Pioneer Fund. EC was supported by the National Institutes of Health and the Kavli Institute for Brain and Mind at University of California San Diego. Support for FG was provided by The Mathers Foundation, The JPB Foundation, and the Helmsley Foundation. TS was supported by Howard Hughes Medical Institute, ONR N000141310672, and ONR N000141210299.

ACKNOWLEDGMENTS

We wish to thank J. Fitzpatrick and J. Kasuboski for assistance with imaging. We thank members of the EC, FG, and TS lab for providing helpful comments on this manuscript, and M. L. Gage and S. Skinner for feedback on the manuscript.

REFERENCES

Ahrens, M. B., Orger, M. B., Robson, D. N., Li, J. M., and Keller, P. J. (2013). Whole-brain functional imaging at cellular resolution using light-sheet microscopy. *Nat. Methods* 10, 413–420. doi: 10.1038/nmeth.2434

Babadi, B., and Sompolinsky, H. (2014). Sparseness and expansion in sensory representations. *Neuron* 83, 1213–1226. doi: 10.1016/j.neuron.2014.07.035

Bienkowski, M. S., Bowman, I., Song, M. Y., Gou, L., Ard, T., Cotter, K., et al. (2018). Integration of gene expression and brain-wide connectivity reveals the multiscale organization of mouse hippocampal networks. *Nat. Neurosci.* 21, 1628–1643. doi: 10.1038/s41593-018-0241-y

Boyd, A. M., Sturgill, J. F., Poo, C., and Isaacson, J. S. (2012). Cortical feedback control of olfactory bulb circuits. *Neuron* 76, 1161–1174. doi: 10.1016/j.neuron.2012.10.020

Callaway, E. M., and Luo, L. (2015). Monosynaptic circuit tracing with glycoprotein-deleted rabies viruses. *J. Neurosci.* 35, 8979–8985. doi: 10.1523/JNEUROSCI.0409-15.2015

Davison, I. G., and Ehlers, M. D. (2011). Neural circuit mechanisms for pattern detection and feature combination in olfactory cortex. *Neuron* 70, 82–94. doi: 10.1016/j.neuron.2011.02.047

de Olmos, J., Hardy, H., and Heimer, L. (1978). The afferent connections of the main and the accessory olfactory bulb formations in the rat: an experimental HRP-study. *J. Comp. Neurol.* 181, 213–244. doi: 10.1002/cne.901810202

Fanselow, M. S., and Dong, H.-W. (2010). Are the dorsal and ventral hippocampus functionally distinct structures? *Neuron* 65, 7–19. doi: 10.1016/j.neuron.2009.11.031

Gire, D. H., Restrepo, D., Sejnowski, T. J., Greer, C., De Carlos, J. A., and Lopez-Mascaraque, L. (2013). Temporal processing in the olfactory system: can we see a smell? *Neuron* 78, 416–432. doi: 10.1016/j.neuron.2013.04.033

Gonzalez, R. C., Woods, R. E., and Eddins, S. L. (2004). *Digital Image Processing Using MATLAB*. New Jersey, NJ: Pearson Prentice Hall.

Gourévitch, B., Kay, L. M., and Martin, C. (2010). Directional coupling from the olfactory bulb to the hippocampus during a go/no-go odor discrimination task. *J. Neurophysiol.* 103, 2633–2641. doi: 10.1152/jn.01075.2009

Haberly, L. B., and Price, J. L. (1978). Association and commissural fiber systems of the olfactory cortex of the rat. *J. Comp. Neurol.* 178, 711–740. doi: 10.1002/cne.901780408

Henke, P. G. (1990). Hippocampal pathway to the amygdala and stress ulcer development. *Brain Res. Bull.* 25, 691–695.

Hovis, K. R., Padmanabhan, K., and Urban, N. N. (2010). A simple method of *in vitro* electroporation allows visualization, recording, and calcium imaging of local neuronal circuits. *J. Neurosci. Methods* 191, 1–10. doi: 10.1016/j.jneumeth.2010.05.017

Kay, L. M., and Laurent, G. (1999). Odor- and context-dependent modulation of mitral cell activity in behaving rats. *Nat. Neurosci.* 2, 1003–1009. doi: 10.1038/14801

Kobayakawa, K., Kobayakawa, R., Matsumoto, H., Oka, Y., Imai, T., Ikawa, M. et al. (2007). Innate versus learned odour processing in the mouse olfactory bulb. *Nature* 450, 503–508. doi: 10.1038/nature06281

Leitner, F. C., Melzer, S., Lütcke, H., Pinna, R., Seeburg, P. H., Helmchen, F., et al. (2016). Spatially segregated feedforward and feedback neurons support differential odor processing in the lateral entorhinal cortex. *Nat. Neurosci.* 19, 935–944. doi: 10.1038/nn.4303

Liebmann, T., Renier, N., Bettayeb, K., Greengard, P., Tessier-Lavigne, M., and Flajolet, M. (2016). Three-dimensional study of Alzheimer's disease hallmarks using the idisco clearing method. *Cell Rep.* 16, 1138–1152. doi: 10.1016/j.celrep.2016.06.060

Markopoulos, F., Rokni, D., Gire, D. H., and Murthy, V. N. (2012). Functional properties of cortical feedback projections to the olfactory bulb. *Neuron* 76, 1175–1188. doi: 10.1016/j.neuron.2012.10.028

Martin, C., Beshel, J., and Kay, L. M. (2007). An olfacto-hippocampal network is dynamically involved in odor-discrimination learning. *J. Neurophysiol.* 98, 2196–2205. doi: 10.1152/jn.00524.2007

Mohedano-Moriano, A., de la Rosa-Prieto, C., Saiz-Sanchez, D., Ubeda-Bañon, I., Pro-Sistiaga, P., de Moya-Pinilla, M., et al. (2012). Centrifugal telencephalic afferent connections to the main and accessory olfactory bulbs. *Front. Neuroanat.* 6:19. doi: 10.3389/fnana.2012.00019

Moser, M. B., and Moser, E. I. (1998). Functional differentiation in the hippocampus. *Hippocampus* 8, 608–619.

Oh, S. W., Harris, J. A., Ng, L., Winslow, B., Cain, N., Mihalas, S., et al. (2014). A mesoscale connectome of the mouse brain. *Nature* 508, 207–214. doi: 10.1038/nature13186

Okuyama, T., Kitamura, T., Roy, D. S., Itohara, S., and Tonegawa, S. (2016). Ventral CA1 neurons store social memory. *Science.* 353, 1536–1541. doi: 10.1126/science.aaf7003

Osakada, F., and Callaway, E. M. (2013). Design and generation of recombinant rabies virus vectors. *Nat. Protoc.* 8, 1583–1601. doi: 10.1038/nprot.2013.094

Osakada, F., Mori, T., Cetin, A. H., Marshel, J. H., Virgen, B., and Callaway, E. M. (2011). New rabies virus variants for monitoring and manipulating activity and gene expression in defined neural circuits. *Neuron* 71, 617–631. doi: 10.1016/j.neuron.2011.07.005

Padmanabhan, K., Eddy, W. F., and Crowley, J. C. (2010). A novel algorithm for optimal image thresholding of biological data. *J. Neurosci. Methods* 193, 380–384. doi: 10.1016/j.jneumeth.2010.08.031

Padmanabhan, K., Osakada, F., Tarabrina, A., Kizer, E., Callaway, E. M., Gage, F. H., et al. (2016). Diverse representations of olfactory

information in centrifugal feedback projections. *J. Neurosci.* 36, 7535–7545. doi: 10.1523/JNEUROSCI.3358-15.2016

Padmanabhan, K., and Urban, N. N. (2010). Intrinsic biophysical diversity decorrelates neuronal firing while increasing information content. *Nat. Neurosci.* 13, 1276–1282. doi: 10.1038/nn.2630

Paxinos, G., and Franklin, K. (2004). *The Mouse Brain in Stereotaxic Coordinates, 2nd ed*. San Diego, CA: Elsevier Academic Press.

Petzold, G. C., Hagiwara, A., and Murthy, V. N. (2009). Serotonergic modulation of odor input to the mammalian olfactory bulb. *Nat. Neurosci.* 12, 784–791. doi: 10.1038/nn.2335

Price, J. L., and Powell, T. P. (1970). An experimental study of the origin and the course of the centrifugal fibres to the olfactory bulb in the rat. *J. Anat.* 107, 215–237.

Restrepo, D., Doucette, W., Whitesell, J. D., McTavish, T. S., and Salcedo, E. (2009). From the top down: flexible reading of a fragmented odor map. *Trends Neurosci.* 32, 525–531. doi: 10.1016/j.tins.2009.06.001

Rothermel, M., Carey, R. M., Puche, A., Shipley, M. T., and Wachowiak, M. (2014). Cholinergic inputs from Basal forebrain add an excitatory bias to odor coding in the olfactory bulb. *J. Neurosci.* 34, 4654–4664. doi: 10.1523/JNEUROSCI.5026-13.2014

Secundo, L., Snitz, K., and Sobel, N. (2014). The perceptual logic of smell. *Curr. Opin. Neurobiol.* 25, 107–115. doi: 10.1016/j.conb.2013.12.010

Shipley, M. T., and Adamek, G. D. (1984). The connections of the mouse olfactory bulb: a study using orthograde and retrograde transport of wheat germ agglutinin conjugated to horseradish peroxidase. *Brain Res. Bull.* 12, 669–688.

Stettler, D. D., and Axel, R. (2009). Representations of odor in the piriform cortex. *Neuron* 63, 854–864. doi: 10.1016/j.neuron.2009.09.005

Van Groen, T., and Wyss, J. M. (1990). Extrinsic projections from area CA1 of the rat hippocampus: olfactory, cortical, subcortical, and bilateral hippocampal formation projections. *J. Comp. Neurol.* 302, 515–528. doi: 10.1002/cne.903020308

van Strien, N. M., Cappaert, N. L., and Witter, M. P. (2009). The anatomy of memory: an interactive overview of the parahippocampal-hippocampal network. *Nat. Rev. Neurosci.* 10, 272–282. doi: 10.1038/nrn2614

Wesson, D. W., Carey, R. M., Verhagen, J. V., and Wachowiak, M. (2008). Rapid encoding and perception of novel odors in the rat. *PLoS Biol.* 6:e82. doi: 10.1371/journal.pbio.0060082

Wickersham, I. R., Finke, S., Conzelmann, K.-K., and Callaway, E. M. (2007). Retrograde neuronal tracing with a deletion-mutant rabies virus. *Nat. Methods* 4, 47–49. doi: 10.1038/nmeth999

Wilson, D. A., and Stevenson, R. J. (2003). The fundamental role of memory in olfactory perception. *Trends Neurosci.* 26, 243–247. doi: 10.1016/S0166-2236(03)00076-6

Yan, Z., Tan, J., Qin, C., Lu, Y., Ding, C., and Luo, M. (2008). Precise circuitry links bilaterally symmetric olfactory maps. *Neuron* 58, 613–624. doi: 10.1016/j.neuron.2008.03.012

Conflict of Interest Statement: The authors declare that the research was conducted in the absence of any commercial or financial relationships that could be construed as a potential conflict of interest.

frontiers in Neuroanatomy

ORIGINAL RESEARCH
published: 13 March 2019
doi: 10.3389/fnana.2019.00023

Uncovering the Functional Link Between *SHANK3* Deletions and Deficiency in Neurodevelopment Using iPSC-Derived Human Neurons

*Guanqun Huang[1,2†], Shuting Chen[1†], Xiaoxia Chen[1†], Jiajun Zheng[1], Zhuoran Xu[3], Abolfazl Doostparast Torshizi[3,4], Siyi Gong[1], Qingpei Chen[1], Xiaokuang Ma[2], Jiandong Yu[1], Libing Zhou[1], Shenfeng Qiu[2], Kai Wang[3,4] and Lingling Shi[1,5]**

[1] Guangdong-Hongkong-Macau Institute of CNS Regeneration, Ministry of Education CNS Regeneration Collaborative Joint Laboratory, Jinan University, Guangzhou, China, [2] Department of Basic Medical Sciences, College of Medicine – Phoenix, The University of Arizona, Phoenix, AZ, United States, [3] Department of Biomedical Informatics, Columbia University, New York, NY, United States, [4] Children's Hospital of Philadelphia, Philadelphia, PA, United States, [5] Co-innovation Center of Neuroregeneration, Nantong University, Nantong, China

SHANK3 mutations, including *de novo* deletions, have been associated with autism spectrum disorders (ASD). However, the effects of *SHANK3* loss of function on neurodevelopment remain poorly understood. Here we generated human induced pluripotent stem cells (iPSC) *in vitro*, followed by neuro-differentiation and lentivirus-mediated shRNA expression to evaluate how *SHANK3* knockdown affects the *in vitro* neurodevelopmental process at multiple time points (up to 4 weeks). We found that *SHANK3* knockdown impaired both early stage of neuronal development and mature neuronal function, as demonstrated by a reduction in neuronal soma size, growth cone area, neurite length and branch numbers. Notably, electrophysiology analyses showed defects in excitatory and inhibitory synaptic transmission. Furthermore, transcriptome analyses revealed that multiple biological pathways related to neuron projection, motility and regulation of neurogenesis were disrupted in cells with *SHANK3* knockdown. In conclusion, utilizing a human iPSC-based neural induction model, this study presented combined morphological, electrophysiological and transcription evidence that support that *SHANK3* as an intrinsic, cell autonomous factor that controls cellular function development in human neurons.

Keywords: induced pluripotent stem cells, neural stem cells, *SHANK3*, electrophysiology, RNA-Seq, autism, transcriptome

OPEN ACCESS

Edited by:
Basilis Zikopoulos,
Boston University, United States

Reviewed by:
Thomas Bourgeron,
Institut Pasteur, France
Chiara Verpelli,
Institute of Neuroscience (IN), Italy

****Correspondence:***
Lingling Shi
tlingshi@jnu.edu.cn

† These authors have contributed equally to this work

Received: *01 June 2018*
Accepted: *07 February 2019*
Published: *13 March 2019*

Citation:
Huang G, Chen S, Chen X, Zheng J, Xu Z, Doostparast Torshizi A, Gong S, Chen Q, Ma X, Yu J, Zhou L, Qiu S, Wang K and Shi L (2019) Uncovering the Functional Link Between SHANK3 Deletions and Deficiency in Neurodevelopment Using iPSC-Derived Human Neurons. Front. Neuroanat. 13:23. doi: 10.3389/fnana.2019.00023

INTRODUCTION

Autism spectrum disorders (ASD) are neurodevelopmental disorders characterized by impairments in social communication and interaction, and repetitive behaviors and restricted interests (Freitag et al., 2010; State and Levitt, 2011; Lyall et al., 2017; Rubeis et al., 2018). Multiple studies have indicated a strong connection between ASD and genetic variations of synapse-related genes and proteins, including neuroligins (*NLGNs*), postsynaptic density protein 95 (PSD-95), and SH3 and multiple ankyrin repeat domains proteins (*SHANKs*) (Xing et al., 2016; Nakanishi et al., 2017;

Kathuria et al., 2018). In particular, genetic association studies have identified a significant role for *SHANK3*, which encodes a major scaffolding protein at postsynaptic densities (PSD). The *SHANK3* protein contains multiple structural domains including ankyrin repeat, Src homologous, PDZ, proline-rich, Homer binding site, sterile alpha motif (Du et al., 1998; Grabrucker et al., 2011; Monteiro and Feng, 2017; Ponna et al., 2018), through which other PSD proteins extensively interact to form the post-synaptic protein signaling complex. Genomic sequencing and exon sequencing from ASD patients have indicated a strong connection between rare mutations in *SHANK3* and ASD (Durand et al., 2007; Nemirovsky et al., 2015).

Currently, it is unclear how *SHANK3* mutations confer ASD risks by affecting the developmental trajectory of the brain, particularly the excitatory glutamatergic synapses. Several studies have utilized mouse models (Peca et al., 2011; Wang et al., 2016, 2017; Chen et al., 2017; Harony-Nicolas et al., 2017; Luo et al., 2017; Zhao et al., 2017; Amal et al., 2018; Kerrisk Campbell and Sheng, 2018; Qin et al., 2018) and neuronal cell models (Bidinosti et al., 2016; Lu et al., 2016; Bey et al., 2018; Taylor et al., 2018) to explore the role of *SHANK3* gene in synaptic function and animal behavior. The variation of *SHANK3* at different loci resulted in distinct behavioral phenotypes when modeled in mice. Most of these *SHANK3* mutant mice showed deficits in social interactions, with or without cognitive impairment, repetitive behavior, anxiety and motor deficit. Abnormal cortico-striatal circuits, disrupted excitability and inhibitory (E/I) balance, and synaptic dysfunction have been identified to be associated with the mechanism of ASD-like behavior (Bozdagi et al., 2010; Peca et al., 2011; Wang et al., 2011; Mei et al., 2016; Vicidomini et al., 2017; Bey et al., 2018). These analysis of synaptic physiology and mice behavior revealed a strong causal connection between *SHANK3* mutations and ASD-like endophenotypes.

Despite the above cited studies, analyses on animal models cannot completely simulate human genetic background on neurodevelopment. In some cases, human brain tissue sample has been collected for neural development disease study (Konopka et al., 2012; Parikshak et al., 2016), however, the sample resource is very limited. More than 10 years ago, Takahashi and Yamanaka made a remarkable breakthrough in stem cell research when they generated ES-like cells from adult somatic cells using a cocktail of transcription factors (Takahashi et al., 2007). More recently, new methods have been developed to reprogram adult somatic cells (such as fibroblasts) into iPSC. Following the discovery of iPSC, several studies have fueled enthusiasm for their use in neurological disorders, and iPSC have been validated to develop into many kinds of neural subtype cells (Chambers et al., 2009; Shi et al., 2012; Kang et al., 2017; Lin et al., 2018). Creating neuronal cultures from iPSC has received wide attention for the potential to create translatable disease-in-a-dish models. This development has made it possible to mimic human neuron development defect following disease candidate gene dysfunction. One advantage of iPSC is that the cells possess genetic background that is distinctly human; the other is that stem cells could mimic certain aspects of human neural development courses *in vitro*. So far, iPSC have been increasingly recognized as a significant *in vitro* cellular model to study the function of susceptible genes in neurological diseases and neurodevelopment diseases. iPSC have successfully used to model the cellular physiology and guide therapeutic endeavors in Rett syndrome, Alzheimer's disease and schizophrenia by revealing the functional effects of genetic mutations with single neuron resolution (Marchetto et al., 2010; Mitne-Neto et al., 2011; Israel et al., 2012). We have also previously used iPSC models to study the functional effects of *NRXN1* deletion and *NLGN4X* deletions (Shi et al., 2013), in which we found that such synaptic genes as *NLGN4X/NRXN1* deletion directly impacts neurodevelopmental process, synaptic adhesion and neuron differentiation during the formation of neurons and their connections. *NLGNs*, which bind presynaptic *NRXNs*, are anchored in scaffold protein *SHANK3* indirectly. *SHANK3* interacts with multiple key synaptic components including glutamate receptors and their anchoring proteins, ion channels (Du et al., 1998), thus serves as a master organizer of the PSD (Naisbitt et al., 2000; Hayashi et al., 2009). *NLGNs/NRXNs/SHANK3* gene complex play an import role in synapse generation and neuron function formation.

To gain insights on the critical cellular and molecular effects of *SHANK3* in human neuron development, we generated functional neurons derived from iPSC and transduced by shRNA-based lentivirus against *SHANK3*, as well as a control shRNA. Utilizing this iPSC-based *in vitro* model, we investigated the transcriptome alteration, coupled with morphology and electrophysiological analyses to determine the impacts of *SHANK3* knockdown in the developing human neurons.

MATERIALS AND METHODS

The Generation of iPSC-Derived Neural Development Model

Human urine epithelium-derived cells were reprogrammed into iPSC [generated by Dr. Pei's lab (Zhou et al., 2011)]. The iPSC were cultured in Matrigel (BD Matrigel^{TM}, hESC-qualified Matrix)-coated six-well plates. MTeSR^{TM} medium (Stemcell Technologies) was added to each well (2 ml per well) and replaced once a day. After reaching 95% confluence, the cells were passaged with EDTA (1:3) in Matrigel-coated 12-well plates. Once the cells density reached almost 100%, the medium was switched to neural induction medium (N_2B_{27} + 2 inhibitors (5 μmol/L Dorsomorphin and 5 μmol/L SB431542, Selleck). Dorsomorphin and SB431542 effectively inhibit SMAD signaling pathway by blocking phosphorylation of ALK4, ALK5, ALK7 receptors and successfully improve the efficiency of neural induction. At day 8, the cells were mechanically scraped to Matrigel-coated six-well plates with neural proliferation system I (N_2B_{27}, Thermo-Fisher Scientific) medium. At day 16, the cells in 6-well cell plates were mechanically scraped to T25 flasks and were cultured with neural proliferation system II (N_2B_{27} + 20 ng/mL bFGF + 20 ng/mL EGF, Thermo-Fisher Scientific). NPCs were expanded for three passages with Accutase (StemPro Accutase cell dissociation reagent), single cells of NPCs were directly plated at a density of 10^5 cells per well on glass coverslips coated with glial cell feeder layer (prepared from rat astrocyte, P0–P3), and Matrigel in 24-well plates for morphology analysis. At the same time, the single

cells of NPCs were directly plated at a density of $2.5 \times 10^{\wedge 6}$/well in Matrigel-coated 6-well plates for q-PCR and sequencing. The medium was switched to neuron differentiation medium (N_2, B_{27}, Thermo Fisher Scientific; 1 μM dibutyryl-cAMP, Sigma-Aldrich; 20 ng bdnf, PeproTech). The plates were kept at 37°C thereafter in a humidified incubator with 95% air and 5% CO_2.

Virus Transduction and Quantitative Real-Time-PCR

Single cells of NPCs were directly cultured on Matrigel-coated plates. The next day the cells were infected by shControl and shSHANK3 lentivirus in proper titers. (TRIPZ Human *SHANK3* shRNA, Dharmacon, Inc., ID: V2THS_264172, 1×10^8 TU/mL). Six hours after infection, the viruses were removed and replaced with NPCs proliferation system containing doxycycline (1 μg/mL). Three days after infection, medium was switch to NPCs proliferation system containing doxycycline (1 μg/mL) and puromycin (1 μg/mL). The cells were lysed with Trizol, total RNA was extracted using an RNeasy mini kit. RNA concentration (OD_{260}/OD_{280}) was measured using Nanodrop 2000C Spectrophotometer. Total RNA was reverse transcribed into cDNA using the PrimeScript™ RT reagent Kit with gDNA Eraser (Perfect Real Time). Real-time quantitative PCR was performed with SYBR Premix Ex Taq™ II detection System and Inumin detection instrument. The primer sequences are as follows:

Human SHANK3-F, CAGGACGCGCTCAACTATG;
Human SHANK3-R, GCATAAACTCGCCGCTTGTA;
Human GAPDH-F, CATGTTCGTCATGGGTGTGAA;
Human GAPDH-R, AGTGATGGCATGGACTGTGGT.
All data was normalized to the GAPDH mRNA level and shSHANK3 knockdown efficiency were calculated.

Morphology Analysis

Neurons were sparsely infected with lentivirus (1×10^8 TU/mL) packed with a tetracycline-controlled red fluorescent protein (RFP) expression sequence to obtain fluorescent images. Neurons plated on glass coverslips were used for morphological construction at 3–28 days after plating. Standard immunohistochemistry protocols were used. The neurons were fixed using 4% paraformaldehyde for 30 min, washed with PBS, permeabilized with 0.3% Triton X (Thermo Scientific) in PBS and blocked with 1% BSA (VETEC™) in PBS. The neurons were stained by double immunofluorescence with DAPI (Thermo Scientific, D1306, 1:1000) and the following antibodies: Mouse-Oct4 (BD Pharmingen, 6765-100, 1:200), Mouse-SSEA4 (Invitrogen, 41-4000, 1:100), Mouse-SOX2 (R&D Systems, MAB2018, 1:500), Rabbit-Nestin (Millipore, ABD9, 1:1000), Mouse-TBR1(Abcam, ab31940, 1:800), Mouse-TUJ1 (Covance, Princeton, T8660, 1:1000), Tau1 (Millipore, MAB3420, 1:500), Ribbat-Map2 (2a + 2b) (Millipore, AB5622, 1:1000), Mouse-PSD95 (Thermo Fisher, MA1-045, 1:150), Rabbit-synapsin I (Millipore, AB1543, 1:1000), secondary antibodies used include: donkey anti-mouse Alexa-488 (Invitrogen, R37114, 1:1000), donkey anti-mouse Alexa-546 (Invitrogen, A10036, 1:1000). Images of neurons were visualized with 20, 40, and 60× objective (Imager Z2, Zeiss) and digitized using a Zeiss camera (Axiocam 506 mono, Zeiss). The soma area, growth cone area, neurite length and branches were analyzed and quantified with ImageJ. The complexity of neurite arborization was analyzed with the ImageJ/FIJI. Statistic results were analyzed by two-way ANOVA with GraphPad Prism 5.01. Growth cone was categorized into three types (blunt ended, filopodial and lamellipodial) as described by Khazaei et al. (2014).

Electrophysiological Recording

The RFP-expressing iPSC-derived neurons were perfused with artificial spinal cerebral fluid (pH 7.4, in mM: 126 NaCl, 2.5 KCl, 2 $CaCl_2$, 2 $MgCl_2$, 26 $NaHCO_3$, 1.25 NaH_2PO_4 and 10 D-glucose) bubbled with 95% O_2 and 5% CO_2 at RT (25 ± 1°C). The neurons were visualized with a 40× water objective on an IR-DIC microscope (Nikon Eclipse FN-1 microscope) and recorded using an amplifier (MultiClamp 700B, Molecular Devices). Borosilicate microelectrodes with a resistance of 4–8 MΩ were pulled using a pipette puller (Narishige PC10) and the glass pipette was filled with filtered intracellular recording solution (pH 7.3, 290–310 mOsm, in mM: 126 *K*-gluconate, 4 KCl, 0.3 Na_2-ATP, 4 Mg-GTP, 10 phosphocreatine, 10 HEPES). Recordings were filtered at 3 kHz (low pass) and digitized at 20 kHz (DigiData 1550A, Molecular Devices), and statistical analysis of electrophysiology data was collected and analyzed with pClamp10 (Molecular Devices). The input resistance of the cells (R_{in}) was recorded as the slope of linear fits of current-voltage plots responded to 1 s current injection steps (−10, 2, or 3 pA steps) in current-clamp mode. Cells were held at resting membrane potential (RMP), not corrected for a liquid junction potential. Spontaneous excitatory (EPSCs) and inhibitory (IPSCs) postsynaptic currents were recorded at a −70 and 0 mV, respectively, for 3 min in voltage-clamp mode. sEPSCs and sIPSCs were verified by complete blockade of kynurenic acid (KyA, 3 mM, Sigma-Aldrich) or SR95531 (10 μM, Tocris). The sodium currents (I_{Na}) were recorded at −70 mV in voltage-clamp mode and elicited by 200 ms voltage steps from −20 to 50 mV at 5 mV increments.

Illumina Transcriptome Library Preparation and Sequencing

The total RNA was subject to RNA-Seq analysis. RNA concentration was measured using Nanodrop 2000C Spectrophotometer and Qubit 3.0 (Invitrogen). RNA integrity number and the library length were detected by BioAnalyzer 2100 (Agilent). Library construction was performed with Truseq RNA Access library Pre Kit (Illumina, RS-301-2001). The library was sequenced on a HiSeq X platform (Illumina).

Western Blot Analysis

Cultured cells were washed twice with PBS (1 mL/well), then 200 μl cell lysis buffer (RIPA buffer (Thermo scientific) supplemented with protease inhibitor (Calbiochem, 50:1) were added to each well. Cells were collected with a cell scraper (NEST Biotechnology). Cell suspension was collected and allowed to stand on ice for 30 min, and then centrifuged at 4°C, 14,000 rpm

for 15 min. After centrifugation, supernatant was transferred to a new tube and protein concentration was quantified using Pierce™ BCA Protein Assay Kit (Thermo Fisher Scientific). Samples were mixed with 10× loading buffer (Takara) and boiled for 10 min 20 μg proteins were loaded each lane and separated by SDS-PAGE gel. The proteins were then transferred to PVDF membranes (Millipore), incubated with an antibody against *SHANK3* protein (Santa Cruz Biotechnology), diluted in 5% BSA overnight at 4°C. The PVDF membranes were then washed three times, and further processed with HRP-conjugated secondary antibodies for 2 h at room temperature. Protein signals were developed using ChemiDoc Touch Imaging System. The optical density of immunoreactive bands was quantified by ImageJ.

Bioinformatics Analysis of RNA-Seq Data

All the sequencing data were obtained as FASTQ files for 16 samples with four different measurement times at days 0, 7, 9, and 28. To improve the quality of alignment, we used FastQC (Andrews, 2010) to investigate the quality of reads in the dataset and Cutadapt (Martin, 2011) for removing adapter sequences. The reads were then mapped to the reference human genome (GRCh38) and gene count data were produced using STAR (Dobin et al., 2013). Then, we proceeded with downstream analysis after assuring that the rates of uniquely mapped reads for all samples were higher than 80%.

Generalized linear model was used to identify differentially expressed genes between *SHANK3* knockdown group and the control group over time using DESeq2 (Love et al., 2014). MA-plot (**Supplementary Figure S6**) and dispersion estimate plot (**Supplementary Figure S7**) were generated for quality control before further analysis. After performing regularized-logarithm transformation on the raw counts data using *rlog* function in DESeq2, we plotted a sample hierarchical clustering heatmap using Euclidian distance to assess the similarity among samples. The limma R package (Ritchie et al., 2015) was used for correcting batch effects among the samples produced from two different sequencing experiments. Benjamini and Hochberg correction methods (Benjamini and Hochberg, 1995) for multiple-testing adjustment were adopted in moderated *t*-test to identify differentially expressed genes. The genes with adjusted *p*-value less than 0.05 were selected as differentially expressed genes, which represent the ones at one or more time points with a gene-specific difference accounting for the difference at time 0. Then Kyoto Encyclopedia of Genes and Genomes (KEGG) pathways and Gene Ontology (GO) enrichment analysis were performed for function annotation on WebGestalt (Wang et al., 2013), and FDR < 0.01 was used as the threshold to examine significant results.

RESULTS

Generation of Neural Development Model *in vitro*

To study the effect of *SHANK3* loss of function on neurodevelopment, we generated iPSC-derived neural development model *in vitro* with two-inhibitor culture system (Dorsomorphin and SB4315242) and collected neural cells for knockdown efficiency or morphology analysis at multiple time points (days 3, 7, 9, 14, 21, and 28). The iPSC were induced into neural progenitor cells (NPC), which were cultured in floating, and then differentiated into neurons on coverslips. The 1st day of induction on coverslip was defined as day 0 (D0).

The human iPSC used in this experiment were stained positive with specific iPSC marker proteins (OCT4 and SSEA4) (**Figure 1A**) and specific neural stem cells marker proteins (SOX2, nestin) (**Figure 1B**), indicating that the cells have the potential of differentiating into neurons. NPC were directly plated on glass coverslips coated with rat glial cell feeder layer and Matrigel in 24-well plates for sample collection in different time points. The neuron-specific marker protein TUJ-1, Tau-1, Map2, deep layer cortical neuron marker protein TBR1, and subtype neuron marker protein VGLUT1, GABA, TH were detected by immunohistochemistry (**Figure 1C** and **Supplementary Figure S1**). The results showed that neurons derived from iPSC could be differentiated into multiple CNS neuron types, reflecting a highly induction efficiency (estimated > 90%) using our method. We have further quantified that in this *in vitro* induced neural model, the proportion of glutamatergic neurons is about 10.7%, dopaminergic neurons is about 17.3%, GABAergic neurons is approximately 54.9%.

SHANK3 expression pattern data from Allan Brain Institute pointed to abundant expression in the developing brain at very early development stage[1] (**Supplementary Figure S2A**), that is consistent with our Western blot result of *SHANK3* (**Supplementary Figure S2B**). We also found that expression of *SHANK3* emerged in early neuronal development stages (P0-7), and continue to increase into young adulthood (P42). This increased levels of *SHANK3* protein may reflect the time course of cortical synapse maturation (**Supplementary Figures S2A,B**).

Morphological Effects of *SHANK3* Knockdown on Neurodevelopment

We have generated two sets of neural induced model from two separate iPSC lines in this whole project, and we used one clone of each line to collect data for morphology analysis (**Supplementary Figure S3**). To knockdown *SHANK3* expression in NPC, we infected NPC with shRNA-based lentivirus against *SHANK3* or with a control lentivirus, here after referred as shSHANK3 and shControl, respectively. RFP signals were observed in 1 week post infection. Knockdown efficiency was verified at multiple levels, including qRT-PCR (**Figure 2A**), Western blot analysis (**Figure 2B**) and immunocytochemistry staining of cultured neurons (**Figure 2C**). These data suggest lentiviral-mediated *SHANK3* knockdown was highly effective.

We next investigated the impact of *SHANK3* knockdown on neurite length. Neuron morphology was traced and reconstructed by ImageJ. Sholl analysis was used to quantify neurite complexity. We further classified neurons into three groups in our *in vitro* model, excitatory neurons ($VGLUT1^+$), inhibitory neurons ($GABA^+$), and putative dopamine neurons

[1] http://developingmouse.brain-map.org/

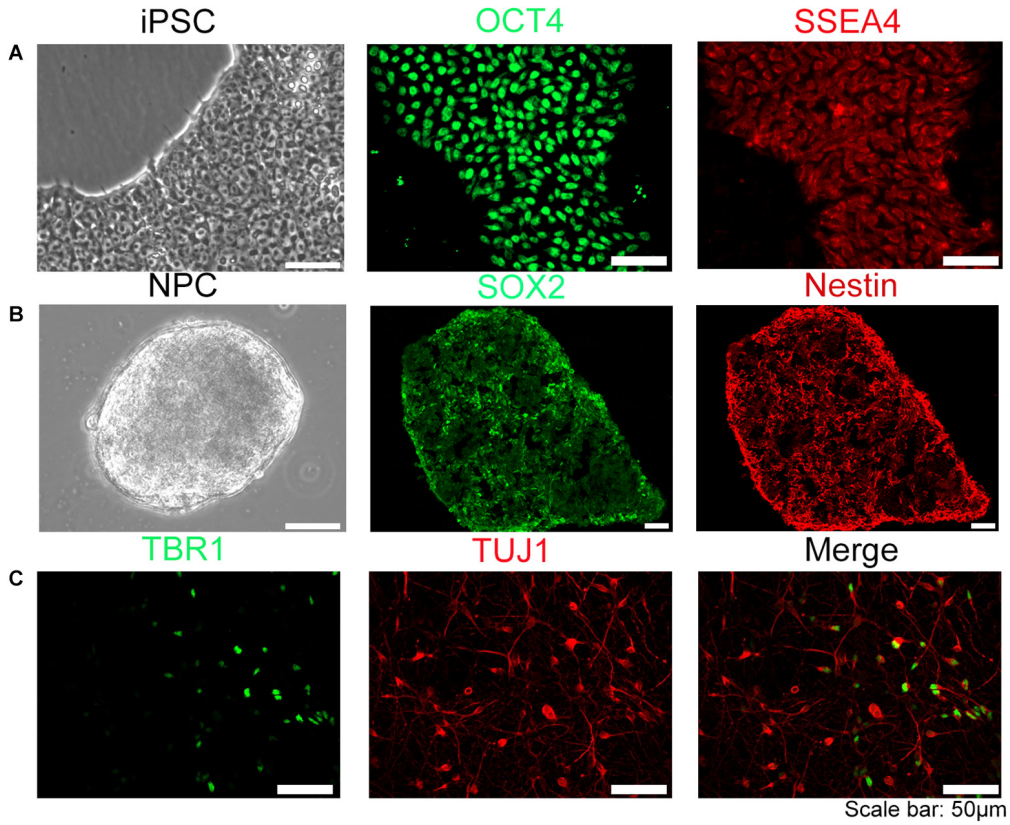

FIGURE 1 | Establishment of human iPSC model. The iPSC were induced into neural progenitor cells (NPC) and further differentiated into neurons. **(A)** iPSC used in our experiment were OCT4, SSEA4 positive stain. **(B)** NPC induced form iPSC were SOX2, Nestin positive. **(C)** Neurons differentiated from NPC were TUJ-1 or TBR1 positive, suggesting that NPC can be differentiated into multiple categories of neural cells. Scale bar: 50 μm.

(TH^+) (**Supplementary Figure S1**). To distinguish axons and dendrites, we used MAP2 and Tau1 antibody to co-stain dendrites ($MAP2^+$) and axons ($Tau1^+$) (**Supplementary Figure S1**). Neuronal morphology was constructed base on RFP expression. We examined the effects of *SHANK3* knockdown on neurite development (e.g., length and the number of branches) at different time points. We observed that, the total dendrites length of VGLUT1 positive neuron decreased significantly with *SHANK3* knockdown on D14 ($p = 0.0003$), D21 ($p < 0.0001$) (**Figures 2D,E**); GABA positive neuron dendritic length decreased significantly on D9 ($p = 0.0181$), D14 ($p = 0.0219$), D21 ($p = 0.0037$) (**Figures 2H,I**); while TH positive neuron dendritic length decreased significantly on D9 ($p = 0.0159$), D14 ($p = 0.2482$), D21 ($p = 0.0035$) (**Figures 2L,M**). These results indicate that *SHANK3* gene is required for the development of neurite length in iPSC derived human neurons.

To further assess of neurite complexity, Sholl analysis was used to quantify neurite branches number. We observed that *SHANK3* knockdown had significant effect on neurite complexity in excitatory neurons at D21 (**Figure 2F**), especially on the neurite branches number close to the cell body area within 100 microns, while *SHANK3* deficit had few effect on neurite complexity of inhibitory neurons and dopamine neurons (**Figures 2J,N**). These results indicate that *SHANK3* gene is required for the development of excitatory neuronal branches in iPSC-derived human neurons.

We next investigated the morphological differences following *SHANK3* knockdown in iPSC-derived human neurons, we analyzed soma and growth cone development in shControl and shShank3 groups. We observed that soma area of VGLUT1 positive neuron significantly decreased with *SHANK3* knockdown at D21 ($p = 0.0097$), the soma area of GABA positive neurons decreased at D9 ($p = 0.0254$), D21 ($p = 0.0108$), the soma area of TH positive neurons decreased at D9 ($p = 0.0294$), D14 ($p = 0.0002$) (**Figures 2G,K,O**). We have identified TH and GABA positive neuronal soma size in D9, as VGLUT1 antibody specifically stained excitatory neuron at least in D14 in our study. The results indicate that *SHANK3* gene knockdown affects the development of neuronal soma in early neuronal development of D9, at least in GABA and TH positive neurons. In addition, *SHANK3* knockdown has a significant effect on VGLUT1 positive neuron in D21.

Next, we examined whether *SHANK3* is required for growth cone formation. We found that the area of the growth cone significantly decreased with *SHANK3* knockdown at all-time points (days 9, 12, 15, and 21) (**Figure 3**). These results indicate

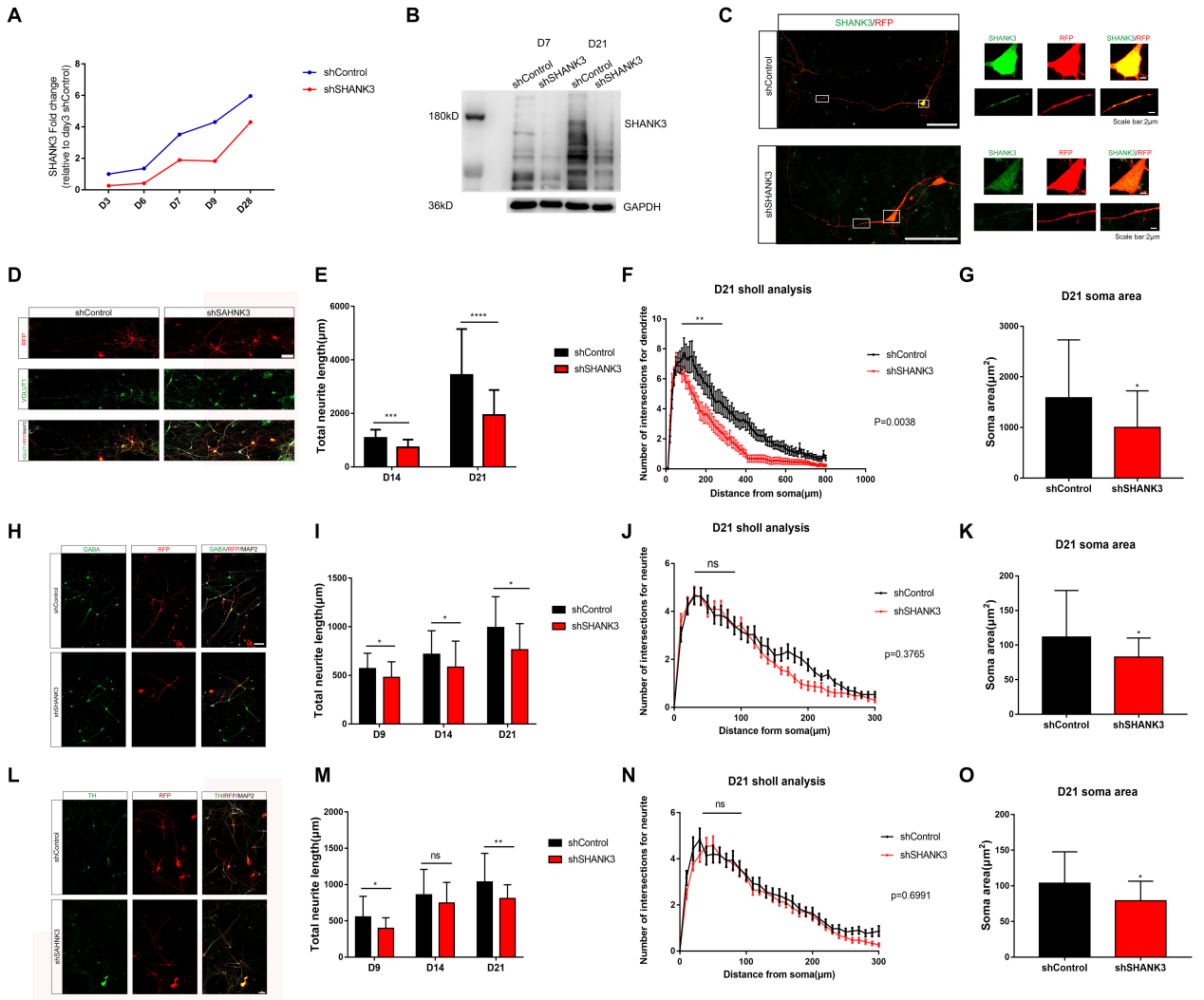

FIGURE 2 | *SHANK3* knockdown profoundly affects neurite length, complexity of neurite arborization and soma area. **(A–C)** The efficiency of *SHANK3* knockdown in iPSC-derived neurons was verified by qRT-PCR (D3, D7, and D28), Western blot (D7 and D21), and immunofluorescence staining (D28). **(D,H,L)** Immunofluorescence staining of VGLUT1, GABA, TH, and MAP2 confirms generation of multiple types of differentiated neurons in our culture system. Scare bar: 50 μm. **(E,I,M)** Comparison of neurite length in neurons infected with shShank3 and shControl viruses. Data are shown as mean ± SEM. *$p < 0.05$, **$p < 0.01$, ***$p < 0.001$, and ****$p < 0.0001$. (D9: GABA: $n = 33$ control and 35 *SHANK3* knockdown cells, $p = 0.0181$; TH: $n = 33$ control and 33 *SHANK3* knockdown cells, $p = 0.0159$); D14: VGLUT1: $n = 22$ control and 22 *SHANK3* knockdown cells, ($p = 0.0003$), GABA: $n = 33$ control and 34 *SHANK3* knockdown cells ($p = 0.0219$), TH: $n = 34$ control and 37 *SHANK3* knockdown cells ($p = 0.2482$); D21: VGLUT1: $n = 22$ control and 24 *SHANK3* knockdown cells ($p < 0.0001$), GABA: $n = 30$ control and 29 *SHANK3* knockdown cells ($p = 0.0037$), TH: $n = 30$ control and 30 *SHANK3* knockdown cells, ($p = 0.0035$). **(F,J,N)** Analysis of the effect of *SHANK3* gene knockdown on the complexity of neurite arborization. Statistical significance was evaluated by two-way ANOVA, $p = 0.0038$ (D21), $p = 0.3765$ (D21), $p = 0.6991$ (D21), data are shown as mean ± SEM. *$p < 0.05$, **$p < 0.01$, ***$p < 0.001$. **(G,K,O)** Statistic analysis of the effect of *SHANK3* knockdown on neuronal soma area. Statistical significance was evaluated by two-way ANOVA, data are shown as mean ± SEM. *$p < 0.05$, **$p < 0.01$, ***$p < 0.001$. (D21: VGLUT1: $n = 22$ control and 24 *SHANK3* knockdown cells, GABA: $n = 30$ control and 29 *SHANK3* knockdown cells, TH: $n = 30$ control and 30 *SHANK3* knockdown cells).

that *SHANK3* knockdown affects the development of neuronal growth cone area.

SHANK3 Knockdown Affects the Electrophysiological Properties of Developing Human Neurons

To investigate functional outcomes of *SHANK3* knockdown, we conducted whole cell patch clamp recording on RFP-expressing neurons at 3.5 and 5.5 weeks (**Figure 4**). To determine if excitatory synaptic transmission was altered in neurons with *SHANK3* knockdown, were recorded spontaneous excitatory post-synaptic currents (sEPSCs). We found that the frequency of sEPSC from *SHANK3* knockdown neurons was reduced relative to control neurons at 3.5 and 5.5 weeks (**Figure 4C**). In addition, spontaneous inhibitory post-synaptic currents (IPSCs) were recorded to determine the effect of *SHANK3* down-regulation in inhibitory synaptic transmission. We found that the frequency of

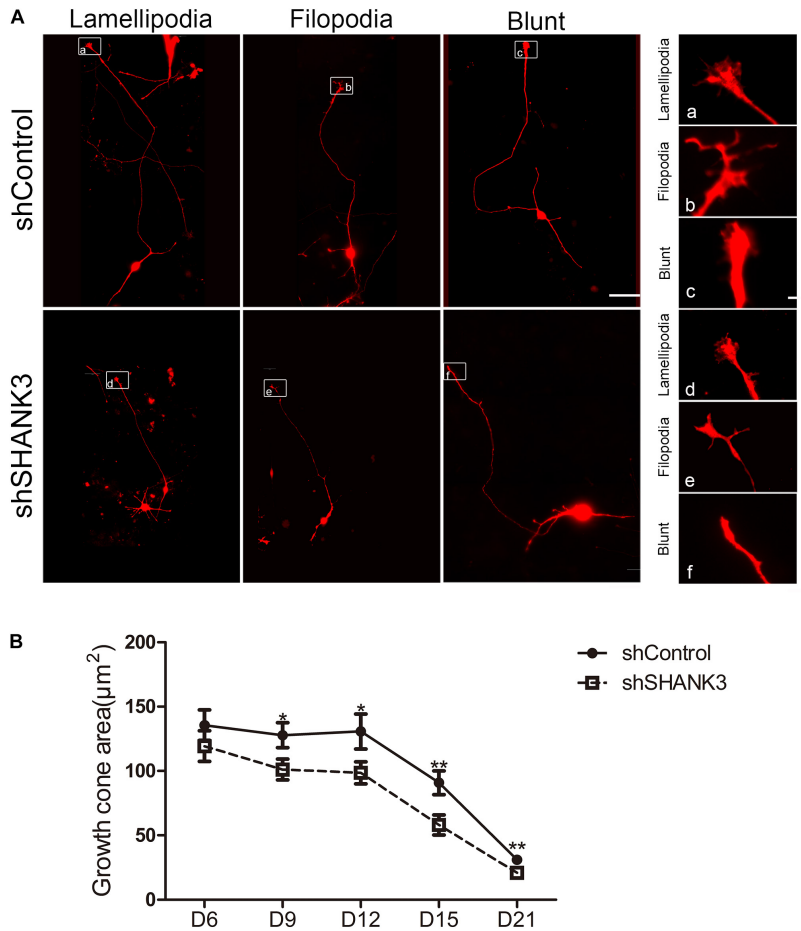

FIGURE 3 | The effects of *SHANK3* knockdown on neurons growth cone area. **(A)** Representative images of the growth cones of shControl and shSHANK3 transduced neurons. Scare bar: schematic diagram 50 μm; enlarged area 5 μm. **(B)** Analysis of the effect of *SHANK3* knockdown on the growth cone area of neurons. Statistical significance was evaluated by two-way ANOVA, date are shown as mean ± SEM. $^{*}p < 0.05$, $^{**}p < 0.01$. (D6: $n = 57$; D9: $n = 67$ control and 62 *SHANK3* knockdown cells; D12: $n = 64$ control and 63 *SHANK3* knockdown cells; D15: $n = 65$ control and 61 *SHANK3* knockdown cells; D21: $n = 67$ control and 64 *SHANK3* knockdown cells; D28: $n = 65$).

sIPSC recorded from *SHANK3* knockdown neurons was reduced relative to control neurons at 3.5 and 5.5 weeks (**Figure 4D**). Taken together, these results suggest that both excitatory synaptic transmissions and inhibitory synaptic transmission are impaired in neurons with *SHANK3* knockdown.

Next, we investigated sodium currents threshold (I_{Na}). The results showed that neurons with *SHANK3* knockdown exhibited an increase in the threshold of sodium currents at 3.5 weeks and increased significantly ($p = 0.2245$) relative to control neurons at 5.5 weeks (**Figure 4F**), suggesting that down-regulation of *SHANK3* may extensively alter receptors for neurotransmission and voltage gated ion channels.

Effects of *SHANK3* Knockdown on Transcriptome Regulation

We first examined the overall similarity between samples by using hierarchical clustering. It can be seen from the heatmap (**Figure 5A** and **Supplementary Figure S8**) that samples from the same measurement time points were clustered together regardless of the *SHANK3* knockdown status. These results indicate that time exerted more important influence in determining gene expression variation comparing with *SHANK3* knockdown.

Next, differentially expressed genes were estimated between *SHANK3* knockdown and control groups across four measurement time points (**Supplementary Table S1**). The main question is whether *SHANK3* knockdown can alter gene expression over time and which genes would show this gene-specific differences. Considering the correlation of the response variable among different measurement time points and batch effects from two different experiments, we designed a generalized linear model with independent variables of batch, time, *SHANK3* knockdown and an interaction term with *SHANK3* and time. By testing the interaction term with likelihood ratio test, we identified 1576 differentially expressed genes (**Supplementary Figure S5**) over time with adjusted *p*-value less than 0.05 (p-adj < 0.05). Among those overall differentially expressed genes, 1078 genes showed significant difference at day 28, which can be seen obviously in the heatmap of differentially expressed genes (**Figure 5B**). The down regulated expression level of

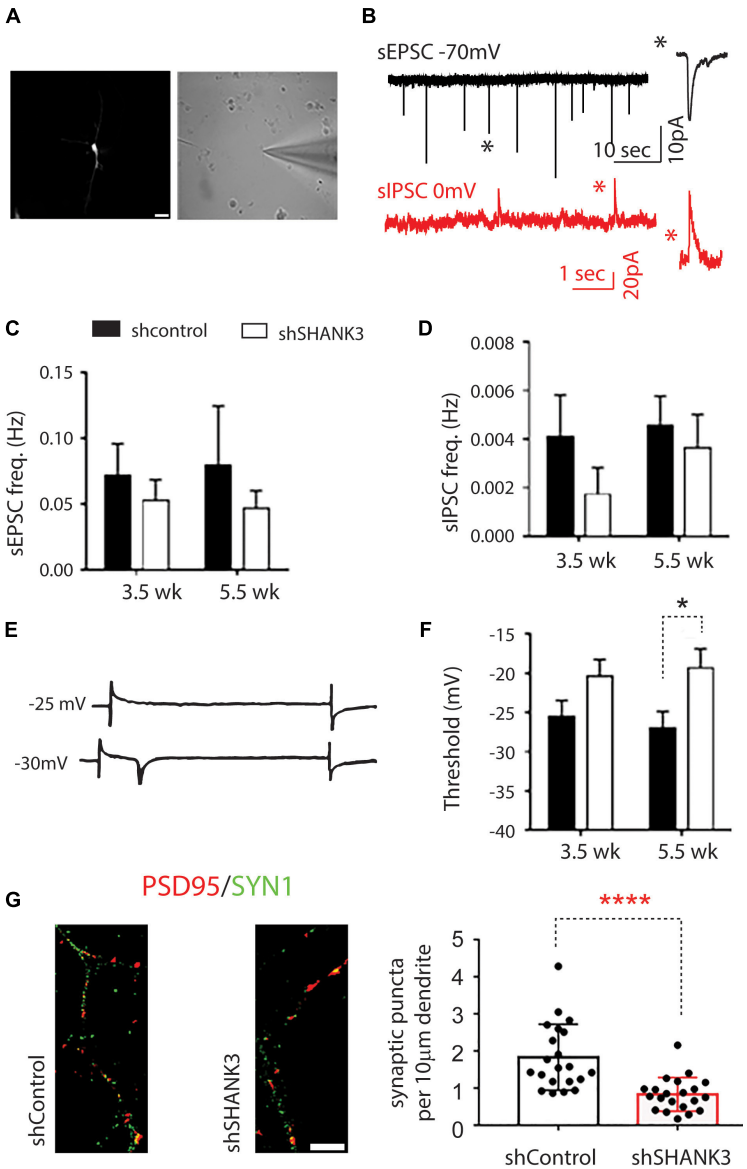

FIGURE 4 | The effects of *SHANK3* gene knockdown on neurons function. **(A)** RFP-expressing cell visualized under differential interference contrast microscopy. **(B)** Sample recordings of sEPSC (top panel) and sIPSC (bottom panel). **(C)** Averaged frequency of spontaneous EPSCs at 3.5 and 5.5 weeks in culture (3.5 weeks: n = 17 control and 12 *SHANK3* knockdown cells; 5.5 weeks: n = 11 control and 15 *SHANK3* knockdown cells). **(D)** Averaged frequency of spontaneous IPSCs (3.5 weeks: n = 10 control and 7 *SHANK3* knockdown cells; 5.5 weeks: n = 15 control and 13 *SHANK3* knockdown cells). **(E)** Illustration of sodium currents elicited by voltage step commands. **(F)** The threshold of sodium currents (3.5 weeks: n = 19 control and 12 *SHANK3* knockdown cells; 5.5 weeks: n = 15 control and 15 *SHANK3* knockdown cells). *$p < 0.05$. **(G)** Synapse number changes following *SHANK3* knockdown: PSD95 (GFP) and Synapsin I (RFP) co-staining showed the synaptic puncta was reduced after *SHANK3* knockdown (n = 21, ****$p < 0.0001$).

SHANK3 gene and 9 genes with smallest p-adj values are shown in **Supplementary Figure S5**.

Next, we examined whether these top differentially expressed genes shared common pathways or functional categories. We performed over representation enrichment analysis for pathways and gene ontology (**Supplementary Figure S4**). The results showed that *SHANK3* down-regulation led to hippo signaling pathway (Hsa04390, FDR = 1.33e-05) and focal adhesion (Hsa04510, FDR = 1.84e−08) abnormalities. In addition, terms in GO analysis including neuron projection development (GO: 0031175, FDR = 0e+00, BP), regulation of neurogenesis (GO: 0050767, FDR = 0e+00, BP), central nervous system development (GO: 0007417, FDR = 0e+00, BP), focal adhesion (GO: 0005925, FDR = 1.2e−09, CC) and calcium ion binding (GO: 0005509, FDR = 4.7e−11, MF) were significantly enriched (**Table 1**). These transcriptome data, in combination with the morphological and functional alternations, suggest *SHANK3* has a previously uncircumscribed role in developing neurons

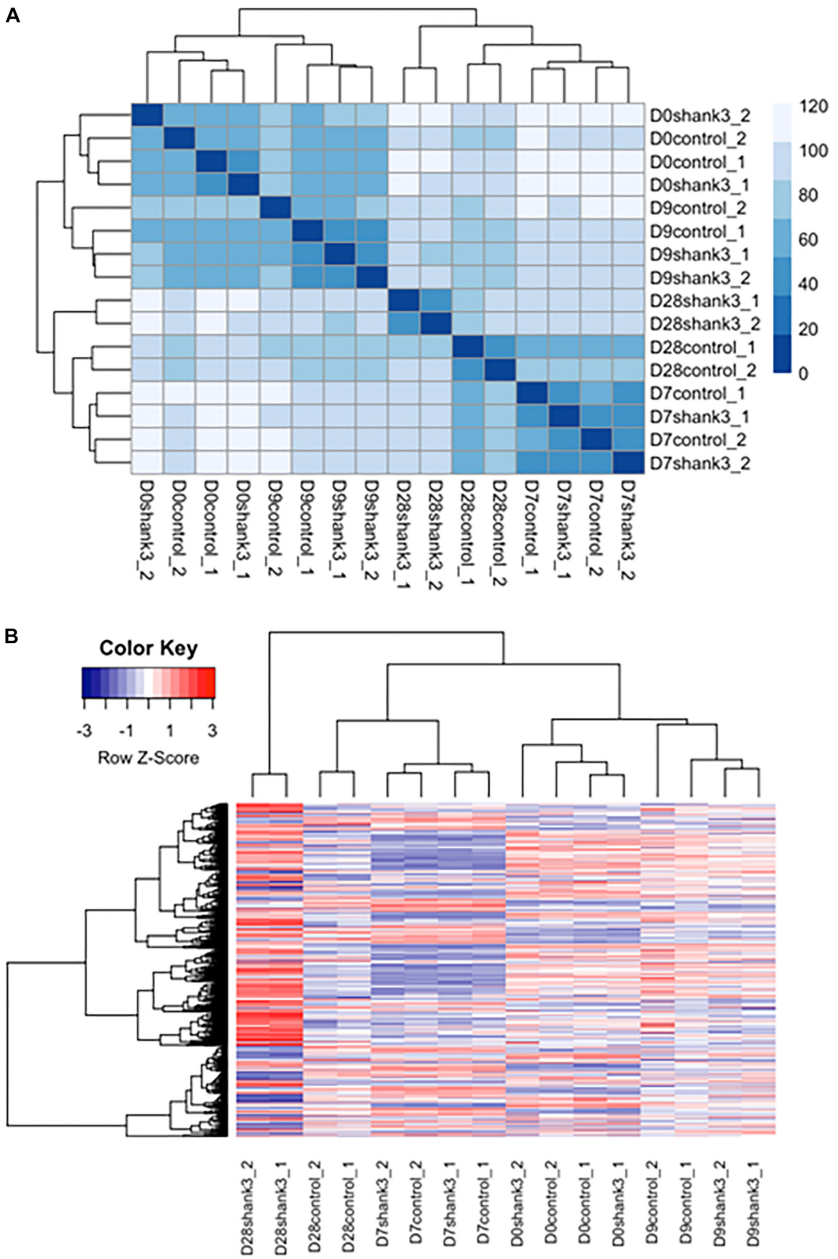

FIGURE 5 | Heatmap of differentially expressed genes associated with *SHANK3* loss of function. **(A)** Euclidian distances were used for constructing sample distance matrix. After eliminating batch effect that would separate the samples from two different experiments apart, samples measured at the same time points were clustered together over influence of gene knockdown. **(B)** Heatmap for 1576 differentially expressed genes (p-adj<0.05) over time. It can be seen obviously that the expression difference mainly occurred at day 28.

in addition to its function as a postsynaptic scaffold protein in mature synapse.

DISCUSSION

In this study, we investigated the impact of *SHANK3* loss of function in neurodevelopment by combining morphology, electrophysiology and transcriptomics analyses in neurons derived from iPSC. *SHANK3* is a PSD components of glutamatergic synapses that plays a key role in excitatory synaptic transmission in adult brain (Rubeis et al., 2018). There is strong indication that *SHANK3* gene mutations or variations are associated with increased autism risks, *SHANK3* point mutations, truncations, and disruption by chromosome translocation have been all reported in ASD cases (Durand et al., 2007; Gauthier et al., 2009; Sykes et al., 2009; Peca et al., 2011; Boccuto et al., 2013). Consistently, mice

TABLE 1 | Affected signaling pathways and gene ontology categories.

GO	Name	FDR	Observed counts	Expected counts	Enrichment ratio	*P*-value
Has:04390	Hippo signaling pathway	1.33e−05	32	11.84	2.7	1.32e−07
Has:04510	Focal adhesion	1.84e−08	45	16.16	2.78	1.21e−10
GO:0031175	Neuron projection development	0e+00	132	62.24	2.12	0e+00
GO: 0050767	Regulation of neurogenesis	0e+00	119	51.79	2.3	0e+00
GO:0007417	Central nervous system development	0e+00	143	68.37	2.09	0e+00
GO: 0005925	Focal adhesion	1.2e−09	60	23.7	2.53	2.34e−11
GO:0005509	Calcium ion binding	4.7e−11	106	49.32	2.15	2.6e−14

mutant for *SHANK3* display multiple neurological deficits including compulsive and repetitive behaviors, that are associated with deficits in corticostriatal circuits (Peca et al., 2011; Xiaoming et al., 2011; Bariselli et al., 2016; Sebastiano and Camilla, 2016; Zhou et al., 2016; Bariselli and Bellone, 2017; Jin et al., 2018). However, the molecular targets of *SHANK3* that are causally linked to the ASD-like behavioral deficits, and how disruption of *SHANK3* derails the normal neurodevelopmental trajectory in human brain remain largely unclear. In this study, we took advantage of an iPSC neuron induction model, and used shRNA to induce *SHANK3* loss of function to investigate the neurodevelopmental role of *SHANK3* protein in human neurons. Consistent with previous reports (Durand et al., 2012), we found that synapse numbers were reduced, and synaptic transmissions are impaired in *SHANK3* knockdown neurons.

It's worth noting that *SHANK3* protein expressed in early developing stage from NPC to mature neuron based on our qRT-PCR and Western blot results. This is consistent with the curated data on the Allen Brain Atlas, which show that *SHANK3* mRNA is abundant (**Supplementary Figure S2**). This early *SHANK3* expression suggests a functional role in developing neuronal morphology and emergence of function, in addition to being a postsynaptic scaffold protein at the mature glutamatergic synapses at later developmental stages. We also found that *SHANK3* deficiency affects the morphology at early development stages, before the synaptic transmission are established and mature. Our results show that *SHANK3* knockdown reduces dendritic arborization in three major types of differentiated neurons (glutamatergic/GABAergic/dopamine). We also found that the soma size and growth cone area of glutamatergic/GABAergic/dopamine neuron were reduced as a result. We further confirmed *SHANK3* protein did localize in dendrite and soma by immunofluorescence staining experiments. A few previous studies have reported that *SHANK3* localization in neuron soma, dendrite, growth cone (Du et al., 1998; Boeckers et al., 2002; Durand et al., 2012; Halbedl et al., 2016) and the dendritic deficits (Durand et al., 2012) following *SHANK3* deficiency in human neurons. *SHANK3* protein is found to be located at the tip of actin filaments and promotes growth cone motility in developing neuron by enhancing actin polymerization (Durand et al., 2012; Halbedl et al., 2016). A *de novo SHANK3* mutation in the ankyrin domain (Q312R) is associated with growth cone formation and motility in animal models (Durand et al., 2012; Kathuria et al., 2018). Kathuria et al. (2018) uncovered the *SHANK3*'s critical role in neuronal morphogenesis and the early defects which are associated with ASD-associated mutations. Our data are consistent with previous studies. Morphology analyses indicates strong correlation between *SHANK3* knockdown and dendritic branching abnormalities; neuron soma area, neurite number and length, complexity of neurite arborization and growth cone area are all significantly affected by *SHANK3* knockdown.

Another important finding from this study is that *SHANK3* knockdown changes the transcriptome landscape across the time course of neural development. We identified genes with temporal changes of expression patterns across four time points between control shRNA and the shSHANK3 groups, and performed pathway enrichment analysis. We showed that even in early stage, the development-associated pathways can be affected by *SHANK3* knockdown, which is consistent with the observed abnormality of neuronal morphology following *SHANK3* knockdown in early stage of neurodevelopment. The PI3K associated pathway has been enriched in transcriptome analysis in our study, which also support the hypothesis that *SHANKs* mutation serves to cross-link further disease related signaling cascades (mTOR/PI3K). Altogether, these results indicate that *SHANK3* has a previously unappreciated role in early neuronal development, in addition to its well established functional role as a postsynaptic scaffold protein in the mature synapse.

Our electrophysiology results are generally consistent with the morphological findings. We found that both excitatory synaptic transmissions and inhibitory synaptic transmission are impaired in *SHANK3* knockdown neurons. However, the underlying mechanism of the synaptic transmission impairment in *SHANK3* knockdown neurons should be investigated in future studies. Taken together, our study show *SHANK3* loss of function profoundly derails the developmental trajectory of human neurons. Many functional domains of neural development are impaired, including dysplasia of neuronal soma, stunted neurite and growth cone, and altered of transcriptome. These changes suggest *SHANK3* loss of function as an intrinsic, cell autonomous factor that impairs cellular development in human neurons both in early and in mature stages, which may account for the brain pathological changes in neurodevelopmental diseases such as ASD.

AUTHOR CONTRIBUTIONS

LS designed the study and contributed to transcriptome data analysis, wrote and approved the final version of the manuscript. GH, SC, XC, QC, ZX, SG, and XM conducted cell culture experiments, neural morphology, and other data analysis. GH and SC co-wrote the final version of the manuscript. JZ and JY generated the electrophysiological data. KW and AT contributed to performing transcriptome data analysis. LZ and SQ contributed to the experimental design, data analyses, and preparation of the manuscript.

FUNDING

This project was supported by the National Natural Science Foundation of China (81771222) (LS), National Key Research and Development Program of China, Stem Cell and Translational Research (2017YFA0105102) (LS), Guangzhou Science and Technology Innovation Development special fund project (201804010212) (LS), Fundamental Research Funds for the Central Universities of China (11617435) (LS), and Program of Introducing Talents of Discipline to Universities (B14036) (LS).

ACKNOWLEDGMENTS

We thank Prof. Duanqing Pei (Chinese Academy of Sciences) for providing the iPSC models used in the study.

SUPPLEMENTARY MATERIAL

The Supplementary Material for this article can be found online at: https://www.frontiersin.org/articles/10.3389/fnana.2019.00023/full#supplementary-material

FIGURE S1 | Expression of MAP2 (GFP), Tau1 (RFP), VGLUT1 (GFP), GABA (GFP), and TH (GFP) in D28 neurons in our *in vitro* model, further supporting successful differentiation into various mature neuron types.

FIGURE S2 | Expression of *SHANK3* mRNA and protein at very early developmental stages in mouse brain. **(A)** *SHANK3* mRNA is abundantly expressed in the developing brain at early development stage (source: Allen Brain Atlas). **(B)** *SHANK3* protein can be detected by Western blot in developing mouse cortex tissues as early as P0, but increase as the brain matures.

FIGURE S3 | Two sets of neural induced model from two separate iPSC lines have been generated in this whole project, and we used one clone of each line to collect data for morphology analysis. Both of these two clone showed significant decrease on dendritic length and soma size after *SHANK3* knockdown. Comparison of neurite length in another iPSC line neurons infected with shShank3 and shControl viruses. Morphology reconstructed with ImageJ, statistical significance was evaluated by *T*-test, data are shown as mean ± SEM. $^*p < 0.05$. **(A)** D9: GABA: $n = 35$ control and 33 *SHANK3* knockdown cells, ($p = 0.0037$); **(B)** D9: TH: $n = 30$ control and 31 *SHANK3* knockdown cells, ($p = 0.0340$); **(C)** Detailed Vector Map of the pTRIPZ lentiviral vector.

FIGURE S4 | Bar charts of gene ontology function categories.

FIGURE S5 | Effects of *SHANK3* knockdown on gene expression levels. Expression level were transformed into log10 scale. Green lines represent *SHANK3* knockdown group and red lines represent control group. **(A)** Expression level of *SHANK3* gene over time between knockdown and control group. **(B)** Expression level of top 9 genes with smallest *p*-adj values.

FIGURE S6 | RNA sequence data MA plot. Each dot represents a gene. *X*-axis is the average expression over all samples. *Y*-axis is the log2 fold change between *SHANK3* knockdown and control group. Genes with FDR<0.01 are shown in red. This plot demonstrates that only genes with a large average normalized count contain more information to yield a significant call.

FIGURE S7 | Dispersion estimation plot for raw counts data. The dispersion fit is an exponentially decaying curve where dispersion decreased as the counts increased of all genes. Each black point represents the dispersion estimates for each gene across all the eight samples. The red line is fitted trend line, which shows the dispersions' dependence on the mean. Blue points are the final estimates from black points shrunk to the red fitted line. The blue circles are genes which are labeled as dispersion outliers and are not shrunk toward the fitted trend line. *X*-axis is the average expression over all eight samples. *Y*-axis is the dispersion value. The dispersion fit for all genes is an exponentially decaying curve where dispersion decreased with the mean of normalized counts.

FIGURE S8 | The list of top 150 differentially expressed (DE) at each time point between the knockdown and control samples.

TABLE S1 | Differential expression between SHANK3 knockdown and control groups.

REFERENCES

Amal, H., Barak, B., Bhat, V., Gong, G., Joughin, B. A., Wang, X., et al. (2018). Shank3 mutation in a mouse model of autism leads to changes in the S-nitroso-proteome and affects key proteins involved in vesicle release and synaptic function. *Mol. Psychiatry*. doi: 10.1038/s41380-018-0113-6

Andrews, S. (2010). *FastQC: A Quality Control Tool for High Throughput Sequence Data*. Available online at: http://www.bioinformatics.babraham.ac.uk/projects/fastqc

Bariselli, S., and Bellone, C. (2017). VTA DA neuron excitatory synapses in *SHANK3* Deltaex(4-9) mouse line. *Synapse* 71, doi: 10.1002/syn.21955

Bariselli, S., Tzanoulinou, S., Glangetas, C., Prévost-Solié, C., Pucci, L., Viguié, J., et al. (2016). *SHANK3* controls maturation of social reward circuits in the VTA. *Nat. Neurosci.* 19, 926–934. doi: 10.1038/nn.4319

Benjamini, Y., and Hochberg, Y. (1995). Controlling the false discovery rate: a practical and powerful approach to multiple testing. *J. R. Stat. Soc. Ser. B* 57, 289–300. doi: 10.1111/j.2517-6161.1995.tb02031.x

Bey, A. L., Wang, X., Yan, H., Kim, N., Passman, R. L., Yang, Y., et al. (2018). Brain region-specific disruption of *SHANK3* in mice reveals a dissociation for cortical and striatal circuits in autism-related behaviors. *Transl. Psychiatry* 8:94. doi: 10.1038/s41398-018-0142-6

Bidinosti, M., Botta, P., Krüttner, S., Proenca, C. C., Stoehr, N., Bernhard, M., et al. (2016). CLK2 inhibition ameliorates autistic features associated with *SHANK3* deficiency. *Science* 351, 1199–1203. doi: 10.1126/science.aad5487

Boccuto, L., Lauri, M., Sarasua, S. M., Skinner, C. D., Buccella, D., Dwivedi, A., et al. (2013). Prevalence of *SHANK3* variants in patients with different subtypes of autism spectrum disorders. *Eur. J. Hum. Genet.* 21, 310–316. doi: 10.1038/ejhg.2012.175

Boeckers, T. M., Bockmann, J., Kreutz, M. R., and Gundelfinger, E. D. (2002). ProSAP/Shank proteins - a family of higher order organizing molecules of the postsynaptic density with an emerging role in human neurological disease. *J. Neurochem.* 81, 903–910. doi: 10.1046/j.1471-4159.2002.00931.x

Bozdagi, O., Sakurai, T., Papapetrou, D., Wang, X., Dickstein, D. L., Takahashi, N., et al. (2010). Haploinsufficiency of the autism-associated *SHANK3* gene leads to deficits in synaptic function, social interaction, and social communication. *Mol. Autism* 1:15. doi: 10.1186/2040-2392-1-15

Chambers, S. M., Fasano, C. A., Papapetrou, E. P., Mark, T., Michel, S., and Lorenz, S. (2009). Highly efficient neural conversion of human ES and iPS

cells by dual inhibition of SMAD signaling. *Nat. Biotechnol.* 27, 275–280. doi: 10.1038/nbt.1529

Chen, C. H., Chen, H. I., Liao, H. M., Chen, Y. J., Fang, J. S., Lee, K. F., et al. (2017). Clinical and molecular characterization of three genomic rearrangements at chromosome 22q13.3 associated with autism spectrum disorder. *Psychiatr. Genet.* 27, 23–33. doi: 10.1097/ypg.0000000000000151

Dobin, A., Davis, C. A., Schlesinger, F., Drenkow, J., Zaleski, C., Jha, S., et al. (2013). STAR: ultrafast universal RNA-seq aligner. *Bioinformatics* 29, 15–21. doi: 10.1093/bioinformatics/bts635

Du, Y., Weed, S. A., Xiong, W.-C., Marshall, T. D., and Parsons, J. T. (1998). Identification of a novel cortactin SH3 domain-binding protein and its localization to growth cones of cultured neurons. *Mol. Cell. Biol.* 18, 5838–5851. doi: 10.1128/MCB.18.10.5838

Durand, C. M., Catalina, B., Boeckers, T. M., Juergen, B., Pauline, C., Fabien, F., et al. (2007). Mutations in the gene encoding the synaptic scaffolding protein *SHANK3* are associated with autism spectrum disorders. *Nat. Genet.* 39, 25–27. doi: 10.1038/ng1933

Durand, C. M., Perroy, J., Loll, F., Perrais, D., Fagni, L., Bourgeron, T., et al. (2012). *SHANK3* mutations identified in autism lead to modification of dendritic spine morphology via an actin-dependent mechanism. *Mol. Psychiatry* 17, 7184. doi: 10.1038/mp.2011.57

Freitag, C. M., Staal, W., Klauck, S. M., Duketis, E., and Waltes, R. (2010). Genetics of autistic disorders: review and clinical implications. *Eur. Child Adolesc. Psychiatry* 19, 169–178. doi: 10.1007/s00787-009-0076-x

Gauthier, J., Spiegelman, D., Piton, A., Lafreniere, R. G., Laurent, S., St-Onge, J., et al. (2009). Novel de novo *SHANK3* mutation in autistic patients. *Am. J. Med. Genet. Part B Neuropsychiatr. Genet.* 150B, 421–424. doi: 10.1002/ajmg.b.30822

Grabrucker, A. M., Schmeisser, M. J., Schoen, M., and Boeckers, T. M. (2011). Postsynaptic ProSAP/Shank scaffolds in the cross-hair of synaptopathies. *Trends Cell Biol.* 21, 594–603. doi: 10.1016/j.tcb.2011.07.003

Halbedl, S., Schoen, M., Feiler, M. S., Boeckers, T. M., and Schmeisser, M. J. (2016). *SHANK3* is localized in axons and presynaptic specializations of developing hippocampal neurons and involved in the modulation of NMDA receptor levels at axon terminals. *J. Neurochem.* 137, 26–32. doi: 10.1111/jnc.13523

Harony-Nicolas, H., Kay, M., Hoffmann, J. D., Klein, M. E., Bozdagi-Gunal, O., Riad, M., et al. (2017). Oxytocin improves behavioral and electrophysiological deficits in a novel Shank3-deficient rat. *eLife* 6:e18904. doi: 10.7554/eLife.18904

Hayashi, M. K., Tang, C., Verpelli, C., Narayanan, R., Stearns, M. H., Xu, R. M., et al. (2009). The postsynaptic density proteins homer and shank form a polymeric network structure. *Cell* 137, 159–171. doi: 10.1016/j.cell.2009.01.050

Israel, M. A., Yuan, S. H., Bardy, C., Reyna, S. M., Mu, Y., Herrera, C., et al. (2012). Probing sporadic and familial Alzheimer's disease using induced pluripotent stem cells. *Nature* 482, 216–220. doi: 10.1038/nature10821

Jin, C., Kang, H., Ryu, J. R., Kim, S., Zhang, Y., Lee, Y., et al. (2018). Integrative brain transcriptome analysis reveals region-specific and broad molecular changes in shank3-overexpressing mice. *Front. Mol. Neurosci.* 11:250. doi: 10.3389/fnmol.2018.00250

Kang, S., Chen, X., Gong, S., Yu, P., Yau, S., Su, Z., et al. (2017). Characteristic analyses of a neural differentiation model from iPSC-derived neuron according to morphology, physiology, and global gene expression pattern. *Sci. Rep.* 7:12233. doi: 10.1038/s41598-017-12452-x

Kathuria, A., Nowosiad, P., Jagasia, R., and Aigner, S. (2018). Stem cell-derived neurons from autistic individuals with *SHANK3* mutation show morphogenetic abnormalities during early development. *Mol. Psychiatry* 23, 735–746. doi: 10.1038/mp.2017.185

Kerrisk Campbell, M., and Sheng, M. (2018). USP8 deubiquitinates *SHANK3* to control synapse density and *SHANK3* activity-dependent protein levels. *J. Neurosci.* 38, 5289–5301. doi: 10.1523/jneurosci.3305-17.2018

Khazaei, M. R., Girouard, M. P., Alchini, R., Ong Tone, S., Shimada, T., Bechstedt, S., et al. (2014). Collapsin response mediator protein 4 regulates growth cone dynamics through the actin and microtubule cytoskeleton. *J. Biol. Chem.* 289, 30133–30143. doi: 10.1074/jbc.M114.570440

Konopka, G., Wexler, E., Rosen, E., Mukamel, Z., Osborn, G. E., Chen, L., et al. (2012). Modeling the functional genomics of autism using human neurons. *Mol. Psychiatry* 17, 202–214. doi: 10.1038/mp.2011.60

Lin, H., Li, Q., Du, Q., Wang, O., Wang, Z., Akert, L., et al. (2018). Integrated generation of induced pluripotent stem cells in a low-cost device. *Biomaterials* 189, 23–36. doi: 10.1016/j.biomaterials.2018.10.027

Love, M. I., Huber, W., and Anders, S. (2014). Moderated estimation of fold change and dispersion for RNA-seq data with DESeq2. *Genome Biol.* 15:550. doi: 10.1186/s13059-014-0550-8

Lu, C., Chen, Q., Zhou, T., Bozic, D., Fu, Z., Pan, J. Q., et al. (2016). Micro-electrode array recordings reveal reductions in both excitation and inhibition in cultured cortical neuron networks lacking Shank3. *Mol. Psychiatry* 21, 159–168. doi: 10.1038/mp.2015.173

Luo, J., Feng, Q., Wei, L., and Luo, M. (2017). Optogenetic activation of dorsal raphe neurons rescues the autistic-like social deficits in *SHANK3* knockout mice. *Cell Res.* 27, 950–953. doi: 10.1038/cr.2017.52

Lyall, K., Schweitzer, J. B., Schmidt, R. J., Hertz-Picciotto, I., and Solomon, M. (2017). Inattention and hyperactivity in association with autism spectrum disorders in the CHARGE study. *Res. Autism Spectr. Disord.* 35, 1–12. doi: 10.1016/j.rasd.2016.11.011

Marchetto, M. C., Carromeu, C., Acab, A., Yu, D., Yeo, G. W., Mu, Y., et al. (2010). A model for neural development and treatment of Rett syndrome using human induced pluripotent stem cells. *Cell* 143, 527–539. doi: 10.1016/j.cell.2010.10.016

Martin, M. (2011). Cutadapt removes adapter sequences from high-throughput sequencing reads. *EMBnet. J.* 17, 10–12. doi: 10.14806/ej.17.1.200

Mei, Y., Monteiro, P., Zhou, Y., Kim, J. A., Gao, X., Fu, Z., et al. (2016). Adult restoration of *SHANK3* expression rescues selective autistic-like phenotypes. *Nature* 530, 481–484. doi: 10.1038/nature16971

Mitne-Neto, M., Machado-Costa, M., Marchetto, M. C., Bengtson, M. H., Joazeiro, C. A., Tsuda, H., et al. (2011). Downregulation of VAPB expression in motor neurons derived from induced pluripotent stem cells of ALS8 patients. *Hum. Mol. Genet.* 20, 3642–3652. doi: 10.1093/hmg/ddr284

Monteiro, P., and Feng, G. (2017). SHANK proteins: roles at the synapse and in autism spectrum disorder. *Nat. Rev. Neurosci.* 18, 147–157. doi: 10.1038/nrn.2016.183

Naisbitt, S., Valtschanoff, J., Allison, D. W., Sala, C., Kim, E., Craig, A. M., et al. (2000). Interaction of the postsynaptic density-95/guanylate kinase domain-associated protein complex with a light chain of myosin-V and dynein. *J. Neurosci.* 20, 4524–4534. doi: 10.1523/JNEUROSCI.20-12-04524.2000

Nakanishi, M., Nomura, J., Ji, X., Tamada, K., Arai, T., Takahashi, E., et al. (2017). Correction: functional significance of rare neuroligin 1 variants found in autism. *PLoS Genet.* 13:e1007035. doi: 10.1371/journal.pgen.1007035

Nemirovsky, S. I., Marta, C., Zaiat, J. J., Completa, S. P., Vega, P. A., Dolores, G. M., et al. (2015). Whole genome sequencing reveals a de novo *SHANK3* mutation in familial autism spectrum disorder. *PLoS One* 10:e0116358. doi: 10.1371/journal.pone.0116358

Parikshak, N. N., Swarup, V., Belgard, T. G., Irimia, M., Ramaswami, G., Gandal, M. J., et al. (2016). Genome-wide changes in lncRNA, splicing, and regional gene expression patterns in autism. *Nature* 540:423. doi: 10.1038/nature20612

Peca, J., Feliciano, C., Ting, J. T., Wang, W., Wells, M. F., Venkatraman, T. N., et al. (2011). *SHANK3* mutant mice display autistic-like behaviours and striatal dysfunction. *Nature* 472, 437–442. doi: 10.1038/nature09965

Ponna, S. K., Ruskamo, S., Myllykoski, M., Keller, C., Boeckers, T. M., and Kursula, P. (2018). Structural basis for PDZ domain interactions in the post-synaptic density scaffolding protein Shank3. *J. Neurochem.* 145, 449–463. doi: 10.1111/jnc.14322

Qin, L., Ma, K., Wang, Z. J., Hu, Z., and Matas, E. (2018). Social deficits in Shank3-deficient mouse models of autism are rescued by histone deacetylase (HDAC) inhibition. *Nat. Neurosci.* 21, 564–575. doi: 10.1038/s41593-018-0110-8

Ritchie, M. E., Phipson, B., Wu, D., Hu, Y., Law, C. W., Shi, W., et al. (2015). limma powers differential expression analyses for RNA-sequencing and microarray studies. *Nucleic Acids Res.* 43:e47. doi: 10.1093/nar/gkv007

Rubeis, S. D., Siper, P. M., Durkin, A., Weissman, J., Muratet, F., Halpern, D., et al. (2018). Delineation of the genetic and clinical spectrum of Phelan-McDermid syndrome caused by *SHANK3* point mutations. *Mol. Autism* 9:31. doi: 10.1186/s13229-018-0205-9

Sebastiano, B., and Camilla, B. (2016). VTA DA neuron excitatory synapses in *SHANK3* Δex(4-9) mouse line. *Synapse* 71, doi: 10.1002/syn.21955

Shi, L., Chang, X., Zhang, P., Coba, M. P., Lu, W., and Wang, K. (2013). The functional genetic link of NLGN4X knockdown and neurodevelopment in neural stem cells. *Hum. Mol. Genet.* 22, 3749–3760. doi: 10.1093/hmg/ddt226

Shi, Y., Kirwan, P., and Livesey, F. J. (2012). Directed differentiation of human pluripotent stem cells to cerebral cortex neurons and neural networks. *Nat. Protoc.* 7, 1836–1846. doi: 10.1038/nprot.2012.116

State, M. W., and Levitt, P. (2011). The conundrums of understanding genetic risks for autism spectrum disorders. *Nat. Neurosci.* 14, 1499–1506. doi: 10.1038/nn.2924

Sykes, N. H., Toma, C., Wilson, N., Volpi, E. V., Sousa, I., Pagnamenta, A. T., et al. (2009). Copy number variation and association analysis of *SHANK3* as a candidate gene for autism in the IMGSAC collection. *Eur. J. Hum. Genet.* 17, 1347–1353. doi: 10.1038/ejhg.2009.47

Takahashi, K., Tanabe, K., Ohnuki, M., Narita, M., Ichisaka, T., Tomoda, K., et al. (2007). Induction of pluripotent stem cells from adult human fibroblasts by defined factors. *Cell* 131, 861–872. doi: 10.1016/j.cell.2007.11.019

Taylor, S. E., Taylor, R. D., Price, J., and Andreae, L. C. (2018). Single-molecule fluorescence in-situ hybridization reveals that human *SHANK3* mRNA expression varies during development and in autism-associated *SHANK3* heterozygosity. *Stem Cell Res. Ther.* 9:206. doi: 10.1186/s13287-018-0957-3

Vicidomini, C., Ponzoni, L., Lim, D., Schmeisser, M. J., Reim, D., Morello, N., et al. (2017). Pharmacological enhancement of mGlu5 receptors rescues behavioral deficits in *SHANK3* knock-out mice. *Mol. Psychiatry* 22, 689–702. doi: 10.1038/mp.2016.30

Wang, J., Duncan, D., Shi, Z., and Zhang, B. (2013). WEB-based gene set analysis toolkit (WebGestalt): update 2013. *Nucleic Acids Res.* 41, W77–W83. doi: 10.1093/nar/gkt439

Wang, W., Li, C., Chen, Q., van der Goes, M.-S., Hawrot, J., Yao, A. Y., et al. (2017). Striatopallidal dysfunction underlies repetitive behavior in Shank3-deficient model of autism. *J. Clin. Invest.* 127, 1978–1990. doi: 10.1172/JCI87997

Wang, X., Bey, A. L., Katz, B. M., Badea, A., Kim, N., David, L. K., et al. (2016). Altered mGluR5-Homer scaffolds and corticostriatal connectivity in a *SHANK3* complete knockout model of autism. *Nat. Commun.* 7:11459. doi: 10.1038/ncomms11459

Wang, X., McCoy, P. A., Rodriguiz, R. M., Pan, Y., Je, H. S., Roberts, A. C., et al. (2011). Synaptic dysfunction and abnormal behaviors in mice lacking major isoforms of Shank3. *Hum. Mol. Genet.* 20, 3093–3108. doi: 10.1093/hmg/ddr212

Xiaoming, W., Mccoy, P. A., Rodriguiz, R. M., Yanzhen, P., Shawn, J. H., Roberts, A. C., et al. (2011). Synaptic dysfunction and abnormal behaviors in mice lacking major isoforms of Shank3. *Hum. Mol. Genet.* 20, 3093–3108. doi: 10.1093/hmg/ddr212

Xing, J., Kimura, H., Wang, C., Ishizuka, K., Kushima, I., Arioka, Y., et al. (2016). Resequencing and association analysis of Six PSD-95-related genes as possible susceptibility genes for schizophrenia and autism spectrum disorders. *Sci. Rep.* 6:27491. doi: 10.1038/srep27491

Zhao, H., Tu, Z., Xu, H., Yan, S., Yan, H., Zheng, Y., et al. (2017). Altered neurogenesis and disrupted expression of synaptic proteins in prefrontal cortex of SHANK3-deficient non-human primate. *Cell Res.* 27:1293. doi: 10.1038/cr.2017.95

Zhou, T., Benda, C., Duzinger, S., Huang, Y., Li, X., Li, Y., et al. (2011). Generation of induced pluripotent stem cells from urine. *J. Am. Soc. Nephrol.* 22, 1221–1228. doi: 10.1681/ASN.2011010106

Zhou, Y., Kaiser, T., Monteiro, P., Zhang, X., Van der Goes, M. S., Wang, D., et al. (2016). Mice with *SHANK3* mutations associated with ASD and schizophrenia display both shared and distinct defects. *Neuron* 89, 147–162. doi: 10.1016/j.neuron.2015.11.023

Conflict of Interest Statement: The authors declare that the research was conducted in the absence of any commercial or financial relationships that could be construed as a potential conflict of interest.

frontiers in Neuroanatomy

ORIGINAL RESEARCH
published: 17 April 2019
doi: 10.3389/fnana.2019.00044

Whole Brain Mapping of Long-Range Direct Input to Glutamatergic and GABAergic Neurons in Motor Cortex

*Pan Luo[1,2], Anan Li[1,2,3], Yanxiao Zheng[1,2], Yutong Han[1,2], Jiaojiao Tian[1,2], Zhengchao Xu[1,2], Hui Gong[1,2,3] and Xiangning Li[1,2,3]**

[1] Britton Chance Center for Biomedical Photonics, Wuhan National Laboratory for Optoelectronics-Huazhong University of Science and Technology, Wuhan, China, [2] MoE Key Laboratory for Biomedical Photonics, School of Engineering Sciences, Huazhong University of Science and Technology, Wuhan, China, [3] HUST-Suzhou Institute for Brainsmatics, Suzhou, China

Long-range neuronal circuits play an important role in motor and sensory information processing. Determining direct synaptic inputs of excited and inhibited neurons is important for understanding the circuit mechanisms involved in regulating movement. Here, we used the monosynaptic rabies tracing technique, combined with fluorescent micro-optical sectional tomography, to characterize the brain-wide input to the motor cortex (MC). The whole brain dataset showed that the main excited and inhibited neurons in the MC received inputs from similar brain regions with a quantitative difference. With 3D reconstruction we found that the distribution of input neurons, that target the primary and secondary MC, had different patterns. In the cortex, the neurons projecting to the primary MC mainly distributed in the lateral and anterior portion, while those to the secondary MC distributed in the medial and posterior portion. The input neurons in the subcortical areas also showed the topographic shift model, as in the thalamus, the neurons distributed as outer and inner shells while the neurons in the claustrum and amygdala were in the ventral and dorsal part, respectively. These results lay the anatomical foundation to understanding the organized pattern of motor circuits and the functional differences between the primary and secondary MC.

Keywords: motor cortex, whole brain, long-range input, distinct distribution, 3D

OPEN ACCESS

Edited by:
Yun-Qing Li,
Fourth Military Medical University, China

Reviewed by:
Kazunari Miyamichi,
RIKEN Center for Biosystems Dynamics Research, Japan
Mitsuko Watabe-Uchida,
Harvard University, United States

***Correspondence:**
Xiangning Li
lixiangning@mail.hust.edu.cn

Received: *30 January 2019*
Accepted: *29 March 2019*
Published: *17 April 2019*

Citation:
Luo P, Li A, Zheng Y, Han Y, Tian J, Xu Z, Gong H and Li X (2019) Whole Brain Mapping of Long-Range Direct Input to Glutamatergic and GABAergic Neurons in Motor Cortex. Front. Neuroanat. 13:44. doi: 10.3389/fnana.2019.00044

INTRODUCTION

The motor cortex (MC) plays a crucial role in the generation and control of movement and motor learning (Sanes and Donoghue, 2000; Tanji, 2001; Peters et al., 2017). Dysfunction of the MC can cause many neurological diseases, such as Parkinson's disease, amyotrophic lateral sclerosis, Huntington's disease and Alzheimer's disease (Ferreri et al., 2011; Shepherd, 2013). There are two functional subregions in the MC, primary motor cortex (MOp) and the secondary motor cortex (MOs) (Sul et al., 2011; Guo J. Z. et al., 2015). A study based on intracortical microstimulation revealed that stimulation of the MOp and MOs induced movements of the forelimbs and whiskers in mice, respectively (Tennant et al., 2011). The MOs is more involved in cognitive-related motor control processing, such as motor decision, motor planning, motor learning, and spatial memory (Barthas and Kwan, 2017). The functional differences between the MOp and MOs rely on integrating information from upstream areas and sending information to downstream areas through dendrites and axons. Investigation of the connectivity patterns, including the input and output circuits, are essential to dissect the diverse functions of these subregions. With viral neuronal

tracing, the output circuit pattern MC has been well-identified, in which the projections from the MOp and MOs showed unique and separate tract pathways, despite targeting similar areas (Jeong et al., 2016). However, the organization patterns of the upstream circuits in the whole brain, especially the direct input to the subregions of the MC, are not clear at present.

Previous studies revealed that the MC integrates inputs from many brain areas, such as the orbital cortex, primary somatosensory cortex (especially the barrel field, SSp-bfd), secondary somatosensory cortex (SSs), ventrolateral thalamic nucleus (VL) and the ventromedial thalamic nucleus (VM) in the thalamus, and basal forebrain (Hooks et al., 2013; Zingg et al., 2014; Zaborszky et al., 2015). But these studies were based on tracing methods that cannot identify the whole brain input to the specific type of neurons, while the neurons in the MC can be divided into two main categories: glutamatergic neurons and GABAergic neurons (Huang, 2014). The former sends long-range axons to other areas for innervation, and the latter mainly establishes the connection in the local area to carry on the regulation, accounting for about 20% of the total cortical neurons. The monosynaptic rabies tracing technique has been widely used to characterize the presynaptic inputs of desired starter neurons with high accuracy and efficiency (Wickersham et al., 2007a; Wall et al., 2010; Ogawa et al., 2014). The inputs to glutamatergic neurons and three subtypes of GABAergic neurons in the MC has been revealed (Zhang et al., 2016). But structure information of the upstream circuits of the subregions of the MC, including the MOp and MOs, especially the whole-brain input to different types of neurons, remains indistinct.

To map the whole brain inputs to glutamatergic and GABAergic neurons in the MOp and MOs, here, we used a dual-color monosynaptic rabies tracing technique combined with fluorescent Micro-Optical Sectional Tomography (fMOST) (Gong et al., 2016) and performed systematic analyses and comparisons.

MATERIALS AND METHODS

Animal

Adult (2–4 months) C57BL/6J mice Thy1-cre mice (JAX: 006143) and Vgat-cre mice (JAX: 028862) were used in this study, targeting glutamatergic neurons (Campsall et al., 2002; Yang H. et al., 2016; Yang Y. et al., 2016) and GABAergic neurons (Vong et al., 2011; Chen et al., 2018), respectively. All animals were housed in normal cages in an environment with a 12-h light/dark cycle and were free to get enough food and water. All animal experiments were approved by the Animal Ethics Committee of Huazhong University of Science and Technology.

Surgery and Stereotaxic Injection of Virus

The mice were intraperitoneally injected with 1% pentobarbital sodium for anesthesia. The anesthetized mice were attached to a mouse adapter. A drill was used to make a small hole in the skull above the target area. A virus was injected into the target area using a pressure injection pump (Nanoject II: Drummond Scientific, Co., Broomall, PA, United States). The wound was cleaned alternately with iodine and 75% alcohol to prevent inflammation.

In this study, we used a monosynaptic rabies tracing technique to label the whole-brain inputs to specific cell types in the MOp and MOs simultaneously in a same transgenic mouse. First, 150 nl AAV helper mixtures were injected into the ipsilateral MOp (AP:1.54 mm, ML:1.70 mm, DV:−1.50 mm) and MOs (AP:1.54 mm, ML:0.50 mm, DV:−1.35 mm) in Thy1-cre or Vgat-cre mice respectively, mixed with rAAV2/9-Ef1α-DIO-BFP-2a-TVA-WPRE-pA and rAAV2/9-Ef1α-DIO-RG-WPRE-pA as the ratio of 1:2. Three weeks later, 300 nl RV-△G-EnVA-EGFP and RV-△G-EnVA-Dsred were injected into the two subregions of the MC respectively. One week later, the mice were perfused. The titer of both AAVs is 2.00E+12 vg/ml, while the titer of RV is 2.00E+8 IFU/ml. The virus used was produced by BrainVTA. The amplification origins of RVs were from SAD△G-EGFP (EnvA) (Wickersham et al., 2007b; Osakada et al., 2011). The AAV virus vectors were constructed by BrainVTA. The coding region of the TVA element and RG element were obtained from the AAV-EF1a-FLEX-GT plasmid (Addgene plasmid 26198) and pAAV-EF1a-FLEX-RG plasmid (Addgene plasmid 98221) respectively, and were separately constructed into the DIO cassette of the plasmid pAAV-EF1a-DIO-hChR2 (H134R)-EYFP (Addgene plasmid 20298) (Hu et al., 2016).

During the stereotaxic injection, we set the Bregma as the zero point of the stereotactic coordinate. Briefly, Bregma is the junction of the coronal suture and the sagittal suture of the skull, and Lambda is the point of intersection of the bestfit lines passing through the sagittal suture and the left and right portions of the lambdoid suture. When Bregma and Lambda are on the same level and the left and right hemispheres are symmetric in the plane with the center line, the Bregma was set as the zero point.

Histology

All histological procedures followed previous reports (Gong et al., 2016; Ren et al., 2018). The anesthetized mice received cardiac perfusion using 0.01 M phosphate-buffered saline (PBS, Sigma-Aldrich, United States) and 4% paraformaldehyde (PFA, Sigma-Aldrich, United States) in 0.01 M PBS. Brains were separated and then post-fixed with 4% PFA for 48 h. After fixation, the brain tissues were rinsed with PBS overnight.

To perform three-dimensional reconstruction analysis, some brains were embedded with GMA resin for whole brain imaging with the fMOST system. Briefly, the brains were dehydrated in a graded ethanol series (50, 70, and 95% ethanol, changing from one concentration to the next every 1 h at 4°C). Then, the brains were immersed in a graded glycol methacrylate (GMA, Ted Pella, Inc., Redding, CA, United States): 70, 85, and 100% GMA for 2 h each, and 100% GMA overnight at 4°C, and into a pre-polymerization of GMA for 3 days for penetration. Last, the samples were polymerized in a vacuum oven at 48°C for 24 h.

Imaging

To detect labeling signals, some brains were manually sectioned with 50 μm coronal slices using the vibrating

slicer (Leica 1200S). Then, the slices were imaged using confocal microscopy (Zeiss LSM710).

For whole brain imaging, the brains were embedded with GMA resin and sectioned and imaged automatically and continuously using the fMOST system, with the voxel resolution of 0.32 μm × 0.32 μm × 2 μm (Gong et al., 2016). We processed the images following the procedures used in our previous work (Gong et al., 2016; Li et al., 2017, 2018). For the whole brain dataset, we uploaded the images into Amira software (v5.2.2, Mercury Computer Systems, San Diego, CA, United States) and Fiji (NIH) to perform the basic operations, including extraction of areas of interest, resampling, maximum projection etc. In order to distinguish the brain region boundary, the down sampling data were registered into the Allen Reference Atlas (the voxel resolution of 10 μm × 10 μm × 10 μm) (Kuan et al., 2015). For registration, we performed the following steps: (1) image preprocessing, including uneven illumination correction, image contour outside background noise removal; (2) extracting regional features of anatomically invariants in the whole brain such as the ventricles, the hippocampus, the corpus callosum, etc.; (3) used the current advanced gray-level based registration algorithm (SyN) to register the extracted features, and to obtain the corresponding relationship between the image dataset and Allen CCFv3 brain atlas. (4) the registration parameters were applied to the whole dataset. For the three-dimensional (3D) reconstruction analysis and presentation, we extracted the cell body information by NeuroGPS software (Quan et al., 2016) and placed them in the corresponding 3D brain region contour.

Statistical Analysis

We used 50 μm of maximum fluorescence signal projection or 50 μm sections from eight brains to perform cell counting using Fiji software. For cell counting in each area, we imported the image to the Fiji software and used its cell counter module to perform the manual cell count. Every two slices or sections were counted. We counted all the long-range upstream brain regions (upstream brain regions except for injection site -namely the MOp and MOs at the same hemisphere with the injection sites). If the number of cell bodies in any region of any sample was over 10, we regarded it as valid and there were 48 valid upstream regions. Then, we compared the percentage of input neurons of each valid region as the total input neurons with one-way ANOVA followed by Tukey's Honest Significant Difference test using SPSS (version 13.0) (Beier et al., 2015). To quantify the similarity in input patterns, we calculated Pearson's correlation coefficients.

RESULTS

Monosynaptic Inputs to Glutamatergic and GABAergic Neurons in Subdomains of MC

For mapping the whole brain monosynaptic input to the MC, we used viral neuronal tracing with an AAV helper and the modified rabies (RV), which could perform the direct monosynaptic inputs tracing. The RV pseudo typed with the avian sarcoma leucosis virus glycoprotein EnvA, can only infect cells expressing a cognate receptor (TVA protein) and requires the rabies virus to envelope the glycoprotein (RG) to spread retrogradely into the presynaptic cells. To compare the inputs to different categories of MC, we used the Thy1-cre mice and Vgat-cre mice respectively, that expressed a cre recombinant enzyme in glutamatergic or GABAergic neurons in all layers of cortex (**Figure 1A**). Combining cre-line mice with the cre-dependent AAV helper of the RV system, we could perform the inputs tracing, targeting the presynaptic neurons projecting to the specific type of neuron.

To investigate the input differences between the MOp and MOs, we selected two representative sites of these regions. One for forelimb motor controlling and the other for vibrissa motor controlling (Jeong et al., 2016). The dual-color monosynaptic rabies tracing technique was performed to label the input neurons of these sites respectively. In simple terms, an AAV helper that could express the TVA and G protein in specific neurons were injected in ipsilateral MOp and MOs of cre-line mice. Three weeks later, the RV expressing GFP (RV-△G-EnVA-GFP) or Dsred (RV-△G-EnVA-Dsred) were injected into the MOp and MOs respectively (**Figure 1A**). Thus, we could label monosynaptic inputs to specific type neurons of these regions in individual brains simultaneously. To confirm that the starter cells restricted to the injection site area, we injected one type of rabies virus in individual mice (**Supplementary Figure S1**) while the control was injected with TVA-BFP and RV, without RG in cre-line mice (**Supplementary Figure S2**). And the continuous coronals around the injection sites of dual-color RV also indicated that there was almost no crosstalk between the two RVs injected in the MOp and MOs (**Supplementary Figure S3**). With immunohistochemical staining, we further confirmed the cell specificity of starter cells in Thy1-cre mice (**Supplementary Figure S4**). We also performed control experiments in C57BL/6J mice to ensure that the leaked labeling had no effect on the analysis of our experiments (**Supplementary Figure S5**).

To analyze the whole brain inputs from the perspective of a 3D space, the brains were embedded with GMA resin, then sectioned and imaged automatically and continuously using the fMOST system. Through the 3D reconstruction, we could observe the whole brain input distribution characteristics of the MOp and MOs in a three-dimensional space (**Figures 1B,C**). Obviously, we found that the upstream neurons of both glutamatergic and GABAergic neurons, were mainly concentrated in the cortical area near the injection site and the thalamic area.

In order to show the signal distribution characteristics of these input brain regions more clearly, we performed the 50 μm maximum intensity projection on continuous 2 μm images (**Figure 2**). The GFP labeling neurons indicate populations projecting to the MOp, and the Dsred labeling neurons indicate populations projecting to the MOs. Overall, we found that the whole brain input distribution of glutamatergic neurons and GABAergic neurons are similar in the same subregions of the MC. But the whole brain input distribution to glutamatergic neurons or GABAergic neurons are basically separated in different subregions of the MC. In general, we observed that the glutamatergic neurons and GABAergic neurons in the MOp receive projections from the cortical plate (ORB, SSp-ul/m,

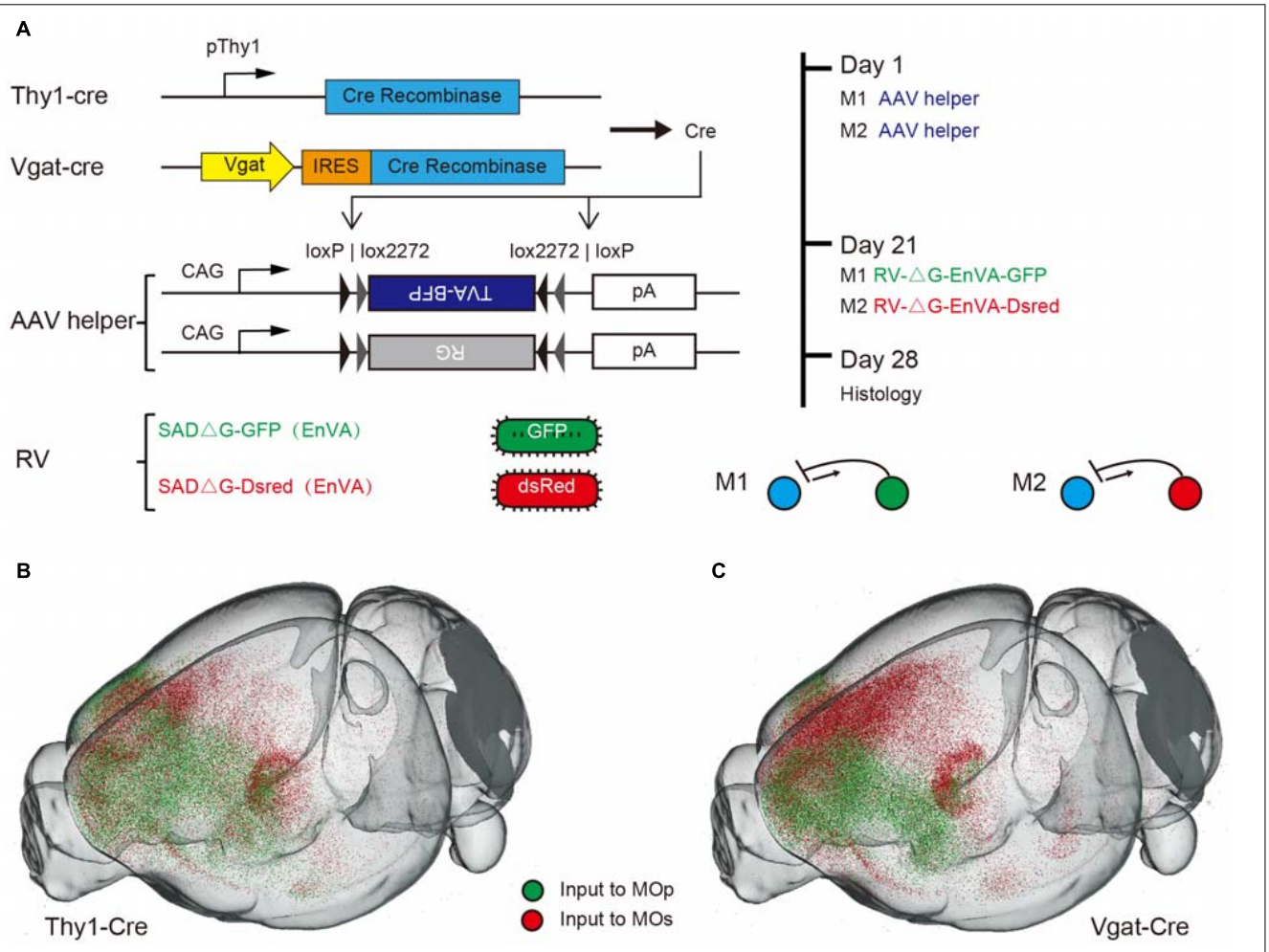

FIGURE 1 | Monosynaptic rabies tracing the inputs to specific neurons in MC. **(A)** Schematic showing the dual-color monosynaptic rabies tracing technique with cre dependent mice (Thy1-cre mice and Vgat-cre mice) and viral vectors. **(B,C)** 3D reconstruction of the whole brain dataset acquired using the fMOST system. Green dots denote neurons projecting to the MOp while red dots denote neurons projecting to the MOs.

SSp-bfd, SSs, ECT), cortical subplate (CLA, BLA), thalamus (VAL, VM, PO, PF), pallidum (NDB, SI, PALd), and the midbrain (VTA, DR, CS, PPN). The glutamatergic neurons and GABAergic neurons in the MOs receive projections from the cortical plate (ORB, ACA, RSP, SSp-ll /tr, SSp-bfd, SSs, ECT, hippocampus), cortical subplate (CLA, BLA), thalamus (AM, MD, LP, VAL, VM, PO, PF), pallidum (MS, NDB, SI, PALd), and the midbrain (VTA, DR, CS, PPN). The distribution of upstream neurons labeled with single RV is similar to the results of dual-color RVs (**Supplementary Figure S6**). The abbreviations of brain regions are summarized in **Supplementary Table S1**.

Quantitative Comparison of Inputs to Specific Cell Types Between Subdomains of MC

To quantitatively compare the input distribution of different subregions, we counted input neurons in each upstream region and normalized to the total number of the whole brain. To accurately distinguish the brain regions, we registered consecutive three-dimensional data to the Allen Reference Atlas. As shown in **Figure 3**, most areas projecting to the MOp also project to the MOs. However, there are a small number of brain regions such as the cortex (DP/TT, RSP, VISam, VISl), thalamus (LP, MD, CL) and the HIP that almost only project to the MOs, and not the MOp. In addition, the MOp receives convergent inputs. For example, there are only four of 48 areas with an input percentage greater than 5% for inputs to the glutamatergic neurons in the MOp, only nine of 48 areas with an input percentage greater than 2%, and the total percentage of these four main input areas is 69.2 ± 6.9%. Relatively, the MOs receives divergent inputs, with five of 48 areas with an input percentage greater than 5% for inputs to the glutamatergic neurons in the MOs, with 16 of 48 areas with an input percentage greater than 2%, and the total percentage of these five main input areas is 41.9 ± 7.4%. In detail, the MOp receives a large projection from both the SSp-bfd and SSs, from which the MOs receives a relatively small projection; the MOs receives a certain number

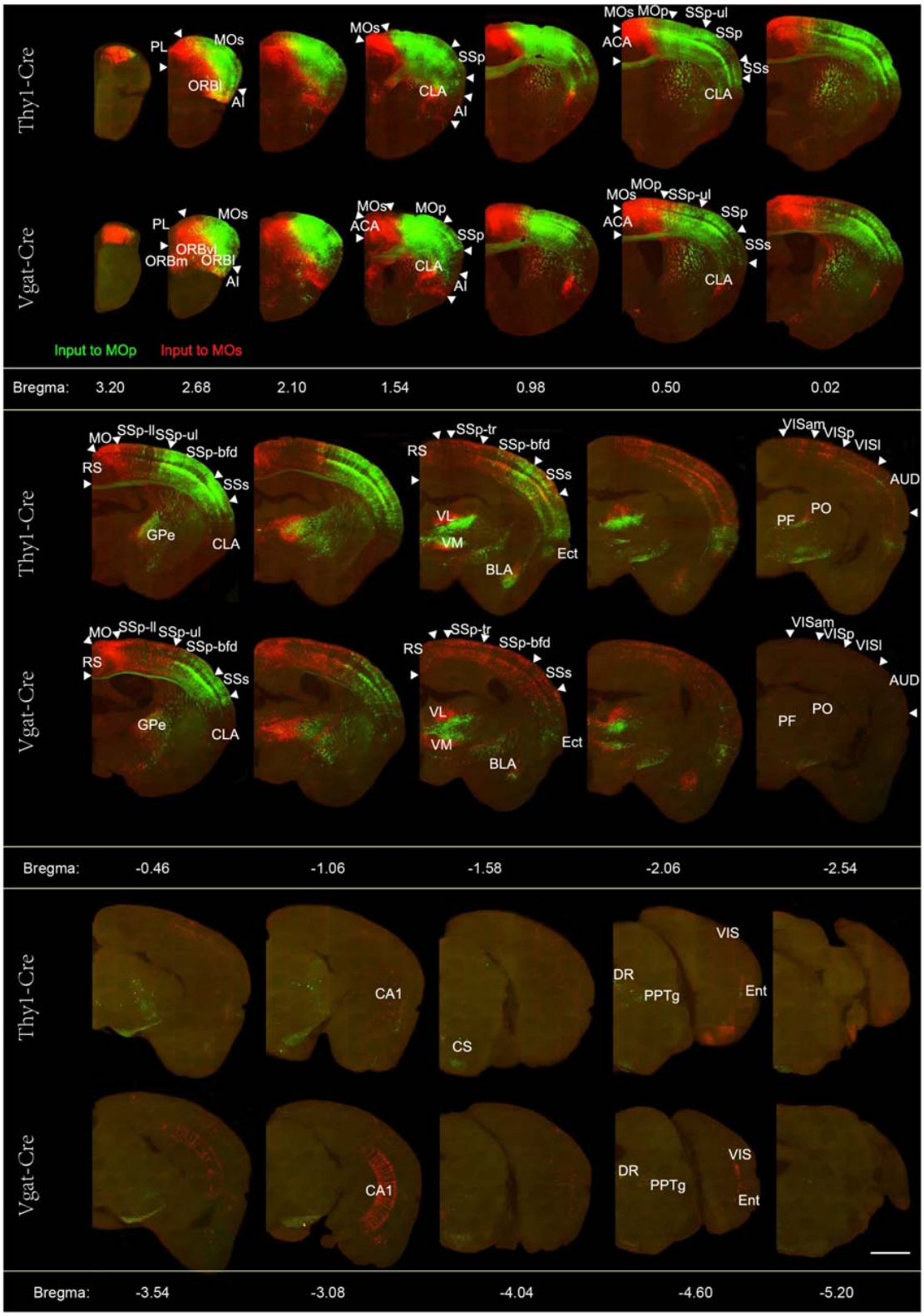

FIGURE 2 | Representative images of selected regions with monosynaptic inputs to the glutamatergic and GABAergic neurons in the motor cortex. Continuous coronal view of maximum intensity projection of the Z stack (50 μm) across the entire brain. RV-labeled neurons identified by the green signal show the neurons projecting to the Mop, while the red signal indicates the neurons projecting to the MOs. Scale bar = 1 mm.

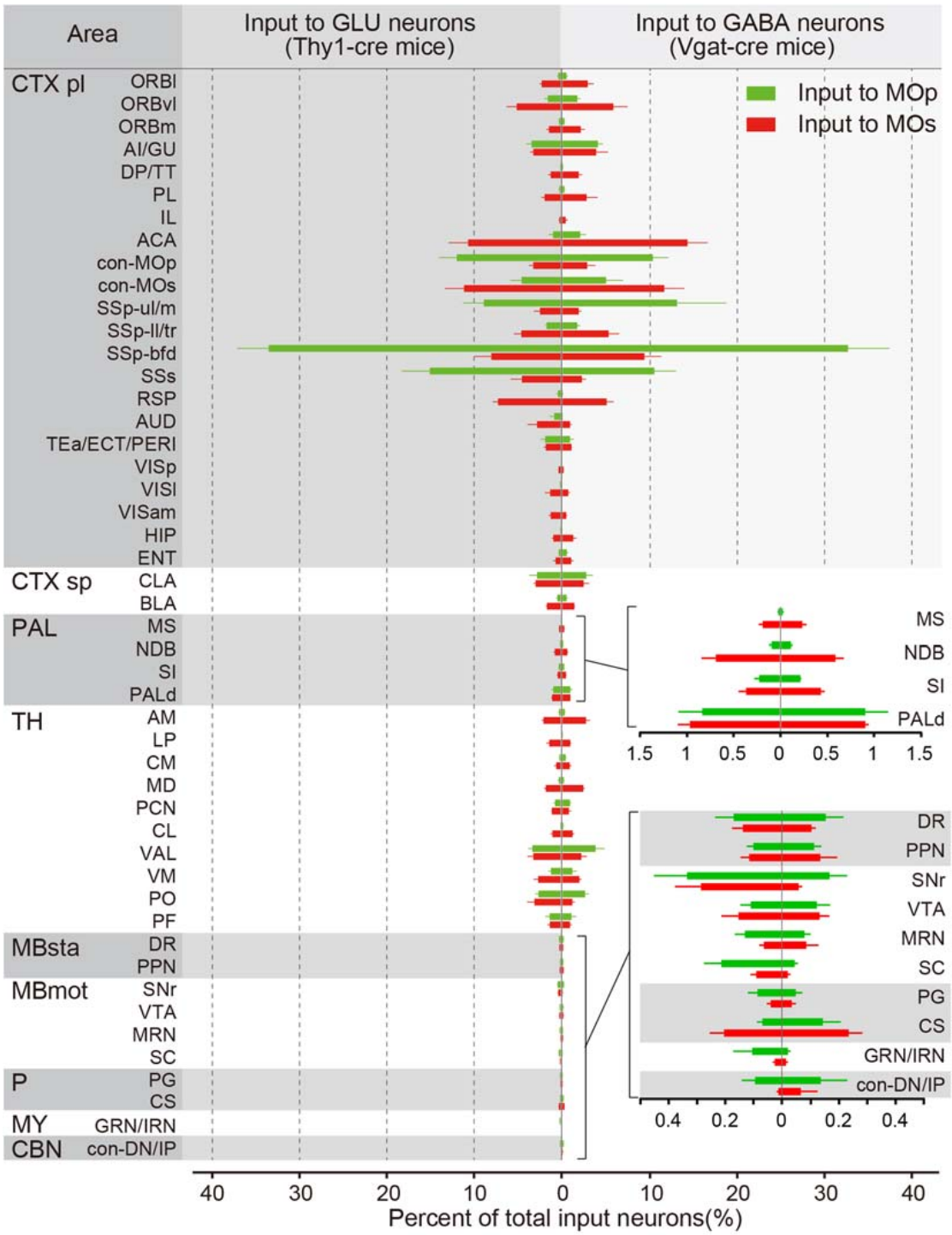

FIGURE 3 | The proportions of the whole-brain input to the glutamatergic and GABAergic neurons in the MOp and MOs. The percentage of inputs from 48 upstream brain regions across the whole brain. (Left) Monosynaptic inputs to the glutamatergic neurons (GLU) in the MOp (green) and MOs (red). (Right) Monosynaptic inputs to GABAergic neurons (GABA) in the MOp (green) and MOs (red). Details of proportions of subregions in the pallidum (superior) and the midbrain, hindbrain, and the cerebellar nuclei (inferior) are shown in the lower right. The abbreviations of brain regions are provided in **Supplementary Table S1**. Mean ± SEM. Vgat-cre mice, $n = 4$; Thy1-cre mice, $n = 4$.

of projections from the ACA and RSP, but the MOp receives almost no projection from these sites; Both the MOp and the MOs receives a small number of innervations from modulatory nuclei in the pallidus and midbrain.

Distinct Input to the MOp and MOs but Similar to the Glutamatergic and GABAergic Neurons

To quantify the correlation between these four groups of inputs to the MC, we conducted a correlation analysis (**Figure 4**). We compared the inputs of glutamatergic neurons and GABAergic neurons in the same brain region and compared the inputs of the same types of neurons in the MOp and MOs. Each circle in the scatter plot represents one brain region (significant differences in red, $P < 0.05$), and the diagonal line represents the same input proportion for each pair (Ogawa et al., 2014).

The correlation coefficient of input to the glutamatergic and GABAergic neurons in the MOp is 0.98 ($P < 0.001$), and only one of 48 upstream regions (SC, $P = 0.017$) showed a significant difference (**Figure 4A**). As for the input to the glutamatergic and GABAergic neurons in the MOs, the correlation coefficient is 0.95

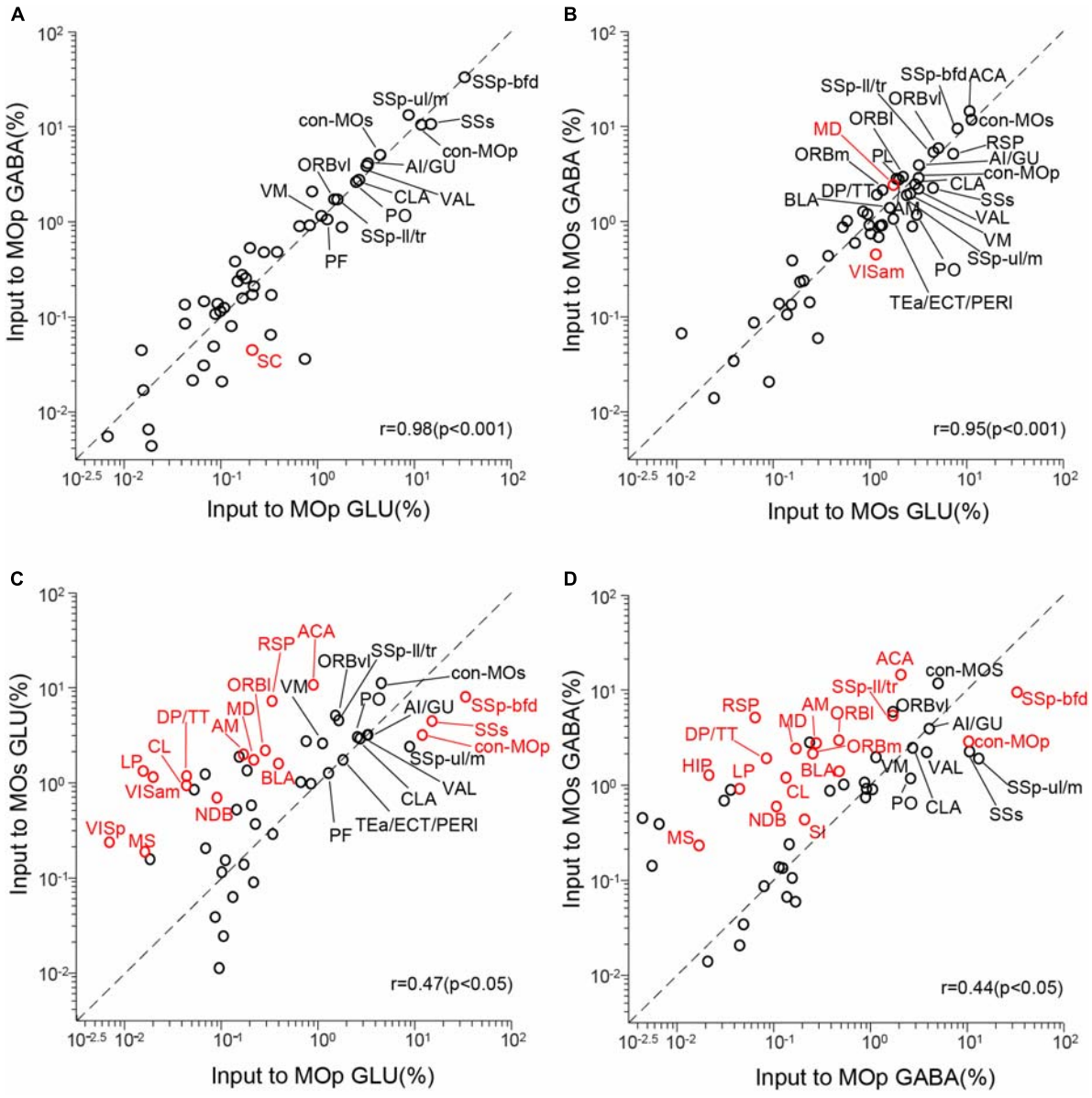

FIGURE 4 | Comparisons of monosynaptic inputs to motor cortex. **(A)** Comparison between inputs to the glutamatergic neurons (GLU) and GABAergic neurons (GABA) in the MOp. **(B)** Comparison between inputs to the GLU and GABA in the MOs. **(C)** Comparison between inputs to the GLU in the MOp and MOs. **(D)** Comparison between inputs to the GABA in the MOp and MOs. Values are the means of the percentage of the total inputs from each region. Red circles indicate significant differences ($P < 0.05$, corrections for multiple comparisons with Tukey's Honest Significant Difference test). r: Pearson's correlation coefficient.

($P < 0.001$), and two upstream regions (MD, $P = 0.038$; VISm, $P = 0.014$) showed a significant difference (**Figure 4B**). These results show that the input patterns to the glutamatergic and GABAergic neurons in the MC are similar. When we compared the input to the glutamatergic neurons in the MOp and MOs, the correlation coefficient is 0.47 ($P < 0.05$), and 16 upstream regions show a significant difference (**Figure 4C**). The correlation coefficient of input to the GABAergic neurons in the MOp and MOs is 0.44 ($P < 0.05$), and 17 areas show a significant difference (**Figure 4D**). All these data indicate that the input patterns of the same type of neurons in different subregions of the MC are of great distinction. We then focused on the comparison of input patterns between different subregions.

Region-Specific Projection to the MOp and MOs

To certify the difference between the input pattern of the MOp and MOs, we compared the distribution of input neurons in the individual brain, that was labeled with a dual-color RV. Using the whole brain dataset, we reconstructed the cortical areas in 3D. As shown in **Figure 5**, the cortex region is regionally specific for the MOp and MOs projection. The coronal slices exhibit a significant regional disjunction between the cortical inputs of subregions of the MC (**Figure 5A**). Based on the results of the 3D reconstruction (**Figure 5B**), we present a schematic diagram of the cortical projection to subregions of the MC (**Figure 5C**). In detail, the MOp mainly receives projections from the lateral portion of the ORB, the anterolateral portion of the MOs/MOp and the anterior portion of the SSp-bfd/SSs. The MOs mainly receives projections from the medial portion of the ORB/MOs, the posterior portion of the MOp/SSp-bfd/SSs/ACA and the anterior RSP/visual areas. The MOp and MOs both receive projections from the middle area of the SSp-bfd and SSp-ul/tr. The cortical circuits were divided into somatosensory motor subnetworks, medial subnetworks and lateral subnetworks in a previous study (Zingg et al., 2014). We found that the MOp mainly receives input from the lateral portion of the somatosensory motor subnetworks, while the MOs mainly receives input from the medial portion of the somatosensory motor subnetworks. The medial sub-networks have almost no projection to the MOp but has a large projection to the MOs, especially the ACA and the RSP in the second medial sub-network. The lateral subnetworks have a few projections to both the MOp and MOs.

The thalamus has a region-specific projection to the MOp and MOs as well. The results of the two-dimensional coronal plane exhibited that the AM, VAL, and the CM in the anterior

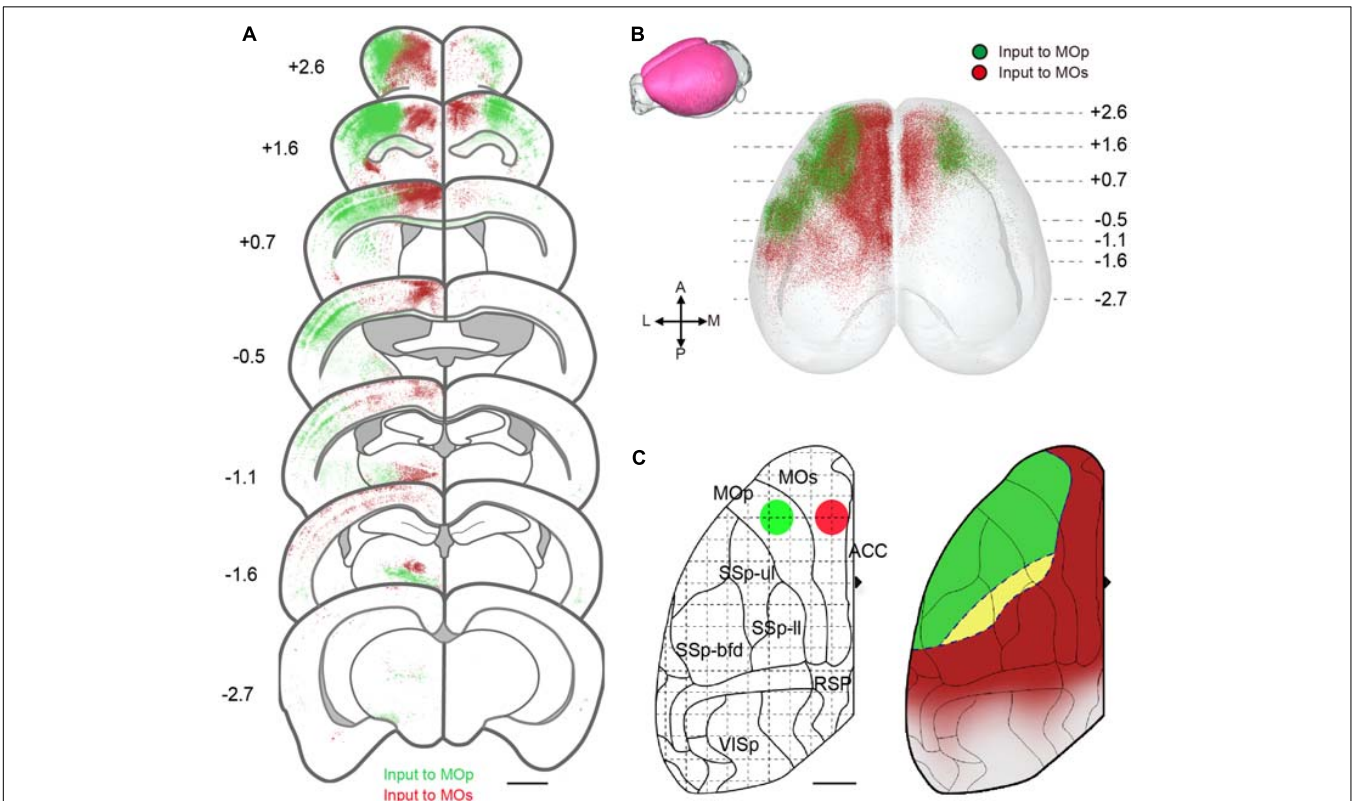

FIGURE 5 | Region-specific cortical projection to MOp and MOs. **(A)** Coronal sections show inputs to the motor cortex from different cortical regions. The green signals indicate the neurons projecting to the Mop, while the red signals indicate the neurons projecting to the MOs. Scale bar = 1 mm. **(B)** Three-dimensional reconstruction of cortical areas. A dot denotes one neuron projecting to the MOp (green) or MOs (red). **(C)** Schematic diagram for input areas projecting to subregions of the MC. The green and red circles represent injection site positions. Green areas indicate regions mainly projecting to the Mop, while red areas indicate regions mainly projecting to the MOs; yellow areas indicate regions projecting to both the MOp and MOs. Scale bar = 1 mm.

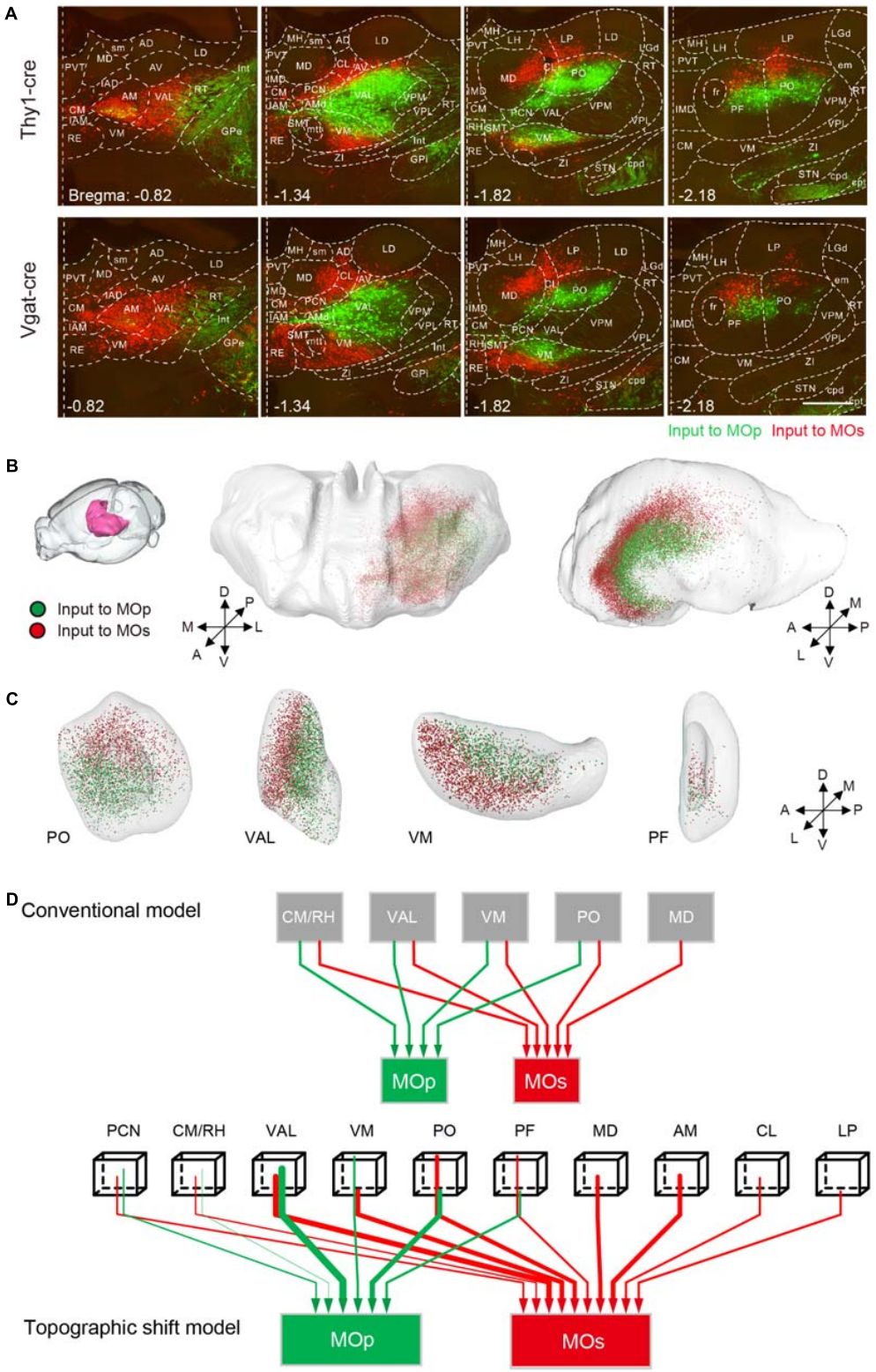

FIGURE 6 | Region-specific thalamic projection to MOp and MOs. **(A)** Distribution of inputs to the MOp and MOs in the thalamus at different positions. The green signal indicates the neurons projecting to the MOp, while the red signal indicates the neurons projecting to the MOs. Scale bar = 500 μm. **(B)** Three-dimensional reconstruction of the thalamic areas. Green dots denote the thalamic neurons projecting to the MOp, while red dots denote the thalamic neurons projecting to the MOs. **(C)** Three-dimensional reconstruction of the PO, VAL, VM, and PF. **(D)** Schematic summary of the thalamic-cortical projection pattern. In the topographic shift model, the beginning tips of wirings indicate the relative spatial positions, and the thickness of wirings in both panels indicates the degree of projection.

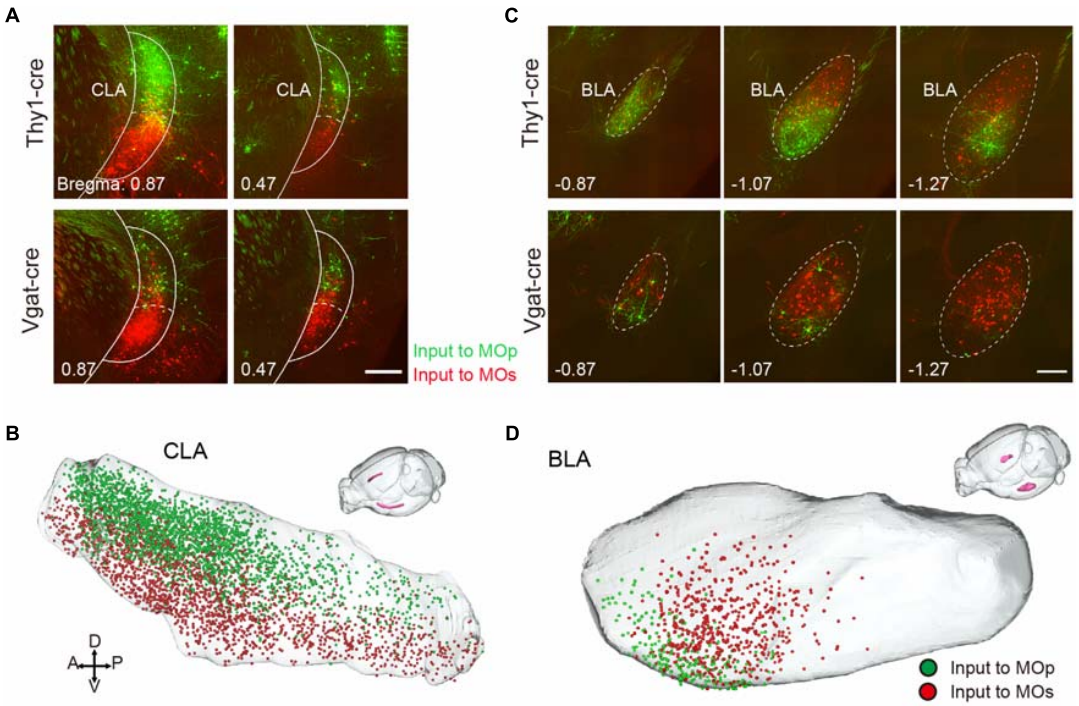

FIGURE 7 | Region-specific projection from CLA and BLA. **(A)** Distribution of input neurons to the MOp and MOs in the CLA. The green signal indicates the neurons projecting to the Mop, while the red signal indicates the neurons projecting to the MOs. Scale bar = 500 μm. **(B)** Three-dimensional reconstruction of the CLA where green dots denote the neurons projecting to the MOp, while red dots denote the neurons projecting to the MOs. **(C)** Distribution of the input neurons to the MOp and MOs in the BLA. Scale bar = 500 μm. **(D)** Three-dimensional reconstruction of the BLA.

part of the thalamus, have a certain number of projections to the MOs but not to the MOp. In the posterior portion of the thalamus, neurons projecting to the MOp gradually appear from the central part of the thalamus including the VAL, VM, PO, and the PF. While those neurons projecting to the MOs, gradually transfer to the dorsal and ventral sides including the VM, PO and the PF (**Figure 6A** and **Supplementary Figure S7**). With 3D reconstruction, the populations projecting to the MOp and MOs in the thalamus show an inner shell and an outer shell, respectively, while the outer shell encloses the inner shell (**Figure 6B**). In detail, the inner shell is mainly composed of the posterior portion of the VAL, the dorsal portion of the VM and the ventral portion of the PO/PF (**Figure 6C**). While the outer shell is mainly composed of the AM, the MD, the anterior portion of the VAL, the ventral portion of the VM and the dorsal portion of the PO/PF (**Figures 6A,B**). Based on the projection model of the thalamus to the MOp and MOs previously shown (Oh et al., 2014), we concluded a three-dimensional projection model with more information based on our data (**Figure 6D**).

In other regions, the MOp and MOs also receive region-specific projections from the CLA and BLA. The neurons projecting to the MOp appear in the dorsal part of the CLA, while those projecting to the MOs focus in the ventral part of the CLA (**Figures 7A,B**). The neurons projecting to the MOp, and MOs focus in the ventral and dorsal part of the anterior BLA, respectively (**Figures 7C,D**). Although the projections from the basal forebrain regions to the MOp and MOs were not large, they showed regularity. In the MOp, almost no projections came from the anterior nucleus of the basal forebrain: the MS and the anterior part of the NDB. When we compared the distribution pattern into the basal forebrain (**Figure 3**), the ratio of projection to the MOp increased from the anterior parts to the posterior parts, as from the MS, NDB, SI to the PALd. These results were consistent with the results obtained in previous studies using retrograde fluorescent dyes (Zaborszky et al., 2015). Surprisingly, we found that the MOp receives a small number of projections from the contralateral cerebellar nuclei DN and the IP, with almost no projections to the MOs, and neither the MOp nor the MOs received projections from the ipsilateral DN and the IP. It has been thought that the cerebellum generally projects indirectly to the cortex, which mainly transmits information to the thalamus region as a relay station (Dum and Strick, 2003; Ramnani, 2006). Now, we are the first to reveal that the contralateral cerebellum nuclei can innervate the MOp directly.

DISCUSSION

Using a monosynaptic rabies tracing strategy, combined with continuously imaging using the fMOST system, we mapped the whole brain inputs to specific cell types in the subregions of the MC. We validated the afferent connections of the subregions of the MC revealed by previous studies, but with cell-type specificity and systematical comparison. The distribution

patterns of inputs to the glutamatergic and GABAergic neurons in the MC are similar, which means that different cell types of individual brain regions receive inputs from the same areas. These results are in agreement with previous studies of the DR (Ogawa et al., 2014), the VTA (Beier et al., 2015), the SSp-bfd (Wall et al., 2016), the basal forebrain (Do et al., 2016), the dorsal striatum (Guo Q. et al., 2015). However, it is still unclear if these glutamatergic and GABAergic neurons are innervated by the same type of neurons and the same upstream circuits.

Importantly, using a 3D reconstruction, we found that the distribution of the input neurons that project to the primary and secondary MC are significantly different. In the cortex, the MOp is mainly innervated by the lateral portion of the somatosensory motor subnetworks, while the MOs is mainly innervated by medial portion of it. The medial subnetworks primarily project to the MOs instead of the MOp. Such a cortical connection pattern may indicate that, compared with the MOp, which mainly integrates somatosensory information to generate motion, the MOs integrates more sensory information (visual and auditory) and plays an important role in motor cognitive function (Sul et al., 2011; Murakami et al., 2014; Barthas and Kwan, 2017). In the thalamus, the projection from the VAL, VM, PO and the PF to subregions of the MC show regional specificity. The populations in the thalamus projecting to the MOp and MOs are like an inner shell and an outer shell respectively. Such a topographic relationship is similar to the distribution patterns of fibers in the thalamic areas, projecting from layer6 neurons in the MOp and MOs, respectively (Jeong et al., 2016). It verifies the reciprocal correspondence projection relationship between the subregions in the thalamus and cortex (Allendoerfer and Shatz, 1994; Hunnicutt et al., 2014; Oh et al., 2014). The motor thalamus nucleus, VAL and the VM, project to both the MOp and MOs, while the limbic thalamus, AM, and the MD, have a certain number of projections to the MOs but not to the MOp. These connections match the functional roles of the subregions of the MC, showing that the MOp may be involved in more motion generation and control, while the MOs is more inclined to be cognitively related to motion control. In addition, the connection patterns can provide a reference for the boundary demarcation of the thalamic nucleus (Hunnicutt et al., 2014) which is not clear in the cytoarchitecture.

Current results show that the neurons that project to the MOp, and MOs are regionally specific in the CLA and BLA. In previous studies on the projection from the CLA to the MOs and the ACA (Zingg et al., 2014), these results suggest that the CLA can be divided into different subregions that connect with different cortical areas with parallel and distinct circuits. The BLA has more projections to the MOs than to the MOp, which suggests that the BLA affects the excitability of the two subregions of the MC to varying degrees (Gokdemir et al., 2018). We found that the MOs receives large projections from the CA1 in the hippocampus. while the MOp does not. This may provide an anatomical reference that the MOs is involved in the regulation of spatial memory (Yamawaki et al., 2016). Here, we have not discussed the regions or populations innervating to the MOp and MOs simultaneously in the limitation of the dual-color RV labeling. In the technique, the rabies virus that was expressed in input neurons of the MOp in MOs, can get a supplement of the G protein in the MOs, then perform transsynaptic labeling of the MOs. In the single RV labeling experiments, the results showed that populations projected to the MOp, while the MOs segregated, which is consistent with the dual-color RV labeling.

In summary, we obtained a complete dataset of the inputs to specific cell types in the subregions of the MC. As far as we know, this study is the first to analyze and compare inputs to specific cell types in the subregions of the MC. Our results revealed a segregated but regional-specific projection pattern to the MOp and MOs. The distinct input patterns may be the root cause of functional differences between the MOp and MOs. Our results will be helpful in further understanding sophisticated brain connectivity and the function distinctions between the two subregions of the MC as well as lay a solid foundation to explore the behavioral impacts of them.

ETHICS STATEMENT

All animal experiments were approved by the Animal Ethics Committee of Huazhong University of Science and Technology.

AUTHOR CONTRIBUTIONS

XL and HG conceived and designed the study. PL, YZ, and JT performed the experiments and analyzed the data. YH performed the whole-brain data acquisition. ZX and AL performed the whole-brain data processing. XL and PL wrote the manuscript.

FUNDING

This work was financially supported by the NSFC projects (Grant Nos. 61721092, 91749209, and 31871088), and the Director Fund of WNLO.

ACKNOWLEDGMENTS

We thank Hong Ni, Ayizuoheri·Tudi, Mei Yao, Peilin Zhao, Qingtao Sun, Miao Ren, Jing Yuan, and Xueyan Jia for their help with the experiments and data analysis. We thank the Optical Bioimaging Core Facility of HUST for their support with data acquisition.

SUPPLEMENTARY MATERIAL

The Supplementary Material for this article can be found online at: https://www.frontiersin.org/articles/10.3389/fnana.2019.00044/full#supplementary-material

REFERENCES

Allendoerfer, K. L., and Shatz, C. J. (1994). The subplate, a transient neocortical structure: its role in the development of connections between thalamus and cortex. *Annu. Rev. Neurosci.* 17, 185–218. doi: 10.1146/annurev.neuro.17.1.185

Barthas, F., and Kwan, A. C. (2017). Secondary motor cortex: where 'Sensory' Meets 'Motor' in the rodent frontal cortex. *Trends Neurosci.* 40, 181–193. doi: 10.1016/j.tins.2016.11.006

Beier, K. T., Steinberg, E. E., DeLoach, K. E., Xie, S., Miyamichi, K., Schwarz, L., et al. (2015). Circuit architecture of VTA dopamine neurons revealed by systematic input-output mapping. *Cell* 162, 622–634. doi: 10.1016/j.cell.2015.07.015

Campsall, K. D., Mazerolle, C. J., De Repentingy, Y., Kothary, R., and Wallace, V. A. (2002). Characterization of transgene expression and Cre recombinase activity in a panel of Thy-1 promoter-Cre transgenic mice. *Dev. Dyn.* 224, 135–143. doi: 10.1002/dvdy.10092

Chen, C., Cheng, M., Ito, T., and Song, S. (2018). Neuronal organization in the inferior colliculus revisited with cell-type-dependent monosynaptic tracing. *J. Neurosci.* 38, 3318–3332. doi: 10.1523/JNEUROSCI.2173-17.2018

Do, J. P., Xu, M., Lee, S. H., Chang, W. C., Zhang, S., Chung, S., et al. (2016). Cell type-specific long-range connections of basal forebrain circuit. *eLife* 5:e13214. doi: 10.7554/eLife.13214

Dum, R. P., and Strick, P. L. (2003). An unfolded map of the cerebellar dentate nucleus and its projections to the cerebral cortex. *J. Neurophysiol.* 89, 634–639. doi: 10.1152/jn.00626.2002

Ferreri, F., Pasqualetti, P., Maatta, S., Ponzo, D., Guerra, A., Bressi, F., et al. (2011). Motor cortex excitability in Alzheimer's disease: a transcranial magnetic stimulation follow-up study. *Neurosci. Lett.* 492, 94–98. doi: 10.1016/j.neulet.2011.01.064

Gokdemir, S., Gunduz, A., Ozkara, C., and Kiziltan, M. E. (2018). Fear-conditioned alterations of motor cortex excitability: the role of amygdala. *Neurosci. Lett.* 662, 346–350. doi: 10.1016/j.neulet.2017.10.059

Gong, H., Xu, D., Yuan, J., Li, X., Guo, C., Peng, J., et al. (2016). High-throughput dual-colour precision imaging for brain-wide connectome with cytoarchitectonic landmarks at the cellular level. *Nat. Commun.* 7:12142. doi: 10.1038/ncomms12142

Guo, J. Z., Graves, A. R., Guo, W. W., Zheng, J., Lee, A., Rodriguez-Gonzalez, J., et al. (2015). Cortex commands the performance of skilled movement. *eLife* 4:e10774. doi: 10.7554/eLife.10774

Guo, Q., Wang, D., He, X., Feng, Q., Lin, R., Xu, F., et al. (2015). Whole-brain mapping of inputs to projection neurons and cholinergic interneurons in the dorsal striatum. *PLoS One* 10:e0123381. doi: 10.1371/journal.pone.0123381

Hooks, B. M., Mao, T., Gutnisky, D. A., Yamawaki, N., Svoboda, K., and Shepherd, G. M. (2013). Organization of cortical and thalamic input to pyramidal neurons in mouse motor cortex. *J. Neurosci.* 33, 748–760. doi: 10.1523/JNEUROSCI.4338-12.2013

Hu, R., Jin, S., He, X., Xu, F., and Hu, J. (2016). Whole-brain monosynaptic afferent inputs to basal forebrain cholinergic system. *Front. Neuroanat.* 10:98. doi: 10.3389/fnana.2016.00098

Huang, Z. J. (2014). Toward a genetic dissection of cortical circuits in the mouse. *Neuron* 83, 1284–1302. doi: 10.1016/j.neuron.2014.08.041

Hunnicutt, B. J., Long, B. R., Kusefoglu, D., Gertz, K. J., Zhong, H., and Mao, T. (2014). A comprehensive thalamocortical projection map at the mesoscopic level. *Nat. Neurosci.* 17, 1276–1285. doi: 10.1038/nn.3780

Jeong, M., Kim, Y., Kim, J., Ferrante, D. D., Mitra, P. P., Osten, P., et al. (2016). Comparative three-dimensional connectome map of motor cortical projections in the mouse brain. *Sci. Rep.* 6:20072. doi: 10.1038/srep20072

Kuan, L., Li, Y., Lau, C., Feng, D., Bernard, A., Sunkin, S. M., et al. (2015). Neuroinformatics of the allen mouse brain connectivity atlas. *Methods* 73, 4–17. doi: 10.1016/j.ymeth.2014.12.013

Li, X., Yu, B., Sun, Q., Zhang, Y., Ren, M., Zhang, X., et al. (2018). Generation of a whole-brain atlas for the cholinergic system and mesoscopic projectome analysis of basal forebrain cholinergic neurons. *Proc. Natl. Acad. Sci. U.S.A.* 115, 415–420. doi: 10.1073/pnas.1703601115

Li, Y., Gong, H., Yang, X., Yuan, J., Jiang, T., Li, X., et al. (2017). TDat: an efficient platform for processing petabyte-scale whole-brain volumetric images. *Front. Neural Circuits* 11:51. doi: 10.3389/fncir.2017.00051

Murakami, M., Vicente, M. I., Costa, G. M., and Mainen, Z. F. (2014). Neural antecedents of self-initiated actions in secondary motor cortex. *Nat. Neurosci.* 17, 1574–1582. doi: 10.1038/nn.3826

Ogawa, S. K., Cohen, J. Y., Hwang, D., Uchida, N., and Watabe-Uchida, M. (2014). Organization of monosynaptic inputs to the serotonin and dopamine neuromodulatory systems. *Cell Rep.* 8, 1105–1118. doi: 10.1016/j.celrep.2014.06.042

Oh, S. W., Harris, J. A., Ng, L., Winslow, B., Cain, N., Mihalas, S., et al. (2014). A mesoscale connectome of the mouse brain. *Nature* 508, 207–214. doi: 10.1038/nature13186

Osakada, F., Mori, T., Cetin, A. H., Marshel, J. H., Virgen, B., and Callaway, E. M. (2011). New rabies virus variants for monitoring and manipulating activity and gene expression in defined neural circuits. *Neuron* 71, 617–631. doi: 10.1016/j.neuron.2011.07.005

Peters, A. J., Liu, H., and Komiyama, T. (2017). Learning in the rodent motor cortex. *Annu. Rev. Neurosci.* 40, 77–97. doi: 10.1146/annurev-neuro-072116-031407

Quan, T., Zhou, H., Li, J., Li, S., Li, A., Li, Y., et al. (2016). NeuroGPS-Tree: automatic reconstruction of large-scale neuronal populations with dense neurites. *Nat. Methods* 13, 51–54. doi: 10.1038/nmeth.3662

Ramnani, N. (2006). The primate cortico-cerebellar system: anatomy and function. *Nat. Rev. Neurosci.* 7, 511–522. doi: 10.1038/nrn1953

Ren, M., Tian, J., Zhao, P., Luo, J., Feng, Z., Gong, H., et al. (2018). Simultaneous acquisition of multicolor information from neural circuits in resin-embedded samples. *Front. Neurosci.* 12:885. doi: 10.3389/fnins.2018.00885

Sanes, J. N., and Donoghue, J. P. (2000). Plasticity and primary motor cortex. *Annu. Rev. Neurosci.* 23, 393–415. doi: 10.1146/annurev.neuro.23.1.393

Shepherd, G. M. (2013). Corticostriatal connectivity and its role in disease. *Nat. Rev. Neurosci.* 14, 278–291. doi: 10.1038/nrn3469

Sul, J. H., Jo, S., Lee, D., and Jung, M. W. (2011). Role of rodent secondary motor cortex in value-based action selection. *Nat. Neurosci.* 14, 1202–1208. doi: 10.1038/nn.2881

Tanji, J. (2001). Sequential organization of multiple movements: involvement of cortical motor areas. *Annu. Rev. Neurosci.* 24, 631–651. doi: 10.1146/annurev.neuro.24.1.631

Tennant, K. A., Adkins, D. L., Donlan, N. A., Asay, A. L., Thomas, N., Kleim, J. A., et al. (2011). The organization of the forelimb representation of the C57BL/6 mouse motor cortex as defined by intracortical microstimulation and cytoarchitecture. *Cereb. Cortex* 21, 865–876. doi: 10.1093/cercor/bhq159

Vong, L., Ye, C., Yang, Z., Choi, B., Chua, S Jr., and Lowell, B. B. (2011). Leptin action on GABAergic neurons prevents obesity and reduces inhibitory tone to POMC neurons. *Neuron* 71, 142–154. doi: 10.1016/j.neuron.2011.05.028

Wall, N. R., De La Parra, M., Sorokin, J. M., Taniguchi, H., Huang, Z. J., and Callaway, E. M. (2016). Brain-wide maps of synaptic input to cortical interneurons. *J. Neurosci.* 36, 4000–4009. doi: 10.1523/JNEUROSCI.3967-15.2016

Wall, N. R., Wickersham, I. R., Cetin, A., De La Parra, M., and Callaway, E. M. (2010). Monosynaptic circuit tracing in vivo through Cre-dependent targeting and complementation of modified rabies virus. *Proc. Natl. Acad. Sci.* 107, 21848–21853. doi: 10.1073/pnas.1011756107

Wickersham, I. R., Finke, S., Conzelmann, K. K., and Callaway, E. M. (2007a). Retrograde neuronal tracing with a deletion-mutant rabies virus. *Nat. Methods* 4, 47–49. doi: 10.1038/nmeth999

Wickersham, I. R., Lyon, D. C., Barnard, R. J. O., Mori, T., Finke, S., Conzelmann, K.-K., et al. (2007b). Monosynaptic restriction of transsynaptic tracing from single, genetically targeted neurons. *Neuron* 53, 639–647. doi: 10.1016/j.neuron.2007.01.033

Yamawaki, N., Radulovic, J., and Shepherd, G. M. (2016). A corticocortical circuit directly links retrosplenial cortex to M2 in the mouse. *J. Neurosci.* 36, 9365–9374. doi: 10.1523/JNEUROSCI.1099-16.2016

Yang, H., Yang, J., Xi, W., Hao, S., Luo, B., He, X., et al. (2016). Laterodorsal tegmentum interneuron subtypes oppositely regulate olfactory cue-induced innate fear. *Nat. Neurosci.* 19, 283–289. doi: 10.1038/nn.4208

Yang, Y., Wang, Z.-H., Jin, S., Gao, D., Liu, N., Chen, S.-P., et al. (2016). Opposite monosynaptic scaling of BLP–vCA1 inputs governs hopefulness- and helplessness-modulated spatial learning and memory. *Nat. Commun.* 7:11935. doi: 10.1038/ncomms11935

Zaborszky, L., Csordas, A., Mosca, K., Kim, J., Gielow, M. R., Vadasz, C., et al. (2015). Neurons in the basal forebrain project to the cortex in a complex topographic organization that reflects corticocortical connectivity patterns: an experimental study based on retrograde tracing and 3D reconstruction. *Cereb. Cortex* 25, 118–137. doi: 10.1093/cercor/bht210

Zhang, S., Xu, M., Chang, W. C., Ma, C., Hoang Do, J. P., Jeong, D., et al. (2016). Organization of long-range inputs and outputs of frontal cortex for top-down control. *Nat. Neurosci.* 19, 1733–1742. doi: 10.1038/nn.4417

Zingg, B., Hintiryan, H., Gou, L., Song, M. Y., Bay, M., Bienkowski, M. S., et al. (2014). Neural networks of the mouse neocortex. *Cell* 156, 1096–1111. doi: 10.1016/j.cell.2014.02.023

Conflict of Interest Statement: The authors declare that the research was conducted in the absence of any commercial or financial relationships that could be construed as a potential conflict of interest.

frontiers in Neuroanatomy

ORIGINAL RESEARCH
published: 30 April 2019
doi: 10.3389/fnana.2019.00045

Distribution Patterns of Three Molecularly Defined Classes of GABAergic Neurons Across Columnar Compartments in Mouse Barrel Cortex

*Zsuzsanna Almási[1], Csaba Dávid[1], Mirko Witte[2] and Jochen F. Staiger[2]**

[1] Department of Anatomy, Histology and Embryology, Semmelweis University, Budapest, Hungary, [2] Center Anatomy, Institute for Neuroanatomy, Georg-August-University Göttingen, Göttingen, Germany

The mouse somatosensory cortex is an excellent model to study the structural basis of cortical information processing, since it possesses anatomically recognizable domains that receive different thalamic inputs, which indicates spatial segregation of different processing tasks. In this work we examined three genetically labeled, non-overlapping subpopulations of GABAergic neurons: parvalbumin- (PV+), somatostatin- (SST+), and vasoactive intestinal polypeptide-expressing (VIP+) cells. Each of these subpopulations displayed a unique cellular distribution pattern across layers. In terms of columnar localization, the distribution of these three populations was not quantitatively different between barrel-related versus septal compartments in most layers. However, in layer IV (LIV), SST+, and VIP+, but not PV+ neurons preferred the septal compartment over barrels. The examined cell types showed a tendency toward differential distribution in supragranular and infragranular barrel-related versus septal compartments, too. Our data suggests that the location of GABAergic neuron cell bodies correlates with the spatial pattern of cortical domains receiving different kinds of thalamic input. Thus, at least in LIV, lemniscal inputs present a close spatial relation preferentially to PV+ cells whereas paralemniscal inputs target compartments in which more SST+ and VIP+ cells are localized. Our findings suggest pathway-specific roles for neocortical GABAergic neurons.

Keywords: barrel cortex, GABAergic neuron, parvalbumin, somatostatin, vasoactive intestinal peptide (VIP), cortical laminae, septa

OPEN ACCESS

Edited by:
Kathleen S. Rockland, Boston University, United States

Reviewed by:
Joshua C. Brumberg, Queens College (CUNY), United States
Akiya Watakabe, RIKEN Center for Brain Science (CBS), Japan

****Correspondence:***
Jochen F. Staiger
jochen.staiger@med.uni-goettingen.de

Received: *21 January 2019*
Accepted: *02 April 2019*
Published: *30 April 2019*

Citation:
Almási Z, Dávid C, Witte M and Staiger JF (2019) Distribution Patterns of Three Molecularly Defined Classes of GABAergic Neurons Across Columnar Compartments in Mouse Barrel Cortex. Front. Neuroanat. 13:45. doi: 10.3389/fnana.2019.00045

INTRODUCTION

The neocortex contains two main groups of neurons: the excitatory glutamatergic cells and the inhibitory GABAergic cells, which both are crucial for sensory information processing (Harris and Mrsic-Flogel, 2013). These two groups are molecularly, morphologically and physiologically distinct. Excitatory pyramidal cells make up approximately 80–90% of all neocortical cells and can be grouped according to laminar location and projection targets (Huang, 2014; Harris and Shepherd, 2015). Inhibitory GABAergic neurons comprise only about 10–20% of the total

population of neocortical neurons, but their diversity is surprisingly large (Markram et al., 2004; Rudy et al., 2011; De Felipe et al., 2013; Tremblay et al., 2016; Feldmeyer et al., 2018). The parvalbumin (PV+), somatostatin (SST+), and vasoactive intestinal polypeptide (VIP+) expressing cells account for the majority of GABAergic neurons (roughly 40% PV, 30% SST, and 10–15% VIP). These three distinct classes show minimal overlap in all examined cortical areas (Pfeffer et al., 2013; Tremblay et al., 2016), and have diverse molecular, structural and electrophysiological features. However, their detailed distribution and specific functions are largely unknown. A non-uniform distribution would imply distinct functions in local circuits of the barrel cortex (Feldmeyer et al., 2013). In this frame, we described the spatial distribution of these neuron types, in order to investigate their relationship to cortical compartments receiving different thalamic afferentation.

Sensory information from the whisker pad is transmitted via modularly organized parallel pathways to the barrel cortex (Diamond et al., 2008; Feldmeyer et al., 2013; Zembrzycki et al., 2013). The trigeminal nerve projects to several nuclei in the brainstem, namely the mesencephalic, principal (or pontine) and spinal nucleus. The lemniscal pathway originates in the principal trigeminal nucleus and relays tactile information via the barreloids of the ventral posteromedial nucleus (VPM) of the thalamus. The paralemniscal pathway routes its information through the spinal trigeminal nucleus (intermediate part) and medial part of the posterior thalamic nucleus (POm). From thalamus, ascending information reaches different cortical areas and layers. The primary site of termination is the barrel cortex, where the lemniscal thalamocortical fibers strongly project to layer IV (LIV) and thus also define supragranular and infragranular compartments, which are radially aligned with a barrel (Woolsey and van der Loos, 1970). This leads to the formation of barrel-related columns that are driven by their corresponding whiskers (Staiger et al., 2002; Wagener et al., 2016). Barrel columns are separated by septal compartments (Kim and Ebner, 1999; Alloway et al., 2004). The lemniscal pathway projects via VPM to the barrel columns, most strongly into LIV, layer Vb (LVb), layer VI (LVI), and less strongly to layer II/III (LII/III) (Lu and Lin, 1993; Bureau et al., 2006; Oberlaender et al., 2012), whereas the paralemniscal pathway projects via POm preferentially to layer I (LI) and layer Va (LVa) in a column-overarching manner and sends a few fibers to the LIV septum (Alloway, 2008; Wimmer et al., 2010b).

Single-cell recordings *in vivo* and *in vitro*, combined with biocytin filling and morphological reconstruction, revealed functional and morphological features of the different GABAergic neurons, found in the three subpopulations (Markram et al., 2004; Jiang et al., 2015; Tremblay et al., 2016; Feldmeyer et al., 2018). PV+ cells are located in all cortical layers (but LI). They prefer layers IV and Vb, however (Celio, 1986). Their dendritic and axonal arbors can show diverse patterns, depending on the precise laminar location of the soma; in this home layer the densest axonal as well as dendritic arborization can be found (Wang et al., 2002; Munoz et al., 2014; Koelbl et al., 2015). Their inhibitory influence strongly affects their own population (Tamas et al., 2000; Staiger et al., 2009; Pfeffer et al., 2013), but they can effectively inhibit other GABAergic interneuron types (David et al., 2007; Jiang et al., 2015; Karnani et al., 2016b; Walker et al., 2016). Furthermore, they are classically considered to be (together with the rare axo-axonic cell) the most effective inhibitors of pyramidal cells (Kubota et al., 2015; Neske et al., 2015).

SST+ cells show a bias toward infragranular layers. However, the different subpopulations, namely Martinotti and non-Martinotti cells, can show very distinct patterns of soma localization and axonal targeting (Oliva et al., 2000; Ma et al., 2006; Urban-Ciecko and Barth, 2016; Nigro et al., 2018). Compared to PV+ cells, they rather seem to avoid inhibiting other SST+ cells, but impose strong inhibition on other interneurons and pyramidal cells, in a cell type-specific manner (Caputi et al., 2009; Pfeffer et al., 2013; Xu et al., 2013). To exert their likely distal dendritic inhibition, they send dense axonal projections strongly but not exclusively into LI whereas their dendritic arborization is far less wide-ranging but usually not restricted to the home layer (Ma et al., 2006; McGarry et al., 2010; Nigro et al., 2018).

By contrast, VIP+ cells show a preferential location in the supragranular layers of mouse and rat barrel cortex (Bayraktar et al., 2000; Prönneke et al., 2015) and have recently been implicated in parallel disinhibitory and inhibitory circuits, impinging on pyramidal cells (Lee et al., 2013; Pi et al., 2013; Garcia-Junco-Clemente et al., 2017; Kuchibhotla et al., 2017; Zhou et al., 2017). In terms of input-output patterns, we have recently suggested that L II/III VIP+ cells have a dendritic tree that is largely restricted to L I-III but an axonal arbor that reaches all layers of a barrel-related column. On the other hand, VIP+ neurons in L IV-VI display a variable dendritic tree that could span all layers, whereas the axon is basically confined to infragranular layers (Prönneke et al., 2015). A major connectivity motif is VIP+ cells inhibiting SST+ Martinotti cells, in barrel as well as visual cortex (Caputi et al., 2009; Pfeffer et al., 2013; Karnani et al., 2016a; Walker et al., 2016).

As already noted above, thalamocortical projections and interneuron somata show layer preferences. However, there are also columns as another organizational principle of the cortex (Mountcastle, 1997). Although a barrel-related column preference of lemniscal and a septal compartment (often also called column) preference of paralemniscal thalamocortical fibers are well described, there is very little information available about the barrel- or septum-related columnar preferences of GABAergic neurons. There are only few cases, where not only the laminar, but the horizontal distribution was examined (Hajós et al., 1998; Nogueira-Campos et al., 2012). It is known that different types of interneurons can be the target of thalamocortical fibers of different origin (Staiger et al., 1996a,b; Porter et al., 2001; Cruikshank et al., 2010; Ji et al., 2016; Audette et al., 2017; Maffei, 2017). However, a more refined knowledge on the distribution pattern could help design experiments to further analyze thalamic inputs to GABAergic neurons in more detail.

Thus, in the present study, we aimed to answer the question whether PV+, SST+, and VIP+ neurons show a preference for the laminar and columnar compartments of the barrel cortex, as defined by the two main thalamocortical pathways.

Since LIV has a unique and central role as an access point of tactile information to the cortex and the barrel versus septum distinction is most obvious there, we put a special focus on this layer. The main question thus was, whether a compartment-associated distribution of GABAergic neurons can be found? Our results show that although laminar and columnar preferences obviously do exist for the soma locations of PV+, SST+, and VIP+ cells, only in LIV and only for SST+ and VIP+ cells, these differences reach statistical significance.

MATERIALS AND METHODS

Animals

Three different genetically engineered mouse strains were used for the present experiments: (1) a cross breed of PVcre/tdTomato mice (crossed B6;129P2-Pvalbtm1(cre)Arbr/J with B6.Cg-Gt(ROSA)26Sortm9(CAG-tdTomato)Hze/J mice) and GIN (Oliva et al., 2000) mice (PV-GIN; n = 6, male), which expressed the red fluorescent protein tdTomato in PV cells and green fluorescent protein (GFP) in a subset of SST cells, (2) SSTcre/tdTomato mice (crossed Ssttm2.1(cre)Zjh/J with B6.Cg-Gt(ROSA)26Sortm9(CAG-tdTomato)Hze/J mice) (n = 7, male) were used for visualizing all somatostatin cells, and (3) VIPcre/tdTomato mice (crossed VIPtm1(cre)Zjh with B6.Cg-Gt(ROSA)26Sortm9(CAG-tdTomato)Hze/J mice) (n = 9, male), were used to label all vasoactive intestinal polypeptide (VIP) cells. The age of animals was between 6 and 8 weeks. All used animals were obtained from the breeding facility of the University Medical Center Göttingen (Germany). Animal numbers and their suffering were restricted to the minimum. This study was carried out in accordance with the principles of the Basel Declaration and German laws on animal research (TierSchG and TierSchVersV, 2013). The protocol was approved by the LAVES (Niedersächsisches Landesamt für Verbraucherschutz und Lebensmittelsicherheit).

Tissue Preparation and Immunocytochemistry

The animals were anesthetized with an overdose of ketamin (Essex Tierarznei) and transcardially perfused with 0.9% NaCl solution to remove blood from vessels, followed by 4% paraformaldehyde dissolved in 0.1 M phosphate buffer (PB, pH 7.4). The brains were removed and the two hemispheres separated. The left hemispheres were flattened (Welker and Woolsey, 1974) whereas the right ones were kept unmodified, and all tissue was postfixed for 2 h in the same fixative. The right hemispheres were cut in the coronal plane, the left hemispheres tangentially on a vibratome (VT 1200S, Leica), both with a nominal section thickness of 50 μm.

The sections of PV-GIN animals were incubated with rabbit anti-GFP (Invitrogen) 1:2500 in TRIS-buffered saline with 0.3% Triton X-100 (TBST) for 2 days (in a cold room), followed by an anti-rabbit IgG coupled with Alexa-488 (Invitrogen) 1:500 in TBST for 2 h. The PV+ cells contained a sufficient amount of tdTomato, therefore they did not need further signal amplification. The sections of SSTcre/tdTomato and VIPcre/tdTomato animals were stained with guinea pig anti-vesicular glutamate transporter 2 (vGlut2; Millipore) 1:10,000 in TBST for 2 days, followed by an anti-guinea pig IgG coupled with Alexa 488 (Invitrogen) 1:500 in TBST for 2 h, in order to identify barrels. In a last step, sections of all strains were stained with DAPI (1:1000, Molecular Probes) to label cell nuclei. The sections were then embedded in AquaPolymount (Polysciences).

Image Acquisition

Microphotographs were taken with an epifluorescence microscope (AxioImager.M2, Zeiss, Jena, Germany; 5x A-Plan objective, NA 0.12 or 10x C-Plan Neofluar objective, NA 0.3) as "virtual tissue photomontages" controlled by Neurolucida software (MBF Bioscience, Colchester, VT, United States). Filter sets used were: for DAPI #49 (BP 365; BS 395, BP 445/50), for Alexa488/GFP #44 (BP 475/40; BS 500, BP 530/50), and for tdTomato #45 (Bp 560/40; BS 585, BP 630/75. To maintain illumination intensity comparable across sections, the dynamic range was set according to the saturation of a few (3–5) brightest pixels that belonged to somata.

Data Extraction

Please consult **Supplementary Figure 1** for a more intuitive illustration of the work flow. Consecutive tangential sections were aligned according to the pattern of vertically oriented cortical blood vessels. Neurolucida was used for registering cells and cortical domains. First, the barrels were identified and labeled individually, based on DAPI staining that was correlated with either intense PV neuropil or vGluT2 immunostaining, which is caused by thalamocortical projections into layer (L) IV. In coronal sections, the borders between LI, LII/LIII and LVa, LVb, and LVI were identified on the basis of DAPI staining. The pia mater and the LVI/white matter border were also delineated throughout the entire barrel field. Then, the location of all PV, SST, and VIP cells was registered independent of the laminar boundaries, thus the borders of the cortical domains did not bias the data collection. The resulting data files were analyzed in Neurolucida Explorer (MBF Biosciences). The following parameters were extracted: (i) cell numbers, (ii) areas of all delineated cortical domains (barrels, septa, and the related layers of the respective cortical columns), and (iii) the coordinates of all the GABAergic neurons with their distance from pia mater and white matter.

Data Processing

After identifying each barrel in coronal sections, the depth of the borders between cortical layers was measured for each, and the medio-lateral and rostro-caudal coordinates were also registered. These parameters were used to correct the measured volumina of the flattened tangential sections. After that procedure, the tangential sections were re-binned into 20 sections. In coronal sections we found the cortical thickness to be 1019,164 ± 38,550 μm. In case of 50 μm-thick sections it would contain a total number of ca. 20 tangential sections. By cutting the brain tangentially, we had diverse section numbers (15–19), depending on applied pressure during flattening. Therefore, we standardized the cortical thickness through re-binning the

sections with the following methods. First we divided each section in 20 virtual subsections and divided the cell count of a given section equally between its virtual subsections. For example, in an animal with n = 17 sections (n = original section number), we got n' = 340 subsections (n' = number of a new subsection, n' = n* 20). Then, we created normalized tangential sections: one 20th of n' of all subsections were binned together (in the example above, 17 subsections were binned in one new normalized section (**Supplementary Figure 2**).

The densities of cells of interest (PV+, SST+, VIP+) were plotted and the borders of cortical layers were defined, using the inflection points of these curves (Pohlkamp et al., 2014). Since the cortical and laminar thickness varies according to rostro-caudal and medio-lateral position, the extracted raw data had to be transformed to obtain statistically comparable quantities. The normalization of cortical thickness utilized landmarks, e.g., points of inflection on laminar borders as described previously for each of the markers examined (Pohlkamp et al., 2014). This normalization process transformed all the data into the same thickness range, therefore it made the comparison (or pooling) of coronally- versus tangentially-cut as well as more rostrally or medially versus more caudally or laterally located tissue possible.

To determine whether our data showed Gaussian distribution, we used the Shapiro–Wilk normality test. Since the Shapiro–Wilk test failed in all cases of studied cell types, the non-parametric Kruskal–Wallis test was used to determine statistically significant differences. Alpha levels were adjusted with the Bonferroni method. For comparison of numbers from tangential versus coronal sections, data were plotted and the correlation coefficient was calculated (Mystat, Systat Software, Inc., United States). We collected data from coronal sections to compare our results to previous literature. Tangential section were used to collect data about absolute numbers in the whole posteromedial barrelfield and because the identification of barrels and interbarrel septa was much more obvious. Coronal and tangential data series correlated highly with each other, therefore the density values of coronal and tangential section were pooled for the analysis.

RESULTS

PVcre/tdTomato-Expressing (PV+) GABAergic Neurons

These cells show a dominant location within the termination zones of the lemniscal thalamic projections (Chmielowska et al., 1989; Wimmer et al., 2010b), namely LIV and the LVb/VI border but also within the termination zone of paralemniscal thalamic projections (Wimmer et al., 2010b), namely layer Va (**Figure 1A**). Indeed, 26.17 ± 2.73% of all PV+ cells were located in LIV, 14.84 ± 1.94% in LVa and 27.15 ± 1.49% in LVb, whereas in layers II/III and VI together only 31.83 ± 1.99% were found. In LIV, the neuropil labeling led to the clear delineation of barrels, in coronal as well as tangential sections (**Figures 1A,B**).

Laminar Distribution

We studied the PV+ cell distribution in coronal sections of 3 hemispheres and in tangential sections of another 3 hemispheres. The coronal and tangential sections correlated with each other in terms of cell number and distribution (n = 6; r^2 = 0.925) (**Figure 3D**), therefore they were pooled for further analysis (**Table 1** and **Figure 3A**).

When extrapolated in number to 1 mm^3, PV+ cells preferred LIV and LV (a and b) in approximately equal numbers, were much sparser in LII/III and LVI and avoided LI (**Table 1** and **Figures 1A,B**, **3**; significance levels are listed in **Supplementary Table 1**, Kruskal–Wallis test was used to determine statistically significant differences). Thus, PV+ cell numbers showed a differential distribution between layers, which was very similar in the two analyzed columnar compartments (see also below).

Columnar (Barrel Versus Septum) Distribution

In layers II throughout VI, the distribution of PV+ cells was found to be similar for barrel- and septum-related compartments. However, this more or less even distribution of cell bodies was masked by the differential distribution of PV+ neuropil, which strongly preferred barrels (**Figure 1B** and **Table 1**). There were slightly more cells in barrels versus septa (**Figures 2A,D,G,J**, **3A**, LIVc versus LIVs), but this difference was not statistically significant (p = 0.885; significance levels are listed in **Supplementary Table 2**, Kruskal–Wallis test was used to determine statistically significant differences). Considering soma and neuropil labeling in PV+ neurons, in LIV this resulted in a complementary distribution profile, contrasting with VIP+ and SST+ GABAergic neurons (see below).

SST-Expressing (SST+) GABAergic Neurons

The overall distribution of SST+ cells was unique in several aspects (**Figures 1C,D**). Whereas PV+ cells showed an increased density in layers IV and Vb (as noted above), SST+ cells strongly preferred infragranular layers V-VI. In fact, 73.69 ± 5.37% of the cells were located in the infragranular layers, whereas only 26.31 ± 5.37% were found in layers I-IV. This suggests that projections like the one from M1 with heavy terminal labeling in infragranular layers might be a preferential input to these neurons (Kinnischtzke et al., 2014) but also that paralemniscal inputs have ample opportunity in targeting this class of cells in LI and LVa, whereas lemniscal inputs should preferentially innervate cells in LVb/LVI (Wimmer et al., 2010b; Audette et al., 2017).

Laminar Distribution

We studied the SST+ cell distribution in coronal sections of 3 hemispheres and in tangential sections of another three hemispheres, too. The coronal and tangential sections (total n = 6) correlated highly with each other (r^2 = 0.94) (**Figure 3D**), therefore the neurons were pooled for further analysis (**Table 2** and **Figure 3B**).

The SST+ neurons were similar in number in layers Va, Vb, and VI. Each of these layers possessed significantly more cells than LIV, LII/III, and LI, respectively. LII/III SST+ cells did not differ in number from LIV cells. The lowest number of SST+ cells was found in LI, which was significantly different from

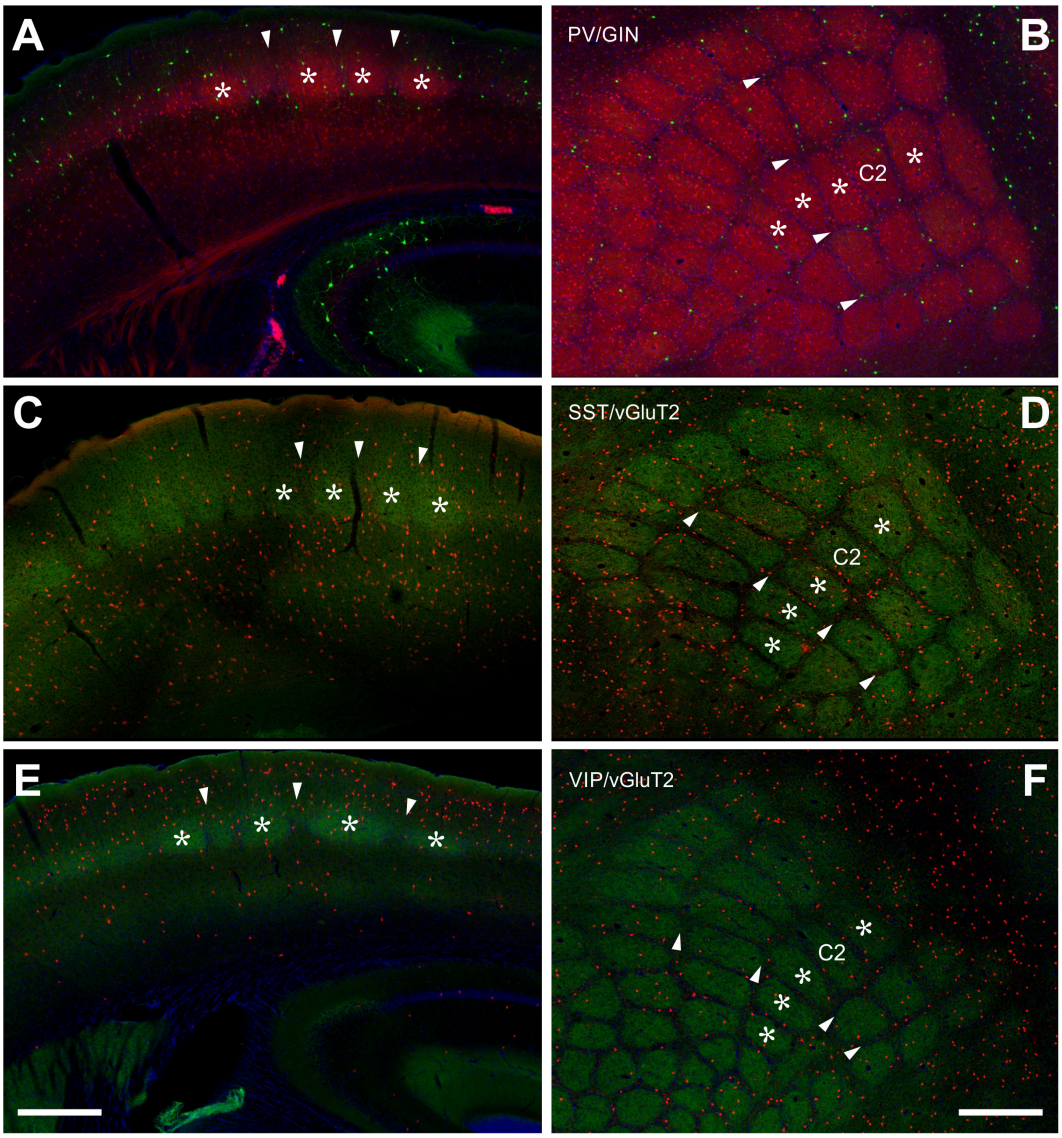

FIGURE 1 | Localization of PV+, SST+, and VIP+ interneurons in the barrel cortex. **(A,B)** Double labeling of PV+ (red, from PVcre/tdTomato animals) and SST+ (green, GIN line) shows a clear delineation of barrel-related columns in the coronal section **(A)** and a whisker-related somatotopic pattern in layer IV of tangential sections **(B)**. Indication of barrels (*asterisks*) and septa (*arrowheads*) holds for all images. PV+ cells seem to prefer barrels, but quantitative analysis showed that the cell bodies are distributed homogenously. GIN cells, however, displayed an obvious preference for the septal compartment. **(C,D)** SST+ cells (red, from SSTcre/tdTomato animals) were located preferentially in the infragranular layers **(D)**, somewhat aligned to interbarrel septa **(C,D)**. VGluT2 (green) strongly labels the lemniscal thalamic termination zone in layer IV barrels. **(E,F)** VIP+ cells (red; from VIPcre/tdTomato animals) preferred supragranular layers **(E)** and interbarrel septa **(F)**. Scale bars: 500 μm.

all other layers (significance levels are listed in **Supplementary Table 3**; Kruskal–Wallis test was used to determine statistically significant differences).

Columnar (Barrel Versus Septum) Distributions

When comparing the barrel with the septal compartment, we found that SST+ cells were distributed more or less homogenously between these compartments in all layers, except LIV (**Table 2**). As shown in **Figures 2B,E,H,K**, **3B**, in LIV, the septal compartment contained significantly more cells than the barrel compartment ($p < 0.0001$) (significance levels are listed in **Supplementary Table 4**; Kruskal–Wallis test was used to determine statistically significant differences).

VIP-Expressing (VIP+) GABAergic Neurons

Interestingly, VIP+ cells show an inverse relationship to SST+ cells, as they display a strong preference for the supragranular layers (**Figure 1E**). Indeed, 70.24% of all cells were located

TABLE 1 | Cell density of PV-expressing neurons, differentiated by barrel column and septum.

	Cell density in column (1/mm^3)	± SD (1/mm^3)	Cell density in septum (1/mm^3)	± SD (1/mm^3)
Layer I	0	0	0	0
Layer II/III	4995.65	1278.58	5050.46	2012.55
Layer IV	8426.59	1405.35	8252.19	1751.12
Layer Va	8510.96	1766.67	7904.56	2217.68
Layer Vb	8964.038	2143.11	8244.73	3170.58
Layer VI	3017.66	1003.13	2766.40	877.38

in layers I-III, whereas only 29.76% were found in layers IV-VI. Since the subpopulation located in LI and LII/III shows extensive dendritic arborization in layer I (Prönneke et al., 2015), projections like those from motor cortex or basal forebrain can strongly target these cells (Mechawar et al., 2000; Lee et al., 2013), as does the lemniscal thalamus in deep LII/III (Staiger et al., 1996b; Wall et al., 2016).

Laminar Distribution

We studied the VIP+ cell distribution in coronal sections of three hemispheres and in tangential sections of another three hemispheres. The cell numbers in these sections (total $n = 6$) were again correlated highly with each other ($r^2 = 0.973$) (**Figure 3D**), thus, the values were pooled for further analysis (**Table 3** and **Figure 3C**).

VIP+ cells in LII/III outnumbered those in all other layers significantly whereas LI had significantly lower numbers than all other layers (except LVI). Also the gradient from LIV to LVI reached statistical significance, with each deeper layer housing less neurons than the one located pialward (significance levels are listed in **Supplementary Table 5**; Kruskal–Wallis test was used to determine statistically significant differences).

Columnar (Barrel Versus Septum) Distribution

When comparing the columnar and septal compartments, there was no obvious difference in the supragranular and infragranular layers. However, in LIV we found significantly more cells in septa than in barrels ($p < 0.0001$; Kruskal–Wallis test was used to determine statistically significant differences), which can be seen in **Figures 1F**, **2C,F,I,L**, **3C**. This columnar segregation was therefore restricted to the granular layer where the cell density in septa was approximately two times higher than in barrels (significance levels are listed in **Supplementary Table 6**; Kruskal–Wallis test was used to determine statistically significant differences).

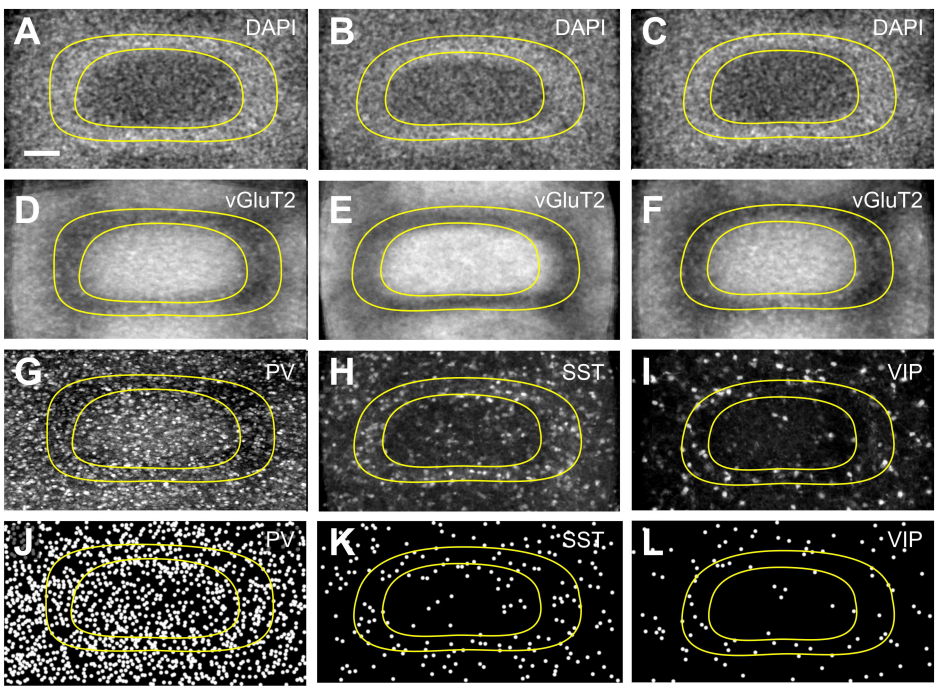

FIGURE 2 | Distribution of interneurons across layer IV barrels and septa. Fine-grained distribution of **(A,D,G,J)** PV+, **(B,E,H,K)** SST+, and **(C,F,I,L)** VIP+ interneuron somata, using tangential sections to allow a better delineation of septal and barrel compartments. DAPI staining **(A–C)** or vGluT2 immunostaining **(D–F)** was used to reveal the border of the barrels in a complementary manner. Images of nominally 50 μm thick sections of PV+ **(G)**, SST+ **(H),** and VIP+ **(I)** somata and neuropil, in conjunction with the respective Neurolucida reconstructions **(J–L)** reveal a homogenous distribution of PV+ as well as a septal preference of SST+ and VIP+ cells. Since SST and VIP neurons appear in a quite low density, especially in the granular layer, we had to project numerous barrels onto each other, in order to be able to display the uneven distribution of these cells. For that purpose, we collected barrels, which could be fit into an idealized (averaged) barrel, and then the images were projected to a single image plane using ImageJ Sum Slices function. This was not necessary for PV cells since the cell density was much higher, but for the sake of comparability we performed the same protocol on PV images. Scale bars: 50 μm.

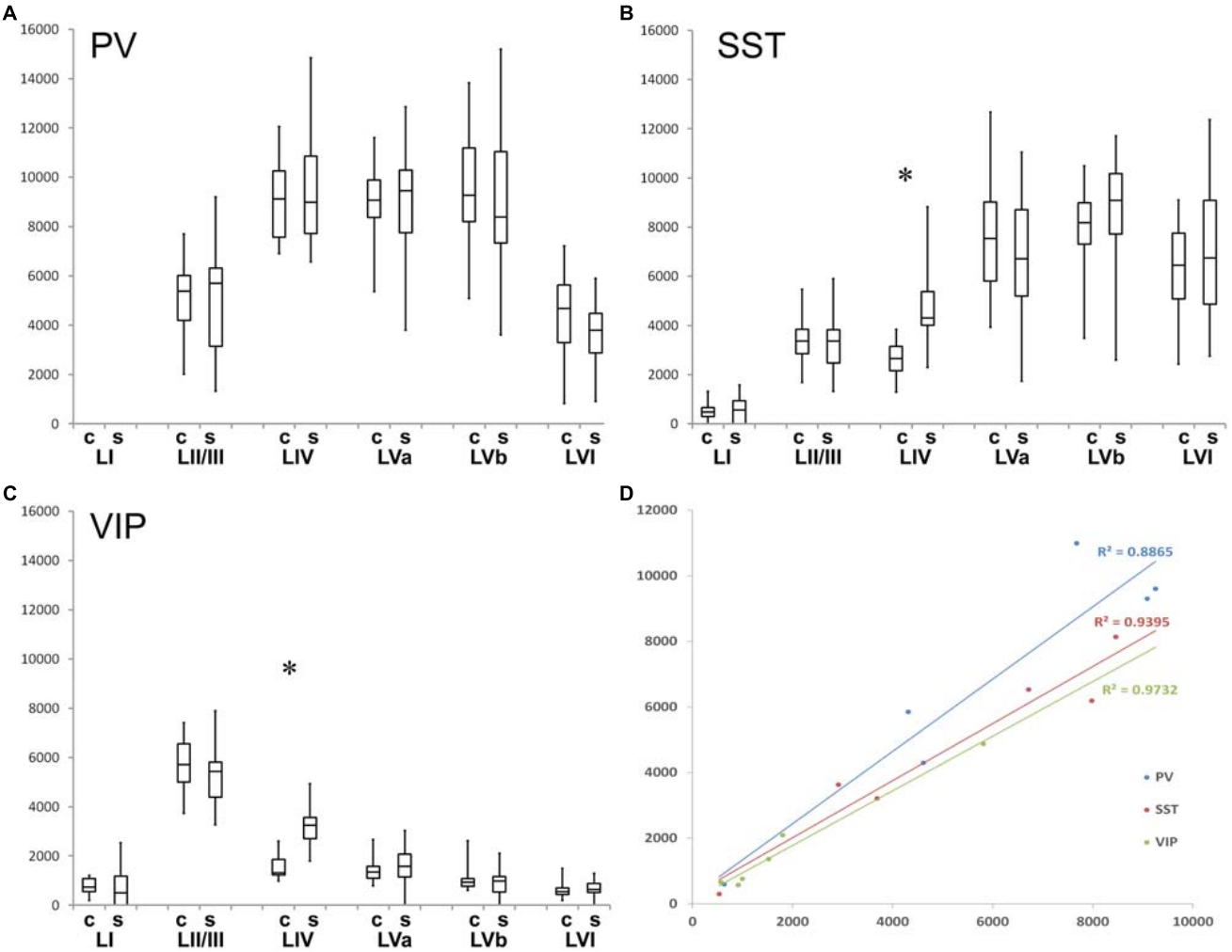

FIGURE 3 | Quantification of layer- and column-related distribution of GABAergic interneurons. Box and whisker plot of laminar density of **(A)** PV+, **(B)** SST+, and **(C)** VIP interneurons. Note the statistically significant difference between barrel column (C)- and septum (S)-associated compartments for VIP+ and SST+ cells in layer IV. Significant laminar distribution differences were not denoted because of figure transparency, details were explained above. The graphs also show that all of the studied interneurons completely (PV+) or largely (SST+, VIP+) avoid LI. **(D)** Diagram shows the cell densities of coronal versus tangential sections. Correlation coefficients (R) are close to 1, so the numbers are highly correlated to each other ($R_{PV.}$ = 0.925; R_{SST} = 0.940; R_{VIP} = 0.973).

In summary, we could reproduce the general pattern of a dominance of PV+ cells in lemniscal thalamorecipient layers (LIV and Vb) but show a frequent occurrence on the paralemniscal thalamorecipient LVa, too. SST+ showed a strong abundance in LVa/b and LVI whereas VIP+ were preferentially distributed in LII/III and LIV (**Supplementary Figure 3**). In addition, when comparing barrel-related columns with septum-associated compartments, only in LIV we could detect a statistically significant preference of SST+ and VIP+ cells for the latter (**Supplementary Figure 3**).

DISCUSSION

In the present study, we confirmed and extended the laminar distribution profiles of major subpopulations of GABAergic neurons in the mouse barrel cortex (for recent reviews see Staiger et al., 2015; Tremblay et al., 2016; Feldmeyer et al., 2018). In agreement with these previous studies, we show in tdTomato-expressing mouse lines that PV+ cells prefer layers IV and Vb, whereas SST+ cells prefer all infragranular and VIP+ cells supragranular (LII/III) layers. We extend these findings by showing that PV+ cells do not have a preferential localization within columnar compartments, since cell counts show a very similar distribution between barrel column- and septum-associated compartments. Thus, it is an anisotropic distribution of PV+ neuropil labeling that accentuates barrels in coronal as well as tangential sections. On the other hand, SST+ and VIP+ cells were significantly more frequent in the septum than the barrel (in LIV), whereas this unique distribution was just a trend, if anything, outside of LIV. These findings led us to propose that different subpopulations of neocortical GABAergic

TABLE 2 | Cell density of SST-expressing neurons, differentiated by barrel column and septum.

	Cell density in column (1/mm^3)	± SD (1/mm^3)	Cell density in septum (1/mm^3)	± SD (1/mm^3)
Layer I	512.67	356.23	566.29	558.33
Layer II/III	3353.63	903.46	3318.67	1159.57
Layer IV	2661.42	697.03	4772.67	1535.58
Layer Va	7594.97	2459.81	6752.20	2268.18
Layer Vb	8064.99	1587.00	8675.49	2425.20
Layer VI	6344.08	1985.93	6856.99	2454.67

TABLE 3 | Cell density of VIP-expressing neurons, differentiated by barrel column and septum.

	Cell density in column (1/mm^3)	± SD (1/mm^3)	Cell density in septum (1/mm^3)	±SD (1/mm^3)
Layer I	788.87	335.88	571.67	536.68
Layer II/III	5596.69	968.70	5150.93	1090.85
Layer IV	1574.74	481.32	3204.72	908.99
Layer Va	1448.33	492.38	1594.11	709.10
Layer Vb	1007.70	454.04	852.38	596.40
Layer VI	630.11	285.53	672.18	313.03

neurons could be differentially associated with different input pathways, as initially suggested for the archicortex (Somogyi et al., 1998). This notion was also referred to in the sensorimotor cortex (Kubota et al., 2007; Cruikshank et al., 2010; Audette et al., 2017), although these, as well as more recent studies in auditory and visual cortex, did not reveal a very refined picture (Ji et al., 2016). Since it is obvious that soma location is only a poor predictor for the entire input space of a neuron, we and others are currently trying to substantiate the hypothesis of thalamic (and other) input specificity on different classes of GABAergic neurons with optogenetics and whole cell recordings.

Technical Considerations

We compared and finally pooled results obtained from coronal and tangential sections of the barrel cortex (Woolsey and van der Loos, 1970). The advantage of frontal sectioning is that laminar borders can be identified with high certainty, whereas in tangential sections the barrel versus septal regions can be delineated unequivocally. Since tangential sectioning requires a certain compression of the cortex, and the cortex is not evenly thick along its medio-lateral axis, the distance of the cells from the pia mater had to be adjusted, in order to match laminar location in tangential with coronal sections. After adjustment, the cell density read-out from coronal and tangential sections was virtually identical, allowing us to pool the data. Our laminar density results of VIP+ cells are in very good agreement with that previously described for the barrel cortex (Prönneke et al., 2015) and with PV+ and SST+ cell counts from other ongoing projects (own unpublished results).

Here, we used staining for vGlut2 and DAPI as pre- and postsynaptic markers, respectively, to determine barrel and septum borders, building on our previous experience (Wagener et al., 2010). Because of putative plasticity of thalamocortical fibers (Wimmer et al., 2010a), the vGlut2-defined barrel borders could vary, thus the additional use of DAPI staining is important to define the actual barrel size and further helps to distinguish barrel and septal compartments (Erzurumlu and Kind, 2001).

It should also be noted that we have counted tdTomato-expressing cell bodies distributed across the various layers and columns, which does not necessarily mean that they are specifically and comprehensively reflecting the entire population of interest, as represented by the different cre-driver lines. However, previous studies already showed a reasonable overlap of tdTomato-fluorescence with the respective markers (GAD1, PV, SST, and VIP (Taniguchi et al., 2011; Pfeffer et al., 2013); and our own published and still ongoing efforts to characterize these mouse lines revealed a very high specificity and an excellent sensitivity (Prönneke et al., 2015).

Comparison to Previous Studies

To the best of our knowledge, the numbers of GABAergic neurons in mouse barrel cortex had not been established before and the partitioning of GABAergic neurons between barrel- and septal column was completely lacking. It has to be acknowledged that there is a comprehensive quantification with an immunohistochemical approach available, the area-densities reported there being in general agreement with our results (Xu et al., 2010). Here, we started to overcome this lack of detailed knowledge by counting soma numbers of neurons expressing tdTomato-fluorescence under the control of three marker genes that are currently viewed as the best candidates to separate the population of GABAergic neurons into three different classes (Taniguchi et al., 2011; Tremblay et al., 2016).

In PVcre/tdTomato mice, we could detect a distribution across layers that was both, qualitatively and quantitatively similar to the rat somatosensory cortex (van Brederode et al., 1991; Ren et al., 1992). We showed numbers peaking in layers IV, Va, and Vb, which would mean that major layers receiving lemniscal or paralemniscal input (Wimmer et al., 2010b) house a feedforward inhibition motif in their circuitry (Cruikshank et al., 2010; Naka and Adesnik, 2016), which does strongly influence their *in vivo* physiology (Bruno and Sakmann, 2006; de Kock et al., 2007; Yu et al., 2016).

Surprisingly, in tangential sections we did not find a significant difference between barrel and septal compartments, although PV has been used as a marker for barrels (Sukhov et al., 2016). This means that barrels are highlighted in PV staining by virtue of the neuropil labeling (mainly being axonal boutons) and not by somatodendritic profiles. This could be explained by anisotropic axonal arbors of basket cells displaying a bias toward barrel centers (Munoz et al., 2014; Koelbl et al., 2015). Further evidence that there is a profound difference between the organization of PV+ cells' dendrites versus axons in barrels versus septa comes from a recent study that showed their gap junction coupling to occur in a cell type- and location-specific manner (Shigematsu et al., 2018).

In SSTcre/tdTomato mice, we were able to show that all infragranular layers express high numbers of these cells, where

they recently have been shown also to be most diverse in structure and function (Nigro et al., 2018). In contrast, the fewer cells located in LII/III all seem to be Martinotti cells (Munoz et al., 2017; Nigro et al., 2018), which was also consistently reported in the GIN mouse line (Oliva et al., 2000; Ma et al., 2006; Walker et al., 2016). The minority population in LI remains to be better characterized (Ma et al., 2014).

The analysis in tangential sections, revealing a preferential location in septa when compared to barrels, is without precedent. One has to know that septa in mice are very small compartments, as compared to rats, thus it is very difficult to specifically record from them, in order to assess their function (Welker and Woolsey, 1974). We can only speculate that the increased number of SST+ neurons (but also VIP+ cells, see below) might serve to flexibly adjust the receptive field size of septal neurons, which is usually larger than that of barrel-related column neurons (Brecht and Sakmann, 2002).

In VIPcre/tdTomato mice, we obtained cell numbers across the different layers that were in good agreement with previous reports (Xu et al., 2010; Prönneke et al., 2015), pinpointing a preferential role of these neurons to relay information originating from diverse sources via axonal projections into layers I-III. This information is then relayed to all layers of the respective barrel column- or septum-associated compartment by virtue of their "column-filling" axonal arbors, probably impinging on excitatory and inhibitory neurons in parallel (Garcia-Junco-Clemente et al., 2017; Kuchibhotla et al., 2017; Zhou et al., 2017).

As noted already above, a novel finding was the differential distribution of VIP+ somata in barrels versus septa, with approximately twice as many cells in the septa than in the barrels. Interestingly, a previous study has reported a differential distribution of VIP+ boutons, which were more numerous in the side region than within the hollow (Zilles et al., 1993). Since a "side" is the barrel wall and the septum pooled (Welker and Woolsey, 1974) and since VIP neurons in layer II/III and IV have a radially restricted axonal arbor (Prönneke et al., 2015), these findings are complementary to ours.

Functional Implications

As noted above, the soma location alone is a very limited predictor of the input space of a neuron. However, since the dendritic arbors of GABAergic neurons are usually more compact than those of pyramidal cells, this could serve as a reasonable first approximation to consider the layer- and column-associated location of the soma as the main input space of the respective neuron (De Felipe et al., 2013).

Thus, we suggest that PV+ neurons are more or less uniformly distributed to fulfill the need of all cortical circuits to operate in a tight excitation-inhibition-balance (Isaacson and Scanziani, 2011), no matter whether feedforward pathways from the thalamus or local pathways activate them. SST+ cells, with their strong bias to infragranular layers and to LIV septa, are rather heterogeneous in their input and output domains, making a more specific functional interpretation than that they are providing widespread dendritic inhibition difficult (Urban-Ciecko and Barth, 2016; Yavorska and Wehr, 2016). VIP+ neurons, with their strong bias to supragranular layers and also LIV septa, can directly participate in sensory processing, potentially by strong disinhibitory mechanisms (Karnani et al., 2016a,b; Walker et al., 2016; Feldmeyer et al., 2018) but they also relay more global salience- or reward-related signals, originating in (pre-)motor cortex or in subcortical neuromodulatory centers to the column (Lee et al., 2013; Kepecs and Fishell, 2014).

The enrichment of SST+ and VIP+ neurons in LIV LIV septa might help to task-dependently switch cortical activity flow (and thus sensory processing) between the nested, partly distinct, partly overlapping, circuits that originate in or are wired through barrel- versus septum-associated compartments of the barrel cortex (Alloway, 2008; Diamond et al., 2008; Feldmeyer et al., 2013). The next task will be to perform optogenetic stimulation of these putative input pathways and record from single identified GABAergic neurons, in order to test our predictions.

AUTHOR CONTRIBUTIONS

ZA and CD conceived and performed the experiments, analyzed the results, and co-wrote the manuscript. MW provided the materials and co-wrote the manuscript. JS conceived the experiments, supervised the project, and wrote the manuscript.

FUNDING

This work was supported by the Deutsche Forschungsgemeinschaft (DFG grant STA 431/14-1).

ACKNOWLEDGMENTS

We want to thank Dr. Robin Wagener for his help with getting the project started. We are grateful to Patricia Sprysch for excellent technical assistance.

SUPPLEMENTARY MATERIAL

The Supplementary Material for this article can be found online at: https://www.frontiersin.org/articles/10.3389/fnana.2019.00045/full#supplementary-material

REFERENCES

Alloway, K. D. (2008). Information processing streams in rodent barrel cortex: the differential functions of barrel and septal circuits. *Cereb. Cortex* 18, 979–989. doi: 10.1093/cercor/bhm138

Alloway, K. D., Zhang, M. L., and Chakrabarti, S. (2004). Septal columns in rodent barrel cortex: Functional circuits for modulating whisking behavior. *J. Comp. Neurol.* 480, 299–309. doi: 10.1002/cne.20339

Audette, N. J., Urban-Ciecko, J., Matsushita, M., and Barth, A. L. (2017). POm thalamocortical input drives layer-specific microcircuits in

somatosensory cortex. *Cereb. Cortex* 28, 1312–1328. doi: 10.1093/cercor/bhx044

Bayraktar, T., Welker, E., Freund, T. F., Zilles, K., and Staiger, J. F. (2000). Neurons immunoreactive for vasoactive intestinal polypeptide in the rat primary somatosensory cortex: morphology and spatial relationship to barrel-related columns. *J. Comp. Neurol.* 420, 291–304. doi: 10.1002/(SICI)1096-9861(20000508)420:3<291::AID-CNE2>3.0.CO;2-H

Brecht, M., and Sakmann, B. (2002). Dynamic representation of whisker deflection by synaptic potentials in spiny stellate and pyramidal cells in the barrels and septa of layer 4 rat somatosensory cortex. *J. Physiol. (Lond.)* 543, 49–70. doi: 10.1113/jphysiol.2002.018465

Bruno, R. M., and Sakmann, B. (2006). Cortex is driven by weak but synchronously active thalamocortical synapses. *Science* 312, 1622–1627. doi: 10.1126/science.1124593

Bureau, I., Saint Paul, F., and Svoboda, K. (2006). Interdigitated paralemniscal and lemniscal pathways in the mouse barrel cortex. *PLoS Biol.* 4:e382. doi: 10.1371/journal.pbio.0040382

Caputi, A., Rozov, A., Blatow, M., and Monyer, H. (2009). Two calretinin-positive GABAergic cell types in layer 2/3 of the mouse neocortex provide different forms of inhibition. *Cereb. Cortex* 19, 1345–1359. doi: 10.1093/cercor/bhn175

Celio, M. R. (1986). Parvalbumin in most gamma-aminobutyric acid-containing neurons of the rat cerebral cortex. *Science* 231, 995–997. doi: 10.1126/science.3945815

Chmielowska, J., Carvell, G. E., and Simons, D. J. (1989). Spatial organization of thalamocortical and corticothalamic projection systems in the rat SmI barrel cortex. *J. Comp. Neurol.* 285, 325–338. doi: 10.1002/cne.902850304

Cruikshank, S. J., Urabe, H., Nurmikko, A. V., and Connors, B. W. (2010). Pathway-specific feedforward circuits between thalamus and neocortex revealed by selective optical stimulation of axons. *Neuron* 65, 230–245. doi: 10.1016/j.neuron.2009.12.025

David, C., Schleicher, A., Zuschratter, W., and Staiger, J. F. (2007). The innervation of parvalbumin-containing interneurons by VIP-immunopositive interneurons in the primary somatosensory cortex of the adult rat. *Eur. J. Neurosci.* 25, 2329–2340. doi: 10.1111/j.1460-9568.2007.05496.x

De Felipe J., López-Cruz P. L., Benavides-Piccione, R., Bielza, C., Larrañaga, P., et al. (2013). New insights into the classification and nomenclature of cortical GABAergic interneurons. *Nat. Rev. Neurosci.* 14, 202–216. doi: 10.1038/nrn3444

de Kock, C. P. J., Bruno, R. M., Spors, H., and Sakmann, B. (2007). Layer and cell type specific suprathreshold stimulus representation in primary somatosensory cortex. *J. Physiol. (Lond.)* 581, 139–154. doi: 10.1113/jphysiol.2006.124321

Diamond, M. E., Von Heimendahl, M., Knutsen, P. M., Kleinfeld, D., and Ahissar, E. (2008). 'Where' and 'what' in the whisker sensorimotor system. *Nat. Rev. Neurosci.* 9, 601–612. doi: 10.1038/nrn2411

Erzurumlu, R. S., and Kind, P. C. (2001). Neural activity: sculptor of 'barrels' in the neocortex. *Trends Neurosci.* 24, 589–595. doi: 10.1016/S0166-2236(00)01958-5

Feldmeyer, D., Brecht, M., Helmchen, F., Petersen, C. C. H., Poulet, J. F. A., Staiger, J. F., et al. (2013). Barrel cortex function. *Prog. Neurobiol.* 103, 3–27. doi: 10.1016/j.pneurobio.2012.11.002

Feldmeyer, D., Qi, G., Emmenegger, V., and Staiger, J. F. (2018). Inhibitory interneurons and their circuit motifs in the many layers of the barrel cortex. *Neuroscience* 368, 132–151. doi: 10.1016/j.neuroscience.2017.05.027

Garcia-Junco-Clemente, P., Ikrar, T., Tring, E., Xu, X., Ringach, D. L., and Trachtenberg, J. T. (2017). An inhibitory pull-push circuit in frontal cortex. *Nat. Neurosci.* 20, 389–392. doi: 10.1038/nn.4483

Hajós, F., Zilles, K., Zsarnovszky, A., Sotonyi, P., Gallatz, K., and Schleicher, A. (1998). Modular distribution of vasoactive intestinal polypeptide in the rat barrel cortex: changes induced by neonatal removal of vibrissae. *Neuroscience* 85, 45–52. doi: 10.1016/S0306-4522(97)00590-3

Harris, K. D., and Mrsic-Flogel, T. D. (2013). Cortical connectivity and sensory coding. *Nature* 503, 51–58. doi: 10.1038/nature12654

Harris, K. D., and Shepherd, G. M. G. (2015). The neocortical circuit: themes and variations. *Nat. Neurosci.* 18, 170–181. doi: 10.1038/nn.3917

Huang, Z. J. (2014). Toward a genetic dissection of cortical circuits in the mouse. *Neuron* 83, 1284–1302. doi: 10.1016/j.neuron.2014.08.041

Isaacson, J. S., and Scanziani, M. (2011). How inhibition shapes cortical activity. *Neuron* 72, 231–243. doi: 10.1016/j.neuron.2011.09.027

Ji, X. Y., Zingg, B., Mesik, L., Xiao, Z. J., Zhang, L. I., and Tao, H. Z. W. (2016). Thalamocortical innervation pattern in mouse auditory and visual cortex: laminar and cell-type specificity. *Cereb. Cortex* 26, 2612–2625. doi: 10.1093/cercor/bhv099

Jiang, X. L., Shen, S., Cadwell, C. R., Berens, P., Sinz, F., Ecker, A.S., et al. (2015). Principles of connectivity among morphologically defined cell types in adult neocortex. *Science* 350:aac9462. doi: 10.1126/science.aac9462

Karnani, M. M., Jackson, J., Ayzenshtat, I., Sichani, A. H., Manoocheri, K., Kim, S., et al. (2016a). Opening holes in the blanket of inhibition: localized lateral disinhibition by VIP interneurons. *J. Neurosci.* 36, 3471–3480. doi: 10.1523/JNEUROSCI.3646-15.2016

Karnani, M. M., Jackson, J., Ayzenshtat, I., Tucciarone, J., Manoocheri, K., Snider, W. G., et al. (2016b). Cooperative subnetworks of molecularly similar interneurons in mouse neocortex. *Neuron* 90, 86–100. doi: 10.1016/j.neuron.2016.02.037

Kepecs, A., and Fishell, G. (2014). Interneuron cell types are fit to function. *Nature* 505, 318–326. doi: 10.1038/nature12983

Kim, U., and Ebner, F. F. (1999). Barrels and septa: separate circuits in rat barrel field cortex. *J. Comp. Neurol.* 408, 489–505. doi: 10.1002/(SICI)1096-9861(19990614)408:4<489::AID-CNE4>3.0.CO;2-E

Kinnischtzke, A. K., Simons, D. J., and Fanselow, E. E. (2014). Motor cortex broadly engages excitatory and inhibitory neurons in somatosensory barrel cortex. *Cereb. Cortex* 24, 2237–2248. doi: 10.1093/cercor/bht085

Koelbl, C., Helmstaedter, M., Lubke, J., and Feldmeyer, D. (2015). A barrel-related interneuron in layer 4 of rat somatosensory cortex with a high intrabarrel connectivity. *Cereb. Cortex* 25, 713–725. doi: 10.1093/cercor/bht263

Kubota, Y., Hatada, S., Kondo, S., Karube, F., and Kawaguchi, Y. (2007). Neocortical inhibitory terminals innervate dendritic spines targeted by thalamocortical afferents. *J. Neurosci.* 27, 1139–1150. doi: 10.1523/JNEUROSCI.3846-06.2007

Kubota, Y., Kondo, S., Nomura, M., Hatada, S., Yamaguchi, N., Mohamed, A. A., et al. (2015). Functional effects of distinct innervation styles of pyramidal cells by fast spiking cortical interneurons. *Elife* 4, 1–27. doi: 10.7554/eLife.07919

Kuchibhotla, K. V., Gill, J. V., Lindsay, G. W., Papadoyannis, E. S., Field, R. E., Sten, T. A. H., et al. (2017). Parallel processing by cortical inhibition enables context-dependent behavior. *Nat. Neurosci.* 20, 62–71. doi: 10.1038/nn.4436

Lee, S., Kruglikov, I., Huang, Z. J., Fishell, G., and Rudy, B. (2013). A disinhibitory circuit mediates motor integration in the somatosensory cortex. *Nat. Neurosci.* 16, 1662–1670. doi: 10.1038/nn.3544

Lu, S. M., and Lin, R. C. S. (1993). Thalamic afferents of the rat barrel cortex: a light- and electron-microscopic study using *Phaseolus vulgaris* leucoagglutinin as an anterograde tracer. *Somatosens Motor Res.* 10, 1–16. doi: 10.3109/08990229309028819

Ma, J., Yao, X. H., Fu, Y. H., and Yu, Y. C. (2014). Development of layer 1 neurons in the mouse neocortex. *Cereb. Cortex* 24, 2604–2618. doi: 10.1093/cercor/bht114

Ma, Y. Y., Hu, H., Berrebi, A. S., Mathers, P. H., and Agmon, A. (2006). Distinct subtypes of somatostatin-containing neocortical interneurons revealed in transgenic mice. *J. Neurosci.* 26, 5069–5082. doi: 10.1523/JNEUROSCI.0661-06.2006

Maffei, A. (2017). Fifty shades of inhibition. *Curr. Opin. Neurobiol.* 43, 43–47. doi: 10.1016/j.conb.2016.12.003

Markram, H., Toledo-Rodriguez, M., Wang, Y., Gupta, A., Silberberg, G., and Wu, C. Z. (2004). Interneurons of the neocortical inhibitory system. *Nat. Rev. Neurosci.* 5, 793–807. doi: 10.1038/nrn1519

McGarry, L. M., Packer, A. M., Fino, E., Nikolenko, V., Sippy, T., and Yuste, R. (2010). Quantitative classification of somatostatin-positive neocortical interneurons identifies three interneuron subtypes. *Front. Neural Circ.* 4:12. doi: 10.3389/fncir.2010.00012

Mechawar, N., Cozzari, C., and Descarries, L. (2000). Cholinergic innervation in adult rat cerebral cortex: a quantitative immunocytochemical description. *J. Comp. Neurol.* 428, 305–318. doi: 10.1002/1096-9861(20001211)428:2<305::AID-CNE9>3.0.CO;2-Y

Mountcastle, V. B. (1997). The columnar organization of the neocortex. *Brain* 120, 701–722. doi: 10.1093/brain/120.4.701

Munoz, W., Tremblay, R., Levenstein, D., and Rudy, B. (2017). Layer-specific modulation of neocortical dendritic inhibition during active wakefulness. *Science* 355, 954–958. doi: 10.1126/science.aag2599

Munoz, W., Tremblay, R., and Rudy, B. (2014). Channelrhodopsin-assisted patching: in vivo recording of genetically and morphologically identified neurons throughout the brain. *Cell Rep.* 9, 2304–2316. doi: 10.1016/j.celrep.2014.11.042

Naka, A., and Adesnik, H. (2016). Inhibitory circuits in cortical layer 5. *Front. Neural Circ.* 10:35. doi: 10.3389/fncir.2016.00035

Neske, G. T., Patrick, S. L., and Connors, B. W. (2015). Contributions of diverse excitatory and inhibitory neurons to recurrent network activity in cerebral cortex. *J. Neurosci.* 35, 1089–1105. doi: 10.1523/JNEUROSCI.2279-14.2015

Nigro, M. J., Hashikawa-Yamasaki, Y., and Rudy, B. (2018). Diversity and connectivity of layer 5 somatostatin-expressing interneurons in the mouse barrel cortex. *J. Neurosci.* 38, 1622–1633. doi: 10.1523/JNEUROSCI.2415-17.2017

Nogueira-Campos, A. A., Finamore, D. M., Imbiriba, L. A., Houzel, J. C., and Franca, J. G. (2012). Distribution and morphology of nitrergic neurons across functional domains of the rat primary somatosensory cortex. *Front. Neural Circ.* 6:57. doi: 10.3389/fncir.2012.00057

Oberlaender, M., de Kock, C. P. J., Bruno, R. M., Ramirez, A., Meyer, H. S., Dercksen, V. J., et al. (2012). Cell type-specific three-dimensional structure of thalamocortical circuits in a column of rat vibrissal cortex. *Cereb. Cortex* 22, 2375–2391. doi: 10.1093/cercor/bhr317

Oliva, A. A., Jiang, M. H., Lam, T., Smith, K. L., and Swann, J. W. (2000). Novel hippocampal interneuronal subtypes identified using transgenic mice that express green fluorescent protein in GABAergic interneurons. *J. Neurosci.* 20, 3354–3368. doi: 10.1523/JNEUROSCI.20-09-03354.2000

Pfeffer, C. K., Xue, M. S., He, M., Huang, Z. J., and Scanziani, M. (2013). Inhibition of inhibition in visual cortex: the logic of connections between molecularly distinct interneurons. *Nat. Neurosci.* 16, 1068–U130. doi: 10.1038/nn.3446

Pi, H. J., Hangya, B., Kvitsiani, D., Sanders, J. I., Huang, Z. J., and Kepecs, A. (2013). Cortical interneurons that specialize in disinhibitory control. *Nature* 503, 521–524. doi: 10.1038/nature12676

Pohlkamp, T., David, C., Cauli, B., Gallopin, T., Bouche, E., Karagiannis, A., et al. (2014). Characterization and distribution of reelin-positive interneuron subtypes in the rat barrel cortex. *Cereb. Cortex* 24, 3046–3058. doi: 10.1093/cercor/bht161

Porter, J. T., Johnson, C. K., and Agmon, A. (2001). Diverse types of interneurons generate thalamus-evoked feedforward inhibition in the mouse barrel cortex. *J. Neurosci.* 21, 2699–2710. doi: 10.1523/JNEUROSCI.21-08-02699.2001

Prönneke, A., Scheuer, B., Wagener, R. J., Möck, M., Witte, M., and Staiger, J. F. (2015). Characterizing VIP neurons in the barrel cortex of VIPcre/tdTomato mice reveals layer-specific differences. *Cereb. Cortex* 25, 4854–4868. doi: 10.1093/cercor/bhv202

Ren, J. Q., Aika, Y., Heizmann, C. W., and Kosaka, T. (1992). Quantitative analysis of neurons and glial cells in the rat somatosensory cortex, with special reference to GABAergic neurons and parvalbumin-containing neurons. *Exp. Brain Res.* 92, 1–14. doi: 10.1007/BF00230378

Rudy, B., Fishell, G., Lee, S., and Hjerling-Leffler, J. (2011). Three groups of interneurons account for nearly 100% of neocortical GABAergic neurons. *Dev. Neurobiol.* 71, 45–61. doi: 10.1002/dneu.20853

Shigematsu, N., Nishi, A., and Fukuda, T. (2018). Gap junctions interconnect different subtypes of parvalbumin-positive interneurons in barrels and septa with connectivity unique to each subtype. *Cereb Cortex* 29, 1414–1429. doi: 10.1093/cercor/bhy038

Somogyi, P., Tamas, G., Lujan, R., and Buhl, E. H. (1998). Salient features of synaptic organisation in the cerebral cortex. *Brain Res. Rev.* 26, 113–135. doi: 10.1016/S0165-0173(97)00061-1

Staiger, J. F., Masanneck, C., Bisler, S., Schleicher, A., Zuschratter, W., and Zilles, K. (2002). Excitatory and inhibitory neurons express c-Fos in barrel-related columns after exploration of a novel environment. *Neuroscience* 109, 687–699. doi: 10.1016/S0306-4522(01)00501-2

Staiger, J. F., Zilles, K., and Freund, T. F. (1996a). Distribution of GABAergic elements postsynaptic to ventroposteromedial thalamic projections in layer IV of rat barrel cortex. *Eur. J. Neurosci.* 8, 2273–2285. doi: 10.1111/j.1460-9568.1996.tb01191.x

Staiger, J. F., Zilles, K., and Freund, T. F. (1996b). Innervation of VIP-immunoreactive neurons by the ventroposteromedial thalamic nucleus in the barrel cortex of the rat. *J. Comp. Neurol.* 367, 194–204. doi: 10.1002/(SICI)1096-9861(19960401)367:2<194::AID-CNE3>3.0.CO;2-0

Staiger, J. F., Zuschratter, W., Luhmann, H. J., and Schubert, D. (2009). Local circuits targeting parvalbumin-containing interneurons in layer IV of rat barrel cortex. *Brain Struct. Funct.* 214, 1–13. doi: 10.1007/s00429-009-0225-5

Staiger, J. F., Möck, M., Proenneke, A., and Witte, M. (2015). What types of neocortical GABAergic neurons do really exist? *e-Neuroforum* 6, 49–56.

Sukhov, A. G., Kirichenko, E., and Belichenko, L. A. (2016). Structural characteristics and spatial organization of parvalbumin-containing neurons in somatosensory zone SI of the cerebral cortex in rats. *Neurosci. Behav. Physiol.* 46, 863–867. doi: 10.1007/s11055-016-0323-9

Tamas, G., Buhl, E. H., Lorincz, A., and Somogyi, P. (2000). Proximally targeted GABAergic synapses and gap junctions synchronize cortical interneurons. *Nat. Neurosci.* 3, 366–371. doi: 10.1038/73936

Taniguchi, H., He, M., Wu, P., Kim, S., Paik, R., Sugino, K., et al. (2011). A resource of cre driver lines for genetic targeting of GABAergic neurons in cerebral cortex. *Neuron* 71, 995–1013. doi: 10.1016/j.neuron.2011.07.026

Tremblay, R., Lee, S., and Rudy, B. (2016). GABAergic interneurons in the neocortex: from cellular properties to circuits. *Neuron* 91, 260–292. doi: 10.1016/j.neuron.2016.06.033

Urban-Ciecko, J., and Barth, A. L. (2016). Somatostatin-expressing neurons in cortical networks. *Nat. Rev. Neurosci.* 17, 401–409. doi: 10.1038/nrn.2016.53

van Brederode, J. F. M., Helliesen, M. K., and Hendrickson, A. E. (1991). Distribution of the calcium-binding proteins parvalbumin and calbindin-D28k in the sensorimotor cortex of the rat. *Neuroscience* 44, 157–171. doi: 10.1016/0306-4522(91)90258-P

Wagener, R. J., David, C., Zhao, S., Haas, C. A., and Staiger, J. F. (2010). The somatosensory cortex of reeler mutant mice shows absent layering but intact formation and behavioral activation of columnar somatotopic maps. *J. Neurosci.* 30, 15700–15709. doi: 10.1523/JNEUROSCI.3707-10.2010

Wagener, R. J., Witte, M., Guy, J., Mingo-Moreno, N., Kugler, S., and Staiger, J. F. (2016). Thalamocortical connections drive intracortical activation of functional columns in the mislaminated reeler somatosensory cortex. *Cereb. Cortex* 26, 820–837.

Walker, F., Möck, M., Feyerabend, M., Guy, J., Wagener, R. J., Schubert, D., et al. (2016). Parvalbumin- and vasoactive intestinal polypeptide-expressing neocortical interneurons impose differential inhibition on martinotti cells. *Nat. Commun.* 7:13664. doi: 10.1038/ncomms13664

Wall, N. R., De La Parra, M., Sorokin, J. M., Taniguchi, H., Huang, Z. J., and Callaway, E. M. (2016). Brain-wide maps of synaptic input to cortical interneurons. *J. Neurosci.* 36, 4000–4009. doi: 10.1523/JNEUROSCI.3967-15.2016

Wang, Y., Gupta, A., Toledo-Rodriguez, M., Wu, C. Z., and Markram, H. (2002). Anatomical, physiological, molecular and circuit properties of nest basket cells in the developing somatosensory cortex. *Cereb. Cortex* 12, 395–410. doi: 10.1093/cercor/12.4.395

Welker, C., and Woolsey, T. A. (1974). Structure of layer IV in the somatosensory neocortex of the rat: description and comparison with the mouse. *J. Comp. Neurol.* 158, 437–454. doi: 10.1002/cne.901580405

Wimmer, V. C., Broser, P. J., Kuner, T., and Bruno, R. M. (2010a). Experience-induced plasticity of thalamocortical axons in both juveniles and adults. *J. Comp. Neurol.* 518, 4629–4648. doi: 10.1002/cne.22483

Wimmer, V. C., Bruno, R. M., de Kock, C. P. J., Kuner, T., and Sakmann, B. (2010b). Dimensions of a projection column and architecture of VPM and POm axons in rat vibrissal cortex. *Cereb. Cortex* 20, 2265–2276. doi: 10.1093/cercor/bhq068

Woolsey, T. A., and van der Loos, H. (1970). The structural organization of layer IV in the somatosensory region (SI) of mouse cerebral cortex. *Brain Res.* 17, 205–242. doi: 10.1016/0006-8993(70)90079-X

Xu, H., Jeong, H. Y., Tremblay, R., and Rudy, B. (2013). Neocortical somatostatin-expressing GABAergic interneurons disinhibit the thalamorecipient layer 4. *Neuron* 77, 155–167. doi: 10.1016/j.neuron.2012.11.004

Xu, X. M., Roby, K. D., and Callaway, E. M. (2010). Immunochemical characterization of inhibitory mouse cortical neurons: three chemically distinct classes of inhibitory cells. *J. Comp. Neurol.* 518, 389–404. doi: 10.1002/cne.22229

Yavorska, I., and Wehr, M. (2016). Somatostatin-expressing inhibitory interneurons in cortical circuits. *Front. Neural Circ.* 10:76. doi: 10.3389/fncir.2016.00076

Yu, J., Gutnisky, D. A., Hires, S. A., and Svoboda, K. (2016). Layer 4 fast-spiking interneurons filter thalamocortical signals during active somatosensation. *Nat. Neurosci.* 19, 1647–1657. doi: 10.1038/nn.4412

Zembrzycki, A., Chou, S. J., Ashery-Padan, R., Stoykova, A., and O'Leary, D. D. M. (2013). Sensory cortex limits cortical maps and drives top-down plasticity in thalamocortical circuits. *Nat. Neurosci.* 16, 1060–U118. doi: 10.1038/nn.3454

Zhou, X. J., Rickmann, M., Hafner, G., and Staiger, J. F. (2017). Subcellular targeting of VIP boutons in mouse barrel cortex is layer-dependent and not restricted to interneurons. *Cereb. Cortex* 27, 5353–5368. doi: 10.1093/cercor/bhx220

Zilles, K., Hajós, F., Csillag, A., Kalman, M., Sotonyi, P., and Schleicher, A. (1993). Vasoactive intestinal polypeptide immunoreactive structures in the mouse barrel field. *Brain Res.* 618, 149–154. doi: 10.1016/0006-8993(93)90438-S

Conflict of Interest Statement: The authors declare that the research was conducted in the absence of any commercial or financial relationships that could be construed as a potential conflict of interest.

frontiers in Neuroanatomy

HYPOTHESIS AND THEORY
published: 19 June 2019
doi: 10.3389/fnana.2019.00064

A Role for the Claustrum in Salience Processing?

Jared B. Smith[1]†, Glenn D. R. Watson[2†], Zhifeng Liang[3], Yikang Liu[4,5], Nanyin Zhang[4,5,6] and Kevin D. Alloway[4,6,7]*

[1]*Molecular Neurobiology Laboratory, Salk Institute for Biological Studies, La Jolla, CA, United States,* [2]*Department of Psychology and Neuroscience, Duke University, Durham, NC, United States,* [3]*Laboratory for Comparative Neuroimaging, Institute for Neuroscience, Chinese Academy of Sciences, Shanghai, China,* [4]*Center for Neural Engineering, Penn State University, Millennium Science Complex, University Park, PA, United States,* [5]*Department of Biomedical Engineering, Penn State University, Millennium Science Complex, University Park, PA, United States,* [6]*Huck Institute of Life Sciences, Penn State University, Millennium Science Complex, University Park, PA, United States,* [7]*Neural and Behavioral Sciences, Center for Neural Engineering, Pennsylvania State University, University Park, PA, United States*

The claustrum (CLA) is a subcortical structure, present only in mammals, whose function remains uncertain. Previously, using resting-state functional magnetic resonance imaging (rs-fMRI) in awake head-fixed rats, we found evidence that the CLA is part of the rodent homolog of the default mode network (DMN; Smith et al., 2017). This network emerged as strong functional connections between the medial prefrontal cortex (mPFC), mediodorsal (MD) thalamus, and CLA in the awake state, which was not present following administration of isoflurane anesthesia. In the present report, we review evidence indicating that the rodent CLA also has connections with structures identified in the rodent homolog of the salience network (SN), a circuit that directs attention towards the most relevant stimuli among a multitude of sensory inputs (Seeley et al., 2007; Menon and Uddin, 2010). In humans, this circuit consists of functional connections between the anterior cingulate cortex (ACC) and a region that encompasses both the CLA and insular cortex. We further go on to review the similarities and differences between the functional and anatomical connections of the CLA and insula in rodents using both rs-fMRI and neuroanatomical tracing, respectively. We analyze in detail the connectivity of the CLA with the cingulate cortex, which is a major node in the SN and has been shown to modulate attention. When considered with other recent behavior and physiology studies, the data reveal a role for the CLA in salience-guided orienting. More specifically, we hypothesize that limbic information from mPFC, MD thalamus, and the basolateral amygdala (BLA) are integrated by the CLA to guide modality-related regions of motor and sensory cortex in directing attention towards relevant (i.e., salient) sensory events.

Keywords: claustrum, amygdala, insula, salience network, functional connectivity, anatomical connectivity, medial prefrontal cortex, thalamus

OPEN ACCESS

Edited by:
Kathleen S. Rockland, Boston University, United States

Reviewed by:
Bang-Bon Koo, Boston University, United States
Hanbing Lu, National Institute on Drug Abuse (NIDA), United States

****Correspondence:***
Jared B. Smith
jasmith@salk.edu

†Co-first authors

Received: *01 September 2018*
Accepted: *06 June 2019*
Published: *19 June 2019*

Citation:
Smith JB, Watson GDR, Liang Z, Liu Y, Zhang N and Alloway KD (2019) A Role for the Claustrum in Salience Processing? Front. Neuroanat. 13:64. doi: 10.3389/fnana.2019.00064

INTRODUCTION

The claustrum (CLA) is a subcortical structure whose precise function remains unknown, but has been implicated in various mechanisms involved in directing attention (Mathur, 2014; Goll et al., 2015; Atlan et al., 2018; White et al., 2018), salience detection (Smythies et al., 2012), multisensory integration (Edelstein and Denaro, 2004), cross-modal transfer (Hadjikhani and Roland, 1998), perceptual binding (Crick and Koch, 2005), cognition (Jackson et al., 2018), and consciousness (Koubeissi et al., 2014; Stiefel et al., 2014; Kurada et al., 2019). In support of this view, the rodent CLA has extensive interhemispheric connections linking modality-related regions of sensory and motor cortex that control exploratory behaviors, such as visual cortex and the frontal eye fields that control visual search (Smith and Alloway, 2010; Smith et al., 2012, 2018; Alloway et al., 2014).

We recently used neuroanatomical tracing in conjunction with resting-state functional magnetic resonance imaging (rs-fMRI) in awake, head-fixed rats to investigate the relationship between the structural and functional connections of the rodent CLA (Smith et al., 2017). This study revealed connections from the CLA to several nodes in the default mode network (DMN) and in the salience network (SN); both of which are thought to serve distinct cognitive functions (Menon, 2011; Smith et al., 2017). In the awake state, our study revealed strong functional connections of the CLA with the medial prefrontal cortex (mPFC) and mediodorsal (MD) thalamus (i.e., nodes of the DMN) that are significantly attenuated in response to anesthetic induced loss of consciousness. In addition to the DMN, we observed strong functional connections of the CLA with cingulate cortex (Cg), a primary node in the human SN.

To gain further insights about the composition and function of the rodent homologs of the DMN and SN (Sforazzini et al., 2014; Gozzi and Schwarz, 2016), this article will examine the anatomical and functional connectivity between the CLA with nodes in both the DMN and SN. Based on recent behavioral and physiology findings on the CLA (Remedios et al., 2014; Atlan et al., 2018; Jackson et al., 2018; White et al., 2018), we propose that the CLA has a role in both salience-guided orienting and in the context-dependent regulation of an organism's state of vigilance (e.g., varying degrees of anxiety related to threat). In support of this theory, anatomical studies have revealed strong inputs to the CLA from limbic structures, especially the basolateral amygdala (BLA; Atlan et al., 2018; Zingg et al., 2018). We hypothesize that these limbic inputs may provide "salience signals" to the CLA, which are then relayed to sensory and motor cortices to coordinate sensory exploration towards relevant stimuli. Our theory outlines clear proposals about future directions in CLA research to elucidate its role in emotional processing related to salience-guided sensory exploration.

Intrinsic Connectivity Networks in the Human Brain

The human brain is thought to be organized into interconnected regions that are functionally co-activated or co-deactivated during specific cognitive activities. The different regions in these large-scale brain networks show significant correlated blood oxygen-level dependent (BOLD) activity related to each function, as measured by fMRI (see **Figure 1** and for a comprehensive review, see Menon, 2011). One such intrinsic connectivity network (ICN) is the DMN, which is thought to be active in the absence of all other overt and covert sensory, motor, cognitive, and emotional processing (Fox et al., 2005). The DMN consists of strongly correlated BOLD signals in the ventromedial prefrontal cortex (vmPFC), posterior cingulate cortex (PCC), and MD thalamus (Fox et al., 2005; Sridharan et al., 2008; Menon and Uddin, 2010).

Two more ICNs are thought to operate in opposition to the DMN: the SN and the executive control network (ECN; **Figure 1**; Seeley et al., 2007; Menon and Uddin, 2010; but see Murphy et al., 2009). In contrast to the DMN, the human SN (**Figures 1A,B,D**) is a distributed set of cortical and subcortical regions involved in detecting and responding to highly relevant (salient) stimuli (Seeley et al., 2007; Menon, 2011). The SN was first identified using conventional fMRI to measure BOLD responses during a spatial working memory task in human patients (Seeley et al., 2007). In this task, several cortical regions displayed significant BOLD responses, including the frontoinsular cortex. This region of insular cortex was subsequently used as a "seed region" for an independent component analysis of its functional connectivity patterns, some of which are shown in **Figure 1A**. The frontoinsular seed revealed strong functional connectivity to the dACC, as well as subcortical areas including MD thalamus, periaqueductal gray, extended amygdala, and others (**Figure 1A**). The known functions and modalities processed in these brain regions (including attention, sensory, visceral, affective, limbic, etc.) led the authors to conclude that this network, anchored by frontoinsular cortex and dACC, processes perceptual salience and thus termed it the "salience network."

The discovery of the SN also revealed an interesting clinical relationship. Specifically, the strength of functional connectivity within the SN was strongly correlated (r^2 = 0.89) with visual analog scores (VAS) from a pre-scan anxiety assay (**Figure 1C**). This correlation suggests a tight link between the strength of the SN and states of vigilance. Subsequent studies have replicated these findings and shown that functional connectivity within the SN is aberrant in many neurological disorders including anxiety (Geng et al., 2016), post-traumatic stress disorder (Brown et al., 2014), depression (Menon, 2011), psychosis with auditory delusions (Mallikarjun et al., 2018), and affective disorders (Menon and Uddin, 2010). As discussed below, this clinical finding has relevance in guiding experimental analysis of the SN in rodent models.

Owing to constraints in the spatial resolution of fMRI, it is difficult to distinguish the contribution of the insula from its surrounding brain regions, particularly the CLA. Conventional neuroanatomical tracing in non-human primates suggests that fMRI signals attributed to the anterior insula (AI) may arise, at least partly, from the CLA (Reser et al., 2016). In support of this view, overlays of SN activation regions onto an anatomical reconstruction show substantial involvement of the ventral CLA

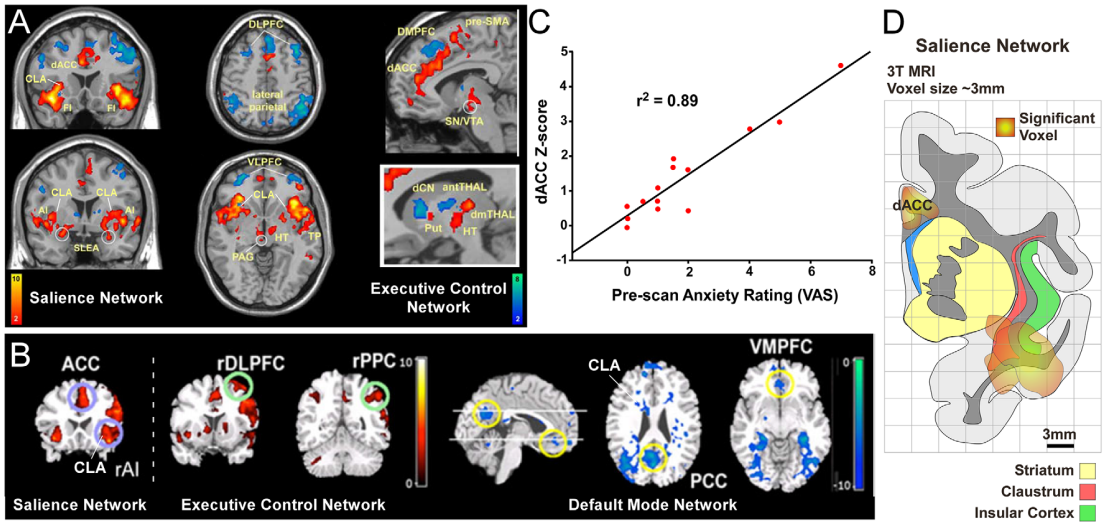

FIGURE 1 | Human functional magnetic resonance imaging (fMRI) studies have identified three distinct intrinsic connectivity networks (ICNs): salience, executive control, and default mode network (DMN). **(A)** Original human fMRI data identifying the salience network (SN; in hot colors) and the executive control network (ECN; in cool colors). The human SN primarily consists of the dorsal anterior cingulate cortex (dACC), anterior insula (AI), and fronto-insular cortex (FI; Seeley et al., 2007). **(B)** Graph from the same study showing a strong correlation between a pre-scan diagnostic of the subjects' anxiety and the strength of connection within the SN. **(C)** Data from a separate study showing activity in the salience and ECNs (activation strength shown in hot colors), and also the DMN (deactivation strength shown in blue) in response to an auditory event transition. The human DMN primarily consists of connections between ventromedial prefrontal cortex (vmPFC) and posterior cingulate cortex (PCC) that appear as negative correlations when the salience and ECNs are active. **(D)** Reconstruction of SN activation area from upper left coronal section in panel **(A)** relative to anatomical boundaries for insula, claustrum and striatum (putamen, caudate, and accumbens). Note the "hotspot" in the insula for the SN encompasses the anatomical region containing the ventral portion of the claustrum (CLA). Panels **(A,C)** modified with permission from Seeley et al. (2007). Panel **(B)** modified with permission from Sridharan et al. (2008). Copyright (2008) National Academy of Science, USA.

(**Figure 1D**). Closer inspection of this data indicates that the CLA is incorporated into both the SN and DMN in humans, with a stronger association to the SN (see **Figures 1A,B**). However, future human fMRI studies should directly test the relative degree to which the CLA is functionally involved in the SN or DMN. Additionally, although recent studies have examined the anatomical connectivity of the human CLA using diffusion tensor imaging (Milardi et al., 2013; Torgerson and Van Horn, 2014; Torgerson et al., 2015), more work is needed to assess the connectivity differences of the CLA with the adjacent insula. Together, such studies would enhance our understanding as to the functional and anatomical relationship between the insula and CLA with the DMN and SN nodes in the human brain.

Claustrum Role in Rodent Homolog of Default Mode and Salience Networks

Large-scale ICNs have been thoroughly characterized in human and non-human primates, but less is known about their function in rodents (for comprehensive review, see Gozzi and Schwarz, 2016). Previous studies have attempted to delineate the rodent DMN and SN by combining anatomical tracing with rs-fMRI in anesthetized animals (Jonckers et al., 2011; Sforazzini et al., 2014). By contrast, our rs-fMRI imaging studies were performed in awake, head-fixed rats that were subsequently anesthetized with isoflurane, allowing us to examine the connectivity differences in the awake and anesthetized states (Zhang et al., 2010; Liang et al., 2011, 2012a, 2013, 2014, 2015; Smith et al., 2017). In both human and rodent studies, the DMN is sensitive to anesthesia, with strong attenuation of functional connectivity in this network in the anesthetized state compared to the awake state (Deshpande et al., 2010; Liu et al., 2015; Bukhari et al., 2017). In fact, this effect of anesthesia represented a major limitation in the interpretation of results reported by rodent imaging studies that used different anesthetic paradigms. By directly imaging BOLD signals during the awake and anesthetized states of the same animal, our work reveals how anesthesia alters the connectivity that is present in the awake, quiescent state.

As shown in **Figure 2**, data from our previous study reveals evidence for the rodent homolog of the DMN. The primary node for identifying the DMN from rs-fMRI seed-based analyses in humans is the vmPFC, which has strong functional connections with PCC (**Figures 1**, **2A**). We, therefore, performed a similar rs-fMRI seed-based analysis of the homologous cortical area in rodents by using the prelimbic (PrL) cortex subdivision of mPFC as the seed region (**Figures 2B–D**; see also top row of **Supplementary Figure S1**). In the awake condition (**Figure 2C**), we observed strong functional connections between mPFC and retrosplenial cortex (RS), which represents the rodent homolog of PCC. Additionally, we observed strong functional mPFC connections with the CLA and MD thalamus. These connections were not present in the isoflurane-induced anesthetized state (**Figure 2D**), as indicated by significant reductions in the connectivity strength of the voxels in these regions (bottom panel **Figure 2B**). The same results were observed using an MD thalamus seed, which showed functional connections with the CLA and mPFC in the awake state that were subsequently

lost in the anesthetized condition (**Figures 2E–G**; see also bottom row of **Supplementary Figure S1**). These results provide evidence of an mPFC-CLA-MD thalamus circuit, the rodent homolog of the DMN, which is disrupted by isoflurane anesthesia. Future studies with other anesthetic agents and/or mechanisms that regulate or disrupt consciousness, as well as electrophysiology studies, under the same conditions would be useful for confirming the contribution of the CLA in regulating the DMN.

Similar to the DMN, recent studies have investigated the rodent homolog of the SN (for comprehensive review, see Gozzi and Schwarz, 2016). In the original report on the human SN, Seeley et al. (2007) define the circuit as anchored by frontoinsular cortex and dACC (**Figures 1A,D**, **3A**). The human frontoinsular region, represented by Brodmann Areas 13 and 14, corresponds to regions of insular cortex in rodents located rostral to Bregma, but posterior to orbitofrontal cortex. The human dACC, which is represented by Brodmann Areas 24, 32, and 33, corresponds to Cg (Area 24) and PrL (Area 32) cortical areas in rodents. Therefore, to determine the nature of CLA connectivity with the rodent homolog of the SN network, we focused our analysis on its connectivity with the Cg, PrL, and insular cortical areas.

As the human SN was first identified by activity in the frontoinsula and its functional connections with dACC (**Figures 1**, **3A**), we initially analyzed an insular seed in our rodent rs-fMRI data. Surprisingly, as seen in **Figures 3B–D** (see also top row of **Supplementary Figure S2**), an insular cortex seed analysis (seed region shown in **Figure 3B**) shows a weak connection between the insula and Cg cortex only under isoflurane anesthesia (**Figure 3D**). In contrast, shown in **Figures 3E–G** (see also bottom row of **Supplementary Figure S2**), a Cg cortex seed shows a strong connection specifically with the CLA in the awake state, but not insular cortex. This result is consistent with a recent rodent rs-fMRI study performed in a stronger magnetic field (7T), which reported that the CLA, but not insula, has functional connections with Cg cortex (Krimmel et al., 2019a).

When considered with the other recent literature on rodent rs-fMRI and homologs of human ICNs (Gozzi and Schwarz, 2016), our data support the presence of the SN and DMN in rat. More importantly, our results suggest that a more careful analysis in human/primate fMRI studies should assess the degree to which the insular cortex is involved in the SN, or if it should be re-defined as a Cg-CLA circuit only. It is possible that the insula is recruited into the SN only under certain conditions, particularly those related to known insular functions (e.g., interoceptive, visceral, etc; see Stephani et al., 2011). Our results also demonstrate unexpected dynamic changes in the functional connections of the CLA in the awake and anesthetized states that should be considered in future studies.

Specificity of Functional Connectivity From Claustrum and Insula With rs-fMRI

Technical limitations and the geometric relationship of the CLA and insular cortex introduce problems with interpreting neuroimaging data related to these structures. While the CLA and insular cortex are separate structures in humans (Stephani et al., 2011), their close proximity often causes both regions to be included together in the large voxels used in human fMRI studies (**Figure 1D**). Thus, it is difficult to disambiguate the precise relationship between the BOLD signal and the activity of the actual neural substrate, as it pertains to the CLA or insula specifically (Reser et al., 2016).

To test this relationship in rats, we compared the connectivity pattern produced by placing a seed in the granular and supragranular layers of insular cortex with the pattern revealed

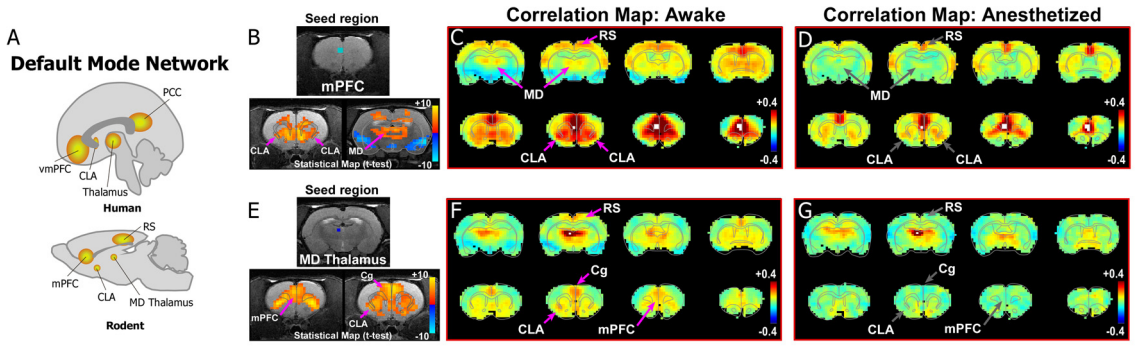

FIGURE 2 | Dynamic functional connectivity in the rodent homolog of the DMN. **(A)** Diagrams illustrating the human and rodent DMNs. **(B–D)** Analysis of resting-state fMRI (rs-fMRI) in awake and anesthetized rats for a medial prefrontal cortex (mPFC) seed shows the rodent homolog of the DMN in the awake state. **(B)** Top panel shows location of seed region in mPFC in a structural T1-MRI. Bottom panels show statistical maps comparing correlation strength in the awake and anesthetized states (voxelwise two-way *t*-test), indicating a significant reduction in the mPFC functional connectivity with CLA and mediodorsal (MD) thalamus. Hot colors show *t*-values for voxels with $p < 0.05$ (false discovery rate), with correlations that significantly decrease in the anesthetized state compared to awake. **(C)** Correlation maps from rs-fMRI with seed-based correlation analysis of mPFC in the awake state reveal strong connections to CLA, MD thalamus and retrosplenial cortex (RS). Color plot indicates scale of correlation strength: hot colors are correlated, cool colors are anti-correlated. **(D)** Correlation maps from rs-fMRI with seed-based analysis of mPFC in the anesthetized state show weaker functional connections with CLA and MD thalamus. **(E–G)** Similar analyses of an MD thalamus seed show strong functional connections with mPFC and CLA in the awake state that are significantly attenuated under isoflurane-induced loss of consciousness. Data modified with permission from Smith et al. (2017).

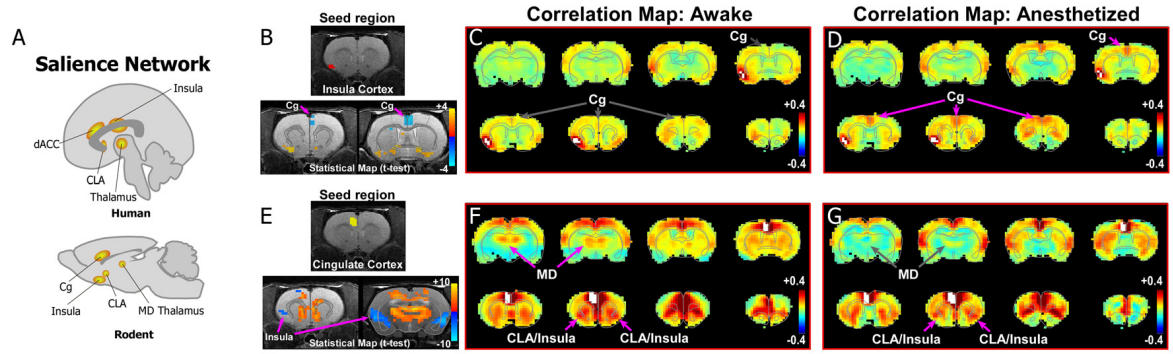

FIGURE 3 | Rodent homolog of the SN. **(A)** Diagrams illustrating the human and rodent SN. **(B–D)** Analysis of rs-fMRI in awake and anesthetized rats for an insular cortex seed. **(B)** Top panel shows location of insular cortex seed in a structural T1-MRI. Bottom panel shows statistical maps comparing the awake and anesthetized states (voxelwise two-way *t*-test), indicating an increase in correlation strength between insula and cingulate cortex (Cg) in the anesthetized state compared to the awake state (blue area identified by pink arrow). Color plot shows *t*-values for voxels with $p < 0.05$ (false discovery rate), in which cool colors indicate a significant increase in correlation under anesthesia compared to the awake state. **(C)** Correlation maps from rs-fMRI with seed-based correlation analysis of insula in the awake state reveal no functional connections with Cg cortex. Color plot indicates scale of correlation strength: hot colors are correlated, cool colors are anti-correlated. **(D)** Correlation maps from rs-fMRI with seed-based analysis of insula in the isoflurane anesthetized state show weak functional connections with Cg cortex. **(E–G)** Similar analyses of a Cg cortex seed show strong functional connections with CLA in the awake and anesthetized states. Cg cortex also showed strong functional connections to MD thalamus in the awake state that is significantly diminished in the anesthetized state, similar to mPFC shown in **Figure 2**. Data modified with permission from Smith et al. (2017).

by placing a seed in a deeper area centered on the CLA. We then compared these patterns with the connectivity revealed by a seed in the striatum. As shown previously (**Figure 3**, **Supplementary Figure S2**) the Cg cortex had strong connectivity with the CLA, but not with the insula, in the awake state. This is further confirmed by seed analyses of the insula (**Figures 4B,B′**) and CLA (**Figures 4C,C′**). By comparison, the striatal seed revealed connectivity that was highly similar to the connectivity that emerged when a seed was placed in the CLA (**Figures 4D,D′**). This similarity is best explained by the fact that the CLA and the dorsal striatum have similar anatomical connections with the mPFC and Cg cortex (Smith and Alloway, 2014; Smith et al., 2016).

Because of the close proximity between the CLA and the surrounding insula, results produced by attempts at dissociating the functional connectivity between these two structures, even with higher magnet strengths in rodent studies (4.7–7T), must be interpreted cautiously (see new method by Krimmel et al., 2019a). We attempted to isolate the CLA from the insula in our study through seed-based analysis in an fMRI with a stronger field strength that allows for smaller voxel size. However, this can still be problematic because some evidence suggests that the CLA may be embedded in layer 6 of insular cortex (Mathur et al., 2009; Mathur, 2014). In support of our findings, a recent study using stronger magnetic fields (7T) for rs-MRI in humans found strong functional connections between the CLA and cingulate cortex, though they did not interrogate differences between claustrum and insula connections (Krimmel et al., 2019b). Thus, more work is needed to precisely clarify the structural and functional connectional differences between CLA and insula, particularly in animal models with a well delineated CLA, such as non-human primates. Such studies would allow for high-field rs-fMRI analyses with subsequent neuroanatomical tracing to make conclusive relationships between structural and functional data. Such studies would also be important for assessing any species differences in connections between these regions.

Clarifying the Structural Connectivity of CLA and Insula With Neuroanatomical Tracing

In our previous anatomical tracing studies, combined injections of both retrograde and anterograde tracers into the CLA revealed substantial reciprocal connectivity with both mPFC and MD thalamus (Smith and Alloway, 2010, 2014; Smith et al., 2017). Interpreting the labeling from tracer injections in the CLA is difficult, however, because it requires tracer injections that are restricted to the CLA without infiltrating the surrounding insula and striatum.

Therefore, to compare the anatomical connectivity of rodent homolog of mPFC with the CLA and insular cortex (**Figure 5**), we made both anterograde and retrograde tracer injections (Fluororuby and Fluorogold, respectively) into Cg cortex (rodent homolog of area 24) and PrL cortex (rodent homolog of area 32; Smith and Alloway, 2014; Smith et al., 2017). Our anterograde tracer injections in Cg cortex revealed connectivity primarily with the contralateral CLA (**Figures 5H–K**), which in turn innervates only Cg of that hemisphere. Consistent with our rs-fMRI data shown in **Figures 3**, **4**, there was no anatomical connectivity between insula and Cg cortex (Smith and Alloway, 2014; White and Mathur, 2018). Additionally, PrL cortex also sends dense projections to the contralateral CLA and weaker projections to the ipsilateral CLA, with little innervation of the insula in either hemisphere. However, PrL cortex does receive inputs from a large number of

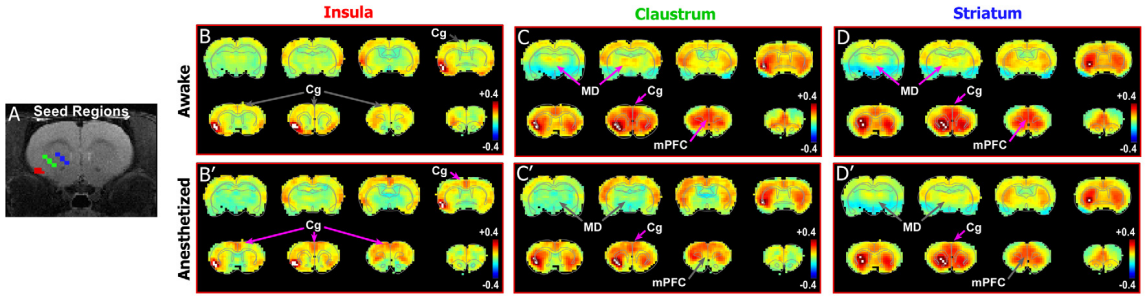

FIGURE 4 | Differences in functional connectivity between striatum, claustrum, and insula. **(A)** Seed regions for insula (red), CLA (green), and striatum (blue) shown on T1-MRI. **(B–D′)** Correlation maps for insula, CLA, and striatum in awake state (top panels) and anesthetized states (bottom panels). Striatum and CLA had highly similar patterns of connectivity with strong connections to Cg cortex and MD thalamus in the awake state, whereas insula was only functionally connected with Cg cortexin the anesthetized state. Data modified with permission from Smith et al. (2017).

neurons in both the CLA and insular cortex of the ipsilateral hemisphere, with very weak projections originating from the contralateral CLA.

Additional tracer injections were made to specify the input-output organization of MD thalamus with mPFC, CLA, and insula. As shown in **Figure 6**, we made large injections of a mixture of anterograde and retrograde tracers (biotinylated dextran amine with Fluorogold) that targeted MD thalamus (Smith et al., 2017). The resulting anterograde labeling revealed dense projections from MD thalamus to mPFC (including both Cg and PrL cortices) and the CLA, but projections to the insula were largely non-existent (**Figures 6B–D**). In contrast, the retrograde labeling had the reverse pattern, showing dense labeling in the deep layers of insular cortex, with few cells being found within the CLA (**Figure 6G**), consistent with previous reports (Mathur et al., 2009).

In addition to the interhemispheric cortico-claustro-cortical circuit linking Cg cortex in each hemisphere, we also observed an interhemispheric cortico-thalamo-cortical loop connecting Cg cortex in each hemisphere *via* MD thalamus (**Supplementary Figure S3**). We have previously shown a similar interhemispheric loop for the more lateral motor region, agranular medial cortex (AGM, a.k.a. M2), which is involved in rodent whisking (Alloway et al., 2008).

Beyond these classic neuroanatomical tracing approaches, more sophisticated viral tracing from CLA-specific transgenic mice and other approaches have confirmed all of these connections (Chia et al., 2017; Wang et al., 2017; Atlan et al., 2018; Zingg et al., 2018). Furthermore, these studies indicate that there is some reciprocal connectivity between CLA and agranular insular cortex, making it more difficult to interpret differences in functional connectivity between CLA and insula given that these structures appear to have direct connections.

A summary of these anatomical results is shown in the circuit diagram in **Figure 7**, which shows that both the CLA and insula have many similar connections, but three distinct differences. First, though PrL cortex projects primarily to the CLA, it receives inputs from both the CLA and insula. Second, only the CLA has connectivity with Cg cortex. Third, MD thalamus projects strongly to the CLA, but the insula provides the dominant projection back to MD thalamus. Understanding these anatomical differences can provide a lens through which to understand changes in functional connectivity as measured by rs-fMRI.

An Amygdaloclaustral Circuit to Evaluate Competing Stimuli

Though the function of the CLA remains largely unknown, recent studies indicate that the CLA plays a role in salience detection, attentional processing, and possibly cognition (Remedios et al., 2010, 2014; Goll et al., 2015; Atlan et al., 2018; Jackson et al., 2018), particularly *via* its connections with Cg cortex (Chia et al., 2017; White and Mathur, 2018; White et al., 2018). Most notably, electrophysiology recordings in the CLA of non-human primates lead the investigators to propose that "the claustrum detects the occurrence of novel or salient sensory events" (Remedios et al., 2014). However, it is unknown what brain regions could imbue the CLA with information about the novelty, importance, or relative value of competing stimuli.

Some authors suggest that the relative salience of stimuli could be determined by the amygdala, and particularly its inputs to the CLA (Gattass et al., 2014). One unique aspect of our previous rs-fMRI study was the finding that the BLA is negatively correlated (anti-correlated) with infralimbic cortex (Liang et al., 2012a). To further investigate this relationship between the amygdala and nodes of interest within the SN, we re-analyzed our data with respect to the boundaries of the amygdala, as well as performing a unilateral seed-based analysis of the BLA. As seen in **Figures 3**, **4**, unilateral seed-based analyses from the CLA and Cg cortex show that their functional connectivity with the BLA is anti-correlated in the awake state (see blue voxels in the BLA). This is in contrast to the strong correlated BOLD activity observed in other forebrain regions. To verify this anti-correlated BOLD pattern, we performed a unilateral BLA seed analysis (**Figures 8A–C**). As predicted from our previous analyses, the BLA is anti-correlated with most of the forebrain in the awake state, including areas of mPFC, striatum, septum, thalamus, and CLA.

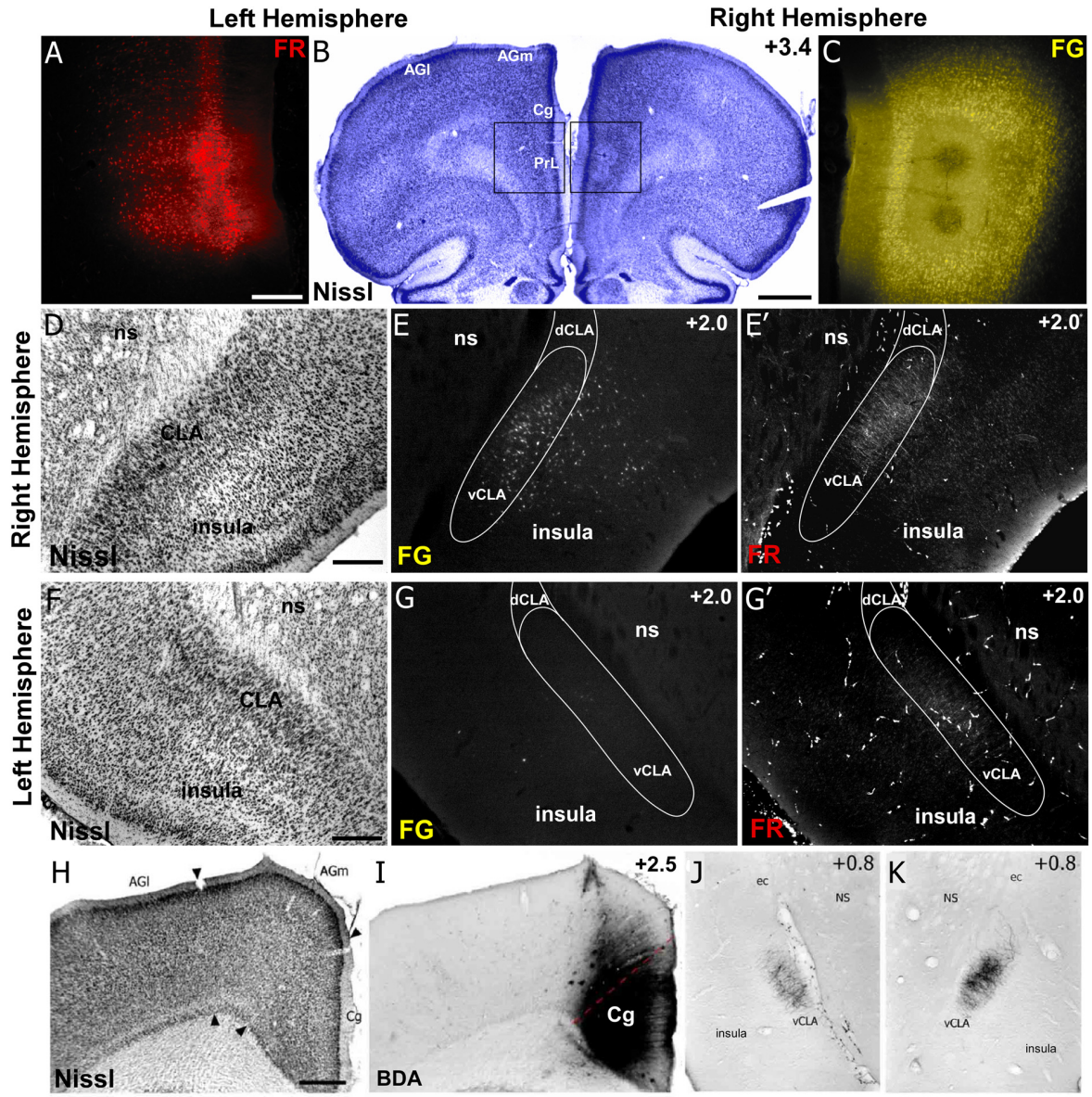

FIGURE 5 | Neuroanatomical tracing clarifies the structural connectivity between mPFC, Cg, CLA, and insula. **(A–C)** Anterograde tracer injection (Fluororuby, FR) in the left hemisphere, shown in panel **(A)**, and retrograde tracer injection (Fluorogold, FG) in the right hemisphere, shown in panel **(C)**, into prelimbic cortex (PrL) of a rat. Injection site locations shown in Nissl stained coronal section in panel **(B)**. **(D–E′)** In the right hemisphere, retrograde labeling **(E)** is visible in both CLA and insular cortex, whereas anterograde labeling **(E′)** was found only in CLA. Panel **(D)** shows location of CLA in Nissl stained coronal section. **(F–G′)** Labeling in the left hemisphere shows very little retrograde labeling in insula or CLA **(G)**, but some anterograde labeling in the claustrum **(G′)**. **(H–K)** Injection of anterograde tracer BDA in Cg cortex shows bilateral labeling in claustrum but no labeling in insula. Numbers in upper right corner of panels indicate distance from Bregma in millimeter. Scale bars: 250 μm in **(A)**; 1 mm in **(B)**; 500 μm in **(D,F,H)**; Data modified with permission from Smith and Alloway (2014) and Smith et al. (2017). Abbreviations: AGl, agranular lateral cortex; AGm, agranular medial cortex; Cg, cingulate cortex; PrL, prelimbic cortex; dCLA, dorsal claustrum; vCLA, ventral claustrum; ns, neostriatum; ec, external capsule.

The precise meaning of anti-correlated functional connectivity is unclear and remains a subject of debate within the rs-fMRI field. It is particularly important to note that negative correlations can result from movement artifacts or data processing methods such as global-signal regression and partial correlation analysis. However, in our studies, we have gone to great lengths to avoid these confounds. First, we do not use global-signal regression as part of our data processing stream. Second, we strictly control for motion artifacts by using stringent motion correction and motion control approaches (full description of our methods can be found in our published research articles: Liang et al., 2011, 2012a, 2015; Smith et al., 2017). As stated above, we previously observed anti-correlated functional connectivity between

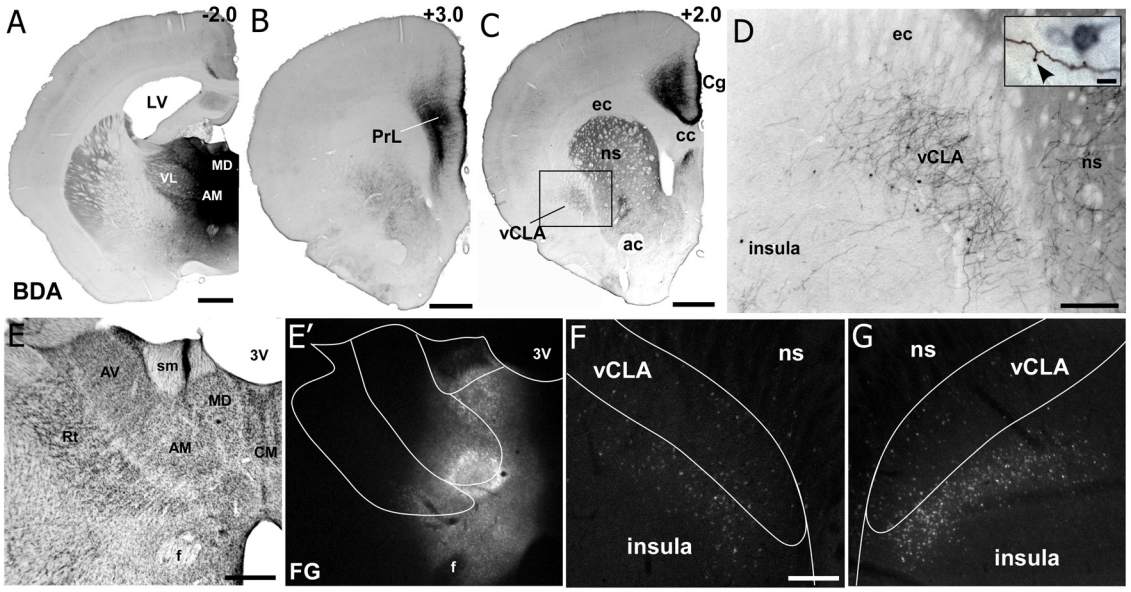

FIGURE 6 | Neuroanatomical tracing from MD thalamus clarifies the connectivity with insular cortex and claustrum. **(A)** Image showing a bi-directional anterograde/retrograde BDA/FG injection into MD thalamus, specifically showing the DAB visualization of the BDA. **(B)** Strong connections are observed with layer 1 as well as layers 5 and 6 of PrL cortex. **(C)** MD thalamus also showed strong connections to Cg cortex, ventral striatum (VS), and CLA. **(D)** Higher magnification of labeling in CLA after MD injection shows mostly terminal labeling, with few retrogradely labeled neurons. Closer inspection of terminals in the inset show a classic "drum-stick" morphology, possibly indicating a "modulator-like" synapse. **(E–G)** Images of the FG labeling from an adjacent section from the injection shown in **(A)**. Not that almost all of the feedback to thalamus originates from insula and not the CLA. Numbers in upper right corner of panels indicate distance from Bregma in millimeter. Scale bars: 1 mm in **(A–C)**; 250 μm in **(D)** and 10 μm in inset. Data modified with permission from Smith et al. (2017). Abbreviations: 3V, third ventricle; LV, lateral ventricle; AM, anteromedial thalamic nucleus; AV, anteroventral thalamic nucleus; VL, ventral lateral nucleus; MD, mediodorsal nucleus; ac, anterior commissure; CM, centromedial thalamic nucleus; cc, corpus callosum; ec, external capsule; ns, neostriatum; Rt, thalamic reticular nucleus; sm, stria medularis; f, fornix; vCLA, ventral claustrum.

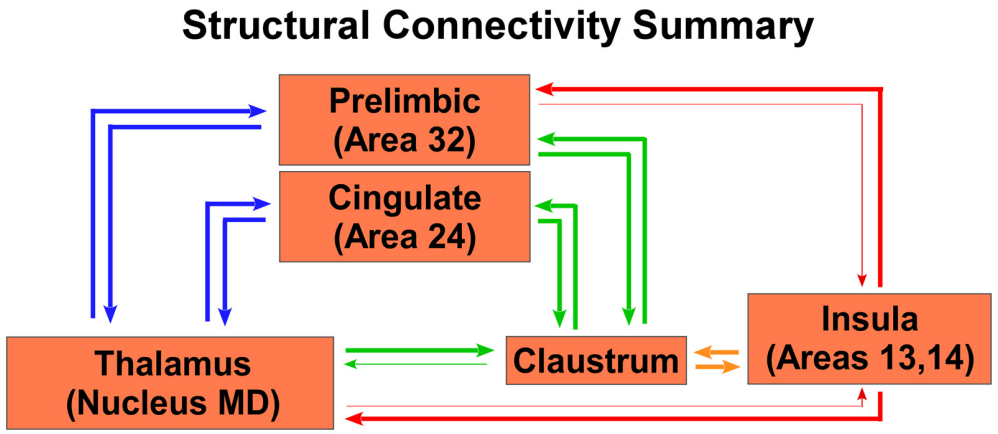

FIGURE 7 | Summary circuit diagram of anatomical connectivity differences between, insula, CLA, PrL, Cg, and MD thalamus. Arrow thickness indicates strength of connection. Parentheticals refer to Brodmann area designations.

BLA and infralimbic cortex that was anatomically specific, reproducible, present under various data processing methods, and was observed in a subgroup of animals whose motion levels were the same as anesthetized animals, indicating our findings are functional and not artifactual. Finally, a rs-fMRI study of the BLA in humans has also shown anti-correlated functional connectivity with the caudate and regions of cortex (Roy et al., 2009), similar to our observations in the rodent, thus supporting our findings. Future experiments using electrophysiological recordings in CLA and BLA are required to ascertain the true functional relationship between these regions, which would also be of great value for understanding how

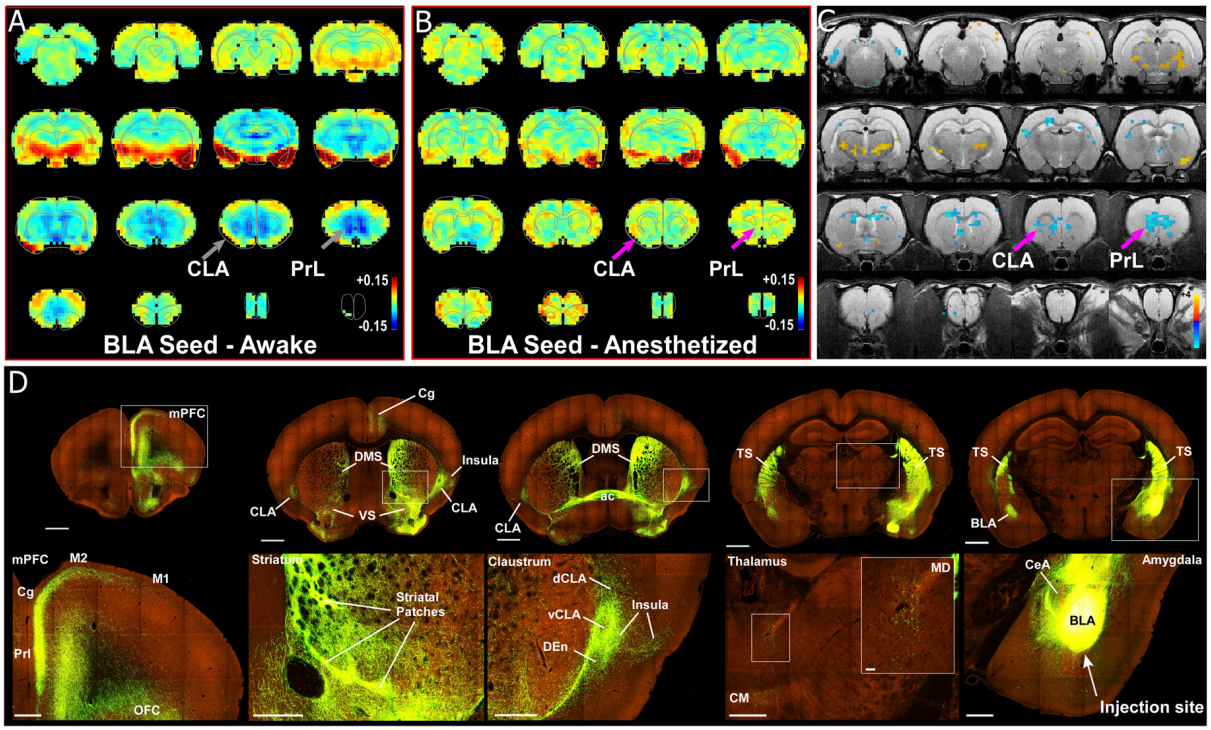

FIGURE 8 | Seed-based analysis and neuroanatomical tracing of basolateral amygdala (BLA) output reveal structural and anti-correlated functional connections with nodes in the SN. **(A)** Unilateral (left hemisphere, images shown in clinical orientation), seed-based analysis of BLA in the awake state. Color plots shown as before with hot colors indicating strong correlations and cool colors indicating anti-correlated blood oxygen level dependent (BOLD) activity. Note the widespread anti-correlation present between BLA and all of mPFC, sensorimotor cortex, dorsal thalamus, and striatum. **(B)** Unilateral, seed-based analysis of BLA in the awake state. Color plots shown as before. **(C)** Statistical map comparing the awake and anesthetized states (voxelwise two-way *t*-test), indicating an increase in correlation strength for functional connections from amygdala to prelimbic cortex (PrL) and claustrum (CLA) in the anesthetized state compared to the awake state (blue area identified by pink arrow). Hot colors show *t*-values for voxels with $p < 0.05$ (false discovery rate), which are significantly weakened in the anesthetized state compared to the awake. Cool colors indicate the reverse, meaning a significant decrease in anti-correlation under anesthesia compared to the awake state. **(D)** Data from the Allen Institute Mouse Connectivity Atlas (Oh et al., 2014) database demonstrate afferent projections from BLA to PrL, Cg, and insular cortices, as well as bilateral projections to striatum and CLA. Image credit: Allen Institute. Scale bars: 1 mm in top row of panel **(D)**; 400 μm in bottom row of panel **(D)**; 40 μm in thalamus inset in bottom row of panel **(D)**.

to interpret negatively correlated functional rs-fMRI signals in general.

To identify the structural connectivity between the BLA and nodes of interest in the SN, we examined the Allen Mouse Brain Connectivity Atlas for adeno-associated virus (AAV) guided tracing of the BLA (Oh et al., 2014). As shown by a representative example in **Figure 8D** (Experiment 113144533), injections restricted to the BLA revealed significant projections to a number of cortical (PrL, Cg, and orbitofrontal cortices) and subcortical targets (bilateral CLA and contralateral BLA). As a control, we also inspected similar injections into the adjacent central nucleus of the amygdala (CeA). As shown in **Supplementary Figure S4A**, and AAV-GFP injection into the CeA (Experiment 146795148) revealed almost no projections to the forebrain, with only weak innervation of ventral striatum (VS), paraventricular thalamus (PV), and the bed nucleus of the stria terminalis (BNST). A summary of the structural connections of the BLA, CeA, and CLA is shown in **Supplementary Figure S4B**. These data support other recent anatomical articles finding connections between the CLA and BLA (Majak et al., 2002; Atlan et al., 2018; Zingg et al., 2018).

Claustrum Involvement in a Rodent "Visual Salience Circuit"

To summarize our view of how the CLA might be involved in salience processing, let us consider an ethologically relevant, hypothetical scenario (**Figure 9A**). Recent behavioral studies in rodent vision have revealed a richer repertoire of functions and versatility than previously appreciated. These studies have shown that the rodent visual system serves a strong role in rodent predation behavior (Hoy et al., 2016), as well as threat detection, particularly regarding over-head, looming stimuli (Wallace et al., 2013; De Franceschi et al., 2016). These overhead visual stimuli likely represent predatory birds, activating a bottom-up visual response from superior colliculus, known to be involved in visual salience (Comoli et al., 2003), which then activates the LP thalamus (pulvinar) and finally the BLA (Uwano et al., 1995; Wei et al., 2015). We now propose that the CLA is the next recipient along this pathway (**Figure 9B**).

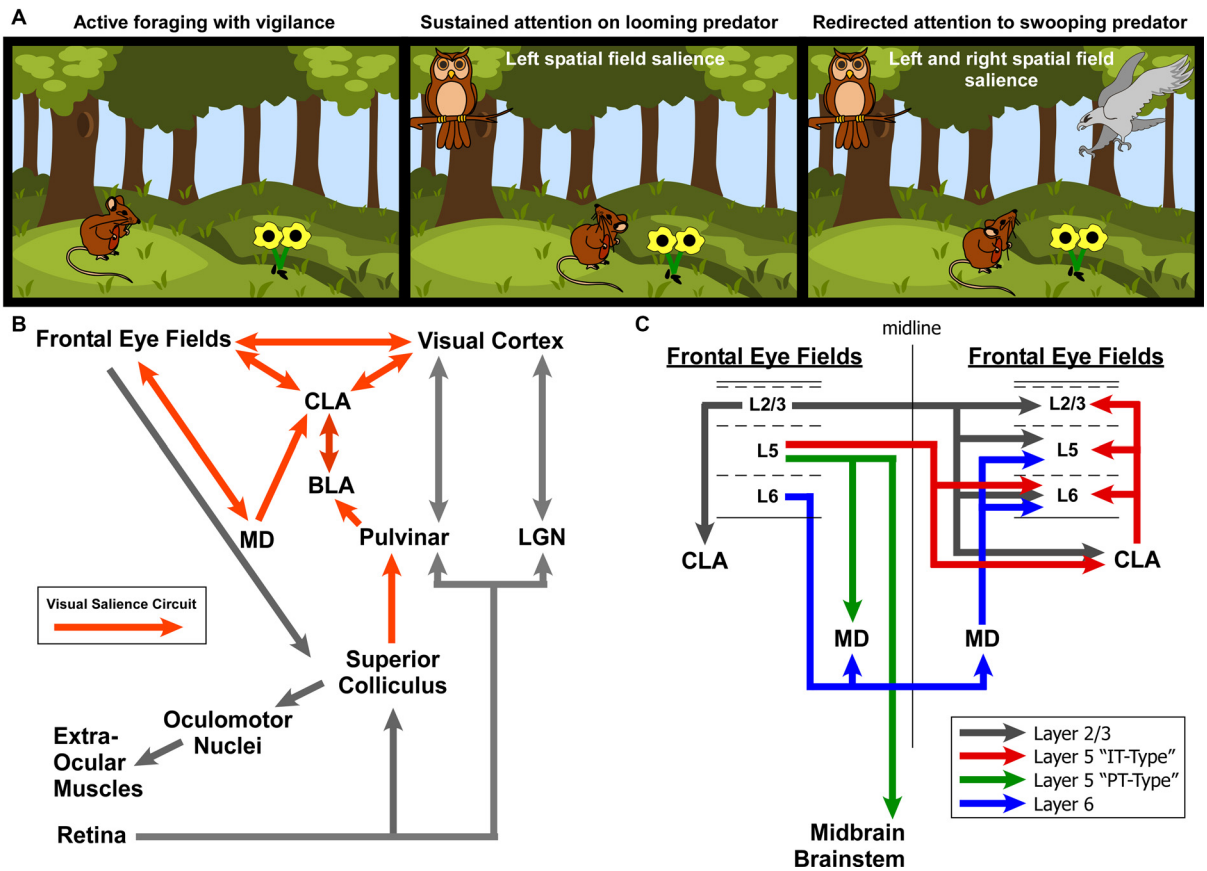

FIGURE 9 | Role for the claustrum in processing visual salience. **(A)** Illustration of ethologically relevant scenario involving rodent vision to orient to predatory salient stimuli while otherwise attempting to actively forage. If predators are in different spatial fields, interhemispheric mechanisms are needed to coordinate attention to these stimuli across disparate visual fields. **(B)** Circuit diagram of the ascending visual processing pathway from the retina and the descending visuomotor pathway for controlling the extra-ocular muscles. Note the proposed "visual salience circuit" emanating from the superior colliculus and relayed to limbic structures (BLA and subsequently CLA) *via* the pulvinar. **(C)** Summary of interhemispheric connections between the rodent frontal eye fields. Summarized from findings from Alloway et al. (2008), Smith and Alloway (2010, 2014) and Smith et al. (2012, 2016, 2017).

Based on the literature of mammalian oculomotor control (mostly primate studies) and other experiments identifying the frontal eye fields in cingulate cortex of rats (Awh et al., 2006; Smith and Alloway, 2014; Coe and Munoz, 2017), we propose two circuit diagrams for visuomotor control in rodents. In **Figure 9B**, we propose a "visual salience circuit" (VSC) consisting of both a bottom-up visual processing pathway and a top-down cortical visuomotor control pathway. We propose that the VSC is a combination of limbic structures (including BLA and MD thalamus) that convey information about stimulus value (valence) to the CLA, which in turn coordinates the frontal eye fields and visual cortices to direct attention *via* cortical visuomotor output; ultimately shifting the eyes toward novel, salient stimuli such as unexpected predators (**Figure 9A**).

When attention needs to be managed across multiple threats in opposing spatial fields (**Figure 9C**), we hypothesize that the strong bilateral projections from the frontal eye fields to the CLA and MD thalamus support the direct cortico-cortical connections to seamlessly shift attention between both threats. In a recent viral tracing study of the cortico-basal ganglia system, we observed cortical cell-type specificity in the pattern of connectivity with the CLA (Smith et al., 2016). Specifically, we found that the projections to CLA from motor cortex (including Cg cortex, M2, M1) originate from Layer 2/3 and Layer 5 IT-type neurons, but not layer 5 PT-type. This is a crucial anatomical observation that suggests the CLA receives information about motor planning *via* IT-type neurons, but not actual motor output, which is conveyed by the PT-type neurons (Shepherd, 2013). Additionally, Layer 6 of frontal eye fields (and AGm) was not observed to provide inputs to the CLA, confirming our previous retrograde injection in the CLA (Smith and Alloway, 2010). However, Layer 6 was found to have its own interhemispheric circuit with MD thalamus (**Supplementary Figure S3**), which may support the interhemispheric claustral network to balance attentional loads across spatial fields. These cell-type specific differences may be crucial to understanding how limbic inputs to the CLA are integrated with IT-type information on motor planning from the frontal eye fields to enable coordination between visual cortex and the FEF.

The connectivity between the CLA and Cg cortex is of particular interest with regards to salience processing. The human SN is defined as coupling between the dACC and a region that appears to encompass the CLA. In addition to our seed-based analysis that corroborates this functional connection in rodents, we have demonstrated anatomical and functional connections from the CLA to Cg cortex. The CLA to Cg cortex circuit seems well-suited to guide salience processing owing to the limbic inputs received by the CLA from the BLA, which are relayed to Cg cortex: a motor output region shown to guide eye movements (Smith and Alloway, 2014). This circuit organization suggests a functional role for the CLA in attention as a "limbic-to-motor" interface. A recent study corroborates the importance of the CLA-Cg connection in salience processing by demonstrating that Cg cortex imbues the CLA with "top-down" expectation signals related to task-relevant sensory information that likely underlies attentional mechanisms (White et al., 2018). Another recent study also found behavioral evidence that the CLA provides resilience to distraction (Atlan et al., 2018), which is another mechanism of attention. We, therefore, believe the CLA-Cg circuit plays a prominent role in the SN and suggest that future studies investigating the function of the CLA focus on its potential role in salience processing. Such circuitry could underlie the classic "cocktail party problem" of attending to a specific stimulus amongst competing noise. Other classic experiments in attention are ripe for testing the involvement of the CLA.

Clinical Implications

Major connectivity networks such as the DMN and SN can have aberrant connectivity patterns that are thought to underlie a host of neurological and psychiatric disorders (Menon, 2011; Uddin, 2015). For example, as shown in **Figure 1B**, a strong correlation exists between a subject's level of anxiety and the connectional strength of the SN, suggesting a role in anxiety disorders and pathological states of hyper vigilance (Seeley et al., 2007; Geng et al., 2016). A variety of other psychiatric disorders are also correlated with the insula and salience dysfunction, including depression (Menon, 2011), psychosis with auditory delusions (Mallikarjun et al., 2018), post-traumatic stress disorder (Brown et al., 2014), affective disorders (Menon and Uddin, 2010), as well as autism, schizophrenia, and dementia (Calaitzakis et al., 2009; Uddin, 2015).

Based on our recent studies, we propose that the CLA plays a role in SN-related neuropsychiatric disorders (Kalaitzakis et al., 2009; Cascella et al., 2011; Smith and Alloway, 2014; Wegiel et al., 2014; Patru and Reser, 2015; Bernstein et al., 2016; Smith et al., 2017). A recent fMRI study of Parkinson's disease patients has found significant decreases in the functional connectivity of the CLA compared to age-matched control patients, especially "with areas mainly involved in visuomotor and attentional systems" (Arrigo et al., 2018). Due to their similar anatomical and functional connections with Cg cortex and the BLA, both the insula and CLA could play a role in regulating levels of vigilance through the SN, which underlie a host of affective disorders.

Future neuroimaging and optogenetic behavioral studies are necessary to demonstrate what role, if any, the CLA plays in emotional processing, particularly with regard to anxiety. Nevertheless, this endeavor represents a new frontier for the treatment of affective neuropsychiatric disorders using deep brain stimulation or drugs that target the CLA. In fact, kappa opioid receptors, which are abundantly expressed in the CLA, may serve a therapeutic role in treating depression (Stiefel et al., 2014). Future research on the CLA will no doubt lead to fundamental breakthroughs in our understanding of emotional processing in health and disease.

CONCLUSION

Our results demonstrate a role for the CLA in both the DMN and the SN. Furthermore, these findings expand the view of the CLA from being only a sensorimotor structure (Smith and Alloway, 2014), and suggest it has a role in emotional and salience processes, owing to its anatomical and functional connectivity with limbic and affective brain regions (**Figure 9**). Together with recent behavioral studies, we propose the CLA serves as a limbic-sensorimotor interface, facilitating salience-guided orienting during sensory exploration.

ETHICS STATEMENT

This study was carried out in accordance with the guidelines and approval of the Institutional Review Board at the University of Massachusetts and Penn State University.

AUTHOR CONTRIBUTIONS

JS and GW wrote the first draft of the manuscript, constructed figures, and performed anatomy experiments and analysis. JS, GW, NZ and KA made significant revisions to multiple drafts of the manuscript. ZL, YL and NZ performed rs-fMRI experiments and analysis. NZ and KA obtained funding and supervised all data collection and analysis. All authors approve this submission and take responsibility for all information contained in this article.

FUNDING

This work was supported by the following grants: National Institute of Neurological Disorders and Stroke: Grant No. K99 NS106528 (JS); National Institute of Health: Grant No. R01NS085200 (NZ); National Institute of Health: Grant No. R01MH098003 (NZ); National Institute of Health: Grant No. R01NS37532 (KA).

ACKNOWLEDGMENTS

We would like to acknowledge the Allen Brain Institute's open access Mouse Connectivity database (http://connectivity.brain-map.org/) for providing anatomical connectivity data about the amygdala. We also acknowledge the following publishers for permission to use copyrighted content: Copyright (2008) National Academy of Science, USA; Springer Nature; Society for

Neuroscience. We also wish to thank Drs. Nick Hollon and Sho Aoki for comments on data interpretation.

SUPPLEMENTARY MATERIAL

The Supplementary Material for this article can be found online at: https://www.frontiersin.org/articles/10.3389/fnana.2019.00064/full#supplementary-material

FIGURE S1 | Claustrum and insula ROIs overlaid on DMN correlation maps. Top row shows the correlation maps from **Figure 2** from a unilateral mPFC seed analysis in the awake (left side) and anesthetized (right) conditions, with the voxels from our CLA (black) and insula (magenta) seed analyses (from **Figure 4**) superimposed. Bottom row is organized in the same manner for our MD thalamus seed analysis from **Figure 2**.

FIGURE S2 | Claustrum and insula ROIs overlaid on SN correlation maps. Top row shows the correlation maps from **Figure 3** from a unilateral insula seed analysis in the awake (left side) and anesthetized (right) conditions, with the voxels from our CLA (black) and insula (magenta) seed analyses (from **Figure 4**) superimposed. Bottom row is organized in the same manner for our Cg cortex seed analysis from **Figure 3**.

FIGURE S3 | Interhemispheric cortico-thalamo-cortical loop between mPFC and Cg *via* MD thalamus. **(A)** Thalamic labeling from the anterograde and retrograde injections in PrL cortex shown in **Figures 5A–C**. Note the anterogradely labeled terminals in the right hemisphere MD thalamus (contralateral to the FR injection site), which are intermingled with retrograde neurons from the FG injection in the right hemisphere PrL. **(B–E)** Thalamic labeling from the BDA injection into Cg cortex shown in **Figure 5I**. Note the terminal labeling in the contralateral MD. Data modified with permission from Smith and Alloway (2014) and Smith et al. (2017). Scale bars: 500 μm in left image of panel **(A)**; 50 μm in right image of panel **(A)**; 250 μm in **(B,D)**; 100 μm in **(C)**. Abbreviations: 3V, third ventricle; AM, anteromedial thalamic nucleus; AV, anteroventral thalamic nucleus; VL, ventral lateral nucleus; VM, ventral medial nucleus; MD, mediodorsal nucleus; Re, reuniens; IAM, interanteromedial nucleus; ac, anterior commissure; CM, centromedial thalamic nucleus; cc, corpus callosum; ec, external capsule; ns, neostriatum; Rt, thalamic reticular nucleus; sm, stria medularis; f, fornix; vCLA, ventral claustrum.

FIGURE S4 | Anatomical connectivity of central amygdala. **(A)** Projections from central nucleus of the amygdala (CeA) by contrast only weakly target the ventral striatum (VS) and bed nucleus of the stria terminalis (BNST) in the forebrain. **(B)** Summary diagram of afferents from the BLA, CeA, CLA and BNST. Scale bars: 1 mm in top row of panel **(A)**; 400 μm in bottom row of panel **(A)**; 40 μm in thalamus inset in bottom row of panel **(A)**. Data from the Allen Institute Mouse Connectivity Atlas (Oh et al., 2014). Image credit: Allen Institute.

REFERENCES

Alloway, K. D., Olson, M. L., and Smith, J. B. (2008). Contralateral corticothalamic projections from MI whisker cortex: potential route for modulating hemispheric interactions. *J. Comp. Neurol.* 510, 100–116. doi: 10.1002/cne.21782

Alloway, K. D., Smith, J. B., and Watson, G. D. W. (2014). Thalamostriatal projections from the medial posterior and parafasicular nuclei have distinct topographic and physiologic properties. *J. Neurophysiol.* 111, 36–50. doi: 10.1152/jn.00399.2013

Arrigo, A., Calamuneri, A., Milardi, D., Mormina, E., Gaeta, M., Corallo, F., et al. (2018). Claustral structural connectivity and cognitive impairment in drug naïve Parkinson's disease. *Brain Imaging Behav.* doi: 10.1007/s11682-018-9907-z[Epub ahead of print].

Atlan, G., Terem, A., Peretz-Rivlin, N., Sehrawat, K., Gonzales, B. J., Pozner, G., et al. (2018). Then claustrum supports resilience to distraction. *Curr. Biol.* 28, 2752.e7–2762.e7. doi: 10.1016/j.cub.2018.06.068

Awh, E., Armstrong, K. M., and Moore, T. (2006). Visual and oculomotor selection: links, causes and implications for spatial attention. *Trends Cogn. Sci.* 10, 124–130. doi: 10.1016/j.tics.2006.01.001

Bernstein, H. G., Ortmann, A., Dobrowolny, H., Steiner, J., Brisch, R., Gos, T., et al. (2016). Bilaterally reduced claustral volumes in schizophrenia and major depressive disorder: a morphometric postmortem study. *Eur. Arch. Psychiatry Clin. Neurosci.* 266, 25–33. doi: 10.1007/s00406-015-0597-x

Brown, V. M., LaBar, K. S., Haswell, C. C., Gold, A. L., Mid-Atlantic MIRECC Workgroup, McCarthy, G., et al. (2014). Altered resting-state functional connectivity of basolateral and centromedial amygdala complexes in posttraumatic stress disorder. *Neuropschopharmacology* 39, 351–359. doi: 10.1038/npp.2013.197

Bukhari, Q., Schroeter, A., Cole, D. M., and Rudin, M. (2017). Resting state fMRI in mice reveals anesthesia specific signatures of brain functional networks and their interactions. *Front. Neural Circuits* 11:5. doi: 10.3389/fncir.2017.00005

Calaitzakis, M. E., Pearce, R. K., and Gentleman, S. M. (2009). Clinical correlates of pathology in the claustrum in Parkinson's disease and dementia with Lewy bodies. *Neurosci. Lett.* 461, 12–15. doi: 10.1016/j.neulet.2009.05.083

Cascella, N. G., Gerner, G. J., Fieldstone, S. C., Sawa, A., and Schretlen, D. J. (2011). The insula-claustrum region and delusions in schizophrenia. *Schizophr. Res.* 133, 77–81. doi: 10.1016/j.schres.2011.08.004

Chia, Z., Silberberg, G., and Augustine, G. J. (2017). Functional properties, topological organization and sexual dimorphism of claustrum neurons projecting to anterior cingulate cortex. *Claustrum* 2:1357412. doi: 10.1080/20023294.2017.1357412

Coe, B. C., and Munoz, D. P. (2017). Mechanisms of saccade suppression revealed in the anti-saccade task. *Philos. Trans. R. Soc. Lond. B. Biol. Sci.* 372:20160192. doi: 10.1098/rstb.2016.0192

Comoli, E., Coizet, V., Boyes, J., Bolam, J. P., Canteras, N. S., Quirk, R. H., et al. (2003). A direct projection from superior colliculus to substantia nigra for detecting salient visual events. *Nat. Neurosci.* 6, 974–980. doi: 10.1038/nn1113

Crick, F. C., and Koch, C. (2005). What is the function of the claustrum? *Philos. Trans. R. Soc. Lond. B. Biol. Sci.* 360, 1271–1279. doi: 10.1098/rstb.2005.1661

De Franceschi, G. D., Vivattansam, T., Saleem, A. B., and Solomon, S. G. (2016). Vision guides selection of freeze or flight defense strategies in mice. *Curr. Biol.* 26, 2150–2154. doi: 10.1016/j.cub.2016.06.006

Deshpande, G., Kerssens, C., Sebel, P. S., and Hu, X. (2010). Altered local coherence in the default mode network due to sevoflurane anesthesia. *Brain Res.* 1318, 110–121. doi: 10.1016/j.brainres.2009.12.075

Edelstein, L. R., and Denaro, F. J. (2004). The claustrum: a historical review of its anatomy, physiology, cytochemistryand functional significance. *Cell. Mol. Biol.* 50, 675–702.

Fox, M. D., Snyder, A. Z., Vincent, J. L., Corbetta, M., Van Essen, D. C., and Raichle, M. E. (2005). The human brain is intrinsically organized into dynamic, anticorrelated functional networks. *Proc. Natl. Acad. Sci. U S A* 102, 9673–9678. doi: 10.1073/pnas.0504136102

Gattass, R., Soares, J. G. M., Desimone, R., and Ungerleider, L. G. (2014). Connectional subdivision of the claustrum: two visuotopic subdivisions in the macaque. *Front. Systems Neurosci.* 8:63. doi: 10.3389/fnsys.2014.00063

Geng, H., Li, X., Chen, J., Li, X., and Gu, R. (2016). Decreased intra- and inter-salience network functional connectivity is related to trait anxiety in adolescents. *Front. Behav. Neurosci.* 9:350. doi: 10.3389/fnbeh.2015.00350

Goll, Y., Atlan, G., and Citri, A. (2015). Attention: the claustrum. *Trends Neurosci.* 38, 486–495. doi: 10.1016/j.tins.2015.05.006

Gozzi, A., and Schwarz, A. J. (2016). Large-scale functional connectivity networks in the rodent brain. *Neuroimage* 127, 496–509. doi: 10.1016/j.neuroimage.2015.12.017

Hadjikhani, N., and Roland, P. E. (1998). Cross-modal transfer of information between the tactile and the visual representations in the human brain: a positron emission tomographic study. *J. Neurosci.* 18, 1072–1084. doi: 10.1523/JNEUROSCI.18-03-01072.1998

Hoy, J. L., Yavorksa, I., Wehr, M., and Niell, C. M. (2016). Vision drives accurate approach behavior during pretty capture in laboratory mice. *Curr. Biol.* 26, 3046–3052. doi: 10.1016/j.cub.2016.09.009

Jackson, J., Karnani, M. M., Zemelman, B. V., Burdakov, D., and Lee, A. K. (2018). Inhibitory control of prefrontal cortex by claustrum. *Neuron* 99, 1029.e4–1039.e4. doi: 10.1016/j.neuron.2018.07.031

Jonckers, E., Van Audekerke, J., De Visscher, G., Van der Linden, A., and Verhoye, M. (2011). Functional connectivity fMRI of the rodent brain: comparison of functional connectivity networks in rat and mouse. *PLoS One* 6:e18876. doi: 10.1371/journal.pone.0018876

Kalaitzakis, M. E., Pearce, R. K., and Gentleman, S. M. (2009). Clinical correlates of pathology in the claustrum in Parkinson's disease and dementia with Lewy bodies. *Neurosci. Lett.* 461, 12–15. doi: 10.1016/j.neulet.2009.05.083

Koubeissi, M. Z., Bartolomei, F., Beltagy, A., and Picard, F. (2014). Electrical stimulation of a small brain area reversibly disrupts consciousness. *Epilepsy Behav.* 37, 32–35. doi: 10.1016/j.yebeh.2014.05.027

Krimmel, S. R., Qadir, H., Hesselgrave, N., White, M. G., Reser, D. H., Mathur, B. N., et al. (2019a). Resting state functional connectivity of the rat claustrum. *Front. Neuroanat.* 13:22. doi: 10.3389/fnana.2019.00022

Krimmel, S. R., White, M. G., Panicker, M. H., Barrett, F. S., Mathur, B. N., and Seminowicz, D. A. (2019b). Resting state functional connectivity and cognitive task-related activation of the human claustrum. *Neuroimage* 196, 59–67. doi: 10.1016/j.neuroimage.2019.03.075

Kurada, L., Bayat, A., Joshi, S., and Koubeissi, M. Z. (2019). The claustrum in relation to seizures and electrical stimulation. *Front. Neuroanat.* 13:8. doi: 10.3389/fnana.2019.00008

Liang, Z., King, J., and Zhang, N. (2011). Uncovering intrinsic connectional architecture of functional networks in awake rat brain. *J. Neurosci.* 31, 3776–3783. doi: 10.1523/JNEUROSCI.4557-10.2011

Liang, Z., King, J., and Zhang, N. (2012a). Intrinsic organization of the anesthetized brain. *J. Neurosci.* 32, 10183–10191. doi: 10.1523/JNEUROSCI.1020-12.2012

Liang, Z., King, J., and Zhang, N. (2014). Neuroplasticity to a single-episode traumatic stress revealed by resting-state fMRI in awake rats. *Neuroimage* 103, 485–491. doi: 10.1016/j.neuroimage.2014.08.050

Liang, Z., Li, T., King, J., and Zhang, N. (2013). Mapping thalamocortical networks in rat brain using resting-state functional connectivity. *Neuroimage* 83, 237–244. doi: 10.1016/j.neuroimage.2013.06.029

Liang, Z., Liu, X., and Zhang, N. (2015). Dynamic resting state functional connectivity in awake and anesthetized rodents. *Neuroimage* 104, 89–99. doi: 10.1016/j.neuroimage.2014.10.013

Liu, X., Li, H., Luo, F., Zhang, L., Han, R., and Wang, B. (2015). Variation of the default mode network with altered alertness levels induced by propofol. *Neuropsychiatr. Dis. Treat.* 11, 2573–2581. doi: 10.2147/ndt.s88156

Majak, K., Pikkarainen, M., Kemppainen, S., Jolkkonen, E., and Pitkanen, A. (2002). Projections from the amygdaloid complex to the claustrum and the endopiriform nucleus: a phaseoulus vulgaris leucoagglutinin study in the rat. *J. Comp. Neurol.* 451, 236–249. doi: 10.1002/cne.10346

Mallikarjun, P. V., Lalousis, P. A., Dunne, T. F., Heinze, K., Reniers, R. L. E. P., Broome, M. R., et al. (2018). Aberrant salience network functional connectivity in auditory verbal hallucinations: a first episode psychosis sample. *Transl. Psychiatry* 8:69. doi: 10.1038/s41398-018-0118-6

Mathur, B. N. (2014). The claustrum in review. *Front. Syst. Neurosci.* 8:48. doi: 10.3389/fnsys.2014.00048

Mathur, B. N., Caprioli, R. M., and Deutch, A. Y. (2009). Proteomic analysis illuminates a novel structural definition of the claustrum and insula. *Cereb. Cortex* 19, 2372–2379. doi: 10.1093/cercor/bhn253

Menon, V. (2011). Large-scale brain networks and psychopathology: a unifying triple network model. *Trends Cogn. Sci.* 15, 483–506. doi: 10.1016/j.tics.2011.08.003

Menon, V., and Uddin, L. Q. (2010). Saliency, switching, attention and control: a network model of insula function. *Brain Struct. Funct.* 214, 655–667. doi: 10.1007/s00429-010-0262-0

Milardi, D., Bramanti, P., Milazzo, C., Finocchio, G., Arrigo, A., Santoro, G., et al. (2013). Cortical and subcortical connections of the human claustrum revealed *in vivo* by constrained spherical deconvolution tractography. *Cereb. Cortex* 25, 406–414. doi: 10.1093/cercor/bht231

Murphy, K., Birn, R. M., Handwerker, D. A., Jones, T. B., and Bandettini, P. A. (2009). The impact of global signal regression on resting state correlations: are anti-correlated networks introduced? *Neuroimage* 44, 893–905. doi: 10.1016/j.neuroimage.2008.09.036

Oh, S. W., Harris, J. A., Ng, L., Winslow, B., Cain, N., Mihalas, S., et al. (2014). A mesoscale connectome of the mouse brain. *Nature* 508, 207–214. doi: 10.1038/nature13186

Patru, M. C., and Reser, D. H. (2015). A new perspective on delusional states -evidence for claustrum involvement. *Front. Psychiatry* 6:158. doi: 10.3389/fpsyt.2015.00158

Remedios, R., Logothetis, N. K., and Kayser, C. (2010). Unimodal responses prevail within the multisensory claustrum. *J. Neurosci.* 30, 12902–12907. doi: 10.1523/JNEUROSCI.2937-10.2010

Remedios, R., Logothetis, N. K., and Kayser, C. (2014). A role of the claustrum in auditory scene analysis by reflecting sensory change. *Front. Syst. Neurosci.* 8:44. doi: 10.3389/fnsys.2014.00044

Reser, D. H., Majka, P., Snell, S., Chan, J. M. H., Watkins, K., Worthy, K., et al. (2016). Topography of claustrum and insula projections to medial prefrontal and anterior cingulate cortices of the common marmoset (*Callithrix jacchus*). *J. Comp. Neurol.* 525, 1421–1441. doi: 10.1002/cne.24009

Roy, A. K., Shehzad, Z., Marguilies, D. S., Kelly, A. M., Uddin, L. Q., Gotimer, K., et al. (2009). Functional connectivity of the human amygdala using resting state fMRI. *Neuroimage* 45, 614–626. doi: 10.1016/j.neuroimage.2008.11.030

Seeley, W. W., Menon, V., Schatzberg, A. F., Keller, J., Glover, G. H., Kenna, H., et al. (2007). Dissociable intrinsic connectivity networks for salience processing and executive control. *J. Neurosci.* 27, 2349–2356. doi: 10.1523/JNEUROSCI.5587-06.2007

Sforazzini, F., Schwarz, A. J., Galbusera, A., Bifone, A., and Gozzi, A. (2014). Distributed BOLD and CBV-weighted resting-state networks in the mouse brain. *Neuroimage* 87, 403–415. doi: 10.1016/j.neuroimage.2013.09.050

Shepherd, G. M. G. (2013). Corticostriatal connectivity and its role in disease. *Nat. Rev. Neurosci.* 14, 278–291. doi: 10.1038/nrn3469

Smith, J. B., and Alloway, K. D. (2010). Functional specificity of claustrum connections in the rat: interhemispheric communication between specific parts of motor cortex. *J. Neurosci.* 30, 16832–16844. doi: 10.1523/JNEUROSCI.4438-10.2010

Smith, J. B., and Alloway, K. D. (2014). Interhemispheric claustral circuits coordinate sensory and motor cortical areas that regulate exploratory behaviors. *Front. Syst. Neurosci.* 8:93. doi: 10.3389/fnsys.2014.00093

Smith, J. B., Alloway, K. D., Hof, P. R., Orman, R., Reser, D. H., Watakabe, A., et al. (2018). The relationship between the claustrum and endopiriform nucleus: a perspective towards consensus on cross-species homology. *J. Comp. Neurol.* 527, 476–499. doi: 10.1002/cne.24537

Smith, J. B., Klug, J. D., Ross, D. L., Howard, C. D., Hollon, N. G., Ko, V. I., et al. (2016). Genetic-based dissection unveils the inputs and outputs of striatal patch and matrix compartments. *Neuron* 91, 1069–1084. doi: 10.1016/j.neuron.2016.07.046

Smith, J. B., Liang, Z., Watson, G. D. R., Alloway, K. D., and Zhang, N. (2017). Interhemispheric resting-state functional connectivity of the claustrum in the awake and anesthetized states. *Brain Struct. Funct.* 222, 2041–2058. doi: 10.1007/s00429-016-1323-9

Smith, J. B., Radhakrishnan, H., and Alloway, K. D. (2012). Rat claustrum coordinates but does not integrate somatosensory and motor cortical information. *J. Neurosci* 32, 8583–8588. doi: 10.1523/JNEUROSCI.1524-12.2012

Smythies, J., Edelstein, L., and Ramachandran, V. (2012). Hypotheses relating to the function of the claustrum. *Front. Integr. Neurosci.* 6:53. doi: 10.3389/fnint.2012.00053

Sridharan, D., Levitin, D. J., and Menon, V. (2008). A critical role for the right fronto-insular cortex in switching between central-executive and default-mode networks. *Proc. Natl. Acad. Sci. U S A* 105, 12569–12574. doi: 10.1073/pnas.0800005105

Stephani, C., Fernandez-Baca Vaca, G., Maciunas, R., Koubeissi, M., and Lüders, H. O. (2011). Functional neuroanatomy of the insular lobe. *Brain Struct. Funct.* 216, 137–149. doi: 10.1007/s00429-010-0296-3

Stiefel, K. M., Merrifield, A., and Holcombe, A. O. (2014). The claustrum's proposed role in consciousness is supported by the effect and target localization of Salvia divinorum. *Front. Integr. Neurosci.* 8:20. doi: 10.3389/fnint.2014.00020

Torgerson, C. M., Irimia, A., Goh, S. Y., and Van Horn, J. D. (2015). The DTI connectivity of the human claustrum. *Hum. Brain Mapp.* 36, 827–838. doi: 10.1002/hbm.22667

Torgerson, C. M., and Van Horn, J. D. (2014). A case study in connectomics: the history, mapping, and connectivity of the claustrum. *Front. Neuroinform.* 8:83. doi: 10.3389/fninf.2014.00083

Uddin, L. Q. (2015). Salience processing and insular cortical function and dysfunction. *Nat. Rev. Neurosci.* 16, 55–61. doi: 10.1038/nrn3857

Uwano, T., Nishijo, H., Ono, T., and Tamura, R. (1995). Neuronal responsiveness to various sensory stimuli and associative learning in rat amygdala. *Neuroscience* 68, 339–361. doi: 10.1016/0306-4522(95)00125-3

Wallace, D. J., Geenberg, D. S., Sawinksi, J., Rulla, S., Notaro, G., and Kerr, J. N. D. (2013). Rats maintain an overhead binocular field at the expense of constant fusion. *Nature* 498, 65–69. doi: 10.1038/nature12153

Wang, Q., Ng, L., Harris, J. A., Feng, D., Li, Y., Royall, J. J., et al. (2017). Organization of the connections between claustrum and cortex in mouse. *J. Comp. Neurol.* 525, 1317–1346. doi: 10.1002/cne.24047

Wegiel, J., Flory, M., Kuchna, I., Nowicki, K., Ma, S. Y., Imaki, H., et al. (2014). Stereological study of the neuronal number and volume of 38 brain subdivisions of subjects diagnosed with autism reveals significant alterations restricted to the striatum, amygdala and cerebellum. *Acta Neuropathol. Commun.* 2:141. doi: 10.1186/s40478-014-0141-7

Wei, P., Liu, N., Zhang, Z., Liu, X., Tang, Y., He, X., et al. (2015). Processing of visually evoked innate fear by a non-canonical thalamic pathway. *Nat. Commun.* 6:6756.

White, M. G., and Mathur, B. N. (2018). Frontal cortical control of posterior sensory and association cortices through the claustrum. *Brain Struct. Funct.* 223, 2999–3006. doi: 10.1007/s00429-018-1661-x

White, M. G., Panicker, M., Mu, C., Carter, A. M., Roberts, B. M., Dharmasri, P. A., et al. (2018). Anterior cingulate cortex input to the claustrum is required for top-down action control. *Cell Rep.* 22, 84–95. doi: 10.1016/j.celrep.2017.12.023

Zhang, N., Rane, P., Huang, W., Liang, Z., Kennedy, D., Frazier, J. A., et al. (2010). Mapping resting-state brain networks in conscious animals. *J. Neurosci. Methods* 189, 186–196. doi: 10.1016/j.jneumeth.2010.04.001

Zingg, B., Dong, H.-W., Tao, H. W., and Zhang, L. I. (2018). Input-output organization of the mouse claustrum. *J. Comp. Neurol.* 526, 2428–2443. doi: 10.1002/cne.24502

Conflict of Interest Statement: The authors declare that the research was conducted in the absence of any commercial or financial relationships that could be construed as a potential conflict of interest.

frontiers in Neuroanatomy

ORIGINAL RESEARCH
published: 06 August 2019
doi: 10.3389/fnana.2019.00076

Distribution of α7 Nicotinic Acetylcholine Receptor Subunit mRNA in the Developing Mouse

Ron S. Broide[1†‡], Ursula H. Winzer-Serhan[2†], Yling Chen[1] and Frances M. Leslie[1]*

[1] Department of Pharmacology, University of California, Irvine, Irvine, CA, United States, [2] Department of Neuroscience and Experimental Therapeutics, Texas A&M University College of Medicine, Bryan, TX, United States

Homomeric α7 nicotinic acetylcholine receptors (nAChRs) are abundantly expressed in the central and peripheral nervous system (CNS and PNS, respectively), and spinal cord. In addition, expression and functional responses have been reported in non-neuronal tissue. In the nervous system, α7 nAChR subunit expression appears early during embryonic development and is often transiently upregulated, but little is known about their prenatal expression outside of the nervous system. For understanding potential short-term and long-term effects of gestational nicotine exposure, it is important to know the temporal and spatial expression of α7 nAChRs throughout the body. To that end, we studied the expression of α7 nAChR subunit mRNA using highly sensitive isotopic *in situ* hybridization in embryonic and neonatal whole-body mouse sections starting at gestational day 13. The results revealed expression of α7 mRNA as early as embryonic day 13 in the PNS, including dorsal root ganglia, parasympathetic and sympathetic ganglia, with the strongest expression in the superior cervical ganglion, and low to moderate levels were detected in brain and spinal cord, respectively, which rapidly increased in intensity with embryonic age. In addition, robust α7 mRNA expression was detected in the adrenal medulla, and low to moderate expression in selected peripheral tissues during embryonic development, potentially related to cells derived from the neural crest. Little or no mRNA expression was detected in thymus or spleen, sites of immune cell maturation. The results suggest that prenatal nicotine exposure could potentially affect the nervous system with limited effects in non-neural tissues.

Keywords: cortex, hippocampus, spinal cord, enteric nervous system, adrenal medulla, kidney, dorsal root ganglia, nicotine

OPEN ACCESS

Edited by:
Francesco Fornai,
University of Pisa, Italy

Reviewed by:
Rita Machaalani,
The University of Sydney, Australia
Jerry Stitzel,
University of Colorado Boulder, United States

***Correspondence:**
Ursula H. Winzer-Serhan
uwserhan@tamhsc.edu;
Winzer-Serhan@tamu.edu

†Co-first authors

‡Present address:
Ron S. Broide,
Allergan plc, Irvine, CA, United States

Received: *15 April 2019*
Accepted: *12 July 2019*
Published: *06 August 2019*

Citation:
Broide RS, Winzer-Serhan UH, Chen Y and Leslie FM (2019) Distribution of α7 Nicotinic Acetylcholine Receptor Subunit mRNA in the Developing Mouse. Front. Neuroanat. 13:76. doi: 10.3389/fnana.2019.00076

INTRODUCTION

Nicotinic acetylcholine receptors (nAChRs) are ligand gated pentameric cation channels, which were first identified in Torpedo electric organ, and are found in vertebrate and non-vertebrate animals (Changeux, 2012). The nAChRs can be broadly classified into muscle and neuronal type nAChRs, based on the compositions of the subunits that form the ion channel. The neuronal type nAChRs exhibit great diversity, and heteromeric receptors are formed by various compositions of alpha (α2–α10) and non-alpha (β2–β4) subunits. In addition, the α7 subunit forms homomeric

pentamers which have high permeability for calcium ions (Papke, 2014; Kabbani and Nichols, 2018).

Neuronal nAChRs are widely distributed in the peripheral (PNS), central (CNS), and enteric (ENS) nervous system, sensory neurons, retina, and in the adrenal medulla. In the brain and spinal cord, α4 and β2 subunits are broadly expressed, and form the widely distributed neuronal heteromeric nAChR that displays high affinity for nicotine, and is primarily located on presynaptic terminals (Papke, 2014). Knock-out of either α4 or β2 mRNAs results in an almost complete loss of high affinity nicotine binding sites in the brain (Baddick and Marks, 2011). Homomeric α7 nAChRs, which are distinguished from neuronal heteromeric nAChRs by their high-affinity binding to α-Bungarotoxin (α-BTX), are also abundantly expressed in the CNS and spinal cord, where they are located at pre-and postsynaptic sites (Tribollet et al., 2004). During development, mRNA expression of several subunits is transiently upregulated, both in terms of intensity and spatial distribution, and different nAChR subtypes may take on specific functions relevant for brain development (Winzer-Serhan and Leslie, 1997, 2005; Broide and Leslie, 1999; Adams et al., 2002; Son and Winzer-Serhan, 2006). In the PNS, nAChRs exert essential functions in the regulation of the sympathetic and parasympathetic nervous systems. Moreover, neuronal nAChRs are expressed at high levels in peripheral ganglia, where heteromeric nAChRs are predominantly found (Wang et al., 2002). Homomeric α7 nAChRs are also detected in the periphery, but their functional role in either the PNS or ENS, particularly during development, is still unclear.

For a long time, the consensus was that neuronal nAChRs are expressed exclusively on neurons. However, in recent years it has become increasingly clear that functional nAChR responses can be found in non-excitable cells, including microglia (Shytle et al., 2004; Suzuki et al., 2006), astrocytes (Papouin et al., 2017), Schwann cells (Petrov et al., 2014), and other non-neuronal tissues (Sharma and Vijayaraghavan, 2002), and that these responses are often mediated by α7 nAChRs. Of particular interest is the expression of α7 nAChRs in the immune system, because of its crucial role in the regulation of the cholinergic anti-inflammatory pathway (Wang et al., 2003). Based on findings from previous studies, neuronal nAChR subunits appear early during brain development (Zoli et al., 1995; Adams et al., 2002; Tribollet et al., 2004). However, at present, little is known about the expression of α7 nAChRs outside of the CNS, especially during embryonic development. To better understand the potential developmental roles of α7 nAChRs, and the possible short-term and long-term effects of gestational nicotine exposure, we used highly sensitive isotopic *in situ* hybridization (Winzer-Serhan et al., 1999) to identify α7 nAChR expression in embryonic and neonatal whole-body mouse sections. The results of this study revealed the expression of α7 mRNA as early as embryonic day 13 in the peripheral nervous system, including dorsal root ganglia, parasympathetic and sympathetic ganglia, followed by strong expression in brain and spinal cord. In addition, α7 subunit mRNA expression was detected in a number of peripheral tissues potentially related to cells derived from the neural crest. In contrast, little or no expression was detected in thymus or spleen, sites of immune cell maturation.

MATERIALS AND METHODS

The following materials were obtained from the sources indicated: bovine serum albumin, ficoll, polyvinylpyrrolidone, poly-L-lysine, and RNase A (Sigma Chemical Co., St. Louis, MO, United States); T3 and T7 RNA polymerases, proteinase K, and yeast tRNA (Roche Molecular); formamide (Fluka, Ronkonkoma, NY, United States); dextran sulfate and Hyperfilm Bmax (Amersham Pharmacia, Arlington Heights, IL, United States); nuclear track emulsion (NTB-2), (Kodak, Rochester, NY, United States); [^{35}S]uridine triphosphate (UTP) (Life Science NEN, Boston, MA, United States).

Tissue Preparation

Male and female mice (C57BL/6; Charles River, Wilmington, MA, United States) were group housed and provided with food and water *ad libitum*. The mice were mated over a 4-day period and females were monitored twice daily (morning and afternoon) for vaginal plugs. The day of mating (presence of a plug) was defined as embryonic day (E) 0 and pups were born on E19. Pregnant female mice were killed by decapitation and their embryos removed at E13, E15, and E17. Select embryonic pups were taken from different litters and their sex was identified whenever possible. Embryonic and postnatal day (P) 0 mice were anesthetized on ice for several minutes before being frozen whole in isopentane at −25°C and stored at −80°C until use. These procedures were approved by the Institutional Animal Care and Use Committee at the University of California, Irvine, in accordance with federal guidelines. Mouse pups (n = 2–3/age) were cryostat sectioned (20 μm) in the sagittal plane from the lateral right side of the body until just past the midline. Tissue sections were mounted onto slides which were coated with either 1% gelatin (for histology) or an additional coating of poly-L-lysine (for *in situ* hybridization) and kept at −20°C. Sections were post-fixed with 4% paraformaldehyde in 0.1 M phosphate buffered saline (PBS), pH 7.4 for 1 h at 22°C, then washed in PBS, air dried and stored desiccated at −20°C until use.

cRNA Probe Preparation and *in situ* Hybridization

cRNA riboprobes labeled with [^{35}S]UTP were prepared from a 279 bp *Pst*I restriction DNA fragment encoding the third intracellular loop of the mouse α7 nAChR subunit (NM_007390.3; nucleotide sequence 1140 to 1419) (Orr-Urtreger et al., 1995). Riboprobes targeted to this region have been used previously to characterize α7 mRNA distribution in developing mice (Orr-Urtreger et al., 2000; Broide et al., 2001) and show the same pattern of expression as those observed using riboprobes targeted to either the 3′ non-coding region or the full-length mouse α7 nAChR cDNA (data not shown). Post-fixed whole-body sections were processed according to a published protocol (Winzer-Serhan et al., 1999). Briefly, slide-mounted sections were first preincubated with 0.1 μg/ml proteinase K for 10 min at

22°C, and then incubated for 18 h at 60°C with a hybridization solution (50% formamide, 10% dextran sulfate, 0.02% Ficoll, 0.02% polyvinyl pyrrolidone, 0.02% bovine serum albumin, 500 μg/ml tRNA, 10 mM dithiothreitol, 0.3 M NaCl, 10 mM Tris, pH 8.0, 1 mM EDTA, pH 8.0) containing [^{35}S]UTP-labeled cRNA riboprobes (1×10^7 cpm/ml) in the antisense orientation. Adjacent sections were incubated with riboprobes in the sense orientation to define non-specific hybridization. Tissue sections were then incubated with RNase A (20 μg/ml) for 30 min at 37°C, followed by high-stringency washes of decreasing salinity in SSC (sodium chloride/sodium citrate) buffer, and a 30 min wash in 0.1 × SSC at 60°C. Sections were dehydrated, apposed to β-max film for 3–6 days at 4°C, and then dipped in liquid NTB-2 emulsion. Following a 2-week exposure, slide were developed in Kodak D-19, fixed, counter-stained with Cresyl-Violet, cover-slipped and analyzed by high-powered microscopy.

Data Analysis

An initial anatomical analysis was undertaken in which autoradiographic images on β-max films were compared to their corresponding Nissl-stained sections, at each developmental age. Emulsion dipped slides were then analyzed by microscopy to more accurately define areas expressing α7 mRNA. Labeled anatomic regions of embryonic and postnatal mouse bodies were identified using several different sources (Kaufman, 1995; Jacobowitz and Abbott, 1998; Kaufman and Bard, 1999; Paxinos et al., 2007). Silver grains in these regions were manually counted at 400× magnification within a 2 × 2 grid area encompassing 50 μm^2 and the results were expressed as the average number of silver grains per single (25 μm^2) grid box. Based on these counts, a score was assigned to the labeled anatomical structure: + (>10 grains/25 μm^2), ++ (>20 grains/25 μm^2), +++ (>50 grains/25 μm^2), ++++ (>90 grains/25 μm^2). In some regions, a double quantitative score was ascribed (e.g., +/+++), which signified lower levels of mRNA surrounding spots of more intense signal. Background labeling (<10 grains/25 μm^2) was established as the density of silver grains in non-neural tissues with high cellular density (such as the liver), or with high density of extracellular matrix (such as cartilage), or the density of grains over neural structures after hybridization with the sense riboprobe.

RESULTS

We began our analysis at E13 because it was previously demonstrated that at this age, low levels of α7 nAChR mRNA expression first appear in several regions of the rat brain (Broide et al., 1995; Adams et al., 2002). However, because our present analysis of the mouse was more broad-based, encompassing the entire body, we conducted a more general investigation of the CNS with greater emphasis on regions showing higher α7 mRNA expression. An initial examination of autoradiographic images revealed that α7 nAChR mRNA was expressed throughout the CNS, including the spinal cord and retina, as early as E13, and up until birth (**Figure 1**). High levels of mRNA transcripts were also found in many PNS and sensory ganglia, and relatively low levels of α7 mRNA labeling were detected in some non-neuronal tissues during development. In general, at E13, α7 nAChR mRNA expression intensity was low to moderate in the PNS and CNS, and low in non-neuronal areas of the body (**Figure 1** and **Tables 1–3**). However, by E15, there was a marked increase in mRNA expression intensity in areas of the nervous system that persisted until birth, whereas expression in non-neuronal areas remained low.

Central Nervous System

Olfactory Bulb

At E13, emulsion dipped, sagittal whole-body sections containing the emerging olfactory bulb showed background labeling in this region (**Figure 2A**). By E15, low levels of α7 nAChR mRNA expression were first observed in the olfactory bulb and were visible throughout embryonic development (**Figures 2B,D** and **Table 1**). The olfactory tubercle exhibited higher levels of mRNA expression that peaked slightly at E17 (**Table 1**).

Telencephalon

In the developing mouse telencephalon, α7 nAChR mRNA was most prominently expressed in the neocortex and the hippocampus (**Figure 2** and **Table 1**). At E13, moderate levels of α7 mRNA were already observed throughout the cortical plate and the emerging hippocampal formation (**Figure 2E**). Levels of α7 mRNA in these regions were increased by E15 and remained high until birth (**Figures 2F–H**). In the neocortex, high levels of α7 mRNA expression were largely restricted to the parietal cortex. Elevated levels of mRNA were also expressed in the emerging layer 6 of the cortex, beginning at E17 (**Table 1**). Lower levels of mRNA labeling were observed in the intermediate and ventricular zones, as well as the basal ganglia, preoptic area, and the septum (**Table 1**).

Diencephalon

Levels of α7 nAChR mRNA in the diencephalon at E13 were extremely low (**Table 1**). However, by E15, mRNA levels were increased in various nuclei throughout the thalamus and hypothalamus, and remained at moderate levels until birth.

Mesencephalon

The developing mesencephalon is comprised of the superior and inferior colliculi at its dorsal subdivision and the tegmentum, including the red nucleus in the ventral subdivision. At E13, mostly background labeling was observed in this region of the brain (**Table 1**). Levels of α7 mRNA in the mesencephalon showed a slight increase by E15 and remained relatively low throughout embryonic development. However, higher levels of mRNA were particularly notable in the red nucleus and the superior and inferior colliculi (data not shown).

Pons

The region of the pons that contains the locus coeruleus (LC) and dorsal raphe (DR), showed strong labeling for α7 nAChR mRNA in the dorsal tegmental and ventral tegmental nuclei from E13 until birth (**Figures 2I–L**). Low to moderate levels of mRNA were found throughout the rest of the pons (**Table 1**).

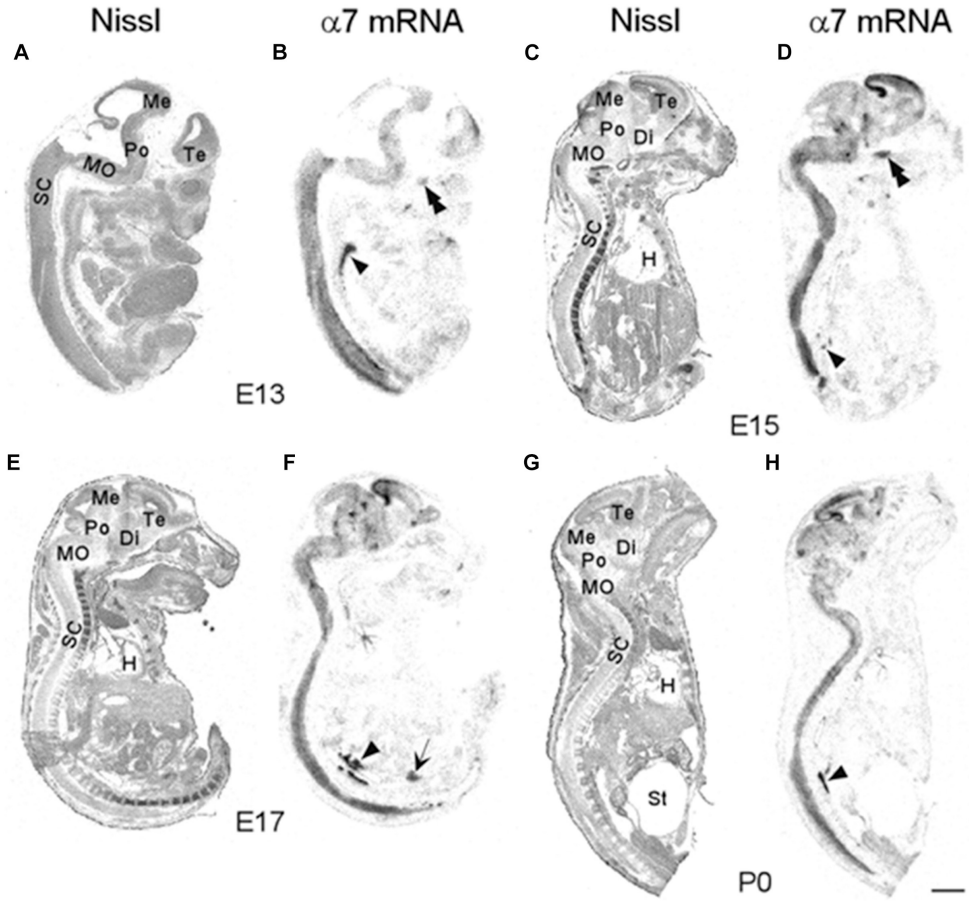

FIGURE 1 | Bright-field micrographs of autoradiographic images showing α7 nAChR mRNA expression in sagittal midline sections of E13 **(B)**, E15 **(D)**, E17 **(F)**, and P0 **(H)** mouse pups. **(A,C,E,G)** Adjacent sections stained with cresyl-violet. Strong mRNA labeling can be seen in the autonomic (arrowhead) and trigeminal (double arrowheads) ganglia as well as the prostate (arrow). Di, diencephalon; H, heart; Me, mesencephalon; MO, medulla oblongata; Po, pons; SC, spinal chord; St, stomach; Te, telencephalon. Scale bar = 1 mm **(A,B)**, 1.5 mm **(C,D)**, 1.7 mm **(E,F)**, and 2 mm **(G,H)**.

Medulla Oblongata

At E13, low levels of α7 nAChR mRNA expression were observed in the medulla oblongata. However, by E15, levels of mRNA were increased, particularly in the ventral region, and remained elevated until birth (**Table 1**). The mRNA expression pattern was mainly scattered with some dense areas of labeling in both the dorsal and ventral regions (**Figures 2I–L**).

Cerebellum

The cerebellum, which was first visible by E15, showed very low levels of α7 mRNA expression throughout embryonic development (**Figures 2I–L** and **Table 1**).

Spinal Cord

Moderate levels of α7 mRNA expression were visible in the spinal cord (SC) at E13 and remained relatively unchanged until birth (**Figures 2M–P** and **Table 1**). In the dorsal region of the SC, the expression of α7 mRNA was homogenous. However, in the ventral region, a band of increased α7 mRNA expression was observed with areas of intense cellular labeling (**Figures 2M–P**).

Retina

The developing retina exhibited background labeling at E13. By E15, low levels of α7 mRNA expression became detectable in the emerging ganglionic cell layer. **Figure 3** shows an example of α7 mRNA labeling in an E17 retina. This level of scattered labeling, which was not found in adjacent sections hybridized with the sense riboprobe (**Figure 3C**), was observed throughout embryonic development and at birth.

Peripheral Nervous System

α7 nAChR mRNA was expressed in all discernible ganglia of the developing mouse PNS. However, due to technical issues in gathering tissue sections, not all ganglia were observed at every age analyzed. Therefore, the representative ganglia that are discussed are those that were visible throughout embryonic development.

Sensory Ganglia

We examined two different sensory ganglia, the trigeminal and the dorsal root ganglion. The trigeminal ganglion (TG) is a

TABLE 1 | α7 nAChR subunit mRNA expression in the developing central nervous system (CNS).

	Age			
Region	**E13**	**E15**	**E17**	**P0**
Olfactory bulb	–	++	++	++
Olfactory tubercle	–	+++	++++	+++
Telencephalon				
Parietal Cortex				
Cortical plate	+++	++++	++++	++++
Layer 6	NA	NA	++++	+++
Intermediate zone	NA	++	++	+
Ventricular zone	–	+	+	–
Hippo. formation	++	++++	++++	+++/++++
Septum	–	–	+	+
Basal ganglia	+	+	+/++	+/++
Preoptic area	++	++	++	++
Diencephalon				
Thalamus				
Lateral	–/+	+/+++	+/++++	+/+++
Medial	–/+	+/++	+/+++	+/+++
Hypothalamus	–/+	+/++	+/+++	+/+++
Mesencephalon				
Lateral	–	+	+/++	+/++
Mediodorsal	+	+	+	++
Medioventral	–	+/++	+/++	+/++
Pons				
Lateral	+	+/++	+/++	+/++
Mediodorsal	+/+++	+/++++	+/++++	+/++++
Medioventral	+	+/+++	+/+++	+/+++
Medulla oblongata				
Lateral	+	++	++	++
Mediodorsal	+/++	++/+++	++/+++	++/+++
Medioventral	+/++	++/++++	++/++++	++/+++
Cerebellum	NA	+	+	+
Spinal chord				
Dorsal	++	+++	+++	+++
Ventral	++/+++	+++/++++	+++/++++	+++/++++

Intensity is based on silver grain counts: + (>10 grains/25 μm^2), ++ (>20 grains/25 μm^2), +++ (>50 grains/25 μm^2), ++++ (>90 grains/25 μm^2). A double quantitative score indicates signified lower levels of mRNA surrounding spots of more intense signal.

TABLE 2 | α7 nAChR subunit mRNA expression in ganglia of the developing peripheral nervous system (PNS).

	Age			
Ganglion	**E13**	**E15**	**E17**	**P0**
Sensory				
Trigeminal (V)	++	+++/++++	+++/++++	+++/++++
Dorsal root	+	+++/++++	+++/++++	+++/++++
Autonomic ganglia				
Sympathetic				
Superior cervical	+++	++++	++++	++++
Stellate	+++	++++	++++	++++
Celiac	+++	++++	++++	++++
Mesenteric	+++	++++	++++	++++
Parasympathetic				
Submandibular (VII)	+++	+++	+++	+++
Otic (IX)	+++	++++	++++	++++
Vagal (X)	+/++	++/++++	++/++++	++/++++
Intracardiac	+++	+++	+++	+++
Intramural	+++	++++	++++	+++
Enteric	+	+++	+++	++/+++

Intensity is based on silver grain counts: + (>10 grains/25 μm^2), ++ (>20 grains/25 μm^2), +++ (>50 grains/25 μm^2), and ++++ (>90 grains/25 μm^2). A double quantitative score indicates signified lower levels of mRNA surrounding spots of more intense signal.

TABLE 3 | Expression of α7 nAChR subunit mRNA in developing non-neuronal tissue.

	Age			
Tissue	**E13**	**E15**	**E17**	**P0**
Adrenal medulla	++	+++	+++	+++/++++
Kidney cortex	–/+	–/+++	–/+++	–/++
Tongue	–	–/+++	–/+++	–/++++
Nasal epithelium	–	+	+	+
Tooth bud	–	+	++	+
Aorta	++	++	++	++
Muscle	+/+++	+/++	+	–

Intensity is based on silver grain counts: + (>10 grains/25 μm^2), ++ (>20 grains/25 μm^2), +++ (>50 grains/25 μm^2), and ++++ (>90 grains/25 μm^2). A double quantitative score indicates signified lower levels of mRNA surrounding spots of more intense signal.

sensory ganglion found at the base of the brain. Primary afferent fibers from this ganglion form much of the fifth cranial nerve (V), which innervates the face, jaw and olfactory mucosa. At E13, the TG exhibited low levels of α7 mRNA labeling (**Figure 4A** and **Table 2**). By E15, levels of mRNA were markedly increased and remained elevated until birth (**Figures 4B–D** and **Table 2**). The α7 mRNA expression pattern in the TG appeared striated with random cells expressing a higher density of mRNA transcripts.

The dorsal root ganglia (DRG) are attached to the dorsal horn on either side, and along the length of the spinal cord. They receive input from the various sensory receptors throughout the body and relay this information to the spinal cord. At E13, the DRG showed very low expression of α7 mRNA transcripts (**Figure 4E** and **Table 2**). The levels of mRNA were markedly increased by E15 and remained elevated until birth (**Figures 4F–H** and **Table 2**). The α7 mRNA expression pattern in the DRG was homogenous, with intermittent clusters of cells expressing a high density of mRNA transcripts.

The vagal (jugular) ganglion (VG), located just behind the cochlea, is a well-marked ganglionic enlargement of the vagus nerve (X) complex that provides afferent somatosensory innervation to the external auditory meatus, cranial meninges, and the tympanic membrane. At E13, the vagal ganglion showed very low levels of α7 mRNA expression (**Figure 4M** and **Table 2**). By E15, the overall levels of α7 mRNA were increased to moderate levels, and random cells were observed expressing very high

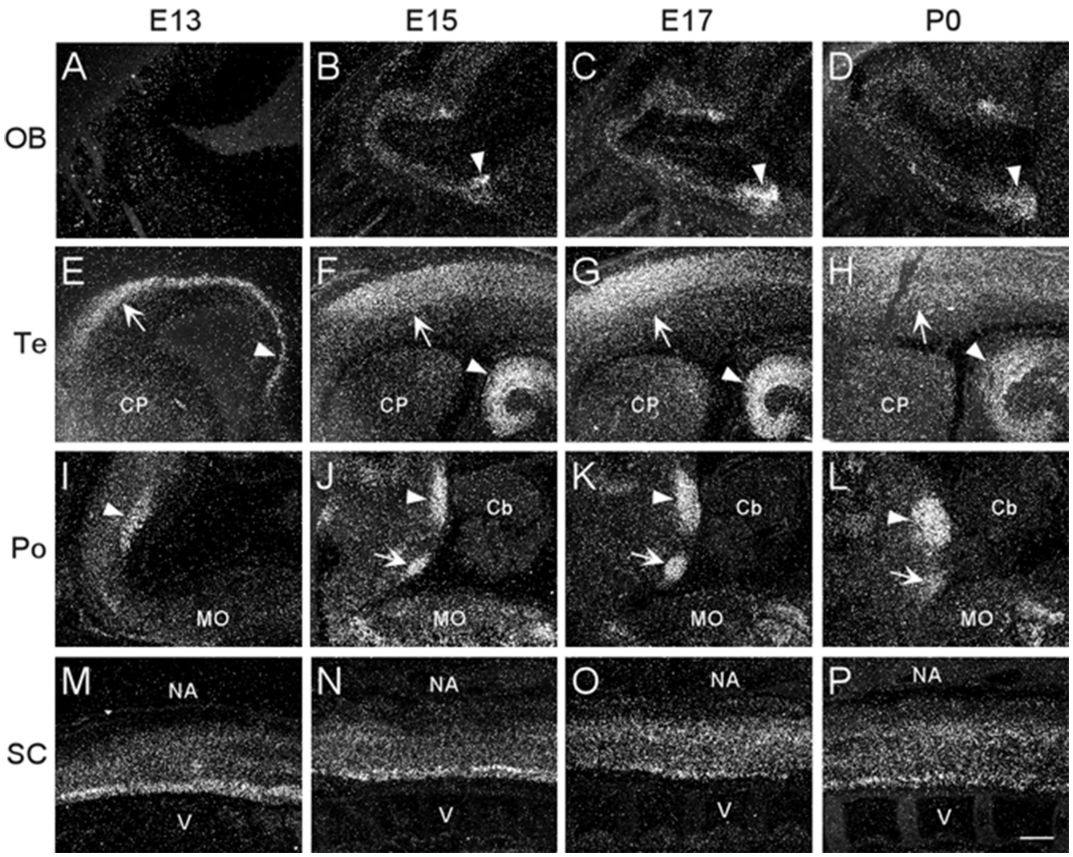

FIGURE 2 | Dark-field photomicrographs showing α7 mRNA distribution in different regions of the CNS from parasagittal sections of E13, E15, E17, and P0 mouse pups. **(A–D)** In the area of the olfactory bulb (OB), arrowheads point to increasing mRNA expression in the olfactory tubercle. **(E–H)** In the telencephalon (Te), strong mRNA expression is observed in the parietal cortex (arrow) and hippocampus (arrowhead). **(I–L)** In the pons, the mRNA expression is highest in the dorsal tegmental (arrowhead) and ventral tegmental (arrow) nuclei. **(M–P)** In the spinal cord (SC), a band of elevated mRNA expression can be seen in the ventral, motor neuron region. Cb, cerebellum; CP, caudate putamen; MO, medulla oblongata; NA, neural arch; V, vertebrate. Scale bar = 300 μm.

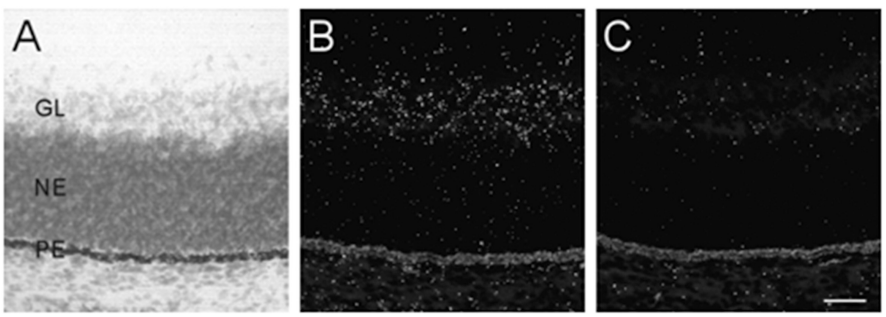

FIGURE 3 | α7 nAChR mRNA distribution in the developing retina. **(A,B)** Bright- and dark-field photomicrographs of an E17 retina showing low levels of α7 mRNA expression in the ganglion cell layer. The section was counterstained with cresyl-violet and retinal layers are indicated: GL, ganglion cell layer; NE, neural epithelium; PE, pigment epithelium. **(C)** Adjacent section showing background labeling with the sense riboprobe. Scale bar = 50 μm.

mRNA levels. This pattern and level of expression persisted until birth (**Figures 4N–P** and **Table 2**).

Autonomic Sympathetic Ganglia

The sympathetic chain of ganglia are located next to the vertebral column and overlying the descending aorta. Together they provide sympathetic innervation to all the organs of the body. Although α7 nAChR mRNA labeling was observed throughout the sympathetic chain, we focused primarily on the larger, superior cervical ganglia (SCG), which are located at the top of this chain and innervate the radial muscle of the iris, the eyelids, the lacrimal and salivary glands, and the heart. At E13, the SCG

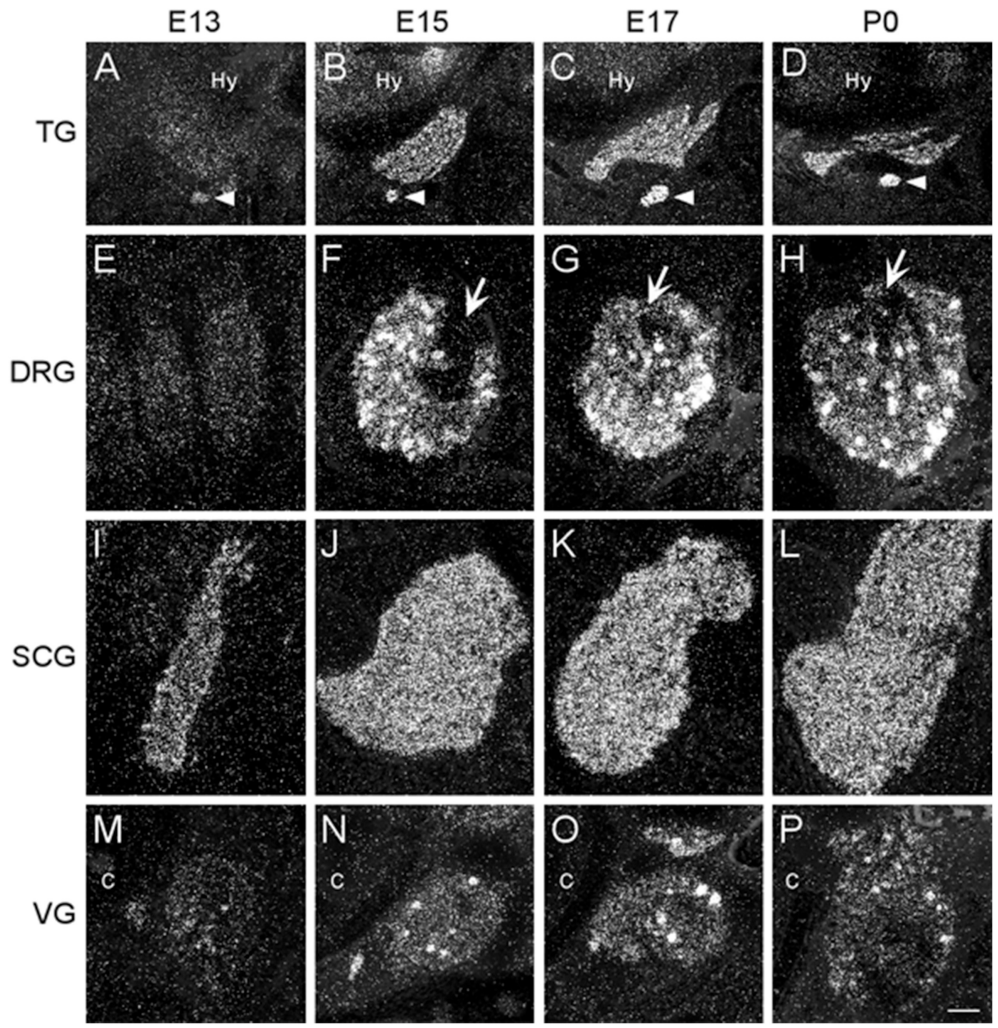

FIGURE 4 | Dark-field photomicrographs of representative sensory and autonomic ganglia at E13, E15, E17, and P0. **(A–D)** Increasing α7 mRNA expression is observed with age in the trigeminal sensory ganglion (TG) and the optic parasympathetic ganglion (arrowhead). **(E–H)** α7 mRNA expression in the dorsal root ganglion (DRG) is low at E13, but shows intense punctate expression starting at E15. The entry point for the dorsal root is indicated (arrows). **(I–L)** An even distribution of strong α7 mRNA expression is observed in the superior cervical ganglion (SCG), part of the chain of sympathetic ganglia along the spinal cord. **(M–P)** Expression of α7 mRNA in the vagal parasympathetic ganglion (VG) at the base of the brain. Hy, hypothalamus; C, cochlea. Space bar = 250 μm **(A–D)**, 100 μm **(E–P)**.

exhibited moderate levels of α7 mRNA expression (**Figure 4I** and **Table 2**). However, by E15, the levels of α7 mRNA in the SCG were increased and remained high until birth (**Figures 4J–L** and **Table 2**). The α7 mRNA expression pattern was homogenous throughout the SCG. Similar spatiotemporal patterns of α7 mRNA expression were also observed in the stellate, celiac, and mesenteric sympathetic ganglia (**Table 2**).

Autonomic Parasympathetic Ganglia

The parasympathetic ganglia are located close to the organs they innervate and are often embedded within their walls. The cranial component of the parasympathetic system originates from four of the twelve cranial nerves that emerge from the brainstem. The glossopharyngeal nerve (IX) synapses onto neurons in the otic ganglion (OG) which innervates the parotid gland. Located just below the TG, the OG exhibited moderate levels of α7 mRNA expression at E13 (**Figure 4A** and **Table 2**). The levels of α7 mRNA were increased by E15 and remained high until birth (**Figures 4B–D** and **Table 2**).

During embryonic development, α7 nAChR mRNA transcripts were also detected in a number of parasympathetic ganglia embedded within different organs (**Table 2**). For example, α7 mRNA was expressed at moderate levels in intracardiac ganglia that are interspersed on top of the atria of the heart (**Figures 5A,B**). High levels of α7 mRNA expression were also found in intramural ganglia surrounding the esophagus, and were observed along its entire length (**Figures 5C,D**). Moderate levels of α7 mRNA expression were detected in submandibular ganglia which are embedded in the submaxillary gland (**Figures 5E,F**), and are innervated by the facial nerve

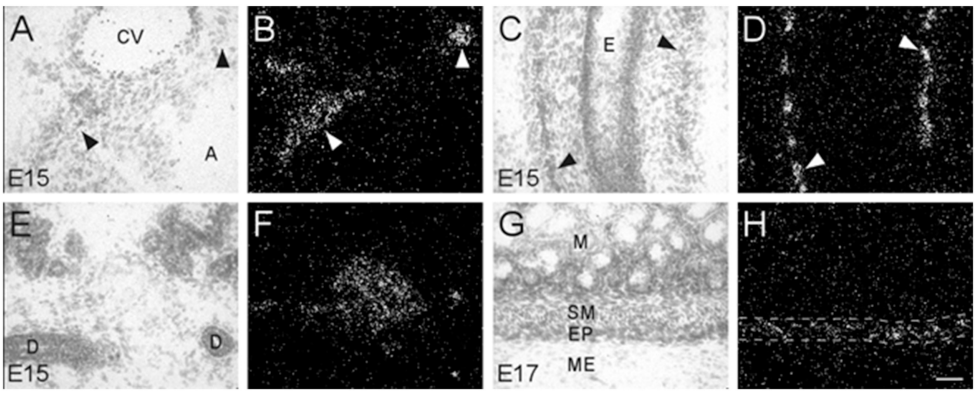

FIGURE 5 | Bright- and dark-field photomicrographs showing α7 nAChR mRNA expression in various intramural ganglia of the parasympathetic system at E15 and E17. **(A,B)** α7 mRNA transcripts are expressed in intracardiac ganglia (arrowheads), that are interspersed on top of the atria. **(C,D)** Intramural ganglia (arrowheads) lining the esophagus **(E)** showing high levels of α7 mRNA expression. **(E,F)** Expression of α7 mRNA is observed in one of the submandibular ganglia within the submaxillary gland. **(G,H)** The enteric plexus of the large colon (area between dashed lines) shows light to moderate expression of α7 mRNA. Sections are counterstained with cresyl-violet. A, atrium; CV, cardiac vessel; D, submaxillary duct; E, esophagus; EP, enteric plexus; M, mucosa; ME, muscularis externa; SM, submucosa. Space bar = 50 μm.

(VII). Finally, ganglia in the enteric plexus of the gut displayed low to moderate levels of α7 mRNA expression during embryonic development. These ganglia were observed throughout the small and large intestine (**Figures 5G,H**).

Non-neuronal Tissues

Adrenal Medulla and Kidney Cortex

In addition to the expression of α7 nAChR mRNA in the nervous system, α7 mRNA transcripts were also detected in a number of non-neuronal tissues throughout the bodies of embryonic and postnatal mice. At E13, low levels of α7 nAChR mRNA were detected in the adrenal medulla (**Table 3**). The mRNA levels increased by E15 and were highest at birth. The mRNA expression pattern delineated the adrenal medulla containing darkly stained chromaffin cells (**Figures 6A,B**). Low levels of α7 mRNA transcripts were observed in the kidney cortex at E13. The levels were notably increased by E15 followed by a slight decrease at birth (**Table 3**). The signal was detected in tubules proximal to the glomeruli (**Figures 6C,D**). Adjacent sections hybridized with the sense riboprobe showed only background levels over the tubules in the kidney cortex (**Figures 6E,F**).

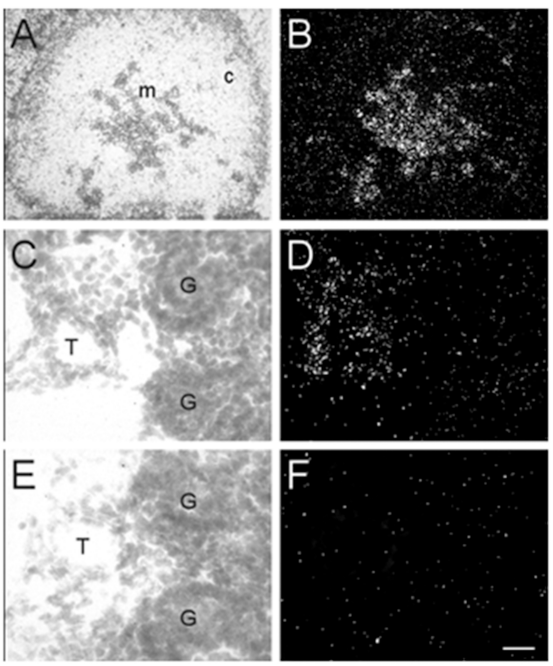

FIGURE 6 | Bright- and dark-field photomicrographs of the adrenal gland and kidney cortex at E17 displaying α7 nAChR mRNA expression. **(A,B)** The adrenal medulla shows high levels of α7 mRNA expression. **(C,D)** In the kidney cortex, α7 mRNA is expressed mainly in tubules close to the glomeruli. **(E,F)** Adjacent section showing background labeling with the sense riboprobe in the kidney cortex. Sections are counterstained with cresyl-violet. C, adrenal cortex; G, glomerulus; M, adrenal medulla; T, kidney tubule. Scale bar = 100 mm **(A,B)**, 25 μm **(C–F)**.

Oral and Nasal Tissues

Transcripts for α7 nAChR mRNA were detected in several different non-neuronal tissues in the head region of embryonic and postnatal mice. These tissues all showed background labeling at E13 (**Table 3**). However, by E15, moderate levels of α7 mRNA expression were first observed in the posterior portion of the tongue, above the frenulum, and were increased by P0. The mRNA labeling exhibited a punctate chain pattern that was confined to the middle region of the tongue (**Figures 7A,B**). Very low levels of α7 mRNA labeling were also found in cells of the nasal epithelium beginning at E15 and up until birth (**Table 3** and **Figures 7D,E**). Finally, low levels of α7 mRNA transcripts were first detected in the developing tooth bud at E15 and were markedly increased by birth (**Table 3**). The mRNA expression was highest in the predentin layer of the tooth bud, an area containing the extended cell bodies of the dentine-forming odontoblasts

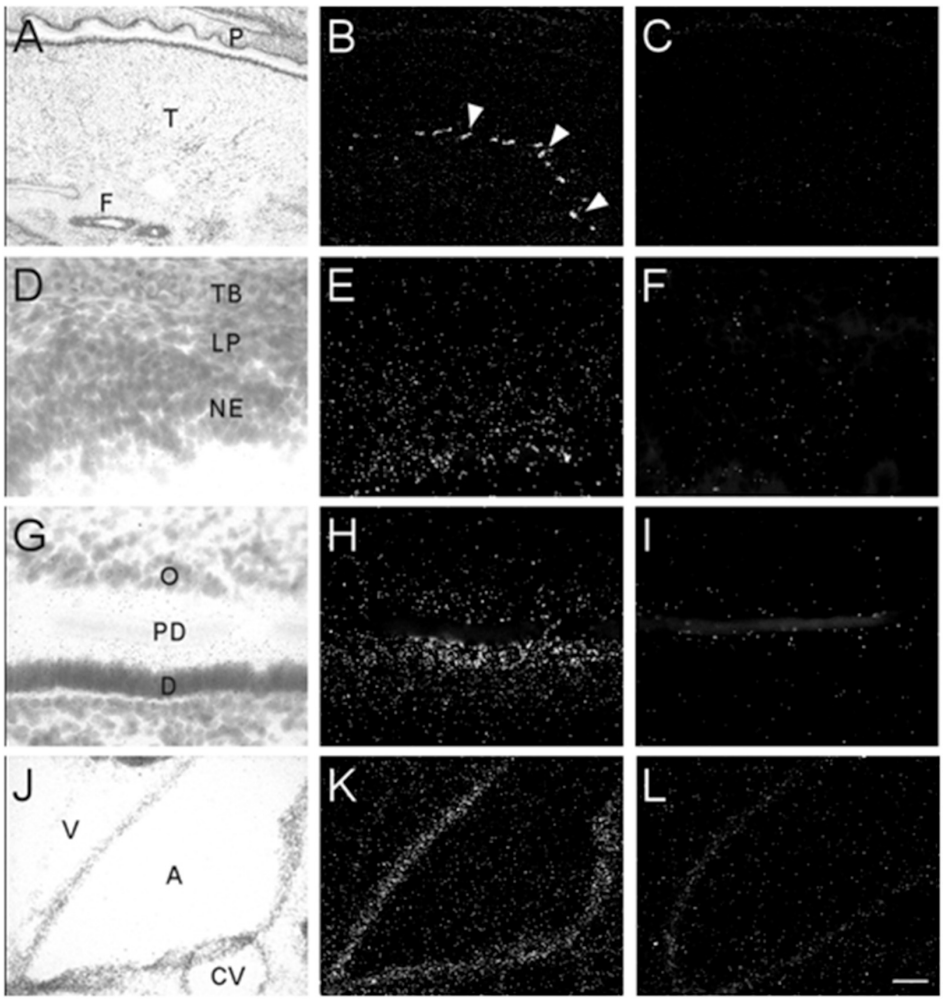

FIGURE 7 | Bright- and dark-field photomicrographs showing α7 nAChR mRNA expression in various non-neuronal tissues from E17 and P0 mouse pups. **(A,B)** Strong punctate expression of α7mRNA in the posterior region of the tongue (arrow heads). **(D,E)** Low expression of α7mRNA is observed in the nasal epithelium. **(G,H)** Moderate levels α7mRNA expression are observed in the predentin layer of the developing tooth bud. **(J,K)** α7 mRNA expression is shown in epithelial cells lining the aorta. Sections are counterstained with cresyl-violet. **(C,F,I,L)** Adjacent sections showing background labeling in each tissue with the sense riboprobe. A, aorta; CV, cardiac vessel; D, dentine; F, frenulum; NE, nasal epithelium; O, odontoblasts; P, palate; PD, predentin; T, tongue; TB, turbinate bone; V, ventricle. Space bar = 250 μm **(A–C)**, 25 μm **(D–I)**, 100 μm **(J–L)**.

(**Figures 7G,H**). Expression of α7 was also detected in the cell line of the aorta (**Figures 7J,K**). Adjacent sections hybridized with the sense probe exhibited background levels of expression (**Figures 7C,F,I,L**).

Prostate and Testes

Male mouse pups were only identified and obtained at E17 and P0. Therefore, our analysis of the prostate and testes was limited to these two ages. At E17, high levels of α7 nAChR mRNA expression were observed in the developing prostate (**Figures 8A,B**). This structure was located and identified just below the iliac artery and slightly dorsal of the bladder in the midline region. We also found low levels of α7 mRNA expression within the seminiferous tubules of the testes (**Figures 8C,D**). This labeling was not detected on adjacent sections hybridized with the sense riboprobe (**Figures 8E,F**). The α7 mRNA transcripts were expressed in the lumen of the tubules over cells with light Nissl staining (**Figures 8G,H**). Female embryos showed only background labeling over their ovaries (data not shown).

Muscle

Interestingly, we found α7 nAChR mRNA expression in developing muscle tissue. However, in contrast to the other body regions analyzed, the muscle showed a decrease in α7 mRNA expression during embryonic development (**Table 3**). Beginning at E13, low levels of α7 mRNA expression were observed over most of the muscle regions, with low to moderate expression levels exhibited in areas of the limbs close to the cartilage (**Figures 9A,B**). By E17, only low levels of mRNA were apparent over all muscle areas (**Figures 9D,E**) and by P0, these levels were the same as background (**Table 3**). Adjacent sections show hybridization signal with the sense probe (**Figures 9C,F**).

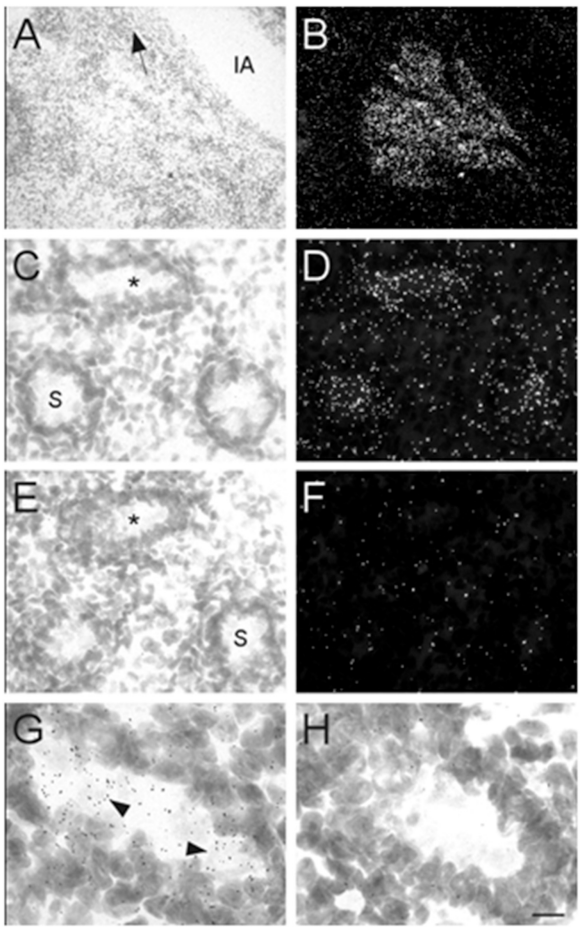

FIGURE 8 | Bright- and dark-field photomicrographs showing α7 nAChR mRNA expression in the prostate and testes at E17. **(A,B)** High expression of α7 mRNA is observed in the mouse prostate, close to the iliac artery (IA). The arrow points toward the bladder. **(C,D)** α7 mRNA labeling can be seen within the seminiferous tubules (S) of the mouse testes. **(E,F)** Adjacent section showing background labeling with the sense riboprobe in the testes. **(G,H)** Higher magnification of tubules in **C** and **E** (asterisk) showing mRNA expression on cells within the seminiferous tubule. Sections are counterstained with cresyl-violet. Scale bar = 100 μm **(A,B)**; 25 μm **(C–F)**; 10 μm **(G,H)**.

DISCUSSION

In the present study, we have demonstrated the widespread distribution of α7 nAChR mRNA throughout the embryonic mouse nervous systems, highlighting the ubiquitous expression of α7 mRNA in the central, peripheral and enteric nervous system during embryonic development. At E13, the youngest age examined, α7 nAChR mRNA expression was already moderately strong in most autonomic ganglia and spinal cord, and expression was also detected at lower levels in the medulla oblongata, pons and mesencephalon. After E13, α7 mRNA expression was generally increased, especially in autonomic and parasympathetic ganglia, and in cortical structures including the hippocampal anlage, and became more refined to specific brain structures and nuclei. These findings confirm previous studies in the rodent (Broide et al., 1995; Messi et al., 1997; Adams et al., 2002), chick (Erkman et al., 2000; Keiger et al., 2003), and human (Hellström-Lindahl et al., 1998; Falk et al., 2002) developing nervous system. Moreover, mRNA expression was observed in various non-neural tissues throughout the body, including adrenal medulla, kidney, tongue, tooth, nasal epithelium, prostate, testis and muscle, but with the exception of the adrenal medulla, expression levels were mostly low. This widespread expression of α7 nAChRs throughout the developing nervous system and the adrenal medulla suggest that these receptors might have important functions during development and that prenatal nicotine exposure may affect nervous system development via aberrant activation of α7 nAChRs (Broide and Leslie, 1999), which could particularly impact brain circuit formation (Lozada et al., 2012) and alter adrenal medulla function (Buttigieg et al., 2009). Additionally, there were low level of α7 mRNA expression in many tissues throughout the body. However, it remains to be determined if the transcripts are translated into protein and subsequently form functional α7 nAChRs.

Technical Considerations

For this study, we utilized an *in situ* hybridization protocol that was developed not only for its sensitivity but also for specificity of signal (Winzer-Serhan et al., 1999). We employed [^{35}S]UTP-labeled cRNA riboprobes transcribed from a 279 bp DNA fragment encoding the third intracellular loop of the mouse α7 nAChR subunit for increased specificity. Riboprobes targeted to this region have been used previously to characterize α7 mRNA distribution in developing mice (Orr-Urtreger et al., 1995, 2000; Broide et al., 2001), and show the same pattern of expression as that observed using riboprobes targeted to the full length mouse α7 nAChR mRNA that have been successfully used in other studies (Broide et al., 1995; Bina et al., 1995; Adams et al., 2002). BLAST analysis revealed no other highly homologous sequences to non-α7 nAChR mouse transcripts, indicating that the possibility of this cRNA probe to cross-hybridize with highly homologous sequences is very low, and we are confident that the hybridization signal shown throughout the embryonic mouse body reflect α7 mRNA expression. While the number of embryos in this study is limited to $n = 2–3$ per age, it must be emphasized that the consistency in α7 nAChR expression within the outlined structures from one age to the next provides an adequate number overall that supports our findings for developmental expression of this receptor.

Our study of α7 nAChR expression during mouse development was focused on mRNA expression and not protein. This was due to the fact that at the early prenatal time points, the autoradiographic signal for [^{125}I]α-BTX binding to α7 receptor proteins in neuronal areas was barely detectable above background. Furthermore, in the periphery, [^{125}I]α-BTX binds to muscle type nAChRs which makes it difficult to distinguish binding to α7 receptors from binding to muscle-type nAChRs. In addition, the use of α7 nAChR subunit antibodies has proven unreliable because of the non-specific binding to unknown sites that persist in α7 nAChR subunit knockout mice (Moser et al., 2007). For this reason, publications describing

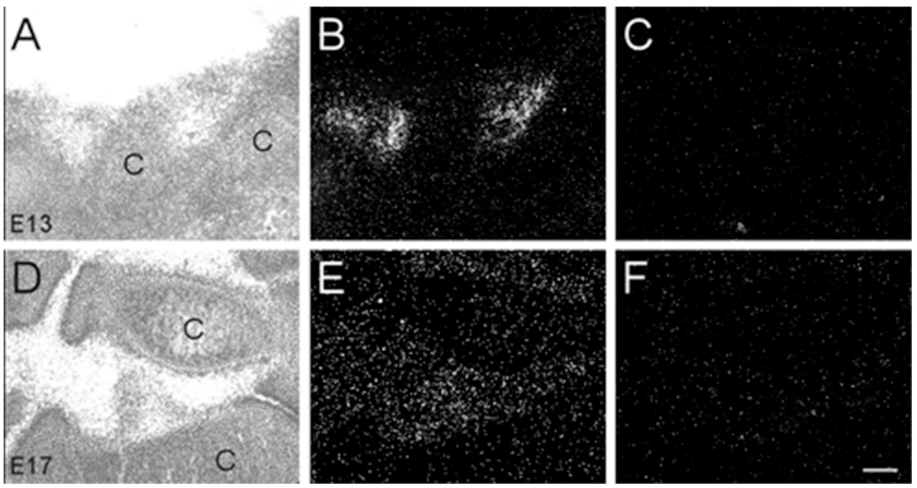

FIGURE 9 | Bright- and dark-field photomicrographs showing α7 nAChR mRNA expression in muscle tissue at E13 and E17. **(A,B)** High expression of α7 mRNA is observed in the inter-digit regions of the limb buds at E13. **(D,E)** Lower expression of mRNA is observed in these regions at E17. **(C,F)** Adjacent sections showing background labeling with the sense riboprobe in the limb bud region. C, cartilage. Space bar = 100 μm.

expression of α7 nAChRs based on antibody staining or Western blotting, are not discussed unless antibody specificity was verified in α7 knockout mice. Therefore, in this study, we focused our analysis on α7 subunit mRNA expression, and are conscious of the fact that while α7 mRNA expression was observed within the areas described herein, this expression may not translate into subunit protein expression and formation of functional α7 nAChRs. However, studies in the chick (Yu and Role, 1998; Shoop et al., 1999; McNerney et al., 2000), rodent (Ospina et al., 1998; Adams et al., 2002; Tribollet et al., 2004) and human (Falk et al., 2002, 2003) have demonstrated expression of α7 nAChR binding sites in the CNS and PNS during embryonic development. Nevertheless, the existence of functional α7 nAChRs in areas of low α7 mRNA expression, and in particular, in non-neuronal tissue, is still unknown, and this issue was not addressed in the current study.

Developmental Expression in Neuronal Tissue

Central Nervous System and Spinal Cord

As early as E13, α7 mRNA expression was strong in the telencephalon, in particular, within the cortical and hippocampal anlage. This is in agreement with a previous study reporting that α-BTX binding can first be detected in murine hippocampus at E13 (Adams, 2003). Furthermore, a similar temporal and spatial expression pattern has been described in rat hippocampus (Adams et al., 2002). Thus, the results from this and other studies suggest that α7 mRNA is translated into α7 nAChRs at an early age, during embryonic cortical and hippocampal development, but it is yet unclear if α7 nAChRs are functional in these immature cortical structures. However, α7 nAChRs have been implicated in hippocampal excitatory synapse formation, suggesting a functional role for α7 nAChRs in the developing hippocampus (Lozada et al., 2012), and there is evidence that α7 nAChRs regulate GABAA receptor function and the developmental GABAergic switch from excitation to inhibition in ganglionic and hippocampal neurons (Liu et al., 2007).

In the spinal cord, another area of robust embryonic α7 nAChR expression, we found mRNA as early as E13, the youngest time-point examined. A previous study had detected α-BTX binding sites at E16 within rat spinal cord suggesting the presence of α7 nAChRs (Tribollet et al., 2004). Furthermore, α7 mRNA expression has been detected in human spinal cord derived from 4 to 12-week-old embryos (Hellström-Lindahl et al., 1998). Moreover, there is experimental evidence that spinal α7 nAChRs are functional and facilitate excitatory neuronal transmission in rat neonates (Genzen and McGehee, 2003; Cordero-Erausquin et al., 2004). Thus, α7 nAChRs are expressed early in the embryonic rodent and human spinal cord and may be involved in the refinement of spinal cord circuits.

Peripheral Nervous System

The PNS serves as an essential relay between the brain and spinal cord, and the rest of the body. Acetylcholine is the major neurotransmitter in the PNS activating muscarinic and nicotinic AChRs in different circuits. In the PNS, the main nAChR subtype is composed of α3β4 subunits, and lack of this heteromeric nAChR results in early postnatal death due to dysregulation of vital body function (Xu et al., 1999; Wang et al., 2003). In contrast, the role of α7 nAChRs in the PNS is not well defined. In this study, we detected α7 mRNA expression in dorsal root ganglia, sympathetic and parasympathetic ganglia, and in the enteric plexus starting at E13, with intensity of expression greatly increasing thereafter. Neonatal expression of α7 nAChR transcripts has also been reported in mouse superior cervical ganglion (Putz et al., 2008). Autoradiographic analysis has shown I^{125}-α-BTX binding to dorsal root ganglia, superior cervical ganglion and sphenopalatine ganglion at E16 (Tribollet et al., 2004). Together these data suggest the presence

of α7 nAChRs in the PNS during embryonic development. Functional α7 nAChRs have been described in dorsal root ganglia (Genzen et al., 2001; Smith et al., 2013) and different ganglionic preparations (Cuevas and Berg, 1998; Yu and Role, 1998; Cuevas et al., 2000; Li et al., 2009). In the embryonic avian ciliary ganglion, neuronal responses to α7 nAChR activation result in changes of intracellular calcium, which has been suggested to play a role in cell survival within the developing autonomic nervous system (Hruska and Nishi, 2007) and may help in synchronizing transmission in the developing ganglion (Chang and Berg, 1999). Furthermore, results from embryonic chick sympathetic neurons suggest the possibility that α7 participates in forming functional heteromeric nAChRs (Yu and Role, 1998). Heteromeric α7β2 nAChRs have since been detected in the brain but may also exist in the PNS (Wu et al., 2016). Altogether, there is strong expression of α7 mRNA and binding site, and ample evidence for α7 nAChR mediated responses in the PNS. However, the functional roles of α7 nACHRs in the PNS during development and in adults are still not clearly defined.

Expression in the Enteric Nervous System

Neuronal nAChRs are essential for fast excitatory neurotransmission in the ENS, and the predominant nAChR subtype mediating the synaptic transmission in the myenteric plexus is the α3β4(α5) heteromeric nAChR ion channel (Galligan and North, 2004). Functional responses mediated by heteromeric nAChRs can be detected in the embryonic ENS at E12.5, and greatly increase in intensity with age (Foong et al., 2015). In contrast, the contributions of α7 nAChRs to ENS functions remains ill defined, although, a potential role for α7 nAChRs as modulator of transmitter release has been proposed (Obaid et al., 2005). In the current study, transcripts for α7 nAChR subunits were detected in the embryonic mouse gut starting at E13 and increasing in intensity shortly thereafter. Similarly, in rat myenteric plexus, expression of α7 nAChR subunit mRNA has been detected in neonates (Garza et al., 2009). However, further studies are needed to address the functional role of α7 nAChRs in the mature and developing ENS.

Developmental Expression in Non-neuronal Tissue

In mammals, neuroendocrine chromaffin cells are located in the medulla of the adrenal glands, which is innervated by the sympathetic splanchnic nerve. Release of acetylcholine triggers the secretion of epinephrine and norepinephrine from the adrenal gland via activation of heteromeric α3β4* nAChRs (Yokotani et al., 2002). Although, α7 nAChRs have been detected in the adrenal medulla, these receptors may not be involved in catecholamine release but exert other functions (Mousavi et al., 2001; Di Angelantonio et al., 2003; Sala et al., 2008; Criado, 2018). In the present study, we detected α7 transcripts in the embryonic adrenal medulla as early as E13, increasing in intensity thereafter. Our results are in agreement with another study using green fluorescent protein (GFP)-tagged α7 subunit expression demonstrating that GFP-immuno-reactivity can be detected in embryonic precursor cells of the adrenal gland as early as E12.5, and in chromaffin cells co-expressed with tyrosine hydroxylase by E18.5 (Gahring et al., 2014). Yet, the role of α7 nAChR in the embryonic adrenal gland is not well understood. However, a functional role for α7 nAChRs during prenatal development can be inferred from a chronic gestational nicotine exposure study where alterations in oxygen sensitivity of adrenal chromaffin cells depended on α7 nAChRs (Nurse et al., 2009). There is also evidence that perinatal nicotine exposure alters KATP channel function in chromaffin cells of the medulla through α7 nAChRs (Buttigieg et al., 2009). Thus, further studies are needed to verify the presence of functional α7 nAChRs in the developing and mature adrenal gland.

The neuroendocrine chromaffin cells (or pheochromocytes) of the adrenal medulla are derived from the neural crest and are related to neurons in the peripheral and enteric nervous system. Neural crest cells are also the precursor for a diverse group of non-neuronal cells. For example, cranial neural crest cells form the craniofacial mesenchyme which differentiates not only into cranial ganglia but also into craniofacial cartilage and bone (Selleck et al., 1993). Neural crest cells contribute to thymus, bones of the middle ear and jaw, and odontoblasts of the tooth primordia. Other neural crest cells are located in the genital glands, the epicardium, and in and around the kidneys. Interestingly, in the mouse embryo, low levels of α7 mRNA expression were detected in cells located within several of these tissues, including tongue, tooth bud, kidney cortex, aorta, prostate and muscle tissue, which are all related to the neural crest. In support of our findings, other studies have also reported expression of α7 during tooth development (Rogers and Gahring, 2012), in fetal muscle tissue (Fischer et al., 1999), and in a subset of circumvallate taste bud cells in rat tongue tissue (Qian et al., 2018). However, it is mostly unclear whether α7 nAChR mRNA is translated into subunit protein and subsequently into functional receptors. It is possible that α7 mRNA expression is only transient in many non-neuronal cell types, as seen in muscle tissue, and that these low levels of mRNA do not actually translate into functional receptors. However, in support of functional receptors despite low level of mRNA expression, there is evidence that α7 nAChRs contribute to proper tooth development since knockout of α7 nAChRs results in altered adult mandibular incisors morphology (Rogers and Gahring, 2012).

Lack of α7 Transcript Detection

In contrast to α7 mRNA hybridization signal found in kidney, transcripts for α7 where not detected in other organs such as heart (except for the expression in ganglia), liver, lung, spleen and thymus. Our findings are in general agreement with a recent study compiling tissue-specific expression patterns of α7 nAChR subunit in mouse tissues. Based on the Mouse ENCODE transcriptome data set, expression of α7 nAChR mRNA in heart, liver, spleen and thymus is extremely limited, with low level of expression detected in adult kidney, lung, and testis in mice (Yue et al., 2014). Similarly, low level of α7 mRNA expression was

detected in human peripheral organs, although, more widespread α7 protein expression was reported[1].

Our data show a lack of α7 mRNA expression in thymus, liver, spleen, and lung, with some expression found in the heart that could be derived from intracardiac ganglia, and are in contrast with others reporting expression of α7 nAChR mRNA in heart (Dvorakova et al., 2005), lung (Sekhon et al., 1999), and developing mouse thymus (Kuo et al., 2002). The reasons for these discrepancies are not immediately clear, but may involve different detection approaches. Several studies used RT-PCR analysis (Kuo et al., 2002; Dvorakova et al., 2005). It cannot be ruled out that mRNA derived from neurons in ganglia embedded in organ tissues, or blood cells like macrophages, contributed to amplification of α7 mRNA transcripts, or that alternative splice variants are expressed which were not detected with our 279 bp probe (Severance et al., 2004).

We expected to detect α7 nAChR mRNA expression in lung, because there is evidence for functional α7 nAChRs in lung bronchial epithelial cells (Wang et al., 2001; Fu et al., 2003, 2009), and prenatal nicotine exposure affects lung function through α7 nicotinic receptors (Wongtrakool et al., 2012). A recent study used a reporter mouse line which indirectly detected expression of α7 nAChR subunits in mouse lung tissue (Gahring et al., 2017). However, we did not detect hybridization signal in lung tissue, which may reflect very low levels of expression in fetal and neonatal lung.

Also puzzling was the lack of expression in the thymus and spleen, organs that are related to the immune system. The α7 nAChR plays a critical role in the cholinergic anti-inflammatory pathway (Wang et al., 2003), and α7 expression has been found in immune cells including lymphocytes and macrophages (Skok et al., 2007; Fujii et al., 2017). A recent study demonstrated expression in macrophages from α7 wildtype but not knockout mice (Garg and Loring, 2019). RT-PCR technology is a highly sensitive approach that detects even minute numbers of transcripts that may go undetected with the isotopic *in situ* hybridization approach. An alternative explanation could be the age of the animals. Adult mice may exhibit higher levels of α7 nAChRs expression in immune system related tissues than fetal or neonatal tissues. However, expression of α7 nAChR mRNA in spleen and thymus is also very limited in adult mice (Yue et al., 2014). It is also possible that the differentiated state of immune cells isolated from blood affects expression of α7 mRNA, or that different splice variants of α7 transcripts are expressed in circulating immune cells. However, this conundrum still needs to be addressed, especially with the increased focus on of α7 role in cholinergic anti-inflammatory pathway.

CONCLUSION

The current study focused on α7 nAChR mRNA expression in embryonic and neonatal tissues. The strongest expression of α7 mRNA was detected in the PNS, including dorsal root ganglia, parasympathetic and sympathetic ganglia, followed by strong expression in brain and spinal cord. In these structures, expression started at E13 and increased in intensity thereafter. This neuronal expression pattern generally corresponds to the distribution of alpha-BTX binding to α7 homomeric nAChRs, as demonstrated by other studies, suggesting the presence of α7 receptors, and a functional role in the PNS, brain and spinal cord during embryonic development. In addition, several reports describe physiologically active α7 nAChRs in embryonic chick ganglion neurons, (Yu and Role, 1998; Shoop et al., 1999; McNerney et al., 2000). Furthermore, there is evidence that α7 nAChRs regulate GABAA receptor function and the developmental GABAergic switch from excitation to inhibition in ganglionic and hippocampal neurons (Liu et al., 2007; Lozada et al., 2012). Thus, nAChRs are expressed early during the development of the peripheral and central nervous systems and may guide important neurodevelopmental processes. Little is known about α7 nAChRs in non-neuronal tissue during development. Although α7 mRNA expression was detected, it remains to be seen if functional receptors are present in perinatal animals. There is a growing number of studies describe anti-inflammatory effects mediated by α7 nAChRs, however, expression of α7 mRNA in immune system-related tissues during embryonic development was below the sensitivity of the *in situ* hybridization approach used in this study. Future functional studies need to determine their role in the developing immune system. Altogether, the presence of α7 nAChR mRNA within the regions described herein may likewise indicate the concomitant existence of protein, albeit at lower abundance outside of the nervous system.

DATA AVAILABILITY

All datasets generated for this study are included in the manuscript and/or the supplementary files.

ETHICS STATEMENT

This study was approved by the Institutional Animal Care and Use Committee at the University of California, Irvine, CA, United States.

AUTHOR CONTRIBUTIONS

RB analyzed the results, prepared the figures, drafted the manuscript. UW-S analyzed the results and wrote the manuscript. YC conducted the experiments. FL planned and oversaw the project.

FUNDING

This study was supported by the NIH grant DA 040440 (FL).

[1]https://www.proteinatlas.org/ENSG00000175344-CHRN$\upalpha$7/tissue

REFERENCES

Adams, C. E. (2003). Comparison of alphα7 nicotinic acetylcholine receptor development in the hippocampal formation of C3H and DBA/2 mice. *Brain Res. Dev. Brain Res.* 143, 137–149. doi: 10.1016/s0165-3806(03)00106-8

Adams, C. E., Broide, R. S., Chen, Y., Winzer-Serhan, U. H., Henderson, T. A., Leslie, F. M., et al. (2002). Development of the alphα7 nicotinic cholinergic receptor in rat hippocampal formation. *Brain Res. Dev. Brain Res.* 139, 175–187. doi: 10.1016/s0165-3806(02)00547-3

Baddick, C. G., and Marks, M. J. (2011). An autoradiographic survey of mouse brain nicotinic acetylcholine receptors defined by null mutants. *Biochem. Pharmacol.* 82, 828–841. doi: 10.1016/j.bcp.2011.04.019

Bina, K. G., Guzman, P., Broide, R. S., Leslie, F. M., Smith, M. A., and O'Dowd, D. K. (1995). Localization of alpha 7 nicotinic receptor subunit mRNA and alpha-bungarotoxin binding sites in developing mouse somatosensory thalamocortical system. *J. Comp. Neurol.* 363, 321–332. doi: 10.1002/cne.903630212

Broide, R. S., and Leslie, F. M. (1999). The α7 nicotinic acetylcholine receptor in neuronal plasticity. *Mol. Neurobiol.* 20, 1–16. doi: 10.1007/bf02741361

Broide, R. S., O'Connor, L. T., Smith, M. A., Smith, J. A., and Leslie, F. M. (1995). Developmental expression of alpha 7 neuronal nicotinic receptor messenger RNA in rat sensory cortex and thalamus. *Neuroscience* 67, 83–94. doi: 10.1016/0306-4522(94)00623-d

Broide, R. S., Orr-Urtreger, A., and Patrick, J. W. (2001). Normal apoptosis levels in mice expressing one alphα7 nicotinic receptor null and one L250T mutant allele. *Neuroreport* 12, 1643–1648. doi: 10.1097/00001756-200106130-00026

Buttigieg, J., Brown, S., Holloway, A. C., and Nurse, C. A. (2009). Chronic nicotine blunts hypoxic sensitivity in perinatal rat adrenal chromaffin cells via upregulation of KATP channels: role of alphα7 nicotinic acetylcholine receptor and hypoxia-inducible factor-2alpha. *J. Neurosci.* 29, 7137–7147. doi: 10.1523/JNEUROSCI.0544-09.2009

Chang, K., and Berg, D. K. (1999). Dependence of circuit function on nicotinic acetylcholine receptors containing α7 subunits. *J. Neurosci.* 19, 3701–3710. doi: 10.1523/jneurosci.19-10-03701.1999

Changeux, J. P. (2012). The nicotinic acetylcholine receptor: the founding father of the pentameric ligand-gated ion channel superfamily. *J. Biol. Chem.* 287, 40207–40215. doi: 10.1074/jbc.R112.407668

Cordero-Erausquin, M., Pons, S., Faure, P., and Changeux, J. P. (2004). Nicotine differentially activates inhibitory and excitatory neurons in the dorsal spinal cord. *Pain* 109, 308–318. doi: 10.1016/s0304-3959(04)00052-1

Criado, M. (2018). Acetylcholine nicotinic receptor subtypes in chromaffin cells. *Pflugers Arch.* 470, 13–20. doi: 10.1007/s00424-017-2050-7

Cuevas, J., and Berg, D. K. (1998). Mammalian nicotinic receptors with α7 subunits that slowly desensitize and rapidly recover from α-bungarotoxin blockade. *J. Neurosci.* 18, 10335–10344. doi: 10.1523/jneurosci.18-24-10335.1998

Cuevas, J., Roth, A. L., and Berg, D. K. (2000). Two distinct classes of functional 7-containing nicotinic receptor on rat superior cervical ganglion neurons. *J. Physiol.* 525(Pt 3), 735–746. doi: 10.1111/j.1469-7793.2000.t01-1-00735.x

Di Angelantonio, S., Matteoni, C., Fabbretti, E., and Nistri, A. (2003). Molecular biology and electrophysiology of neuronal nicotinic receptors of rat chromaffin cells. *Eur. J. Neurosci.* 17, 2313–2322. doi: 10.1046/j.1460-9568.2003.02669.x

Dvorakova, M., Lips, K. S., Brüggmann, D., Slavikova, J., Kuncova, J., and Kummer, W. (2005). Developmental changes in the expression of nicotinic acetylcholine receptor alpha-subunits in the rat heart. *Cell Tissue Res.* 319, 201–209. doi: 10.1007/s00441-004-1008-1

Erkman, L., Matter, J., Matter-Sadzinski, L., and Ballivet, M. (2000). Nicotinic acetylcholine receptor gene expression in developing chick autonomic ganglia. *Eur. J. Pharmacol.* 393, 97–104. doi: 10.1016/s0014-2999(00)00029-7

Falk, L., Nordberg, A., Seiger, A., Kjaeldgaard, A., and Hellström-Lindahl, E. (2002). The alphα7 nicotinic receptors in human fetal brain and spinal cord. *J. Neurochem.* 80, 457–465. doi: 10.1046/j.0022-3042.2001.00714.x

Falk, L., Nordberg, A., Seiger, A., Kjaeldgaard, A., and Hellström-Lindahl, E. (2003). Higher expression of alphα7 nicotinic acetylcholine receptors in human fetal compared to adult brain. *Brain Res. Dev. Brain Res.* 142, 151–160. doi: 10.1016/s0165-3806(03)00063-4

Fischer, U., Reinhardt, S., Albuquerque, E. X., and Maelicke, A. (1999). Expression of functional alphα7 nicotinic acetylcholine receptor during mammalian muscle development and denervation. *Eur. J. Neurosci.* 11, 2856–2864. doi: 10.1046/j.1460-9568.1999.00703.x

Foong, J. P., Hirst, C. S., Hao, M. M., McKeown, S. J., Boesmans, W., Young, H. M., et al. (2015). Changes in nicotinic neurotransmission during enteric nervous system development. *J. Neurosci.* 35, 7106–7115. doi: 10.1523/JNEUROSCI.4175-14.2015

Fu, X. W., Lindstrom, J., and Spindel, E. R. (2009). Nicotine activates and up-regulates nicotinic acetylcholine receptors in bronchial epithelial cells. *Am. J. Respir. Cell Mol. Biol.* 41, 93–99. doi: 10.1165/rcmb.2008-0352OC

Fu, X. W., Nurse, C. A., Farragher, S. M., and Cutz, E. (2003). Expression of functional nicotinic acetylcholine receptors in neuroepithelial bodies of neonatal hamster lung. *Am. J. Physiol. Lung Cell Mol. Physiol.* 285, L1203–L1212.

Fujii, T., Mashimo, M., Moriwaki, Y., Misawa, H., Ono, S., Horiguchi, K., et al. (2017). Expression and function of the cholinergic system in immune cells. *Front. Immunol.* 8:1085. doi: 10.3389/fimmu.2017.01085

Gahring, L. C., Myers, E., Palumbos, S., and Rogers, S. W. (2014). Nicotinic receptor Alphα7 expression during mouse adrenal gland development. *PLoS One* 9:e103861. doi: 10.1371/journal.pone.0103861

Gahring, L. C., Myers, E. J., Dunn, D. M., Weiss, R. B., and Rogers, S. W. (2017). Nicotinic alpha 7 receptor expression and modulation of the lung epithelial response to lipopolysaccharide. *PLoS One* 12:e0175367. doi: 10.1371/journal.pone.0175367

Galligan, J. J., and North, R. A. (2004). Pharmacology and function of nicotinic acetylcholine and P2X receptors in the enteric nervous system. *Neurogastroenterol. Motil.* 16(Suppl. 1), 64–70. doi: 10.1111/j.1743-3150.2004.00478.x

Garg, B. K., and Loring, R. H. (2019). GTS-21 has cell-specific anti-inflammatory effects independent of α7 nicotinic acetylcholine receptors. *PLoS One* 14:e0214942. doi: 10.1371/journal.pone.0214942

Garza, A., Huang, L. Z., Son, J. H., and Winzer-Serhan, U. H. (2009). Expression of nicotinic acetylcholine receptors and subunit messenger RNAs in the enteric nervous system of the neonatal rat. *Neuroscience* 158, 1521–1529. doi: 10.1016/j.neuroscience.2008.11.027

Genzen, J. R., and McGehee, D. S. (2003). Short- and long-term enhancement of excitatory transmission in the spinal cord dorsal horn by nicotinic acetylcholine receptors. *Proc. Natl. Acad. Sci. U.S.A.* 100, 6807–6812. doi: 10.1073/pnas.1131709100

Genzen, J. R., Van Cleve, W., and McGehee, D. S. (2001). Dorsal root ganglion neurons express multiple nicotinic acetylcholine receptor subtypes. *J. Neurophysiol.* 86, 1773–1782. doi: 10.1152/jn.2001.86.4.1773

Hellström-Lindahl, E., Gorbounova, O., Seiger, A., Mousavi, M., and Nordberg, A. (1998). Regional distribution of nicotinic receptors during prenatal development of human brain and spinal cord. *Brain Res. Dev. Brain Res.* 108, 147–160. doi: 10.1016/s0165-3806(98)00046-7

Hruska, M., and Nishi, R. (2007). Cell-autonomous inhibition of alpha 7-containing nicotinic acetylcholine receptors prevents death of parasympathetic neurons during development. *J. Neurosci.* 27, 11501–11509. doi: 10.1523/jneurosci.3057-07.2007

Jacobowitz, D. M., and Abbott, L. C. (1998). *Chemoarchitectonic Atlas of the Developing Mouse Brain*. Boca Raton, FL: CRC Press.

Kabbani, N., and Nichols, R. A. (2018). Beyond the channel: metabotropic signaling by nicotinic receptors. *Trends Pharmacol. Sci.* 39, 354–366. doi: 10.1016/j.tips.2018.01.002

Kaufman, M. H. (1995). *The Atlas of Mouse Development. Revised edition*. Cambridge, MA: Academic Press.

Kaufman, M. H., and Bard, J. B. L. (1999). *The Anatomical Basis of Mouse Development*. San Diego, CA: Elsevier Science Publishing Co Inc.

Keiger, C. J., Prevette, D., Conroy, W. G., and Oppenheim, R. W. (2003). Developmental expression of nicotinic receptors in the chick and human spinal cord. *J. Comp. Neurol.* 455, 86–99. doi: 10.1002/cne.10468

Kuo, Y., Lucero, L., Michaels, J., DeLuca, D., and Lukas, R. J. (2002). Differential expression of nicotinic acetylcholine receptor subunits in fetal and neonatal mouse thymus. *J. Neuroimmunol.* 130, 140–154. doi: 10.1016/s0165-5728(02)00220-5

Li, Y. F., LaCroix, C., and Freeling, J. (2009). Specific subtypes of nicotinic cholinergic receptors involved in sympathetic and parasympathetic

cardiovascular responses. *Neurosci. Lett.* 462, 20–23. doi: 10.1016/j.neulet.2009.06.081

Liu, Z., Zhang, J., and Berg, D. K. (2007). Role of endogenous nicotinic signaling in guiding neuronal development. *Biochem. Pharmacol.* 74, 1112–1119. doi: 10.1016/j.bcp.2007.05.022

Lozada, A. F., Wang, X., Gounko, N. V., Massey, K. A., Duan, J., Liu, Z., et al. (2012). Glutamatergic synapse formation is promoted by α7-containing nicotinic acetylcholine receptors. *J. Neurosci.* 32, 7651–7661. doi: 10.1523/jneurosci.6246-11.2012

McNerney, M. E., Pardi, D., Pugh, P. C., Nai, Q., and Margiotta, J. F. (2000). Expression and channel properties of alpha-bungarotoxin-sensitive acetylcholine receptors on chick ciliary and choroid neurons. *J. Neurophysiol.* 84, 1314–1329. doi: 10.1152/jn.2000.84.3.1314

Messi, M. L., Renganathan, M., Grigorenko, E., and Delbono, O. (1997). Activation of alphα7 nicotinic acetylcholine receptor promotes survival of spinal cord motoneurons. *FEBS Lett.* 411, 32–38. doi: 10.1016/s0014-5793(97)00600-5

Moser, N., Mechawar, N., Jones, I., Gochberg-Sarver, A., Orr-Urtreger, A., Plomann, M., et al. (2007). Evaluating the suitability of nicotinic acetylcholine receptor antibodies for standard immunodetection procedures. *J. Neurochem.* 102, 479–492. doi: 10.1111/j.1471-4159.2007.04498.x

Mousavi, M., Hellström-Lindahl, E., Guan, Z. Z., Bednar, I., and Nordberg, A. (2001). Expression of nicotinic acetylcholine receptors in human and rat adrenal medulla. *Life Sci.* 70, 577–590. doi: 10.1016/s0024-3205(01)01427-8

Nurse, C. A., Buttigieg, J., Brown, S., and Holloway, A. C. (2009). Regulation of oxygen sensitivity in adrenal chromaffin cells. *Ann. N. Y. Acad. Sci.* 1177, 132–139. doi: 10.1111/j.1749-6632.2009.05031.x

Obaid, A. L., Nelson, M. E., Lindstrom, J., and Salzberg, B. M. (2005). Optical studies of nicotinic acetylcholine receptor subtypes in the guinea-pig enteric nervous system. *J. Exp. Biol.* 208(Pt 15), 2981–3001. doi: 10.1242/jeb.01732

Orr-Urtreger, A., Broide, R. S., Kasten, M. R., Dang, H., Dani, J. A., Beaudet, A. L., et al. (2000). Mice homozygous for the L250T mutation in the alphα7 nicotinic acetylcholine receptor show increased neuronal apoptosis and die within 1 day of birth. *J. Neurochem.* 74, 2154–2166. doi: 10.1046/j.1471-4159.2000.0742154.x

Orr-Urtreger, A., Seldin, M. F., Baldini, A., and Beaudet, A. L. (1995). Cloning and mapping of the mouse alpha 7-neuronal nicotinic acetylcholine receptor. *Genomics* 26, 399–402. doi: 10.1016/0888-7543(95)80228-e

Ospina, J. A., Broide, R. S., Acevedo, D., Robertson, R. T., and Leslie, F. M. (1998). Calcium regulation of agonist binding to alphα7-type nicotinic acetylcholine receptors in adult and fetal rat hippocampus. *J. Neurochem.* 70, 1061–1068. doi: 10.1046/j.1471-4159.1998.70031061.x

Papke, R. L. (2014). Merging old and new perspectives on nicotinic acetylcholine receptors. *Biochem. Pharmacol.* 89, 1–11. doi: 10.1016/j.bcp.2014.01.029

Papouin, T., Dunphy, J. M., Tolman, M., Dineley, K. T., and Haydon, P. G. (2017). Septal cholinergic neuromodulation tunes the astrocyte-dependent gating of hippocampal NMDA receptors to wakefulness. *Neuron* 94, 840–854.e7. doi: 10.1016/j.neuron.2017.04.021

Paxinos, G., Koutcherov, Y., Halliday, G. M., Watson, C., and Wang, H. (2007). *Atlas of the Developing Mouse Brain: E17.5, P0 and P6*. Amsterdam: Elsevier.

Petrov, K. A., Girard, E., Nikitashina, A. D., Colasante, C., Bernard, V., Nurullin, L., et al. (2014). Schwann cells sense and control acetylcholine spillover at the neuromuscular junction by α7 nicotinic receptors and butyrylcholinesterase. *J. Neurosci.* 34, 11870–11883. doi: 10.1523/jneurosci.0329-14.2014

Putz, G., Kristufek, D., Orr-Urtreger, A., Changeux, J. P., Huck, S., and Scholze, P. (2008). Nicotinic acetylcholine receptor-subunit mRNAs in the mouse superior cervical ganglion are regulated by development but not by deletion of distinct subunit genes. *J. Neurosci. Res.* 86, 972–981. doi: 10.1002/jnr.21559

Qian, J., Mummalaneni, S., Grider, J. R., Damaj, M. I., and Lyall, V. (2018). Nicotinic acetylcholine receptors (nAChRs) are expressed in Trpm5 positive taste receptor cells (TRCs). *PLoS One* 13:e0190465. doi: 10.1371/journal.pone.0190465

Rogers, S. W., and Gahring, L. C. (2012). Nicotinic receptor Alphα7 expression during tooth morphogenesis reveals functional pleiotropy. *PLoS One* 7:e36467. doi: 10.1371/journal.pone.0036467

Sala, F., Nistri, A., and Criado, M. (2008). Nicotinic acetylcholine receptors of adrenal chromaffin cells. *Acta Physiol.* 192, 203–212. doi: 10.1111/j.1748-1716.2007.01804.x

Sekhon, H. S., Jia, Y., Raab, R., Kuryatov, A., Pankow, J. F., Whitsett, J. A., et al. (1999). Prenatal nicotine increases pulmonary alphα7 nicotinic receptor expression and alters fetal lung development in monkeys. *J. Clin. Invest.* 103, 637–647. doi: 10.1172/jci5232

Selleck, M. A., Scherson, T. Y., and Bronner-Fraser, M. (1993). Origins of neural crest cell diversity. *Dev. Biol.* 159, 1–11. doi: 10.1006/dbio.1993.1217

Severance, E. G., Zhang, H., Cruz, Y., Pakhlevaniants, S., Hadley, S. H., Amin, J., et al. (2004). The alphα7 nicotinic acetylcholine receptor subunit exists in two isoforms that contribute to functional ligand-gated ion channels. *Mol. Pharmacol.* 66, 420–429. doi: 10.1124/mol.104.000059

Sharma, G., and Vijayaraghavan, S. (2002). Nicotinic receptor signaling in nonexcitable cells. *J. Neurobiol.* 53, 524–534. doi: 10.1002/neu.10114

Shoop, R. D., Martone, M. E., Yamada, N., Ellisman, M. H., and Berg, D. K. (1999). Neuronal acetylcholine receptors with alphα7 subunits are concentrated on somatic spines for synaptic signaling in embryonic chick ciliary ganglia. *J. Neurosci.* 19, 692–704. doi: 10.1523/jneurosci.19-02-00692.1999

Shytle, R. D., Mori, T., Townsend, K., Vendrame, M., Sun, N., Zeng, J., et al. (2004). Cholinergic modulation of microglial activation by alpha 7 nicotinic receptors. *J. Neurochem.* 89, 337–343. doi: 10.1046/j.1471-4159.2004.02347.x

Skok, M. V., Grailhe, R., Agenes, F., and Changeux, J. P. (2007). The role of nicotinic receptors in B-lymphocyte development and activation. *Life Sci.* 80, 2334–2336. doi: 10.1016/j.lfs.2007.02.005

Smith, N. J., Hone, A. J., Memon, T., Bossi, S., Smith, T. E., McIntosh, J. M., et al. (2013). Comparative functional expression of nAChR subtypes in rodent DRG neurons. *Front. Cell Neurosci.* 7:225. doi: 10.3389/fncel.2013.00225

Son, J. H., and Winzer-Serhan, U. H. (2006). Postnatal expression of alpha2 nicotinic acetylcholine receptor subunit mRNA in developing cortex and hippocampus. *J. Chem. Neuroanat.* 32, 179–190. doi: 10.1016/j.jchemneu.2006.09.001

Suzuki, T., Hide, I., Matsubara, A., Hama, C., Harada, K., Miyano, K., et al. (2006). Microglial alphα7 nicotinic acetylcholine receptors drive a phospholipase C/IP3 pathway and modulate the cell activation toward a neuroprotective role. *J. Neurosci. Res.* 83, 1461–1470. doi: 10.1002/jnr.20850

Tribollet, E., Bertrand, D., Marguerat, A., and Raggenbass, M. (2004). Comparative distribution of nicotinic receptor subtypes during development, adulthood and aging: an autoradiographic study in the rat brain. *Neuroscience* 124, 405–420. doi: 10.1016/j.neuroscience.2003.09.028

Wang, H., Yu, M., Ochani, M., Amella, C. A., Tanovic, M., Susarla, S., et al. (2003). Nicotinic acetylcholine receptor alphα7 subunit is an essential regulator of inflammation. *Nature* 421, 384–388.

Wang, N., Orr-Urtreger, A., Chapman, J., Rabinowitz, R., Nachman, R., and Korczyn, A. D. (2002). Autonomic function in mice lacking alpha5 neuronal nicotinic acetylcholine receptor subunit. *J. Physiol.* 542(Pt 2), 347–354. doi: 10.1113/jphysiol.2001.013456

Wang, Y., Pereira, E. F., Maus, A. D., Ostlie, N. S., Navaneetham, D., Lei, S., et al. (2001). Human bronchial epithelial and endothelial cells express alphα7 nicotinic acetylcholine receptors. *Mol. Pharmacol.* 60, 1201–1209. doi: 10.1124/mol.60.6.1201

Winzer-Serhan, U. H., Broide, R. S., Chen, Y., and Leslie, F. M. (1999). Highly sensitive radioactive in situ hybridization using full length hydrolyzed riboprobes to detect alpha 2 adrenoceptor subtype mRNAs in adult and developing rat brain. *Brain Res. Brain Res. Protoc.* 3, 229–241. doi: 10.1016/s1385-299x(98)00043-9

Winzer-Serhan, U. H., and Leslie, F. M. (1997). Codistribution of nicotinic acetylcholine receptor subunit alpha3 and beta4 mRNAs during rat brain development. *J. Comp. Neurol.* 386, 540–554. doi: 10.1002/(sici)1096-9861(19971006)386:4<540::aid-cne2>3.0.co;2-2

Winzer-Serhan, U. H., and Leslie, F. M. (2005). Expression of alpha5 nicotinic acetylcholine receptor subunit mRNA during hippocampal and cortical development. *J. Comp. Neurol.* 481, 19–30. doi: 10.1002/cne.20357

Wongtrakool, C., Wang, N., Hyde, D. M., Roman, J., and Spindel, E. R. (2012). Prenatal nicotine exposure alters lung function and airway geometry through α7 nicotinic receptors. *Am. J. Respir. Cell Mol. Biol.* 46, 695–702. doi: 10.1165/rcmb.2011-0028OC

Wu, J., Liu, Q., Tang, P., Mikkelsen, J. D., Shen, J., Whiteaker, P., et al. (2016). Heteromeric α7β2 nicotinic acetylcholine receptors in the brain. *Trends Pharmacol. Sci.* 37, 562–574. doi: 10.1016/j.tips.2016.03.005

Xu, W., Orr-Urtreger, A., Nigro, F., Gelber, S., Sutcliffe, C. B., Armstrong, D., et al. (1999). Multiorgan autonomic dysfunction in mice lacking the β2 and the β4 subunits of neuronal nicotinic acetylcholine receptors. *J. Neurosci.* 19, 9298–9305. doi: 10.1523/JNEUROSCI.19-21-09298.1999

Yokotani, K., Okada, S., and Nakamura, K. (2002). Characterization of functional nicotinic acetylcholine receptors involved in catecholamine release from the isolated rat adrenal gland. *Eur. J. Pharmacol.* 446, 83–87. doi: 10.1016/s0014-2999(02)01819-8

Yu, C. R., and Role, L. W. (1998). Functional contribution of the alphα7 subunit to multiple subtypes of nicotinic receptors in embryonic chick sympathetic neurones. *J. Physiol.* 509(Pt 3), 651–665. doi: 10.1111/j.1469-7793.1998.651bm.x

Yue, F., Cheng, Y., Breschi, A., Vierstra, J., Wu, W., Ryba, T., et al. (2014). A comparative encyclopedia of DNA elements in the mouse genome. *Nature* 515, 355–364. doi: 10.1038/nature13992

Zoli, M., Le Novère, N., Hill, J. A. Jr., and Changeux, J. P. (1995). Developmental regulation of nicotinic ACh receptor subunit mRNAs in the rat central and peripheral nervous systems. *J. Neurosci.* 15(3 Pt 1), 1912–1939. doi: 10.1523/jneurosci.15-03-01912.1995

Conflict of Interest Statement: RB is employed by the company Allergan plc.

The remaining authors declare that the research was conducted in the absence of any commercial or financial relationships that could be construed as a potential conflict of interest.

frontiers in Neuroanatomy

METHODS
published: 20 August 2019
doi: 10.3389/fnana.2019.00077

Fast 3-D Imaging of Brain Organoids With a New Single-Objective Planar-Illumination Two-Photon Microscope

Irina Rakotoson[1,2,3,4†], Brigitte Delhomme[1,2,3†], Philippe Djian[1,2,3†], Andreas Deeg[5], Maia Brunstein[1,2,3], Christian Seebacher[5], Rainer Uhl[5], Clément Ricard[1,2,3‡] and Martin Oheim[1,2,3‡]*

[1]Centre National de la Recherche Scientifique (CNRS) UMR 8118, Brain Physiology Laboratory, Paris, France, [2]Fédération de Recherche en Neurosciences CNRS FR 3636, Paris, France, [3]Faculté de Sciences Fondamentales et Biomédicales, Université Paris Descartes, PRES Sorbonne Paris Cité, Paris, France, [4]Master Program: MASTER Mention Biologie Cellulaire, Physiologie, Pathologies (BCPP), Spécialité Neurosciences, Université Paris Descartes - Paris 5, Paris, France, [5]TILL id GmbH, Munich, Germany

OPEN ACCESS

Edited by:
Fiorenzo Conti, Marche Polytechnic University, Italy

Reviewed by:
Francesco Pasqualini, Harvard University, United States
Reto P. Fiolka, UT Southwestern Medical Center, United States

***Correspondence:**
Martin Oheim
martin.oheim@parisdescartes.fr

†Co-first authors
‡Co-last authors

Elements of this work has been published in the Master thesis of Rakotoson (2018)

Received: *18 January 2019*
Accepted: *16 July 2019*
Published: *20 August 2019*

Citation:
Rakotoson I, Delhomme B, Djian P, Deeg A, Brunstein M, Seebacher C, Uhl R, Ricard C and Oheim M (2019) Fast 3-D Imaging of Brain Organoids With a New Single-Objective Planar-Illumination Two-Photon Microscope. Front. Neuroanat. 13:77. doi: 10.3389/fnana.2019.00077

Human inducible pluripotent stem cells (hiPSCs) hold a large potential for disease modeling. hiPSC-derived human astrocyte and neuronal cultures permit investigations of neural signaling pathways with subcellular resolution. Combinatorial cultures, and three-dimensional (3-D) embryonic bodies (EBs) enlarge the scope of investigations to multi-cellular phenomena. The highest level of complexity, brain organoids that—in many aspects—recapitulate anatomical and functional features of the developing brain permit the study of developmental and morphological aspects of human disease. An ideal microscope for 3-D tissue imaging at these different scales would combine features from both confocal laser-scanning and light-sheet microscopes: a micrometric optical sectioning capacity and sub-micrometric spatial resolution, a large field of view and high frame rate, and a low degree of invasiveness, i.e., ideally, a better photon efficiency than that of a confocal microscope. In the present work, we describe such an instrument that uses planar two-photon (2P) excitation. Its particularity is that—unlike two- or three-lens light-sheet microscopes—it uses a single, low-magnification, high-numerical aperture objective for the generation and scanning of a virtual light sheet. The microscope builds on a modified Nipkow-Petráň spinning-disk scheme for achieving wide-field excitation. However, unlike the Yokogawa design that uses a tandem disk, our concept combines micro lenses, dichroic mirrors and detection pinholes on a single disk. This new design, advantageous for 2P excitation, circumvents problems arising with the tandem disk from the large wavelength difference between the infrared excitation light and visible fluorescence. 2P fluorescence excited by the light sheet is collected with the same objective and imaged onto a fast sCMOS camera. We demonstrate 3-D imaging of TO-PRO3-stained EBs and of brain organoids, uncleared and after rapid partial transparisation with triethanolamine formamide (RTF) and we compare the performance

of our instrument to that of a confocal laser-scanning microscope (CLSM) having a similar numerical aperture. Our large-field 2P-spinning disk microscope permits one order of magnitude faster imaging, affords less photobleaching and permits better depth penetration than a confocal microscope with similar spatial resolution.

Keywords: two photon, light sheet, brain organoids, hiPSC, stem cell, human disease modeling, spinning disc confocal

INTRODUCTION

The development of pharmacological treatments for neuropsychiatric and neurodegenerative diseases has been hampered by the poor availability of preclinical models that adequately capture the complexity of human disorders (Gonzalez et al., 2017).

Human inducible pluripotent stem cells (hIPSCs) offer a promising platform for disease modeling and drug screening. A comparably new technique is the directed differentiation and reprogramming of patient fibroblasts into neurons, astrocytes, microglia and oligodendro-cytes. Their combinational culture permits the growth of embryonic bodies (EBs) and brain organoids, 3-D cultures that—in many aspects—recapitulate the development of the human brain (Fatehullah et al., 2016; Giandomenico and Lancaster, 2017). Together, hIPSCs, EBs, and brain organoids enable observations and experiments that were previously inconceivable, neither on human subjects nor in animal models (Lancaster et al., 2013; Kelava and Lancaster, 2016). Recent reports of functional, fully vascularized brain organoids have spurred hopes of growing even larger 3-D cell assemblies (Mansour et al., 2018), bringing the hitherto theoretical "*brain in a vat*"[1] within reach of the imaginable.

Elucidation of neural circuit (dys-)function would benefit from the detailed, 3-D visualization of the fine structure of neurons, astrocytes and blood vessels over large fields of view and deep in tissue. Large-scale neuroanatomical imaging has become possible in cleared tissue sections (Wan et al., 2018), brain organoids (Renner et al., 2017) or even entire brains (Hama et al., 2015), but in many cases the resolution is rather at the level of cell bodies that at the synaptic scale. In addition to the difficulties associated with transparisation and tissue shrinking, imaging of large tissue volumes at spatial high-resolution presents considerable challenges: confocal and two-photon (2P) laser scanning microscopies set the "gold-standard" for diffraction-limited fluorescence imaging, but—being in most of their implementations point-scanning, i.e., sequential techniques—the image acquisition is often painstakingly slow. The reconstruction of large volumes at high spatial resolution often requires hours if not days of recording, putting high demands on the mechanical stability of the microscope, photostablity of the used fluorescent dyes, and incurring considerable cost for beam time. Line- and multi-spot scanning schemes overcome these limitations by parallelizing *excitation*, but they trade off resolution against speed and having relatively small fields of view, they require image stitching for larger views.

On the other end, selective-plane illumination microscopes (SPIM; Huisken et al., 2004) or light-sheet microscopes (Keller et al., 2008) decouple fluorescence excitation and collection by using orthogonal illumination and detection optical paths. Light-sheet microscopes have established themselves as efficient workhorses for volume imaging in cleared tissue. For example, a recent study used the 3DISCO/iDISCO cleaning method and conventional 1P light-sheet imaging to visualize and analyze early human development (Belle et al., 2017). In light-sheet microscopies, it is the parallelization of *both excitation* and fluorescence *detection* that allows for rapid 3-D imaging (Santi, 2011; Stelzer, 2015). However, one consequence of the lower-NA illumination and a result of excitation-light scattering in not perfectly transparent samples, is that the axial resolution of light-sheet microscopes remains poor compared to the optical sectioning achieved by spot-scanning microscopes. Improvement has been made with 2P light-sheet excitation (Truong et al., 2011; Mahou et al., 2014), by combining 2P-line excitation and confocal slit detection (Baumgart and Kubitscheck, 2012), by the use of Airy- (Vettenburg et al., 2014) or Bessel-beams for excitation (Fahrbach et al., 2013; Zhao et al., 2014; Müllenbroich et al., 2018), or a combination of these techniques (Andilla et al., 2017; Elisa et al., 2018). However, many of these recent techniques are not yet commercial and they afford considerable cost and complexity compared to standard 1- and 2P-laser scanning microscopes.

Another limitation of light-sheet microscopes results from the orthogonal arrangement of excitation and collection objectives: the need for non-standard procedures for embedding and holding the sample. Variants of light-sheet microscopes in which both illumination and detection objectives are mounted at an oblique angle with respect to the tissue surface and the sample half-space is left free exist (Holekamp et al., 2008; Chen et al., 2014; McGorty et al., 2015), but they have remained comparably marginal, and they are typically limited to short working distances and small fields of view.

An ideal microscope for volume imaging in cleared brain tissue (Reynaud et al., 2015) would combine speed, a sub-μm lateral and μm-axial resolution, a mm-field of view, an excitation depth of a few mm, a certain robustness to imperfect sample clearing and a large free space under the objective to accommodate a variety of different samples.

Here, we present a microscope with both excitation- and detection-parallelization that gets close to this ideal by combining

[1]The "*brain in a vat*" or "*brain in a jar*" is a scenario used in a variety of *Gedanken experiments* intended to draw out certain features of human conceptions of knowledge, reality, truth, mind, consciousness and meaning. It is an updated version of René Descartes' evil demon thought experiment. It has been extensively used by Hilary Putnam (*Reason, Truth and History*, 1981), in an argument inspired from Roald Dahl's short story, «*William and Mary*» (1959).

advantages of 2P laser-scanning and light-sheet techniques. Our On-axis 2-photon virtual light-sheet generation *in vivo* imaging system (OASIS) uses a vast array of micro lenses arranged in four nested spirals on a single spinning disk (SD) to simultaneously scan ∼40 independent excitation spots across the focal plane of a single, long-working distance, low-magnification, high-NA objective (Oheim et al., 2001). Rotation of the disk at 5,000 rpm results in rapid multi-spot scanning and creates a planar excitation in the focal plane. The fluorescence generated in each of the excitation spots is imaged through the same objective onto a pinhole in the center of each micro lens. With the remainder of the lens made opaque to out-of-focus and scattered fluorescence by a dichroic coating sparing only the tiny pinhole, only fluorescence emanating from the focal plane is detected. Each pinhole is imaged onto a large-format scientific Complementary Metal Oxide Semiconductor (sCMOS) camera, allowing near-diffraction limited imaging over a large field of view. This patented design, combining micro lenses and perforated dichroic mirrors on a single-SD, allowed us to retain the in-line, single-objective geometry of a classical microscope without the requirement for orthogonal illumination. As a consequence, our OASIS microscope is more versatile than two- or three-objective designs, and it allows the use of a low-mag, high-NA lens that simultaneously offers high spatial resolution and a large field-of-view. With its compact footprint (43 cm by 12 cm, or $17'' \times 5''$), it can accommodate large samples (cells, slices, explants and even entire animals, *in vivo*) without requiring tedious mounting procedures or relying on special sample holders. The OASIS concept combines the optical sectioning, spatial resolution and field-of-view of a 2P-scanning microscope with the speed of a light-sheet microscope. Due to 2P excitation, out-of-focus fluorescence excitation, out-of-focus photo-bleaching and photodamage are much reduced compared to a classical confocal microscope. We here describe this new microscope and compare it to a confocal laser-scanning microscope (CLSM) for imaging non-cleared and RTF-clarified brain organoids with nuclear staining.

MATERIALS AND METHODS

Ethics Statement

All experimental procedures were performed in accordance with the French legislation and in compliance with the European Community Council Directive of November 24, 1986 (86/609/EEC) for the care and use of laboratory animals. Protocols were approved by the local ethics committee.

Sample Preparation

hiPSC Culture and Formation of Embryonic Bodies

Episomal human induced pluripotent stem cells (hIPSCs, Gibco) were cultivated on mitomycin-treated mouse embryonic fibroblasts using DMEM/F12 medium (Invitrogen), supplemented with 10% knockout serum (Gibco). When hIPSCs had reached about 80% confluence, they were detached with versene (ThermoFisher). Cell aggregates were removed and a single-cell suspension obtained with a cell strainer having a 100-μm mesh size (Corning). For EB formation, 10^4 cells were inoculated in 100 μl in each well of an ultra-low attachment, round-bottomed 96-well plate (Corning) and cultivated during 9 days in EB formation medium (StemCell Technologies).

Mouse Embryos

Embryos were of age E10.5 and E14.5. Mice were killed by cervical dislocation, the abdominal cavity was opened and the uterine horns were removed. Embryos were collected under a macroscope (Nikon SMZ800) and immersed in formalin (buffered 10% formaldehyde, VWR) overnight. They then were stored at 4°C in PBS/Sodium Azide 0, 02%. E10.5 embryos were used for whole-embryo cleaning; E14.5 embryos were embedded in Optimal Cutting Temperature (OCT) compound and sliced into 7-μm-thin sections on a cryotome (Cryocut 1800, Leica).

Staining, Clearing and Embedding

Nuclear Staining

The samples were permeabilized by a 0.2% TritonX100 solution in PBS (during 15 min for 7-μm-thin embryo slices and EBs, 20 min for brain organoids, 1 h for the whole-mount E10.5 embryo). They were then incubated overnight in a 1:1,000 solution of TO-PRO3 (Invitrogen) or of chloroform-purified MG (Merck) in PBS and finally washed in PBS. At this point, non-cleared samples were mounted in a PBS-filled chamber under a glass coverslip for microscopy. We used a home-made recording chamber, that was modified from chambers designed for imaging and available as 3-D printer templates[2].

Clearing

After nuclear staining, samples were processed for one of the three following clearing methods: TDE (Aoyagi et al., 2015), Clear^{T2} (Kuwajima et al., 2013) or RTF (Yu et al., 2018).

TDE

Samples were successively immersed in increasing concentrations (20%, 40% and 60%) of TDE (Sigma) solutions in PBS. The duration of each incubation varied as a function of the sample size: 1 h for 7-μm embryo slices and for EBs, 3 h for a whole E10.5 embryo.

Clear^{T2}

Samples were immersed successively in: (i) a 25% formamide (Sigma)/10% polyethylene glycol (PEG8000, Merck) solution in PBS (10 min for embryo slices and EBs, 30 min for a whole E10.5 embryo); (ii) a 50% formamide/20% PEG8000 solution in PBS (5 min for slices and EBs, 15 min for whole embryo); and (iii) a 50% formamide/20% PEG8000 solution in PBS (1 h for slices and for EBs, 3 h for a whole E10.5 embryo).

RTF

Samples were successively immersed in: (i) a 30% triethanolamine (TEA, Sigma)/40% formamide (Sigma) solution (15 min for slices and for EBs, 20 min for brain organoids, 3 h 20 min for a whole E10.5 embryo); (ii) a 60% TEA/25% formamide solution (25 min for slices and for EBs, 30 min for brain organoids, 5 h for embryo); and (iii) a 70% TEA/15%

[2]https://idisco.info/idisco-protocol/

formamide solution (25 min for slices and for EBs, 30 min for brain organoids, 5 h for whole embryo). In either case, after clearing, samples were mounted under a glass coverslip in a chamber filled with the respective final solution.

Microscopy

Confocal Microscopy

We used a Zeiss LSM 710 microscope with a ×63/1.4NA oil-immersion objective, for the acquisition of the confocal data shown in **Figure 2** and **Supplementary Figure S3**, and a ×40/1.0NA water-immersion objective for tissue sections and thick samples (embryo, EB, brain organoid), respectively. For a fair comparison of the performance for imaging thick samples of the confocal and 2P-virtual light-sheet OASIS microscope, we set the confocal pinhole to 2 Airy units and the scanned area was restricted to 900 × 900 pixels with a zoom resulting in an effective pixel size of 0.182 μm, equivalent to the OASIS. We also acquired confocal images at 1 Airy for comparison. The laser powers delivered to the sample are indicated in each figure. For 1PEF, we excited TO-PRO3 using the 633-nm line of a HeNe gas laser (Lasos). Fluorescence was collected in between 646 nm and 725 nm.

2P-Spinning Disk Microscopy

We here give a brief overview of the OASIS microscope setup. A detailed description and full characterization of the system will be published elsewhere (Deeg et al., in preparation). 2PEF is excited in some 40 focused spots that are scanned simultaneously across the sample. The emission from each the spots is confocally filtered like in a Nipkov-Petráň Spinning Disk microscope (Kino, 1995). However, instead of two separate disks housing, respectively, aligned arrays of microlenses and confocal pinholes, we used a single newly engineered disk. For this purpose, a 2-mm thick glass disk was manufactured that features some 5,000 micro lenses (each having 666-μm diameter) on the front side, and a dielectric long-pass coating (715LP) on the rear side. The micro lenses are arranged in four nested spirals. The dielectric coating on the rear side of the disk has 5,000 pinholes (each consisting of a non-coated spot of 60 μm diameter co-axially aligned with one of the microlenses on the front side). For the used Nikon ×25/1.1NA objective, this corresponds to 2 Airy units.

For 2-photon excitation, we expanded an infrared (IR) femtosecond Gaussian laser beam of a Titanium Saphire laser (Spectra-Physics Mai Tai® DeepSee) five times and collimated it to a beam diameter of about 5 mm that was aligned on the rear side of the disk as shown in **Figure 1A**. The disk transmits the IR light and the micro lenses generate a pattern of foci 7.8 mm in front of the disk. This pattern is imaged into the sample plan *via* the tube lens (TL; f = 200 mm) and objective (Nikon ×25/1.1NA, water). The fluorescence generated in each focal spot is then collected by the same objective. However, on the way back, between the TL and the disk two dichroic short-pass mirrors (custom design, SP705 Alluxa, Santa Rosa, CA, USA) are used to introduce a corrective distance, so that the emission of the excitation spots is imaged onto the pinholes of the disk as shown in **Figure 1A**, *inset*. At the pinholes, scattered and out-of-focus fluorescence is blocked like in any confocal microscope. A LP672 long-pass dichroic separates the fluorescence from the IR excitation light. An additional multi-photon emission filter (ET700SP-2P, Chroma) was used to block residual IR excitation light. For detection, the pinhole plane is imaged on to an sCMOS camera chip (PCO Edge 4.2) with a total magnification of ×36. With the current ×5 beam expansion, this optical arrangement results in an image of about 7 mm diameter on the camera chip, corresponding to an effective field-of-view of about 200 μm, which is sampled at 182 nm/px. For image acquisition, the disk is rotated at a constant speed of 5,000 RPM. Due to the four nested spirals, a quarter rotation is sufficient for a homogenous illumination of the sample, so a minimal acquisition time of 3 ms per full frame can be obtained.

The described system (with the exception of the Laser and shutter) is constructed in a monoblock upright microscope system with a voice coil-based objective drive (**Figure 1C**). A movable mirror is used to switch between 2P-spinning disk fluorescence imaging and a bright-field trans- or reflected light mode (with a f = 140 mm TL and a separate USB camera, Point Grey, BFLY-U3-23S6M-C). Having an effective magnification of ×17.5, this alternative optical path can be used to get an overview of the sample and identify regions of interest. The laser, shutter, focus and image acquisition are all controlled by an in-house microcontroller and software (TILL Siam).

Image Analysis and Quantification

Images were analyzed and displayed using FIJI. For a better visibility of the faint fluorescent signals at greater imaging depths, we used a nonlinear look-up table (γ = 0.6) for **Figures 4B–E**, **5C,D**.

Weber contrast was calculated as $C_w = (F - B)/B$, where F and B are the fluorescence intensities of the image and background, respectively. B was measured as the mean intensity of a cell-free region and F corresponded to the mean intensity in a small ROI (18 μm × 18 μm) in the center of the image for **Supplementary Figure S4A**, and to the whole image in **Supplementary Figure S4B**. In **Supplementary Figure S4A**, the sample was inclined respect to the optical axis so that only a small region could be used to quantify the penetration depth.

Statistics

All results are at least triplicates of three independent experiments and are represented as mean ± SD. Student's t-test was used to compare among experiments. Data were processed and figures prepared using IGOR Pro (Wavemetrics).

RESULTS AND DISCUSSION

Wide-Field Two-Photon Microscopy at Diffraction-Limited Resolution

With our OASIS system, we retain the in-line geometry of a classical upright microscope with a single objective lens (OL). We introduce a novel spinning-disk concept, rethought and specifically designed for wide-field 2P-excitation microscopy (**Figure 1A**). Briefly, the expanded and shaped beam of a fs-pulsed infrared laser is focused by an array of micro lenses to produce some 40 evenly lit excitation spots. These spots

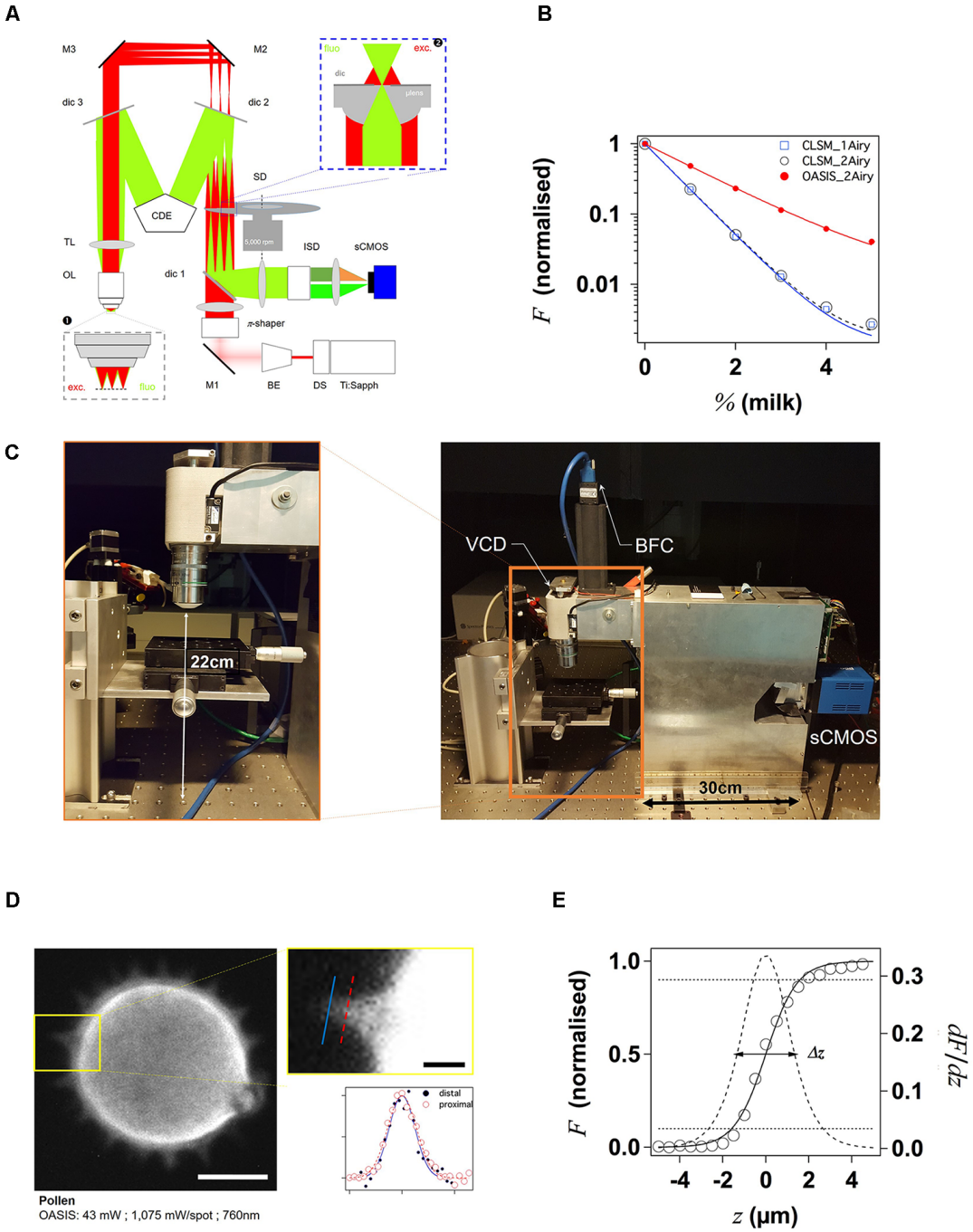

FIGURE 1 | Principle and performance of the On-axis 2-photon virtual light-sheet generation in vivo imaging system (OASIS). **(A)** Simplified optical path of our custom 2P microscope. *Red*: infrared (IR) excitation, *green*: fluorescence. Ti:Sapph, fs-pulsed IR laser; DS, DeepSee module (pulse stretcher); BE, beam expander; π-shaper, optical element that converts the Gaussian beam into a top hat profile; M, mirrors; dic, dichroic mirrors; SD, spinning disk; TL, tube lens; CDE, corrective distance element; OL, objective lens; ISD, image-splitting device; sCMOS, camera. *Inset* ❶: (simplified) multi-spot excitation pattern and epi-collection of the generated fluorescence through the same objective. *Inset* ❷: detail of microlens/pinhole/dichroic coating arrangement. Note the offset between the excitation (exc.) and fluorescence foci (fluo.) at the level of the disk, produced by the CDE. **(B)** Measured depth penetration in turbid samples. Log-plot of 2P-excited fluorescence from a green-fluorescent Chroma test slide, topped either with water (0%) or increasing concentrations of milk (a model for the multi-scale scatterers present in tissue), for the OASIS (red dots) and a ZEISS LSM710. Confocal pinhole diameters were 1 and 2 Airy, as indicated. **(C)** OASIS prototype, note the compact size and space available around the objective, *inset*. VCD, voice coil *z*-drive; BFC, bright-field camera. **(D)** Assessment of OASIS lateral resolution. Equatorial section through an autofluorescent thorny pollen grain. Scale bar, 10 μm. *Inset*: magnified view of an in-focus spine and intensity profiles across the lines shown; Scale bar, 2 μm. **(E)** OASIS *z*- resolution. Axial-intensity profile measured from a *z*-stack of images acquired from a green fluorescent Chroma slide (solid line), and its derivative *dF/dz* (dashed). The 10%–90% intensity range was taken as axial optical sectioning capacity Δz.

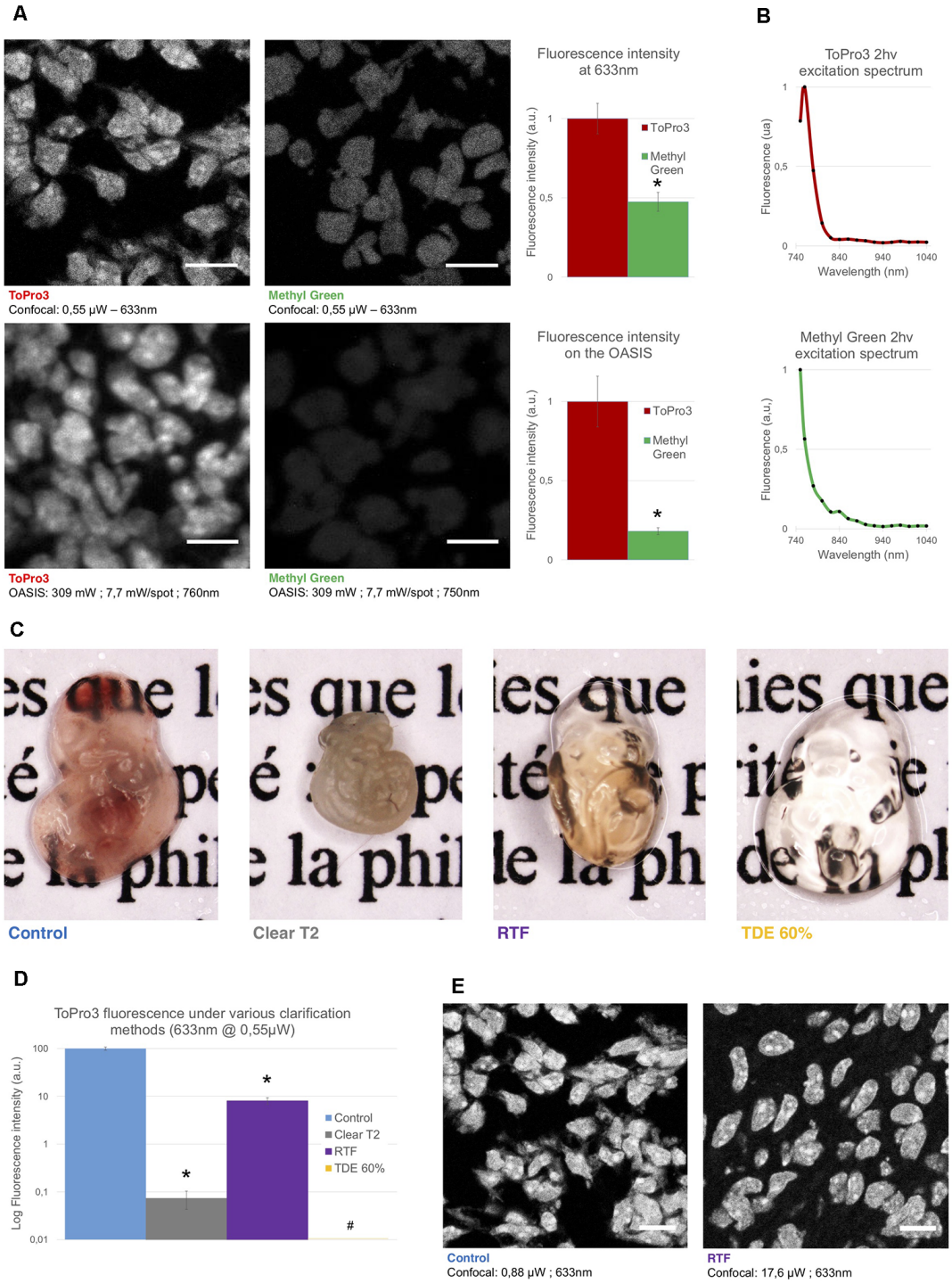

FIGURE 2 | Comparison of the used nuclear stains and clearing methods. **(A)** *Left*, optical section of a slice from an E14.5 embryo, labeled with TO-PRO3 or Methyl Green (MG) and observed on a single-spot confocal laser scanning microscope confocal laser-scanning microscope (CLSM, *top*) or on the OASIS microscope (*bottom*). Scale-bar, 10 µm. *Right*, relative fluorescence intensity of TO-PRO3 and MG in nuclei of E14.5 embryo slices measured on a CLSM (*top right*) or on the OASIS (*bottom right*). **(B)** TO-PRO3 (*top*) and MG (*bottom*) 2P-excitation spectra. Color code as in **(A)**. **(C)** Macro-photographies of E10.5 embryos in control (PBS) and following three clearing protocols [Clear^{T2}, rapid partial transparisation with triethanolamine formamide (RTF) and TDE 60%]. Note the variable degree of transparisation and the volume change. **(D)** Relative fluorescence of TO-PRO3-positive nuclei in E14.5 embryo slices observed on a CLSM after the same clearing protocols as above. Note the log-scale $^{*}P < 0.0001$, $^{\#}$Quantification impossible as the signal is too low. **(E)** Fluorescence loss upon clearing requires high laser powers. Confocal micrographs of slices from an E14.5 embryo labeled with TO-PRO3 under control (*left*) and after RTF clearing (*right*) along with the laser powers required to attain the same signal-to-background ratio. Scale-bar, 10 µm.

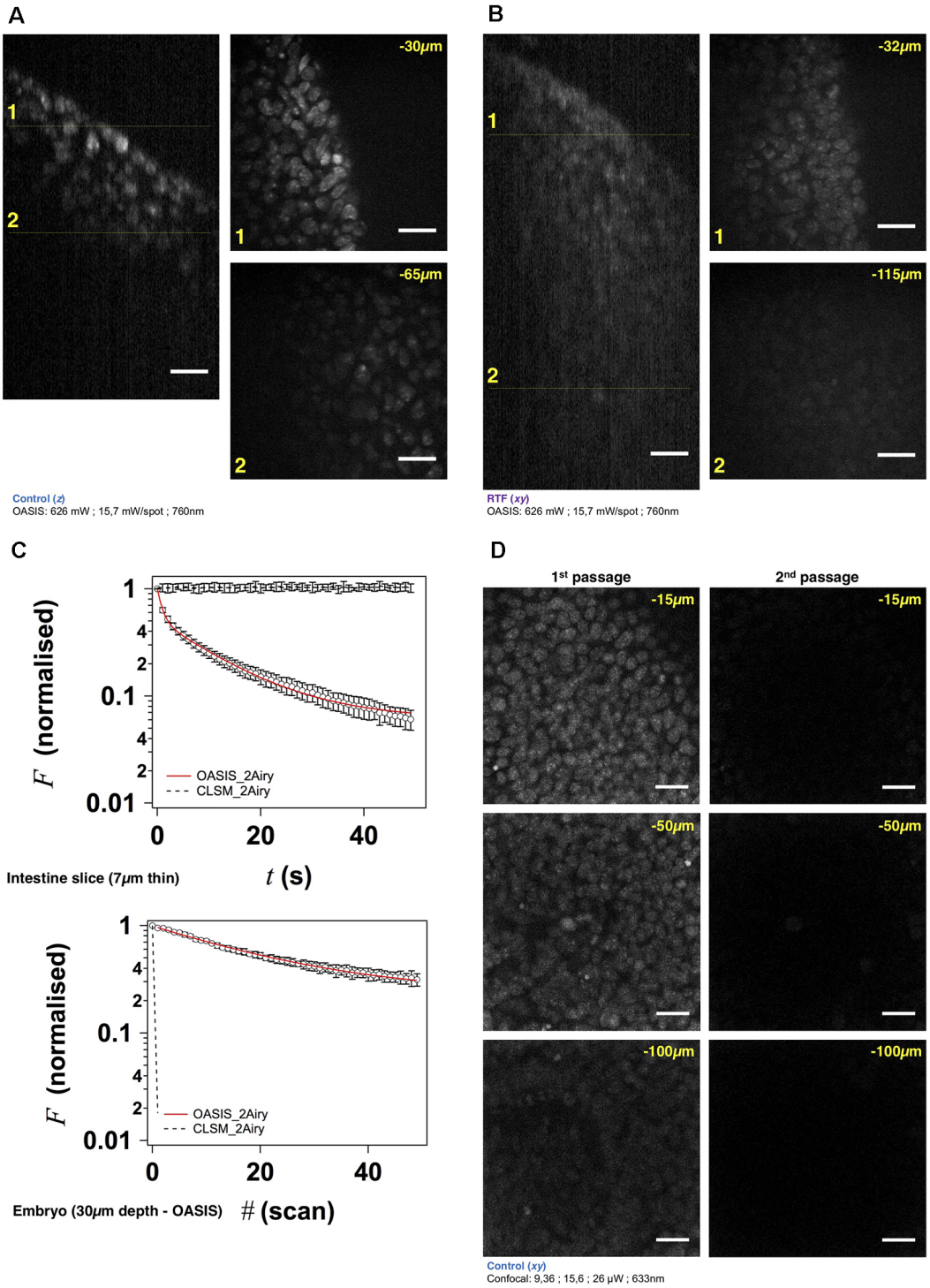

FIGURE 3 | The OASIS microscope outperforms a CLSM point-scanner for 3-D embryo imaging. **(A)** 3-D data set taken with the OASIS in a non-cleared embryo stained with TO-PRO3 (Control). Panels show *xz*- projection of a *z*-stack of images (*right*) and *xy*-planes (*left*) corresponding to the dashed lines at 30 µm (1) and 65 µm imaging depth (2), respectively. Scale-bar, 25 µm. **(B)** same, at 32 µm (1) and 115 µm depth (2), respectively, for an RTF-cleared embryo. Scale-bar, 25 µm, as in **(A)**. **(C)** Representative bleaching curves during continuous acquisitions, from a single *z*-section in—respectively—a thin slice of intestine (*top*) and of TO-PRO3-labeled nuclei (*bottom*) at 30-µm imaging depth in an embryo. **(D)** Representative planes at various imaging depths (15, 50 and 100 µm, respectively) of a 3-D data set (200 planes from the surface to 200 µm, Δz = 1 µm) acquired from a TO-PRO3-labled embryo. The two columns show the sections during the 1st passage (*left*) and during the 2nd passage, after completion of the 1st image stack (*right*). Note the almost complete bleaching prohibiting repetitive volume imaging for the CSLM but not the OASIS microscope. Measured laser powers are given for each depth. Scale-bar, 25 µm.

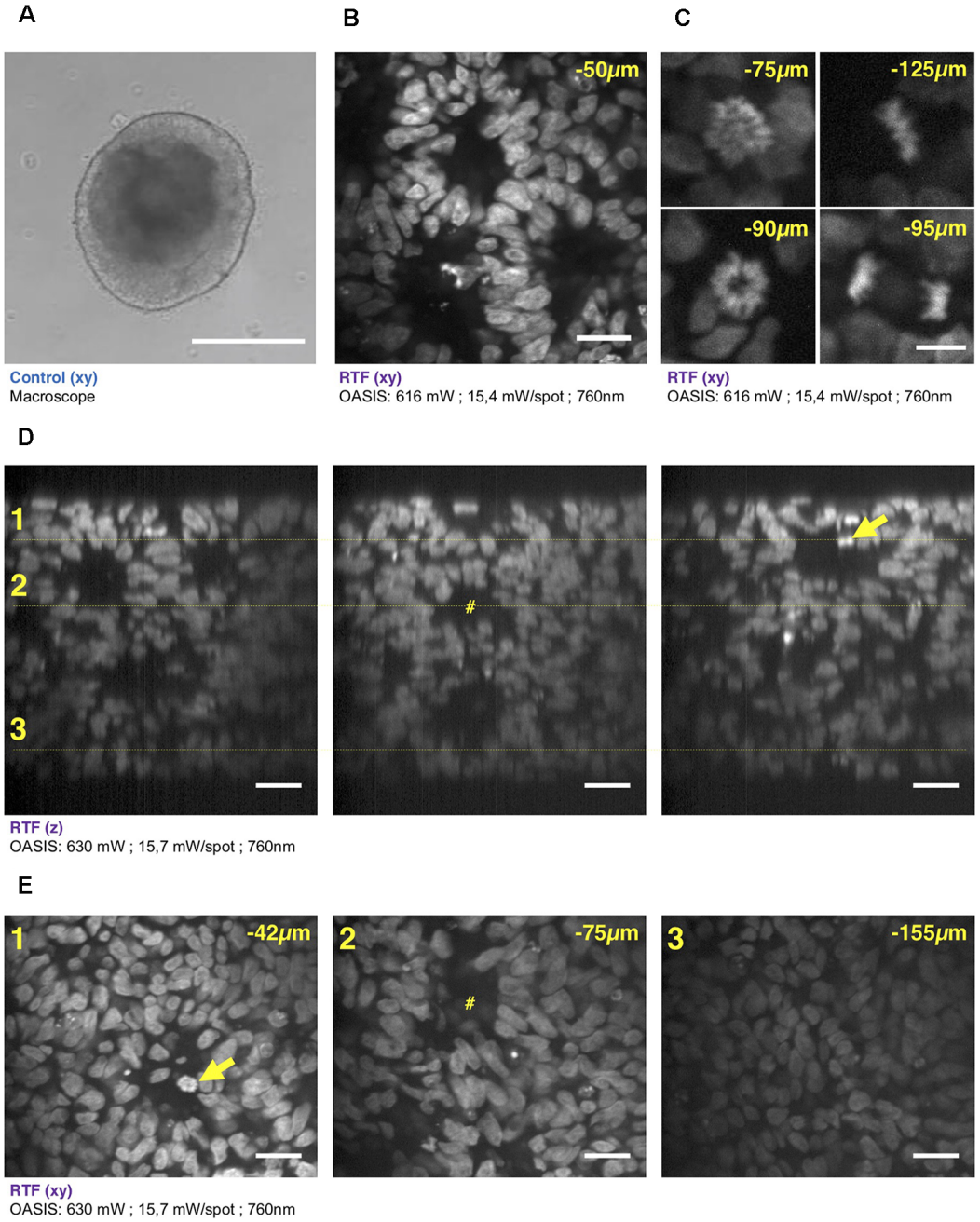

FIGURE 4 | 3-D imaging with the OASIS of the fine structure of embryonic bodies (EBs). **(A)** Macrophotography of a day-7 EB; Scale-bar, 300 µm. **(B)** Image acquired in the center of the organoid after TO-PRO3 staining, 50 µm below the surface. Scale-bar, 25 µm. Note the presence of internal round structures with a lumen. **(C)** Zoom on mitotic figures observed in the EB at various depth (*top left*: prophase; *top right*: metaphase; *bottom left*: early anaphase; *bottom right*: late anaphase); stain: TO-PRO3. Scale-bar for all panels, 10 µm. **(D)** *xz*-pro-jections of a *z*-stack acquired across an entire day-7, TO-PRO3-stained EB. Scale-bar, 25 µm. Arrow points to mitosis also visible in panel **(E)**. #Indicates ventricle-like structure also perceived in **(E)**. **(E)** *xy*-sections across the dotted lines shown in **(D)** at imaging depths of, respectively, 42 µm (1), 75 µm (2) and 155 µm (3). Scale-bar, 25 µm. With the exception of **(A)**, all images were acquired after RTF clearing.

are imaged by the TL and objective into the sample plane where they are each spaced, on average, by 28 µm (**Figure 1A**, *inset* ❶). Almost 5,000 micro lenses are arranged in four spirals that scan these spots upon rotation of the disk. At 5,000 rpm (i.e., one turn every 12 ms, much shorter than camera integration times used here) this multi-photon multi-focal microscope generates a virtual light sheet permitting wide-field excitation, direct-view 2P microscopy. Unlike earlier 2P-spinning disk microscopes (Bewersdorf et al., 1998; Egner et al., 2002; Shimozawa et al., 2013) based on the Yokogawa-type

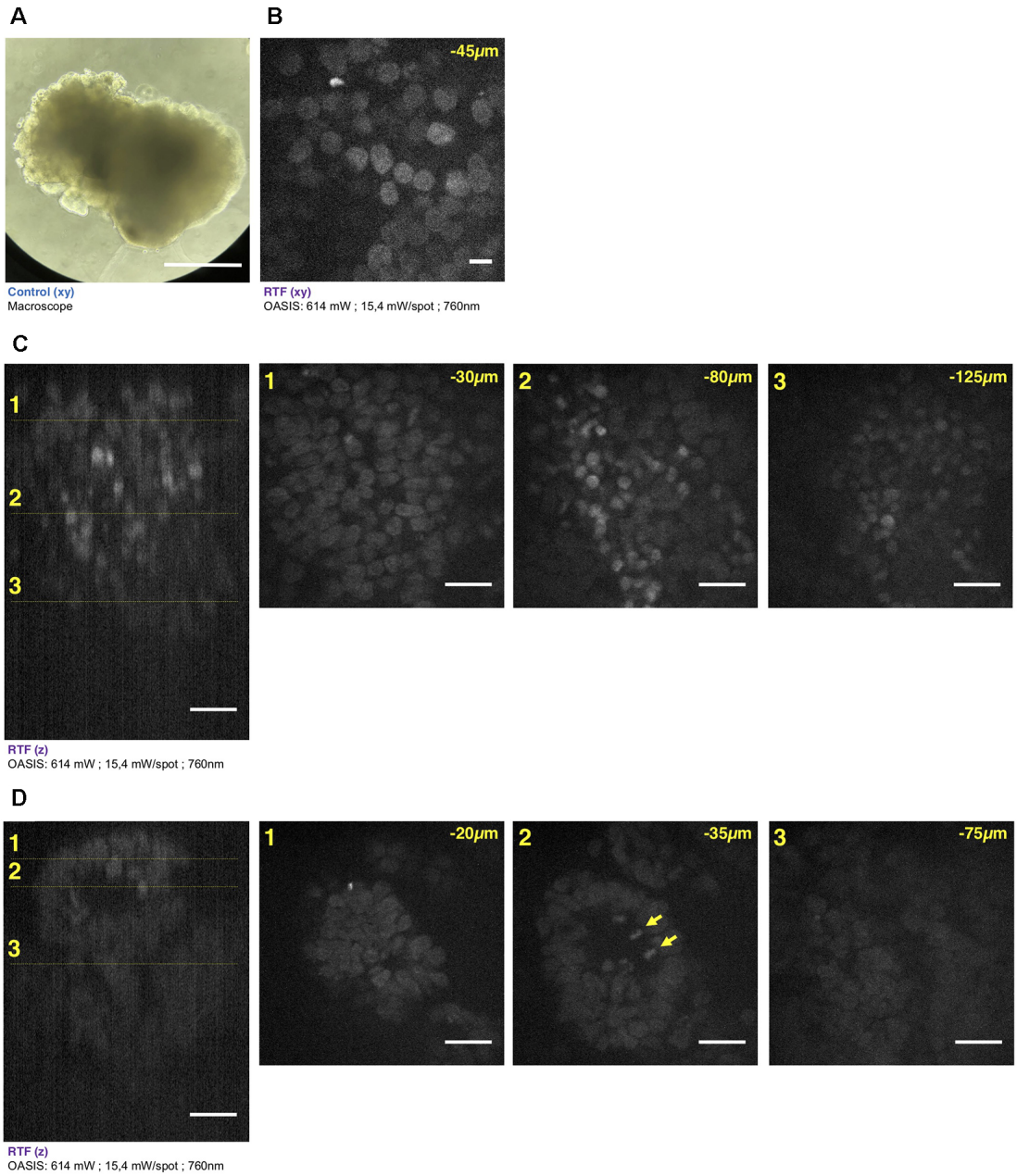

FIGURE 5 | Brain organoid imaging with OASIS. **(A)** Macrophotography of a day 11 brain organoid before clearing and observation on the OASIS microscope; scale-bar: 300 µm. **(B)** Image acquired in the center of the organoid at 45 µm below the surface; stain: TO-PRO3; scale-bar: 10 µm. **(C)** z-reconstruction (left) and xy-acquisition (right) at respectively 30 µm (1), 80 µm (2) and 125 µm (3) below the surface of the organoid; stain: TO-PRO3; scale-bar: 25 µm. Note the change of the morphology of the nuclei in the center of the region of interest when depth increase. **(D)** z-reconstruction (left) and xy-acquisition (right) at respectively 20 µm (1), 35 µm (2) and 75 µm (3) below the surface of the organoid; stain: TO-PRO3; scale-bar: 25 µm. Note the globular structure (neuro-epithelium) that can also be observed on the macroscopy and numerous mitosis inside this structure (arrows). Except in **(A)**, all images were acquired after the clearing of the organoid with the RTF protocol. Note the image quality across the entire imaged volume.

dual-disk design, we conceptualized and built a completely different geometry. Where the Yokogawa design requires two disks, one with micro lenses, the other one with confocal pinholes, our design relies on a single disk on which micro lenses and pinholes are arranged on the different faces of the same optical element. In addition, each micro lens comes with its own dichroic mirror; the dielectric coating on the rear face is omitted over a tiny central circular aperture of 60-µm diameter, thus most of the disk is opaque for fluorescence which must arrive focused in the plane of the disk to pass. The use of a single disk is advantageous in view of the large wavelength difference between the near-infrared excitation and the visible fluorescence,

which had previously reduced the efficiency of 2P-spinning disk microscopes. However, this simplification comes at a price as it required a complete re-design of the microscope optical path. On the *excitation* side, the micro lenses must be uniformly illuminated with an expanded, collimated, flat-profile fs-pulsed IR laser beam to generate an array of focused spots. On the *collection* side, to pass the pinholes, the detected fluorescence must arrive focused at the level of the pinholes. The required optical path-length difference between excitation and emission light is achieved by introducing a corrective distance element (CDE) in the non-infinity space: while the longer-wavelength excitation light passes straight through the device, the shorter-wavelength fluorescence takes a detour and travels a longer path to produce the desired focal offset, *inset* ❷. This patented scheme critically relies on extremely flat shallow-incidence long-pass dichroic mirrors to preserve the phase front of the beam and maintain the optical resolution, but it has the crucial advantage to be compatible with much bigger objective pupils (and hence larger fields of view and working distances) than the Yokogawa dual-disk design where the dichroic cube is sandwiched between the two disks.

The 2P-excited fluorescence generated in each of the spots is collected through the same objective and imaged onto the tiny pinholes in the dichroic coating of the microlenses (**Figure 1A**, *inset* ❷). Relay optics then images these pinholes onto a large-format sCMOS camera. With the ×25/1.1NA objective, the resulting pixel size in the sample plane is 182 nm. As the fluorescence is de-scanned at the level of the disk, this detection is partially confocal (the 60-μm pinhole diameter correspond to a confocal aperture of 2 Airy units), so that ballistic and snake-like photons but not scattered fluorescence are collected. This is illustrated by the exponential fluorescence drop with increasing sample turbidity (i.e., equivalent imaging depth). Yet, as a result of the longer wavelength of excitation light compared to 1P-CLSM, the signal drop observed with the OASIS microscope was only half of that observed upon 1-P 633-nm excitation on the ZEISS LSM710, and this although two photons must combine for fluorescence excitation (leading to a squared exponential fall-off; **Figure 1B**). We can attribute the improved depth penetration of the OASIS uniquely to excitation effects, because stopping down the confocal pinhole of the LSM710 from 2 to 1 Airy units did not measurably alter the fluorescence decay on the CLSM, indicating that at the imaging depths attained, pinhole size effects are minor.

With its small footprint (43 cm by 12 cm) and 22-cm clearance under the objective, the OASIS microscope offers facile access and ample space around the objective, making it an ideal platform for imaging large samples, but also for placing electrodes, application pipettes or external fibers for photostimulation or photochemical uncaging (**Figure 1C**). As a result of the large chip format of the sCMOS detector, we could implement simultaneous dual-color detection by way of a custom image splitter (**Supplementary Figure S1**).

With the MaiTai DeepSee, ×4.6 beam expander (BE) and a ×25/NA1.1w low-mag high numerical aperture (NA) dipping objective (Oheim et al., 2001), the OASIS microscope features an effective field of view with a 190 μm image diagonal. An elongated, larger field of 380 μm by 190 μm would be possible, but it would require more micro-lenses to be illuminated with an elliptical beam, which in turn would require a more powerful fs-pulsed laser than ours.

As a wide-field excitation, direct-view imaging system, the OASIS microscope simultaneously offers a fast frame rate, and it resolves tiny subcellular detail over a large field of view. We illustrate the sub-micrometric resolution by imaging the fine tip of a spine from an autofluorescent pollen grain, a popular sample for testing 2P-microscopes (**Figure 1D**).

For getting a first estimate the optical sectioning capability of our microscope, we recorded the axial (z-) intensity profile when focusing at the interface of a green fluorescent Chroma test slide and we quantified Δz by the taking the full-width at half maximum (FWHM) of a Gaussian fitted with the derivative of the z-profile (König, 2018; **Figure 1E**). Repeating the same experiment on the ZEISS LSM710 demonstrates that OASIS offered a 1.3-fold better optical sectioning with the pinhole diameter set to 2 Airy diameter and with a dipping objective having a similar NA (1.1w for the OASIS vs. 1.0w for the ZEISS; $\Delta z_{OASIS} = 2.75 \pm 0.02$ μm vs. $\Delta z_{\mathrm{CLSM,\,2Airy}} = 3.47 \pm 0.02$ μm). In fact, the optical sectioning of the OASIS microscope is close to that of a CLSM with the pinhole stopped down to 1 Airy diameter ($\Delta z_{\mathrm{CLSM,\,1Airy}} = 2.55 \pm 0.02$ μm; **Supplementary Figure S2**). We note that both values are not optimal due to the refractive-index mismatch between the water immersion and the Chroma test slide, but this does not change the factor between the two (neither of these lenses had a correction collar).

The acquisition speed will in practice be limited by the available signal, but the theoretical minimal exposure time is given by the time to obtain a homogeneous illumination of the sample. With a rotation time of 12 ms at 5,000 rpm and four nested spirals, the minimal exposure time is 3 ms corresponding to a time resolution of 6 ms according to Nyquist's sampling theorem in the temporal domain. Exposure times should be multiples of 3 ms for obtaining homogeneously illuminated field of views. With the 100-fs pulses and <10 mW average laser power, $<P>$, per illumination spot used here, typical exposure times were of the order of 48–120 ms, full-frame, more than one order of magnitude faster than the typical time required for a similarly resolved image with confocal or 2P-scanning microscope.

Taken together, our OASIS 2P-spinning disk microscope offers a larger field, a better depth penetration, a similar if not better spatial resolution and a considerably higher speed than a conventional CSLM.

RTF-Cleared TO-PRO3-Labeled Embryos As a Test Sample for 1- and 2P Microscopies

Next, we evaluated the performance of the OASIS microscope for 3-D imaging of partially cleared brain tissue. We sought for a stereotypic, sparsely but relatively homogenously labeled thick sample. To allow for a direct comparison between 1P-CLSM and our 2P spinning-disk microscope, this labeling needed to be suitable for both linear- and non-linear excitation. To minimize scattering and improve the depth penetration, we

sought a red-excited, deep-red emitting fluorophore. With these constraints in mind we evaluated the nuclear stains TO-PRO3 and Methyl Green (MG), having 1P-fluorescence excitation/emission maxima of 642/661 nm (Bink et al., 2001) and 632/650 nm (Prieto et al., 2014), respectively.

During preliminary experiments in 7-μm thin sections of a fixed (E14.5) mouse embryo, we found TO-PRO3 fluorescence to be 2.1-fold brighter than that of MG upon 633-nm excitation. We observed an even larger intensity ratio (×5.5) upon 2P-excitation at 760 nm (**Figure 2A**). Although non-linear excitation of TO-PRO3 at 1,100 nm has been reported (Smith et al., 2012; Ricard et al., 2018) our own measurement of the 2P-action spectra revealed peak excitations at 760 and 750 nm for TO-PRO3 and MG, respectively (**Figure 2B**). These shorter wavelengths are within the tuning range of the Ti:Sapphire laser and they minimize thermal damage from near-infrared absorption and focal heating (Schmidt and Oheim, 2018), a particular concern for the multi-spot excitation scheme used here.

We next optimized the tissue clearing procedure. Among the available methods (for review, see Richardson and Lichtman, 2015), we focused on TDE (Aoyagi et al., 2015), Clear^{T2} (Kuwajima et al., 2013) and RTF clearing (Yu et al., 2018). The rationale was that these methods require only short clearing episodes and they use solvents compatible with dipping objectives. Mouse embryos were most transparent with TDE (60%), followed by RTF and, by far, Clear^{T2}, for which the tissue was even more opaque than the non-cleared control (probably due to volume shrinkage; **Figure 2C**).

In clearing protocols, transparency is one issue, fluorescence preservation another. Depending on the very method used, the observed fluorescence loss was dramatic, with a 99.9% and 92% attenuation of TO-PRO3 fluorescence following Clear^{T2} and RTF clearing, respectively (**Figure 2D**). Increasing the laser power by a factor of 20 allowed us to acquire confocal images of TO-PRO3 stained nuclei in slices of RTF-cleared embryos (**Figure 2E**), whereas TDE clearing attenuated the fluorescence to undetectable levels (**Supplementary Figure S3**). To develop an order-of-magnitude idea of the laser powers required for obtaining similar signal-to-noise levels with the OASIS and CSLM, we finally compared images acquired upon 1- (at 633 nm) and 2-excitation (at 760 nm) of TO-PRO3 labeled nuclei in a thin section of RTF cleared mouse embryo. At equivalent confocal aperture of 2 Airy, we found a factor of ×4,000 between linear and non-linear excitation (2 μW vs. 8 mW/spot, respectively).

Based on these results, we opted for TO-PRO3 nuclear staining and RTF clearing for directly comparing the performance of confocal and OASIS microscopes.

Many questions in neurobiology require at high-resolution imaging of large sample volumes. The growing field of 3-D cultures, EBs and minibrains is no exception, as many basic neuroanatomical questions remain open. For many developmental biology and neurobiology laboratories, that are not necessarily experts in 2P- or light-sheet microscopies, the single-spot scanning confocal laser scanning microscopy (CLSM) remains the major workhorse. Due to its simplicity and ease of use, our OASIS microscope aims precisely at such end-users, and we, therefore, compared the OASIS with a commercial ZEISS LSM710 confocal, an instrument present on many imaging platforms.

Faster and Less Invasive Acquisition of 3-D Image Stacks Than a CLSM

At 250-nm lateral and micrometric axial sampling and with typical pixel dwell times of 1 (10 μs), sequential single-spot scanning requires 4 (40) ms, 4 (40) s and more than 1 (10) for the acquisition of 3-D image stacks from cubes of 10 μm, 100 μm and 1 mm side-length, respectively. Parallelizing both the excitation and emission detection, as with our OASIS microscope is expected to considerably speed up the imaging of such large data sets.

Using TO-PRO3 nuclear staining as a proxy, we acquired *z*-stacks of images in RTF-cleared mouse embryos. Achievable imaging depth in TF-cleared samples (**Figure 3B** and **Supplementary Figure S4A**) were three-fold increased compared to non cleared mouse embryos (**Figure 3A** and **Supplementary Figure S4A**), 90μm vs. 30 μm. Next, we evaluated, at similar signal-to-noise ratios of the resulting images, the photobleaching with the OASIS (at 760-nm 2P-excitation) vs. the ZEISS LSM710 spot scanning confocal (at 633-nm 1P-excitation). We first compared 2P-large-field and confocal-scanning excitations at shallow imaging depths, by continuously recording images of the same region of interest (ROI) for a 7-μm intestine slice. At the same initial signal-to-noise ratio for either microscope, we observed a ∼3%-intensity loss after the first full-frame with the OASIS microscope (t_{exp} = 480 ms per image, 15.7 mW/spot for the OASIS), whereas the signal remained relatively stable after a single confocal scan. Fitting a monoexponential with the OASIS bleaching data revealed a 1/e (37%) loss of fluorescence every 21 frames (**Figure 3C**). Thus, as expected, the high peak-powers required for non-linear excitation result in a significantly higher bleaching when imaging single planes in superficial tissue layers. However, for 3-D volume imaging of thicker sections, confocal microscopy rapidly produced much faster photobleaching than the OASIS because the entire volume is exposed throughout the acquisition. Also, the CLSM required higher and higher laser powers to maintain image contrast at greater imaging depths; in fact, acquiring the first complete *z*-stack with the CSLM attenuated the TO-PRO-3 fluorescence so much that a second volume acquisition was impossible (**Figure 3D**).

We attribute the much higher volume photobleaching upon 1P confocal imaging in non-cleared embryos to four reasons: (i) tissue scattering at 633 nm was roughly double that of near-infrared light. The exponential scattering losses of excitation photons must be compensated for by exponentially increasing the excitation powers with increasing imaging depth; (ii) as a consequence of linear (1P) excitation, off-focus excitation of fluorophores located above and below the imaged plane causes bleaching, too, i.e., at any plane, bleaching occurs throughout the entire tissue volume while only one plane is imaged; (iii) although not contributing to imaging, the scattered 1P excitation light nevertheless excites (out-of-focus) fluorescence, which—in addition to the ballistic out-of-focus excitation—additionally

results in volume photobleaching. Non-linear (2P) excitation, on the other hand, confines both fluorescence excitation and photobleaching to the focal plane, with the result of better preserving the sample outside the plane which is actually imaged; and (iv) image acquisition was >4-times faster on the OASIS compared to confocal scans (480 ms/image vs. 1.815 s/image for a similar image contrast), reducing the overall exposure of the sample.

We note that the better performance of the OASIS concept comes essentially from the effect 2P-excitation confinement, because on the fluorescence collection side, at 2 Airy, both instruments should perform similarly. Finally, not only taking into account the loss of signal but also Weber contrast, we found a three-fold larger effective depth penetration for the OASIS microscope compared to the CLSM (**Supplementary Figure S4A**).

Taken together, the OASIS microscope combines the advantages of 2P-excitation and excitation and emission parallelization and therefore excels over the ZEISS LSM710. It achieves higher *z*-resolution, affords less photobleaching in 3-D samples and considerably speeds up data acquisition, thus allowing a more efficient and less invasive volume imaging. These properties make it an ideal instrument for imaging EBs, organoids, 3-D cultures and small model organisms.

Fast Volume Acquisition From Mouse Embryonic Bodies and Brain Organoids

We continued our comparison of the OASIS against the CLSM by imaging day-7 EBs (**Figure 4A**), again stained with TO-PRO3. Images acquired at different depths displayed rounded structures with *luminae* inside tissue and revealed strong mitotic activity (**Figure 4B**). The rounded structures presumably correspond to neuroepithelial-like structures that are readily formed within EBs, indicating the inherent ability of the ectoderm to differentiate into neural lineages (Ying and Smith, 2003). The sub-μm resolution of the OASIS microscope allowed us the detailed characterization of the different mitotic figures throughout the entire 160-μm thickness of the EB, which was impossible on the CLSM (**Figure 4C**).

Acquiring 3-D image stacks at a *z*-spacing of 0.5 μm (**Supplementary Figure S4B**) allowed us reconstructing the complete EB volume and realizing high-resolution projections along the orthogonal axes (**Figure 4D**), revealing fine structural detail, including mitosis across its entire volume (**Figure 4E**). Volume imaging of entire EBs was almost 4-times faster with the OASIS compared to the CLSM (a 200-μm *z*-stack with a 0.5-μm z-spacing required 3′12″ vs. 12′6″), with no detectable photobleaching on the OASIS. Together, these features make the OASIS microscope an ideal setup for the detailed 3-D characterisation of EB development.

Similar if not larger *z*-stacks were acquired a from RTF-cleared day-11 brain organoids (**Figure 5A**). At this early developmental stage, the neuroepithelium has been induced and forms buds that undergo 3-D growth within the Matrigel droplets (Lancaster and Knoblich, 2014). Our observations highlight strong morphological modifications during this tissue expansion. A recurrent feature was that TO-PRO-3 labeled nuclei were rounded just below the surface of the brain organoids, whereas polymorph and diamond-shapes prevailed at greater imaging depths (**Figure 5B**). Also, the cell density and nuclear labeling changed markedly with depth. Orthogonal planes revealed compact groups of nuclei with stronger fluorescence (**Figure 5C**), as well as cavities and rounded structures with a neuroepithelium-like shape. As before in the EBs, the resolution of the OASIS microscope allowed us to detect the presence of mitotic figures at the luminal side (**Figure 5D**). Typical achievable imaging depths were now around 200 μm, reflecting the densification and opacification of the tissue during the development of an EB towards a brain organoid.

With its large field-of-view, increased depth penetration, low photobleaching and greater speed compared to the CSLM, the OASIS optical scheme lends itself ideally to the observation of entire EBs and brain organoids. Thin optical sections can be studied at depth with sub-μm lateral resolution, without mechanical slicing. 3-D imaging at subcellular resolution can also be achieved with expansion microscopy, in which a polymer network is introduced into cellular or tissue samples, and this network physically expanded using chemical reactions to increase the size of the imaged brain structures relative to the available microscope resolution (Wassie et al., 2018; Gao et al., 2019). Complementary to and compatible with this type of microscopy, the OASIS microscope is an interesting platform for such expansion strategies. The reduced complexity compared to a classical light-sheet microscope, its compact mono-block design and comparable ease-of-use make it an ideal companion for functional neuroanatomy. The ongoing integration of a compact, fixed-wavelength high-power fs-pulsed laser into this package will make the OASIS a unique, portable, alignment-free bench-top 2P-microcope.

CONCLUSION

Work on brain organoids offers several distinctive advantages over classical disease models: (i) derived from patient fibroblasts, they raise fewer concerns than animal experimentation and work on human explants (see, however, Farahany et al., 2018, for an emerging awareness of the ethical issues associated with these 3-D cultures); (ii) they avoid the limitations of animal models that are often only a poor proxy of human pathology; (iii) they allow studies of rare or sporadic cases, for which genetic models are missing; and (iv) they allow observing the onset of the disease during the early steps of the brain development, opening opportunities for studies that would be impractical or unacceptable on human embryos or infants.

For this rapidly growing field of applications, the OASIS 2P microscope is a compact, versatile and cost-efficient 2P wide-field research instrument allowing imaging of hiPSC cultures, EBs and brain organoids.

ETHICS STATEMENT

All experimental procedures were performed in accordance with the French legislation and in compliance with the

European Community Council Directive of November 24, 1986 (86/609/EEC) for the care and use of laboratory animals. The used protocols were approved by the local ethics committee.

AUTHOR CONTRIBUTIONS

AD, CS and RU designed and conceptualized the OASIS prototype. BD and PD generated iPSCs, EBs and brain organoids. AD, BD, IR, CR, MB and MO performed the experiments. MO wrote the article with contributions from all authors.

FUNDING

This research was financed by the European Union (H2020 Eureka! EUROSTARS project "OASIS," to RU and MO), the CNRS (DEFI Instrumentation aux Limites, to MO), the Agence Nationale de la Recherche (ANR-10-INSB-04-01, grands investissements France-BioImaging, FBI, to MO) and the Region Ile-de-France (DIM cancéropôle, project EDISON, to MO). The Oheim lab is a member of the C'nano IdF and Ecole de Neurosciences de Paris (ENP) excellence clusters for nanobiotechnology and neurosciences, respectively. The funders had neither an influence on the design of the study, nor on the outcome or interpretation of the results.

ACKNOWLEDGMENTS

We thank Dr. Elke Schmidt for help in setting up early experiments, Patrice Jegouzo (fine mechanics and 3-D printing) as well as Claire Mader and her team (CNRS/INSERM UMS 1006, Saints-Pères Central Animal Facility) for expert technical support. Confocal imaging was done at the SCM core facility (Service Commun de Microscopie, with the support of Jennifer Corridon, Paris Descartes).

SUPPLEMENTARY MATERIAL

The Supplementary Material for this article can be found online at: https://www.frontiersin.org/articles/10.3389/fnana.2019.00077/full#supplementary-material

REFERENCES

Andilla, J., Jorand, R., Olarte, O. E., Dufour, A. C., Cazales, M., Montagner, Y. L., et al. (2017). Imaging tissue-mimic with light sheet microscopy: a comparative guideline. *Sci. Rep.* 7:44939. doi: 10.1038/srep44939

Aoyagi, Y., Kawakami, R., Osanai, H., Hibi, T., and Nemoto, T. (2015). A rapid optical clearing protocol using 2,2′-thiodiethanol for microscopic observation of fixed mouse brain. *PLoS One* 10:e0116280. doi: 10.1371/journal.pone.0116280

Baumgart, E., and Kubitscheck, U. (2012). Scanned light sheet microscopy with confocal slit detection. *Opt. Express* 20, 21805–21814. doi: 10.1364/oe.20.021805

Belle, M., Godefroy, D., Couly, G., Malone, S. A., Collier, F., Giacobini, P., et al. (2017). Tridimensional visualization and analysis of early human development. *Cell* 169, 161.e12–173.e12. doi: 10.1016/j.cell.2017.03.008

Bewersdorf, J., Pick, R., and Hell, S. W. (1998). Multifocal multiphoton microscopy. *Opt. Lett.* 23, 655–657. doi: 10.1364/ol.23.000655

Bink, K., Walch, A., Feuchtinger, A., Eisenmann, H., Hutzler, P., Höfler, H., et al. (2001). TO-PRO-3 is an optimal fluorescent dye for nuclear counterstaining in dual-colour FISH on paraffin sections. *Histochem. Cell Biol.* 115, 293–299. doi: 10.1007/s004180100254

Chen, B.-C., Legant, W. R., Wang, K., Shao, L., Milkie, D. E., Davidson, M. W., et al. (2014). Lattice light-sheet microscopy: imaging molecules to embryos at high spatiotemporal resolution. *Science* 346:1257998. doi: 10.1126/science.1257998

Egner, A., Andresen, V., and Hell, S. (2002). Comparison of the axial resolution of practical Nipkow-disk confocal fluorescence microscopy with that of multifocal multiphoton microscopy: theory and experiment. *J. Microsc.* 206, 24–32. doi: 10.1046/j.1365-2818.2002.01001.x

Elisa, Z., Toon, B., De Smedt, S. C., Katrien, R., Kristiaan, N., and Kevin, B. (2018). Technical implementations of light sheet microscopy. *Microsc. Res. Tech.* 81, 941–958. doi: 10.1002/jemt.22981

Fahrbach, F. O., Gurchenkov, V., Alessandri, K., Nassoy, P., and Rohrbach, A. (2013). Light-sheet microscopy in thick media using scanned Bessel beams and two-photon fluorescence excitation. *Opt. Express* 21, 13824–13839. doi: 10.1364/oe.21.013824

Farahany, N., Greely, H., Hyman, S., Koch, C., Grady, C., Pasca, S., et al. (2018). The ethics of experimenting with human brain tissue. *Nature* 556, 429–432. doi: 10.1038/d41586-018-04813-x

Fatehullah, A., Tan, S. H., and Barker, N. (2016). Organoids as an *in vitro* model of human development and disease. *Nat. Cell Biol.* 18, 246–254. doi: 10.1038/ncb3312

Gao, R., Asano, S. M., Upadhyayula, S., Pisarev, I., Milkie, D. E., T.-Liu, L., et al. (2019). Cortical column and whole-brain imaging with molecular contrast and nanoscale resolution. *Science* 363:eaau8302. doi: 10.1126/science.aau8302

Giandomenico, S. L., and Lancaster, M. A. (2017). Probing human brain evolution and development in organoids. *Curr. Opin. Cell Biol.* 44, 36–43. doi: 10.1016/j.ceb.2017.01.001

Gonzalez, D., Gregory, J., and Brennand, K. J. (2017). The importance of non-neuronal cell types in hiPSC-based disease modeling and drug screening. *Front. Cell Dev. Biol.* 5:117. doi: 10.3389/fcell.2017.00117

Hama, H., Hioki, H., Namiki, K., Hoshida, T., Kurokawa, H., Ishidate, F., et al. (2015). ScaleS: an optical clearing palette for biological imaging. *Nat. Neurosci.* 18, 1518–1529. doi: 10.1038/nn.4107

Holekamp, T. F., Turaga, D., and Holy, T. E. (2008). Fast three-dimensional fluorescence imaging of activity in neural populations by objective-coupled planar illumination microscopy. *Neuron* 57, 661–672. doi: 10.1016/j.neuron.2008.01.011

Huisken, J., Swoger, J., Del Bene, F., Wittbrodt, J., and Stelzer, E. H. (2004). Optical sectioning deep inside live embryos by selective plane illumination microscopy. *Science* 305, 1007–1009. doi: 10.1126/science.1100035

Kelava, I., and Lancaster, M. A. (2016). Dishing out mini-brains: current progress and future prospects in brain organoid research. *Dev. Biol.* 420, 199–209. doi: 10.1016/j.ydbio.2016.06.037

Keller, P. J., Schmidt, A. D., Wittbrodt, J., and Stelzer, E. H. (2008). Reconstruction of zebrafish early embryonic development by scanned light sheet microscopy. *Science* 322, 1065–1069. doi: 10.1126/science.1162493

Kino, G. S. (1995). "Intermediate optics in Nipkow disk microscopes," in *Handbook of Biological Confocal Microscopy*, ed. J. B. Pawley (Boston, MA: Springer), 155–165.

König, K. (2018). *Multiphoton Microscopy and Fluorescence Lifetime Imaging: Applications in Biology and Medicine*. Berlin: Walter de Gruyter GmbH and Co KG.

Kuwajima, T., Sitko, A. A., Bhansali, P., Jurgens, C., Guido, W., and Mason, C. (2013). ClearT: a detergent-and solvent-free clearing method for neuronal and non-neuronal tissue. *Development* 140, 1364–1368. doi: 10.1242/dev.091844

Lancaster, M. A., and Knoblich, J. A. (2014). Generation of cerebral organoids from human pluripotent stem cells. *Nat. Protoc.* 9, 2329–2340. doi: 10.1038/nprot.2014.158

Lancaster, M. A., Renner, M., Martin, C.-A., Wenzel, D., Bicknell, L. S., Hurles, M. E., et al. (2013). Cerebral organoids model human brain development and microcephaly. *Nature* 501, 373–379. doi: 10.1038/nature12517

Mahou, P., Vermot, J., Beaurepaire, E., and Supatto, W. (2014). Multicolor two-photon light-sheet microscopy. *Nat. Methods* 11, 600–601. doi: 10.1038/nmeth.2963

Mansour, A. A., Gonçalves, J. T., Bloyd, C. W., Li, H., Fernandes, S., Quang, D., et al. (2018). An *in vivo* model of functional and vascularized human brain organoids. *Nat. Biotechnol.* 36, 432–441. doi: 10.1038/nbt.4127

McGorty, R., Liu, H., Kamiyama, D., Dong, Z., Guo, S., and Huang, B. (2015). Open-top selective plane illumination microscope for conventionally mounted specimens. *Opt. Express* 23, 16142–16153. doi: 10.1364/oe.23.016142

Müllenbroich, M. C., Turrini, L., Silvestri, L., Alterini, T., Gheisari, A., Vanzi, F., et al. (2018). Bessel beam illumination reduces random and systematic errors in quantitative functional studies using light-sheet microscopy. *Front. Cell. Neurosci.* 12:315. doi: 10.3389/fncel.2018.00315

Oheim, M., Beaurepaire, E., Chaigneau, E., Mertz, J., and Charpak, S. (2001). Two-photon microscopy in brain tissue: parameters influencing the imaging depth. *J. Neurosci. Methods* 111, 29–37. doi: 10.1016/s0165-0270(01)00438-1

Prieto, D., Aparicio, G., Morande, P. E., and Zolessi, F. R. (2014). A fast, low cost, and highly efficient fluorescent DNA labeling method using methyl green. *Histochem. Cell Biol.* 142, 335–345. doi: 10.1007/s00418-014-1215-0

Rakotoson, I. (2018). *Validation d'une Approche de Microscopie Optique Pour l'étude Morpho-Fonctionnelle des Corps Embryoïdes et Mini-Brains Issus d'hIPSC.* Paris: Faculté des Sciences Fondamentales et Biomédicales, Université Paris Descartes.

Renner, M., Lancaster, M. A., Bian, S., Choi, H., Ku, T., Peer, A., et al. (2017). Self-organized developmental patterning and differentiation in cerebral organoids. *EMBO J.* 36, 1316–1329. doi: 10.15252/embj.201694700

Reynaud, E. G., Peychl, J., Huisken, J., and Tomancak, P. (2015). Guide to light-sheet microscopy for adventurous biologists. *Nat. Methods* 12, 30–34. doi: 10.1038/nmeth.3222

Ricard, C., Arroyo, E. D., He, C. X., Portera-Cailliau, C., Lepousez, G., Canepari, M., et al. (2018). Two-photon probes for *in vivo* multicolor microscopy of the structure and signals of brain cells. *Brain Struct. Funct.* 223, 3011–3043. doi: 10.1007/s00429-018-1678-1

Richardson, D. S., and Lichtman, J. W. (2015). Clarifying tissue clearing. *Cell* 162, 246–257. doi: 10.1016/j.cell.2015.06.067

Santi, P. A. (2011). Light sheet fluorescence microscopy: a review. *J. Histochem. Cytochem.* 59, 129–138. doi: 10.1369/0022155410394857

Schmidt, E. M., and Oheim, M. (2018). Two-photon imaging induces brain heating and calcium microdomain hyperactivity in cortical astrocytes. *bioRxiv* [Preprint]. doi: 10.1101/321091

Shimozawa, K. Y., Kondo, T., Hayashi, S., Shitamukai, A., Konno, D., Matsuzaki, F., et al. (2013). Improving spinning disk confocal microscopy by preventing pinhole cross-talk for intravital imaging. *Proc. Natl. Acad. Sci. U S A* 110, 3399–3404. doi: 10.1073/pnas.1303361110

Smith, P. G., Baldacchini, T., Carter, J., and Zadoyan, R. (2012). Two-photon microscopy/mutlimodal imaging: femtosecond laser developments advance two-photon imaging. *BioOptics World* 5. Available online at: http://www.bioopticsworld.com/articles/print/volume-5/issue-04/features/femtosecond-laser-developments-advance-two-photon-imaging.html. Accessed July 26, 2019.

Stelzer, E. H. (2015). Light-sheet fluorescence microscopy for quantitative biology. *Nat. Methods* 12, 23–26. doi: 10.1038/nmeth.3219

Truong, T. V., Supatto, W., Koos, D. S., Choi, J. M., and Fraser, S. E. (2011). Deep and fast live imaging with two-photon scanned light-sheet microscopy. *Nat. Methods* 8, 757–760. doi: 10.1038/nmeth.1652

Vettenburg, T., Dalgarno, H. I., Nylk, J., Coll-Lladó, C., Ferrier, D. E., Čižmár, T., et al. (2014). Light-sheet microscopy using an Airy beam. *Nat. Methods* 11, 541–544. doi: 10.1038/nmeth.2922

Wan, P., Zhu, J., Xu, J., Li, Y., Yu, T., and Zhu, D. (2018). Evaluation of seven optical clearing methods in mouse brain. *Neurophotonics* 5:035007. doi: 10.1117/1.nph.5.3.035007

Wassie, A. T., Zhao, Y., and Boyden, E. S. (2018). Expansion microscopy: principles and uses in biological research. *Nat. Methods* 16, 33–41. doi: 10.1038/s41592-018-0219-4

Ying, Q.-L., and Smith, A. G. (2003). Defined conditions for neural commitment and differentiation. *Meth. Enzymol.* 365, 327–341. doi: 10.1016/s0076-6879(03)65023-8

Yu, T., Zhu, J., Li, Y., Ma, Y., Wang, J., Cheng, X., et al. (2018). RTF: a rapid and versatile tissue optical clearing method. *Sci. Rep.* 8:1964. doi: 10.1038/s41598-018-20306-3

Zhao, M., Zhang, H., Li, Y., Ashok, A., Liang, R., Zhou, W., et al. (2014). Cellular imaging of deep organ using two-photon Bessel light-sheet nonlinear structured illumination microscopy. *Biomed. Opt. Express* 5, 1296–1308. doi: 10.1364/BOE.5.001296

Conflict of Interest Statement: RU is the founder and CEO of TILL.id, AD and CS are employees of TILL.id.

The remaining authors declare that the research was conducted in the absence of any commercial or financial relationships that could be construed as a potential conflict of interest.

frontiers in Neuroanatomy

REVIEW
published: 26 November 2019
doi: 10.3389/fnana.2019.00093

Adeno-Associated Virus Technologies and Methods for Targeted Neuronal Manipulation

*Leila Haery[1], Benjamin E. Deverman[2], Katherine S. Matho[3], Ali Cetin[4], Kenton Woodard[5], Connie Cepko[6,7], Karen I. Guerin[1], Meghan A. Rego[1], Ina Ersing[1], Susanna M. Bachle[1], Joanne Kamens[1] and Melina Fan[1]**

[1]Addgene, Watertown, MA, United States, [2]Stanley Center for Psychiatric Research, Broad Institute of MIT and Harvard, Cambridge, MA, United States, [3]Cold Spring Harbor Laboratory, Cold Spring Harbor, NY, United States, [4]Allen Institute for Brain Science, Seattle, WA, United States, [5]Penn Vector Core, Gene Therapy Program, Perelman School of Medicine, University of Pennsylvania, Philadelphia, PA, United States, [6]Department of Genetics, Harvard Medical School, Howard Hughes Medical Institute, Boston, MA, United States, [7]Department of Ophthalmology, Harvard Medical School, Howard Hughes Medical Institute, Boston, MA, United States

Cell-type-specific expression of molecular tools and sensors is critical to construct circuit diagrams and to investigate the activity and function of neurons within the nervous system. Strategies for targeted manipulation include combinations of classical genetic tools such as Cre/loxP and Flp/FRT, use of cis-regulatory elements, targeted knock-in transgenic mice, and gene delivery by AAV and other viral vectors. The combination of these complex technologies with the goal of precise neuronal targeting is a challenge in the lab. This report will discuss the theoretical and practical aspects of combining current technologies and establish best practices for achieving targeted manipulation of specific cell types. Novel applications and tools, as well as areas for development, will be envisioned and discussed.

Keywords: AAV, neuroscience, viral vectors, cell-type specificity, gene delivery, intersectional methods, targeted neuronal manipulation, virus technologies

OPEN ACCESS

Edited by:
Jose L. Lanciego, University of Navarra, Spain

Reviewed by:
Els Henckaerts, KU Leuven, Belgium
Akiya Watakabe, RIKEN Center for Brain Science (CBS), Japan

****Correspondence:***
Melina Fan
mfan@addgene.org

Received: *22 August 2019*
Accepted: *30 October 2019*
Published: *26 November 2019*

Citation:
Haery L, Deverman BE, Matho KS, Cetin A, Woodard K, Cepko C, Guerin KI, Rego MA, Ersing I, Bachle SM, Kamens J and Fan M (2019) Adeno-Associated Virus Technologies and Methods for Targeted Neuronal Manipulation. Front. Neuroanat. 13:93. doi: 10.3389/fnana.2019.00093

INTRODUCTION

Understanding neural networks as they relate to development, behavior, and learning is a critical objective of neuroscience. These questions can be addressed, in part, by understanding the role of specific neural cells and brain regions, as well as the impact of individual molecules in these circuits. The successful execution of these neurobiology studies requires methods that are highly targetable, efficient, and precise. In this regard, recombinant adeno-associated viral vectors (herein referred to as AAV) are powerful tools that can be used both to target and manipulate specific neuronal subtypes (defined based on gene expression, location, and connectivity) and non-neuronal cell types within the nervous system.

Scientists using AAV for gene transfer and/or neuronal targeting must consider various questions about experimental design, including: (1) how to best deliver/administer AAV (**Figure 1A**); (2) which AAV serotype to use (**Figure 1B**); and (3) how to drive gene expression with gene regulatory elements (both within the AAV genome and the host animal or cell line;

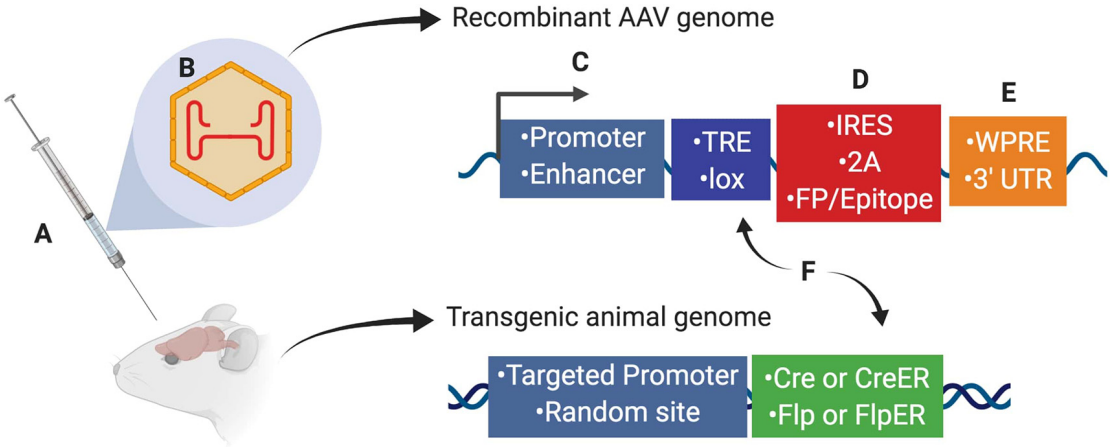

FIGURE 1 | Several aspects of experimental design affect neuronal targeting and manipulation including **(A)** viral delivery method, **(B)** composition of viral capsid proteins, **(C)** promoters and/or enhancers driving transgene expression, **(D)** IRES or 2A elements for multicistronic expression coupled with fluorescent proteins (FP) or protein epitopes, **(E)** post-translational regulatory elements such as WPRE or 3′-UTR, and **(F)** Recombinase (Cre, CreER, Flp, or FlpER) expression from transgenic driver lines (inserted genomically *via* targeted or random integration) and ligand-dependent or recombinase-dependent expression elements such as TRE or lox sites, respectively. Abbreviations: TRE, tetracycline-response element; lox, LoxP sequence; IRES, internal ribosomal entry site; 2A, 2A sequence for self-cleavage; FP, fluorescent protein; WPRE, woodchuck hepatitis virus posttranscriptional regulatory element; 3′-UTR, 3′-untranslated sequence.

Figures 1C–F). These and many other factors can affect how efficiently cells of interest are targeted by AAV. Further, experimental parameters such as AAV titer and dosage can impact AAV efficiency, and these details are often omitted from experimental methods in the literature and can be expensive and timely to determine empirically for each study. Overall, designing an experiment with AAV is multifaceted and suboptimal experimental design can drastically reduce the quality of results. In this report, we will discuss practical aspects of using AAV and considerations for designing experiments.

SELECTING THE ROUTE OF ADMINISTRATION AND CAPSID

AAV tropism, as dictated by AAV capsid proteins, is an important factor affecting transduction efficiency and specificity across cell types. Since the mechanism of AAV transduction is through the interaction of the AAV capsid with cell surface proteins and glycans, protein composition of the capsid (i.e., the AAV serotype) and the cell surface (i.e., based on cell type) determine transduction efficiency. Additionally, as the landscape of cell surface molecules varies across species, the efficiency of AAV may subsequently vary considerably across species and strains (Watakabe et al., 2015; El-Shamayleh et al., 2016; Hordeaux et al., 2018; Huang et al., 2019). Consequently, serotype and route of delivery should be carefully considered when designing experiments (**Figures 1A,B**). For an overview of the primary receptors for AAV serotypes, see Schultz and Chamberlain (2008).

Direct Intraparenchymal Delivery

When injected directly into the brain, many of the naturally-occurring AAV capsids, which share homology ranging from 65% to 99% (Drouin and Agbandje-McKenna, 2013), have distinct but significantly overlapping tropisms and distribution characteristics. AAV1, AAV2, AAV5, AAV8, AAV9 and the engineered variant AAV-DJ are commonly used to target local populations of neurons after direct injections (**Table 1**).

In addition to exhibiting local transduction, several serotypes exhibit transduction distal to the injection site (Burger et al., 2004; Cearley and Wolfe, 2006, 2007; Klein et al., 2006, 2008; Li et al., 2006; Reimsnider et al., 2007; Sondhi et al., 2007; Taymans et al., 2007; Cearley et al., 2008; Hollis et al., 2008; Hadaczek et al., 2009; Masamizu et al., 2011; Bu et al., 2012) and the mechanisms of these phenotypes are active areas of investigation (Castle et al., 2014). The AAV vector purification method has also been shown to impact transduction patterns (Klein et al., 2008).

Furthermore, there are important differences in how far different capsid variants spread from the injection site—AAV2 and AAV-DJ diffusion are more confined and, therefore, these capsids are often chosen for applications that require precise targeting. While expression from AAV2 is mostly neuronal, several serotypes, including AAV1, AAV5, AAV8 and AAV9, also transduce astrocytes and oligodendrocytes.

Despite the tremendous volume of work on serotype-dependent expression patterns and the complexity of the mechanisms both hypothesized and shown to drive these phenotypes, the ability to predict confidently the expression pattern in a particular experimental setup still requires empirical evidence. A non-exhaustive list of reported characteristics for several serotypes is outlined (**Table 2**) and can be used to narrow down suitable serotypes, though the importance of empirical validation at the onset of each study cannot be understated. Importantly, results reported in this table may vary based on anatomical region, though the results have not been summarized in this report to that degree.

TABLE 1 | AAV administration routes for neuroscience.

	Administration route		
	Direct	**Intravenous**	**Delivery into the CSF (IT/ICV/CM)**
Advantages	• Regional expression achievable (serotype dependent; Kaplitt et al., 1994; McCown et al., 1996; Peel et al., 1997)	• CNS or PNS-wide transduction (Zincarelli et al., 2008)	• IT injection can be used to target spinal motor neurons and dorsal root ganglia (Zhang et al., 2010)
	• High levels of expression achievable (high MOI)	• Quick, non-invasive (Stoica et al., 2013)	• Neonatal ICV injections can provide widespread gene delivery to the CNS (Hammond et al., 2017)
	• Requires small volumes of virus	• Does not require surgical expertise (Stoica et al., 2013)	• May (Gray et al., 2013) or may not (Samaranch et al., 2011) allow CNS expression in the presence of neutralizing antibodies
	• Reduced off-target effects	• Lower more uniform expression (Chan et al., 2017)	
		• Sparse labeling is possible (Chan et al., 2017)	
Disadvantages	• Requires invasive surgery (Stoica et al., 2013)	• Higher dose and volume of virus required	• Expression is not confined to the CNS (Hinderer et al., 2014)
	• Damage to the targeted area (Mastakov et al., 2001; Carty et al., 2010)	• Greater risk of immune response (Colella et al., 2018)	• Requires moderately large volumes of virus
	• Challenging in certain deep brain structures	• Off-target effects may confound experiment	• Expression is not as uniform as it is after systemic delivery (Hinderer et al., 2014)
	• Transduction gradient from injection site		
Expression considerations	• High levels of expression may be important for opsin expression (Yazdan-Shahmorad et al., 2018)	• Moderate expression provided by IV AAV-PHP.B/eB may be preferable for GCaMP6 expression (no nuclear expression observed), see Hillier et al. (2017)	• Expression is higher around CSF spaces and the brain/SC surface (Hinderer et al., 2014; Lukashchuk et al., 2016)
	• High-level expression makes cell-type specific transgene expression using regulatory elements more challenging		
Capsids	• AAV2—confined spread, mostly neuronal (Kaplitt et al., 1994; McCown et al., 1996; During et al., 1998; Mandel et al., 1998; Davidson et al., 2000; Burger et al., 2004)	• AAV9 and rh.10—efficient neonatal CNS transduction (Foust et al., 2009, 2010; Zhang et al., 2011; Ruzo et al., 2012)	• AAV7, AAV9, and rh.10 are the most widely tested serotypes for delivery into the CSF (Federici et al., 2012; Samaranch et al., 2013; Gurda et al., 2016; Borel et al., 2016)
	• AAV-DJ—Confined spread, higher expression (vs. AAV2; Grimm et al., 2008)	• AAV-BR1—brain endothelial cell-specific (Marchiò et al., 2016)	• AAV4 enables transduction of ependymal cells (Liu et al., 2005)
	• AAV1, 5 and 8—widespread, moderate expression, neurons and glia (Burger et al., 2004; Tenenbaum et al., 2004; Cearley and Wolfe, 2006; Li et al., 2006; Taymans et al., 2007; Hadaczek et al., 2009; Dodiya et al., 2010; Masamizu et al., 2010, 2011)	• AAV-PHP.B—enhanced neuron and glial transduction after adult IV injection in mice (Deverman et al., 2016; Chan et al., 2017)	• AAV SCH9 and AAV4.18 enable SVZ progenitor cell transduction (Murlidharan et al., 2015; Ojala et al., 2018)

(Continued)

TABLE 1 | (Continued)

	Administration route		
	Direct	**Intravenous**	**Delivery into the CSF (IT/ICV/CM)**
	• AAV2-Retro—widespread distribution, enhanced axonal uptake and retrograde expression (Tervo et al., 2016)	• AAV-PHP.eB—further evolved AAV-PHP.B variant with improved neuronal transduction (Deverman et al., 2016; Chan et al., 2017)	
	• AAV1—paired with Cre exhibits trans-synaptic (anterograde) transduction (Zingg et al., 2017)	• AAV-PHP.S—evolved capsid with improved transduction of peripheral nerves and heart (Chan et al., 2017)	
	• AAV2-HBKO—robust and widespread expression, primarily in neuronal cells, higher expression than parental AAV2 (Sullivan et al., 2018)		
	• AAV-TT—widespread and high transduction of both glia and neuronal cells relative to parental AAV2. Wider spread than AAV9 and rh.10 (Tordo et al., 2018)		

Systemic Delivery

Several natural AAV capsids cross the blood-brain barrier (BBB). In contrast to direct injections, intravenous injections of AAV can provide a central nervous system (CNS)-wide gene delivery. This activity is present across several species and is most pronounced when AAV is administered to the neonate. Neonatal injections of AAV9 and rh.10 have been used to transduce neurons broadly across the CNS. However, when delivered at later developmental stages including in the adult, transduction is more limited and primarily restricted to endothelial cells and astrocytes, with transduction occurring in 1–2% of neurons in the forebrain (Foust et al., 2009; Dufour et al., 2014; Deverman et al., 2016). In this context, engineered AAV capsids have provided new and dramatically more efficient options for widespread gene delivery to the CNS. The first of these vectors, AAV-PHP.B, enabled researchers to deliver genes to more than 50% of neurons and astrocytes across numerous brain regions with a single non-invasive injection (Deverman et al., 2016). Achieving this efficiency requires relatively high viral doses ($\sim 1 \times 10^{14}$ vector genomes/kg), thus requiring large volumes of high titer virus. A further-evolved AAV-PHP.B variant, AAV-PHP.eB, addresses this issue and can achieve >50% transduction of most neuron and astrocyte populations even with a 20-fold reduction in dose (Chan et al., 2017). While the activity of the PHP capsids is not universally observed across all species, or even strains of a given species, the receptor engaged by the PHP capsids during AAV transduction has been identified and can be used to predict permissivities of cell or tissue types to these engineered capsids (Hordeaux et al., 2019; Huang et al., 2019). In addition, the same group has developed an additional AAV variant (the PHP.S variant) that can efficiently transduce dorsal root ganglia and other peripheral neuron populations following systemic administration, which should enable the study of these otherwise difficult to target peripheral neuron populations (Chan et al., 2017).

CSF Delivery

The third option for gene delivery to the CNS is to inject vectors into the cerebral spinal fluid (CSF). Several access points can be used: the lateral ventricle (intracerebroventricular, ICV), the cisterna magna (CM), subpial (Miyanohara et al., 2016) or the intrathecal (IT) space along the spinal cord. When performed in neonates, ICV AAV administration can provide widespread gene delivery. In the adult, ICV and CM injections result in gene delivery in multiple brain regions, however, the expression is not uniform across all brain regions and superficial structures are preferentially targeted. Beyond neurons, ICV injections also provide access to periventricular cell populations. For example, after ICV injection, AAV4 can be used to transduce the ependymal cells (Liu et al., 2005), and two engineered AAV capsids, SCH9 and AAV4.18, enable transduction of subventricular zone neural progenitors (Murlidharan et al., 2015; Ojala et al., 2018). IT injection can be used to deliver genes to spinal cord motor neurons and dorsal root ganglions (Foust et al., 2010; Federici et al., 2012; Schuster et al., 2014).

Retrograde and Anterograde Transport for Circuit Studies

AAV vectors are commonly used as part of circuit studies. Numerous natural AAV serotypes exhibit retrograde trafficking activity from their uptake at axon terminals (see **Table 2**). However, retrograde transduction with natural serotypes such as AAV1, AAV2, AAV6, and AAV9 requires high vector doses due to the relative inefficiency of this transduction mechanism. More recently Tervo et al. (2016) and Davidsson et al. (2018) have created modified capsids AAV2-Retro and AAV MNM008, respectively, that provide efficient transduction of neurons that send axon projections into the injection site. Transduction efficiencies of both capsids are shown to be circuit-dependent, and thus capsids should be validated for circuits of interest when planning experiments. Zingg et al. (2017) report that AAV1 and AAV9 exhibit transsynaptic anterograde transport

TABLE 2 | Transduction characteristics of select AAV serotypes.

Serotype	Transport phenotypes[a]	Transduction levels	Spread from injection site[b]	Transduced cells	Additional notes
AAV1	Retrograde (Burger et al., 2004; Reimsnider et al., 2007; Hollis et al., 2008; Bu et al., 2012)	High, similar to AAV9, AAVrh10 (Cearley et al., 2008; Aschauer et al., 2013)	Greater than AAV2, similar to AAV5, AAV8 (Burger et al., 2004)	Primarily neurons (Burger et al., 2004; Dodiya et al., 2010; Masamizu et al., 2010)	Expression levels were stable over a 9-month period at the injection site (Reimsnider et al., 2007)
	Anterograde (Cearley et al., 2008)		Far from the injection site (Burger et al., 2004; Cearley and Wolfe, 2006; Sondhi et al., 2007; Taymans et al., 2007; Bu et al., 2012; Watakabe et al., 2015)	Astrocytes at low frequency (Tenenbaum et al., 2004; Li et al., 2006; Taymans et al., 2007; Hadaczek et al., 2009)	Expression *via* retrograde transduction decreased over a 9 month period (Reimsnider et al., 2007)
	Anterograde transsynaptic at high titers (Zingg et al., 2017)				
AAV2	Anterograde (Salegio et al., 2013)	Lower than AAV1 and AAV5 (Davidson et al., 2000; Burger et al., 2004; Aschauer et al., 2013)	Smaller than AAV1, AAV5, AAV8 and AAV9 (Burger et al., 2004; Taymans et al., 2007; Sondhi et al., 2007; Watakabe et al., 2015)	Neurons (to different degrees and not all types; Kaplitt et al., 1994; McCown et al., 1996; During et al., 1998; Mandel et al., 1998)	Expression levels were stable over a 9-month period at the injection site (Reimsnider et al., 2007)
	Retrograde at >2 months following gene transfer (Kaspar et al., 2002; Halbert et al., 2006; Sondhi et al., 2007)			Other cell types at low efficiencies (Kaplitt et al., 1994; McCown et al., 1996; Peel et al., 1997; Klein et al., 1998; Lo et al., 1999; Davidson et al., 2000; Cucchiarini et al., 2003)	
				Astrocytes at low frequency (Taymans et al., 2007)	
AAV5	Anterograde (Aschauer et al., 2013)	Higher than AAV2, similar to AAV8 (Davidson et al., 2000; Taymans et al., 2007; Aschauer et al., 2013)	Greater than AAV2, similar to AAV1, AAV8, AAV9 at high doses (Burger et al., 2004; Sondhi et al., 2007; Taymans et al., 2007; Aschauer et al., 2013; Watakabe et al., 2015)	Primarily neurons (Burger et al., 2004)	Expression levels increased over time in cells at the injection site (Reimsnider et al., 2007)
	Retrograde (Burger et al., 2004; Reimsnider et al., 2007)			Astrocyte at low frequency (Tenenbaum et al., 2004; Taymans et al., 2007)	Expression *via* retrograde transduction decreased over a 9-month period (Reimsnider et al., 2007)
			Greater than AAV8 at low doses (Taymans et al., 2007)	Oligodendrocytes (von Jonquieres et al., 2013)	
AAV8	Anterograde (Masamizu et al., 2011)	Higher than AAV2, similar to AAV1, AAV5 (Taymans et al., 2007; Aschauer et al., 2013)	Greater than AAV2, similar to AAV1, AAV5, AAV9 at high doses (Sondhi et al., 2007; Watakabe et al., 2015)	Primarily neurons (Cearley and Wolfe, 2006; Masamizu et al., 2010)	Expression levels then remained stable over a 9-month period (Reimsnider et al., 2007)
	Retrograde (Masamizu et al., 2011)	Higher than AAV9 (Klein et al., 2008)	Smaller than AAV5 at low doses (Taymans et al., 2007)	Astrocytes at low frequency (Taymans et al., 2007)	Expression *via* retrograde transduction increased then decreased over a 9-month period (Reimsnider et al., 2007)
				Oligodendrocytes at low frequency (Masamizu et al., 2011; von Jonquieres et al., 2013)	

(Continued)

TABLE 2 | (Continued)

Serotype	Transport phenotypes[a]	Transduction levels	Spread from injection site[b]	Transduced cells	Additional notes
AAV9	Anterograde (Cearley et al., 2008; Masamizu et al., 2011; Castle et al., 2014) Retrograde (Cearley and Wolfe, 2006; Masamizu et al., 2011) Anterograde transsynaptic at high titers (Zingg et al., 2017)	High, similar to AAV1, AAVrh10 (Cearley and Wolfe, 2006; Cearley et al., 2008; Aschauer et al., 2013) Lower than AAV8, similar to AAVrh10 (Klein et al., 2008)	Similar to AAV1, AAV5, AAV8 and greater than AAV2 (Watakabe et al., 2015)	Primarily neurons (Cearley and Wolfe, 2006; Masamizu et al., 2011) Astrocytes (Hammond et al., 2017) Oligodendrocytes at low frequency (Masamizu et al., 2011)	Transport and Contralateral transduction observed (Cearley and Wolfe, 2006)
AAV rh10	Anterograde (Klein et al., 2008) Retrograde (Klein et al., 2008)	High, similar to AAV1, AAV9, AAVrh10 (Cearley and Wolfe, 2006; Klein et al., 2008)	Far from the injection site (Burger et al., 2004; Cearley and Wolfe, 2006; Sondhi et al., 2007; Bu et al., 2012)	Primarily neurons (Cearley and Wolfe, 2006; Sondhi et al., 2007; Cearley et al., 2008)	

[a] *For relative retrograde transport efficiencies, see Tervo et al. (2016).* [b] *For relative retrograde transport efficiencies, see Tervo et al. (2016).*

at high titers, specifically showing that AAV1-directed Cre can activate Cre-dependent transgene expression in a post-synaptic neuron. Importantly, they note that retrograde transmission also can occur, making interpretation clear only for circuits where there is a unidirectional pattern of connectivity.

AAV Can Cause Toxicity at High Doses

Although AAV is less inflammatory than some other viruses, it is not inert with respect to the innate (Rogers et al., 2011) or adaptive (Mingozzi and High, 2011) immune system, and may also perturb other cellular activities. Several studies have found neurotoxicity when the virus was delivered systemically or *via* direct injections into the CNS, or into the sub-retinal space of the retina. For rabies monosynaptic tracing studies, AAV is often delivered as a helper virus to supply TVA and rabies G protein. A recent study found that high doses of helper did not enable rabies infection or tracing, while diluted preparations did (Lavin et al., 2019). Although the mechanism was not determined, the authors suggest that the high doses were toxic. Similarly, neurotoxicity was seen in piglets injected systemically (Hinderer et al., 2014). In the retina, toxicity was associated with dose, if the viral promoter was expressed in a support cell type, the retinal pigmented epithelium, but not if the viral promoter activity was restricted to photoreceptor cells (Xiong et al., 2019). Innate immunity has been shown to result from stimulation of TLR9, a sensor of unmethylated CpG's, in studies of AAV infection of muscle (Zhu et al., 2009) and liver (Martino et al., 2011). Inclusion of a short TLR9 blocking oligonucleotide within the AAV genome has been shown to alleviate this problem in some instances (Chan et al., 2019). It is thus worth carefully considering this aspect of virus dose when setting up an experiment.

In summary, a consensus of opinion has not been reached regarding the best serotype for each cell type, brain region or application. Choosing the optimal serotype requires reviewing the literature most relevant to the planned experiment and performing pilot testing for new or at least for challenging applications. As new engineered capsids with unique features continue to be developed, the available options will become more numerous and more powerful (Deverman et al., 2016; Tervo et al., 2016; Chan et al., 2017; Davidsson et al., 2018; Ojala et al., 2018).

CONTROLLING GENE EXPRESSION WITH REGULATORY ELEMENTS

Cre and Flp recombinase-dependent expression elements within AAV vectors remain the go-to system for restricting transgene expression to genetically defined cell types in model organisms. However, few Cre or Flp transgenic lines have been developed in other mammalian species. Furthermore, breeding multiple transgenic lines to generate the desired offspring can be time consuming and expensive. Therefore, there is significant interest in developing the means to achieve similar expression specificity in nontransgenic animals using flexible vector-based approaches that will translate across species.

Cis-regulatory elements can be used to control transgene expression from AAV genomes. These elements include promoters and enhancers (**Figure 1C**), as well as introns, micro-RNA recognition sequences, and internal ribosome entry sites (IRES; **Figure 1D**) that can be used to tailor RNA processing, stability, and translation to the experimental needs. Here we will discuss how these regulatory elements can be used to restrict AAV-mediated gene expression.

Enhancers and Promoters

Enhancer and promoters (hereafter referred to as promoters for simplicity) can generally be divided into two classes: general/ubiquitous and cell type-specific. Typically, ubiquitous promoters provide high-level, long-term expression in most cell

types, though some, such as the viral CMV promoter, have been shown to exhibit silencing in specific tissues over time (McCown et al., 1996; Klein et al., 1998; Paterna et al., 2000; Tenenbaum et al., 2004; **Table 3**).

AAV and other single-stranded DNA viruses evolutionarily exhibit some of the smallest viral genomes (Campillo-Balderas et al., 2015), which has generally provided a selective pressure toward shorter promoter sequences. In contrast, the regulatory elements that control mammalian gene transcription are often distributed over thousands to hundreds of thousands of bases. Due to the limited packaging capacity of the AAV genome, identifying AAV-compatible promoters has been challenging and the development of shortened promoters is an area of active study (Nathanson et al., 2009a; de Leeuw et al., 2016). A list of cell type-specific promoters compatible with AAV vectors is provided in **Table 4**. High expression levels are not optimal for every application and alternative regulatory elements, such as those from the mammalian MeCP2 or PGK genes (**Table 3**) may be suitable for experiments where high-level viral enhancer driven expression is not desired. General recommendations for expression levels of various types of transgenes are summarized in **Table 5**.

Multicistronic Vectors

Although AAV vectors have a limited packaging capacity, it is possible to express multiple short transgenes from a single vector using one of several approaches: (1) separate translational units where each cDNA is controlled by separate 5′ and 3′ regulatory elements; (2) using IRES sequences to insert two separate translational units into a single mRNA; or (3) the use of viral 2A sequences to generate separate proteins from the same translational unit (**Figure 1D**). **Table 6** highlights considerations for choosing between the use of IRES sequences and 2A "self-cleaving" peptides.

One important consideration when evaluating expression strategies and determining specificity is that the expression levels required for reporter detection may not match what is necessary for the activity of an opsin, DREADD or recombinase. For example, fluorescent proteins are commonly used to evaluate gene regulatory elements and vector design. However, fluorescent reporter assays may give the false impression of specificity if high levels of expression are seen in target cell types and low-level expression goes undetected in off-target populations. If these same regulatory elements are then used to drive DREADDs or Cre, which can mediate their effects at low expression levels, then the specificity may appear reduced. If this goes unexamined, then the interpretation of experimental results could be compromised. Moreover, though they are commonly used, fluorescent proteins are not necessarily inert and can lead to immune responses in larger animals (Samaranch et al., 2014), and over-expression related toxicities in mice.

Post-transcriptional Regulatory Elements

Transgene expression can also be controlled post-transcriptionally through the use of elements impacting RNA splicing, nuclear export, stability, and translation into proteins (**Figure 1E**). Inclusion of an intron can have positive impacts on expression levels. Introns have also been combined creatively with recombinase sites and partially inverted transgenes to achieve tight intersectional control of transgene expression (Fenno et al., 2014, 2017). Many recombinant AAV genomes also include a woodchuck hepatitis virus posttranscriptional regulatory element (WPRE), which can dramatically enhance expression. For several examples of how

TABLE 3 | Ubiquitous enhancers and promoters.

Promoter	Characteristics	Length (bp)	Notes	References
CMV, Cytomegalovirus early enhancer and promoter	Ubiquitous	590–800	Robust, rapid, long term expression in many cell types. Prone to silencing in some tissues, specifically the hippocampus, striatum, and substantia nigra. Silenced by 10 weeks in the spinal cord. Only modest expression in glial cells in rat. Minimal expression in rAAV2-retro helper- packaged AAV	Thomsen et al. (1984), McCown et al. (1996), Klein et al. (1998), Paterna et al. (2000), Tenenbaum et al. (2004), Gray et al. (2011) and Yaguchi et al. (2013)
CAG, CMV enhancer, CBA promoter, globin intron	Ubiquitous	1,700	Expression in excitatory and inhibitory neurons and glia	Miyazaki et al. (1989) and Nathanson et al. (2009b)
CAGGS, CMV immediate-early enhancer, CBA promoter, hybrid intron (CBA exon1/intron1/rabbit b-globin acceptor)	Ubiquitous, strong in neurons	1,600	Ubiquitous and long term expression in the brain	Niwa et al. (1991) and Klein et al. (1998)
CBh, CBA hybrid intron: CMV early enhancer, CBA promoter, CBA/MVM intron	Ubiquitous, strong in neurons	800	Stronger expression than the CBA promoter	Gray et al. (2011)
EF1a, Elongation Factor 1a	Ubiquitous, strong in neurons	1,200, 2,500	Moderate, lower expression in glia compared with CMV/CAG	Kim et al. (1990) and Gill et al. (2001)
EFS, EF1a short version	Ubiquitous	250		Montiel-Equihua et al. (2012)
UBC, Ubiquitin C	Ubiquitous, weak	400, 1,200		Seita et al. (2019)
PGK, phosphoglycerate kinase	Ubiquitous	425	Weak expression	Qin et al. (2010)

TABLE 4 | Cell type-specific promoters.

Promoter	Characteristics	Length (bp)	Notes	References
hSyn1, human Synapsin1	Neuronal, broad	485	Broadly neuronal in mice, low-level expression in Purkinje cells. Excitatory neuron expression in monkeys and rats. Inhibitory neuron expression also observed, with serotype and brain-region dependent biases	Hoesche et al. (1993), Kügler et al. (2003), Dittgen et al. (2004), Nathanson et al. (2009b) and Yaguchi et al. (2013)
MeCP2, mMeCP2 promoter	Mostly neuronal, broad, weak expression	229	Expresses in neurons and in spinal cord motor neurons	Gray et al. (2011)
NSE, Neuron-specific enolase	Neuronal, broad	1,300, 1,800	Provides strong and long-term expression	Xu et al. (2001)
BM88, Neuron-specific protein	Preferentially neuronal	88		Pignataro et al. (2017)
CaMKII, Ca^{2+}/Calmodulin-dependent kinase II	Neuronal, glutamatergic (cortical)	400, 1,200, 2,300	Excitatory neuron preference expression in monkeys and rat. Some inhibitory neuron expression in mouse varies with serotype, titer, and brain region	Dittgen et al. (2004), Hioki et al. (2007), Nathanson et al. (2009b), Yaguchi et al. (2013) and Scheyltjens et al. (2015)
mDLX, mouse DLX5/6 enhancer, minimal promoter and chimeric intron	Forebrain GABAergic neurons	850	Validated GABAergic neuron specificity in multiple serotypes	Dimidschstein et al. (2016)
mTH/rTH, mouse/rat Tyrosine Hydroxylase	Catecholamine neurons	2,500		Oh et al. (2009) and Chan et al. (2017)
DBH, Dopamine β hydroxylase	Adrenergic and noradrenergic neurons	1,150		Hwang et al. (2001)
PRSx8, DBH synthetic	Adrenergic and noradrenergic neurons	NR	Evaluated in noradrenergic neurons in the LC	Hwang et al. (2001)
PCP2, Purkinje Cell Protein 2 (Ple155)	Purkinje neurons	1,650		de Leeuw et al. (2016) and Chan et al. (2017)
FEV, ETS transcription factor (Ple67)	Serotonergic neurons	2,000	Serotonergic neurons	de Leeuw et al. (2016) and Chan et al. (2017)
MCH, Melanin-concentrating hormone	Subpopulation, dorsal lateral hypothalamus	830		van den Pol et al. (2004)
SLC6A4, Serotonin Transporter (Ple198)		3,050	Expression is strongest in the thalamus	de Leeuw et al. (2016)
NR2E1 (Ple264)	Müller glia	2,030		de Leeuw et al. (2016)
GfABC1D, truncated GFAP	Astrocytes	680		Lee et al. (2008)
Aldh1l1	Astrocytes	1,300		Koh et al. (2017)
mMBP, mouse myelin basic protein	Oligodendrocytes	1,900		Gow et al. (1992)
MAG, Myelin-Associated Glycoprotein	Oligodendrocytes	300, 1,500, 2,200	All provide expression in oligodendrocytes, 1,500 and 2,200 bp versions are more specific	von Jonquieres et al. (2016)
ICAM-2, Intracellular Adhesion Molecule 2	Endothelial	330		Cowan et al. (1998)
CLDN5, Claudin5 (Ple261)	Endothelial	2,960		de Leeuw et al. (2016)
Tie-2, TEK Receptor Tyrosine Kinase	Endothelial	730		Leung et al. (2009)
vWF, von Willebrand Factor	Endothelial	730		Jahroudi and Lynch (1994)
FLT1, Endothelial Growth Factor Receptor	Endothelial	1,030		Morishita et al. (1995)
TRE, rtTA-tTA responsive element	Inducible	320–400, (1,400 w/tTA)		Chenuaud et al. (2004) and Chan et al. (2017)
c-FOS	Activity-dependent	760		Ye et al. (2016)
eSARE	Activity-dependent	980		Kawashima et al. (2014)

the inclusion of a WPRE affects expression from AAV vectors, please see de Leeuw et al. (2016).

Complementary miRNA target sites (TS) are frequently engineered into the 3′-untranslated region (3′-UTR) of recombinant AAV vector genomes to mitigate off-target transgene expression. These sequences are complementary to miRNAs expressed within off-target cell types but not within the target population. miRNA binding to the perfectly complementary miRNA TS results in degradation of the RNA. Inclusion of multiple copies of the short miRNA TS sequences can dramatically lower off-target transgene expression. For example, by incorporating three copies each of miR-1 and miR-122, which are specifically expressed in muscle and liver, respectively, Xie et al. (2011) reduced transgene expression from intravenously administered AAV9 in muscle, heart, and liver, while maintaining brain expression. miRNA TS that enhance the restriction of lentiviral mediated gene expression to GABAergic neurons have also been identified (Xie et al., 2011; Keaveney et al., 2018), as have miRNA TS that result in more selective GCaMP6f expression from a strong ubiquitous promoter (Challis et al., 2019). Given their short lengths, miRNA TS can be multiplexed within the same genome, making them

TABLE 5 | General expression considerations for specific transgenes and applications.

Transgene	Application	Optimal expression level
Opsins	Optogenetics	High
DREADDs	Chemogenetics	Low for optimal specificity
Ca^{2+} sensors	Activity monitoring	Moderate
Voltage sensors	Activity monitoring	Moderate-high
dLight1	Dopamine indicator	Not yet known
Fluorescent reporters (XFPs)	Expression reporters, protein tagging	Moderate
Luciferase/AkaLuc	Expression reporter	Low-High
Cre/FlpO/Dre/KD/B3 Recombinases	Intersectional expression/Circuit studies	Low
CRISPR-Cas9	Gene editing	Moderate-High
TVA and rabies G	Circuit studies/retrograde tracing/TRIO/cTRIO	TVA (low) Rabies G (Moderate)

TABLE 6 | Bicistronic expression options.

	Bicistronic expression elements	
	2A	IRES
Advantages	• Requires minimal sequence space • Results in similar expression of both proteins • Can be used to express >2 proteins	• Protein products are unmodified
Disadvantages	• May reduce expression of both proteins • Adds peptide sequence to the C-terminus of the first protein and proline to the N-terminus of the second protein • Digestion at the 2A site is not always complete and may lead to fusion protein expression	• May not provide equivalent expression of both transgenes • May not provide equivalent expression of both transgenes • IRES sequences are >500 bp

attractive elements for reducing expression outside of the cell type of interest.

Conditional Expression

The mammalian CNS contains extremely diverse types of neurons. These neuronal cell types can be distinguished by their intrinsic gene expression profiles, which are differentially regulated throughout development. Binary expression systems of drivers and reporters can be used to drive transgene expression in genetically-defined cells (reviewed in Huang et al., 2014).

There are two general strategies for using binary expression systems to access genetically-defined cell types: transactivation-based systems (based on tetracycline (TET)-response elements, TRE) and recombination-based systems (based on lox-site recombination, lox) described in (Taniguchi, 2014; **Figure 1F**). Gene targeting techniques can be used to insert *Cre* or *Flp* site-specific recombinases in the mouse genome. These knock-in driver mouse lines express Cre or Flp under the activity of a target gene's endogenous promoter. Thus, Cre and Flp driver mouse lines constitute a genetic switch to turn on a recombinase-dependent reporter or effector. Since the recombinase is only expressed in cells defined by the target gene's endogenous promoter activity, this system allows labeling and manipulation of neurons defined by the targeted gene's expression pattern. A recently developed strategy can direct Cre or Flp activity to cells expressing GFP (Tang et al., 2017). Nanobodies directed against GFP have been engineered as fusion proteins with Cre or Flp. The recombinases are active only in GFP-expressing cells. This method can be used for the activity of only one recombinase, or can be used intersectionally, e.g., mating GFP and Cre mouse lines, infecting with a GFP-dependent Flp-nanobody fusion, and then using a Cre+ and Flp-dependent readout (see further below for intersectional methods). For temporal control, one can use TET-inducible systems to provide rapid and detectable expression at a given time point (Hioki et al., 2009; Sadakane et al., 2015). The TET system also has the advantage of amplified gene expression (Watakabe et al., 2012; Chan et al., 2017). This may be particularly important in studies on non-human primates since transduced cells could be maintained long-term without affecting cell integrity (Sadakane et al., 2015).

The reporter or effector whose expression is dependent on the driver's activity is introduced *in vivo* by either crossing the driver to a transgenic reporter mouse line, using a viral vector, or electroporating the DNA construct into the cells. With the widely used Cre or Flp drivers, the conditional reporter expression depends on the recombination of specific lox or frt sites, respectively. In the case of the TET system, a tet-on, reverse tetracycline transactivator (rtTA) or tet-off (tTA) driver is paired with an AAV vector with a promoter harboring tet-responsive elements (TRE).

Targeting at Random vs. Targeting to a Specific Gene's Locus

Knock-in Cre and Flp recombinases or GFP can be inserted into the genome either randomly or at a particular gene locus (**Figure 1F**). Conventional transgenic and BAC transgenic approaches result in relatively random insertions into the genome. However, knock-in mouse lines targeted to a specific locus by homologous recombination have the advantage that the expression of the inserted gene will recapitulate the expression pattern within cells of the endogenous gene of interest. There are several advantages to using targeted knock-in driver mouse lines (**Table 7**). Targeted knock-in of Cre or Flp or GFP into a specific gene's transcription/translation initiation site can result in the recapitulation of expression of the endogenous locus. When using this strategy, it should be noted that individuals can exhibit variable levels of silencing. Typically, an optimal "non-silencing" male should be identified and used for genetic crosses. However, the offspring of this male may exhibit silencing and must be revalidated.

Temporal Control With Tamoxifen

To control the expression of a reporter in a subset of neurons that uniquely and transiently express a certain marker at a particular time point, tamoxifen-inducible recombinases (Feil et al., 2009),

TABLE 7 | Methods of delivering Cre for cell-type targeting, labeling, and manipulation.

	Method of Cre delivery		
	Targeted knock-in Cre mouse line	**Transgenic Cre mouse line (not generated by homologous recombination)**	**Cre *via* AAV**
Advantages	• Specific and reliable by genetic targeting to the locus of interest (higher certainty that driver activity will reflect the endogenous expression of the gene of interest)	• Cheap and easy to produce mouse lines	• Stable over time
	• Comprehensive with Cre mouse lines	• Lower Cre expression than AAV	• Spatial control: can restrict delivery to a particular region
	• Sparse if using CreER by adjusting tamoxifen dose • Can combine with viral strategies to achieve spatial control or very strong expression • Lower Cre expression than AAV	• Can be delivered broadly by systemic (e.g., tail vein or retro-orbital) injection	
Disadvantages	• Time-consuming and costly to produce and maintain mouse lines • Genetic silencing in mouse lines can affect Cre expression	• Does not necessarily recapitulate the endogenous gene's expression • AAV vectors increase interleukin levels in the animal • Sexual dimorphism can arise that does not reflect the gene's native expression profile • Transgenic animals can lose specificity over time	• Expression gradients from injection site(s) • High levels of Cre protein exhibit cell toxicity

so-called CreER or FlpER, can be used as drivers. In CreER driver mice, activation of the expressed Cre recombinase requires administration of the estrogen receptor modulator drug tamoxifen to the animal, allowing for temporal control of recombination.

The typical tamoxifen dose varies from 10 to 200 mg/kg, depending on the desired degree of recombination at the reporter allele. In effect, this controls the sparseness/density of the labeling of the targeted neuronal population. The timing for tamoxifen administration depends on the temporal characteristics of the promoter driving CreER in the specific population to be targeted. Importantly, the half-life of tamoxifen (approximately 48 h) must be taken into consideration. Tamoxifen preparation is detailed in the published protocol in (Vaughan et al., 2015).

Tamoxifen can be administered in one of three ways, depending on the desired developmental time point for activating the CreER driver: oral gavage to the mother for embryonic induction; subcutaneous injection to offspring for early postnatal induction, or intraperitoneal injection in offspring for late postnatal and adult induction.

Best Practices for Induction of CreER or FlpER Mouse Lines

To generally improve the reliability of results obtained with CreER or FlpER mouse lines, several tamoxifen doses should be evaluated. If the level of recombination of the reporter achieved with a high dose of tamoxifen is low, administration of 4-hydroxytamoxifen (the native form of tamoxifen) can improve activation of CreER (Jahn et al., 2018). Tamoxifen needs to be metabolized in the liver to reach its active 4-hydroxytamoxifen form. Tamoxifen is often preferred over 4-hydroxytamoxifen for routine applications in highly active CreER driver lines due to lower cost and improved solubility. Following tamoxifen induction, CreER or FlpER will be active for ∼48 h, which may impact induction during developmentally active time periods. 4-hydroxytamoxifen is a better choice for tighter control of the window of activation. Administration of tamoxifen or 4-hydroxytamoxifen by gavage to the pregnant mother to induce the pups at embryonic timepoints can lead to problems of miscarriage or poor mothering. When administering tamoxifen at embryonic time-points, use of Swiss or CD1 compared to C57Bl6 mice can improve outcomes in two ways: they produce larger litters and females are better mothers, which overall can improve pup survival.

Validating a Knock-in Driver Mouse Line

Knock-in driver mouse lines are designed to control the expression of reporter probes, sensors, and effectors in genetically-defined cell-types. It is important to validate that the driver mouse line expressing a site-specific recombinase (e.g., Cre, CreER, Flp, FlpER) reflects the endogenous expression pattern of the gene targeted by the knock-in driver. Various approaches can be used separately or jointly to validate a knock-in driver mouse line: (1) Crossing the mice with a suitable reporter like Rosa26-CAG-LSL-td-tomato (Ai14) or Rosa26-CAG-LSL-h2B-GFP and assessing brain-wide expression; (2) Immunostaining of the target regions; and (3) dual fluorescent *in situ* hybridization (dual fISH) with probe for reporter (e.g., RFP or GFP for Rosa26-CAG-LSL-td-tomato (Ai14) or Rosa26-CAG-LSL-h2B-GFP, respectively). Note that assessing Cre lines by crossing to a reporter line gives an integrated view of Cre activity over the lifetime of the animal. To assess Cre activity in the target cell population at the particular age of interest, a viral vector with a Cre-dependent reporter

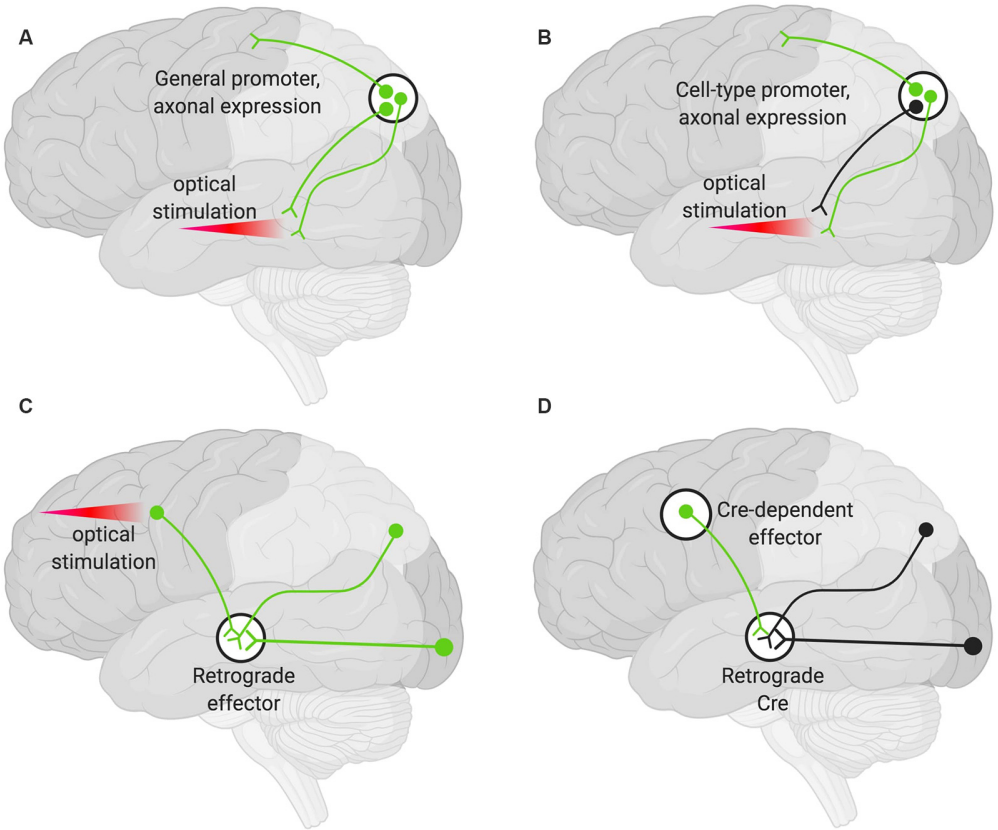

FIGURE 2 | Various strategies for neuronal targeting using AAV. Delivery of neuronal effectors *via* AAV labels (green) axons and terminals with cell bodies at the injection site. **(A)** Effectors under a general promoter express in all transduced neurons with cell bodies at the injection site. Specific regions can be optically stimulated (red beam). **(B)** Effectors under cell-type promoters express only within a cell type. **(C)** Effectors delivered *via* a retrograde AAV express in all transduced neurons with axons that project into the injection site. Cell bodies in regions of interest can be optogenetically stimulated (red beam). **(D)** Delivery of a retrograde AAV expressing Cre recombinase (Retrograde Cre) to the projection site coupled with local delivery of a Cre-dependent effector limits expression to neurons within specific circuits.

in a Cre line can be used. Similarly, for CreER lines tamoxifen induction should be performed at different developmental time-points to assess temporal specificity.

In addition, leakiness of both mouse lines and viruses must be assessed prior to the interpretation of experimental results that rely on the complete restriction of transgene expression. Leakiness of a mouse line can be assessed when validating the mouse line, ensuring that expression of the site-specific recombinase or activator (i.e., Cre, CreER, Flp, FlpER or tTA) is consistent with the gene of interest in its native form. Crossing the driver to a reporter (e.g., fluorescent reporter) and performing dual fluorescent *in situ* hybridization (dual fISH), with probes for the fluorescent reporter and for the gene of interest allows one to check that endogenous expression of the gene and activity of the driver are present in the same cells. Using knock-in driver mouse lines instead of randomly inserted BAC or plasmid driver mouse lines allows for targeted expression, with a higher likelihood of expression within cells expressing the endogenous gene of interest. Leakiness of the tamoxifen-inducible driver mouse line can be assessed by crossing the inducible driver CreER or FlpER to a Cre or Flp dependent fluorescent reporter and checking for expression of the fluorescent protein without administering tamoxifen. Finally, leakiness of the Cre- or Flp-dependent or tTA-activated AAV can be checked by injecting the virus in a mouse that has been crossed to a fluorescent reporter mouse line for the driver/activator. If expression from the virus and from the mouse reporter line match, this indicates that the AAV is specific to the driver/activator. One further evaluation of a given virus prep for background recombination (or leak) is to inject it into a mouse line that does not encode the cognate recombinase. Recombination can occur during the growth of the AAV plasmid in bacteria, and/or during virus preparation in mammalian cells, and should be assessed using this test.

VIRAL STRATEGIES FOR TARGETING DEFINED POPULATIONS

Combining various experimental techniques can enable the precise targeting of specific neuronal populations of interest.

The general advantage of using combinatorial approaches is that the specificity of cell targeting can be improved with each additional technique. Applying known characteristics of AAV and the genetically encoded transgenes they carry, neuronal populations can be specifically targeted and manipulated based on their locations and connectivity. Here we will review several targeting strategies.

Axon Terminals

A viral encoded transgene can be targeted to axon terminals. Such terminals can then be targeted optogenetically in specific areas by only delivering light to the region harboring the terminals of interest (**Figure 2A**). This technique can be further restricted such that only axons of a particular cell type are targeted by using cell-type-specific promoters to drive the AAV expression (**Figure 2B**). Additional specificity can be achieved by choosing an injection site, AAV serotype, and titer so that only desired cell types are infected (Nassi et al., 2015).

Projection Neuron Targeting

Targeting the cell bodies of projection neurons can be important for manipulating only those neurons that terminate at a particular site. To target these neurons, an AAV capable of retrograde transduction (e.g., AAV2-Retro) can be delivered to projection sites and the cell bodies of those neurons terminating at that region will be targeted (Tervo et al., 2016). This method alone will not give rise to pathway specificity. However, if used to deliver optogenetic tools, light can be delivered only to the region harboring the cell bodies of interest (**Figure 2C**; Nassi et al., 2015).

Finally, specific populations of projection neurons can be targeted by coupling local delivery of a Cre-dependent, inducible neuromodulator (e.g., a DREADD or opsin) with retrograde delivery of Cre to the site where the targeted projection neurons originate (**Figure 2D**). Using this approach, a subset of projection neurons (**Figure 2D**), rather than all the projection neurons (**Figure 2C**), then express the Cre-dependent neuromodulator. This has the advantage that effectors (e.g., the DREADD ligand) can then be delivered systemically rather than locally and still only manipulate the subset of projection neurons that have been targeted (Nassi et al., 2015).

AREAS FOR DEVELOPMENT

The arsenal of new sensors, actuators, recombinases, genes, RNA and base editing enzymes, and other genetically encoded tools for studying the nervous system is rapidly growing. AAV vectors remain the most versatile and powerful approach for delivering these tools to the CNS. Nevertheless, delivery challenges remain and efforts are ongoing to develop new vectors that address several key needs including: (1) improved widespread CNS gene transfer *via* IV and ICV routes; (2) AAV vectors capable of more efficient trans-synaptic anterograde transport; (3) vector solutions for delivering transgenes too large to fit in a single AAV virus; (4) capsids that specifically target defined neural cell types and neuronal subtypes; and (5) viral vectors that enable transduction of microglia.

Overall, consistency and repeatability of both existing and newly developed AAV tools can be improved by following best practices and guidelines. While powerful technologies are being developed, each has technical limits that need to be considered both when designing experiments and when interpreting results. To this end, improved platforms for sharing information, including technical guidelines and best practices, will serve the research community by enabling technologies to be used to their fullest capacities consistently across labs.

AUTHOR CONTRIBUTIONS

LH, KG, MR, IE, SB, JK, and MF planned and hosted the workshop where this material was discussed. BD, KM, AC, KW, and CC discussed and established the best practices for the field based on their expertise. LH, BD, and KM wrote the manuscript, which was then edited by AC, KW, CC, KG, MR, IE, SB, JK, and MF.

ACKNOWLEDGMENTS

We thank Gowan Tervo, Sarada Viswanathan, and John Dingus for helpful discussions. We are grateful for the generous support by The Kavli Foundation to hold the meeting that gave rise to this report. We also thank the Research Team and all other members of Addgene for advice and support during the preparation of this manuscript. Figures in this manuscript were created with biorender.com.

REFERENCES

Aschauer, D. F., Kreuz, S., and Rumpel, S. (2013). Analysis of transduction efficiency, tropism and axonal transport of AAV serotypes 1, 2, 5, 6, 8 and 9 in the mouse brain. *PLoS One* 8:e76310. doi: 10.1371/journal.pone.0076310

Borel, F., Gernoux, G., Cardozo, B., Metterville, J. P., Toro Cabreja, G. C., Song, L., et al. (2016). Therapeutic RAAVrh10 mediated sod1 silencing in adult SOD1G93A mice and nonhuman primates. *Hum. Gene Ther.* 27, 19–31. doi: 10.1089/hum.2015.122

Bu, J., Ashe, K. M., Bringas, J., Marshall, J., Dodge, J. C., Cabrera-Salazar, M. A., et al. (2012). Merits of combination cortical, subcortical, and cerebellar injections for the treatment of niemann-pick disease type A. *Mol. Ther.* 20, 1893–1901. doi: 10.1038/mt.2012.118

Burger, C., Gorbatyuk, O. S., Velardo, M. J., Peden, C. S., Williams, P., Zolotukhin, S., et al. (2004). Recombinant AAV viral vectors pseudotyped with viral capsids from serotypes 1, 2, and 5 display differential efficiency and cell tropism after delivery to different regions of the central nervous system. *Mol. Ther.* 10, 302–317. doi: 10.1016/j.ymthe.2004.05.024

Campillo-Balderas, J. A., Lazcano, A., and Becerra, A. (2015). Viral genome size distribution does not correlate with the antiquity of the host lineages. *Front. Ecol. Evol.* 3:143. doi: 10.3389/fevo.2015.00143

Carty, N., Lee, D., Dickey, C., Ceballos-Diaz, C., Jansen-West, K., Golde, T. E., et al. (2010). Convection-enhanced delivery and systemic mannitol increase gene product distribution of AAV vectors 5, 8, and 9 and increase gene product in the adult mouse brain. *J. Neurosci. Methods* 194, 144–153. doi: 10.1016/j.jneumeth.2010.10.010

Castle, M. J., Gershenson, Z. T., Giles, A. R., Holzbaur, E. L. F., and Wolfe, J. H. (2014). Adeno-associated virus serotypes 1, 8, and 9 share conserved mechanisms for anterograde and retrograde axonal transport. *Hum. Gene Ther.* 25, 705–720. doi: 10.1089/hum.2013.189

Cearley, C. N., Vandenberghe, L. H., Parente, M. K., Carnish, E. R., Wilson, J. M., and Wolfe, J. H. (2008). Expanded repertoire of AAV vector serotypes mediate unique patterns of transduction in mouse brain. *Mol. Ther.* 16, 1710–1718. doi: 10.1038/mt.2008.166

Cearley, C. N., and Wolfe, J. H. (2006). Transduction characteristics of adeno-associated virus vectors expressing cap serotypes 7, 8, 9, and Rh10 in the mouse brain. *Mol. Ther.* 13, 528–537. doi: 10.1016/j.ymthe.2005.11.015

Cearley, C. N., and Wolfe, J. H. (2007). A single injection of an adeno-associated virus vector into nuclei with divergent connections results in widespread vector distribution in the brain and global correction of a neurogenetic disease. *J. Neurosci.* 27, 9928–9940. doi: 10.1523/JNEUROSCI.2185-07.2007

Challis, R. C., Ravindra Kumar, S., Chan, K. Y., Challis, C., Beadle, K., Jang, M. J., et al. (2019). Systemic AAV vectors for widespread and targeted gene delivery in rodents. *Nat. Protoc.* 14, 379–414. doi: 10.1038/s41596-018-0097-3

Chan, K. Y., Jang, M. J., Yoo, B. B., Greenbaum, A., Ravi, N., Wu, W. L., et al. (2017). Engineered AAVs for efficient noninvasive gene delivery to the central and peripheral nervous systems. *Nat. Neurosci.* 20, 1172–1179. doi: 10.1038/nn.4593

Chan, Y. K., Wang, S. K., Letizia, A. J., Chan, Y., Lim, E. T., Graveline, A. R., et al. (2019). Engineering adeno-associated 450 viral vectors to evade innate immune and inflammatory responses. In review.

Chenuaud, P., Larcher, T., Rabinowitz, J. E., Provost, N., Joussemet, B., Bujard, H., et al. (2004). Optimal design of a single recombinant adeno-associated virus derived from serotypes 1 and 2 to achieve more tightly regulated transgene expression from nonhuman primate muscle. *Mol. Ther.* 9, 410–418. doi: 10.1016/j.ymthe.2003.12.015

Colella, P., Ronzitti, G., and Mingozzi, F. (2018). Emerging issues in AAV-mediated *in vivo* gene therapy. *Mol. Ther. Methods Clin. Dev.* 8, 87–104. doi: 10.1016/j.omtm.2017.11.007

Cowan, P. J., Tsang, D., Pedic, C. M., Abbott, L. R., Shinkel, T. A., D'Apice, A. J. F., et al. (1998). The human ICAM-2 promoter is endothelial cell-specific *in vitro* and *in vivo* and contains critical Sp1 and GATA binding sites. *J. Biol. Chem.* 273, 11737–11744. doi: 10.1074/jbc.273.19.11737

Cucchiarini, M., Ren, X. L., Perides, G., and Terwilliger, E. F. (2003). Selective gene expression in brain microglia mediated *via* adeno-associated virus type 2 and type 5 vectors. *Gene Ther.* 10, 657–667. doi: 10.1038/sj.gt.3301925

Davidson, B. L., Stein, C. S., Heth, J. A., Martins, I., Kotin, R. M., Derksen, T. A., et al. (2000). Recombinant adeno-associated virus type 2, 4, and 5 vectors: transduction of variant cell types and regions in the mammalian central nervous system. *Proc. Natl. Acad. Sci. U S A* 97, 3428–3432. doi: 10.1073/pnas.97.7.3428

Davidsson, M., Wang, G., Aldrin-Kirk, P., Cardoso, T., Nolbrant, S., Hartnor, M., et al. (2018). Barcoded rational AAV vector evolution enables systematic *in vivo* mapping of peptide binding motifs. *SSRN Electron. J.* doi: 10.2139/ssrn.3245528

Deverman, B. E., Pravdo, P. L., Simpson, B. P., Kumar Ravindra, S., Chan, K. Y., Banerjee, A., et al. (2016). Cre-dependent selection yields AAV variants for widespread gene transfer to the adult brain. *Nat. Biotechnol.* 34, 204–209. doi: 10.1038/nbt.3440

de Leeuw, C. N. De., Korecki, A. J., Berry, G. E., Hickmott, J. W., Lam, S. L., Lengyell, T. C., et al. (2016). RAAV-compatible minipromoters for restricted expression in the brain and eye. *Mol. Brain* 9:52. doi: 10.1186/s13041-016-0232-4

Dimidschstein, J., Chen, Q., Tremblay, R., Rogers, S. L., Saldi, G. A., Guo, L., et al. (2016). A viral strategy for targeting and manipulating interneurons across vertebrate species. *Nat. Neurosci.* 19, 1743–1749. doi: 10.1038/nn.4430

Dittgen, T., Nimmerjahn, A., Komai, S., Licznerski, P., Waters, J., Margrie, T. W., et al. (2004). Lentivirus-based genetic manipulations of cortical neurons and their optical and electrophysiological monitoring *in vivo*. *Proc. Natl. Acad. Sci. U S A* 101, 18206–18211. doi: 10.1073/pnas.0407976101

Dodiya, H. B., Bjorklund, T., Stansell, J. III., Mandel, R. J., Kirik, D., and Kordower, J. H. (2010). Differential transduction following basal ganglia administration of distinct pseudotyped AAV capsid serotypes in nonhuman primates. *Mol. Ther.* 18, 579–587. doi: 10.1038/mt.2009.216

Drouin, L. M., and Agbandje-McKenna, M. (2013). Adeno-associated virus structural biology as a tool in vector development. *Future Virol.* 8, 1183–1199. doi: 10.2217/fvl.13.112

Dufour, B. D., Smith, C. A., Clark, R. L., Walker, T. R., and McBride, J. L. (2014). Intrajugular vein delivery of AAV9-RNAi prevents neuropathological changes and weight loss in Huntington's disease mice. *Mol. Ther.* 22, 797–810. doi: 10.1038/mt.2013.289

During, M. J., Samulski, R. J., Elsworth, J. D., Kaplitt, M. G., Leone, P., Xiao, X., et al. (1998). *in vivo* expression of therapeutic human genes for dopamine production in the caudales of MPTP-treated monkeys using an AAV vector. *Gene Ther.* 5, 820–827. doi: 10.1038/sj.gt.3300650

El-Shamayleh, Y., Ni, A. M., and Horwitz, G. D. (2016). Strategies for targeting primate neural circuits with viral vectors. *J. Neurophysiol.* 116, 122–134. doi: 10.1152/jn.00087.2016

Federici, T., Taub, J. S., Baum, G. R., Gray, S. J., Grieger, J. C., Matthews, K. A., et al. (2012). Robust spinal motor neuron transduction following intrathecal delivery of AAV9 in pigs. *Gene Ther.* 19, 852–859. doi: 10.1038/gt.2011.130

Feil, S., Valtcheva, N., and Feil, R. (2009). Inducible Cre mice. *Methods Mol. Biol.* 530, 343–363. doi: 10.1007/978-1-59745-471-1_18

Fenno, L. E., Mattis, J., Ramakrishnan, C., and Deisseroth, K. (2017). A guide to creating and testing new INTRSECT constructs. *Curr. Protoc. Neurosci.* 80, 4.39.1–4.39.24. doi: 10.1002/cpns.30

Fenno, L. E., Mattis, J., Ramakrishnan, C., Hyun, M., Lee, S. Y., He, M., et al. (2014). Targeting cells with single vectors using multiple-feature boolean logic. *Nat. Methods* 11, 763–772. doi: 10.1038/nmeth.2996

Foust, K. D., Nurre, E., Montgomery, L. C., Hernandez, A., Chan, C. M., and Kaspar, B. K. (2009). Intravascular AAV9 preferentially targets neonatal neurons and adult astrocytes. *Nat. Biotechnol.* 27, 59–65. doi: 10.1038/nbt.1515

Foust, K. D., Wang, X., McGovern, V. L., Braun, L., Bevan, A. K., Haidet, A. M., et al. (2010). Rescue of the spinal muscular atrophy phenotype in a mouse model by early postnatal delivery of SMN. *Nat. Biotechnol.* 28, 271–274. doi: 10.1038/nbt.1610

Gill, D. R., Smyth, S. E., Goddard, C. A., Pringle, I. A., Higgins, C. F., Colledge, W. H., et al. (2001). Increased persistence of lung gene expression using plasmids containing the ubiquitin C or elongation factor 1α promoter. *Gene Ther.* 8, 1539–1546. doi: 10.1038/sj.gt.3301561

Gow, A., Friedrich, V. L., and Lazzarini, R. A. (1992). Myelin basic protein gene contains separate enhancers for oligodendrocyte and schwann cell expression. *J. Cell Biol.* 119, 605–616. doi: 10.1083/jcb.119.3.605

Gray, S. J., Foti, S. B., Schwartz, J. W., Bachaboina, L., Taylor-Blake, B., Coleman, J., et al. (2011). Optimizing promoters for recombinant adeno-associated virus-mediated gene expression in the peripheral and central nervous system using self-complementary vectors. *Hum. Gene Ther.* 22, 1143–1153. doi: 10.1089/hum.2010.245

Gray, S. J., Nagabhushan Kalburgi, S., McCown, T. J., and Jude Samulski, R. (2013). Global CNS gene delivery and evasion of anti-AAV-neutralizing antibodies by intrathecal AAV administration in non-human primates. *Gene Ther.* 20, 450–459. doi: 10.1038/gt.2012.101

Grimm, D., Lee, J. S., Wang, L., Desai, T., Akache, B., Storm, T. A., et al. (2008). *in vitro* and *in vivo* gene therapy vector evolution *via* multispecies interbreeding and retargeting of adeno-associated Viruses. *J. Virol.* 82, 5887–5911. doi: 10.1128/JVI.00254-08

Gurda, B. L., De Guilhem De Lataillade, A., Bell, P., Zhu, Y., Yu, H., Wang, P., et al. (2016). Evaluation of AAV-mediated gene therapy for central nervous system disease in canine mucopolysaccharidosis VII. *Mol. Ther.* 24, 206–216. doi: 10.1038/mt.2015.189

Hadaczek, P., Forsayeth, J., Mirek, H., Munson, K., Bringas, J., Pivirotto, P., et al. (2009). Transduction of nonhuman primate brain with adeno-associated virus serotype 1: vector trafficking and immune response. *Hum. Gene Ther.* 20, 225–237. doi: 10.1089/hum.2008.151

Halbert, C. L., Miller, A. D., McNamara, S., Emerson, J., Gibson, R. L., Ramsey, B., et al. (2006). Prevalence of neutralizing antibodies against adeno-associated virus (AAV) types 2, 5, and 6 in cystic fibrosis and normal populations: implications for gene therapy using AAV Vectors. *Hum. Gene Ther.* 17, 440–447. doi: 10.1089/hum.2006.17.ft-194

Hammond, S. L., Leek, A. N., Richman, E. H., and Tjalkens, R. B. (2017). Cellular selectivity of AAV serotypes for gene delivery in neurons and astrocytes by neonatal intracerebroventricular injection. *PLoS One* 12:e0188830. doi: 10.1371/journal.pone.0188830

Hillier, D., Fiscella, M., Drinnenberg, A., Trenholm, S., Rompani, S. B., Raics, Z., et al. (2017). Causal evidence for retina-dependent and independent visual motion computations in mouse cortex. *Nat. Neurosci.* 20, 960–968. doi: 10.1038/nn.4566

Hinderer, C., Bell, P., Vite, C. H., Louboutin Pierre, J., Grant, R., Bote, E., et al. (2014). Widespread gene transfer in the central nervous system of cynomolgus macaques following delivery of AAV9 into the cisterna magna. *Mol. Ther. Methods Clin. Dev.* 1:14051. doi: 10.1038/mtm.2014.51

Hioki, H., Kameda, H., Nakamura, H., Okunomiya, T., Ohira, K., Nakamura, K., et al. (2007). Efficient gene transduction of neurons by lentivirus with enhanced neuron-specific promoters. *Gene Ther.* 14, 872–882. doi: 10.1038/sj.gt.3302924

Hioki, H., Kuramoto, E., Konno, M., Kameda, H., Takahashi, Y., Nakano, T., et al. (2009). High-level transgene expression in neurons by lentivirus with tet-off system. *Neurosci. Res.* 63, 149–154. doi: 10.1016/j.neures.2008.10.010

Hoesche, C., Sauerwald, A., Veh, R. W., Krippl, B., and Kilimann, M. W. (1993). The 5′-flanking region of the rat synapsin I gene directs neuron-specific and developmentally regulated reporter gene expression in transgenic mice. *J. Biol. Chem.* 268, 26494–26502.

Hollis, E. R. II., Kadoya, K., Hirsch, M., Samulski, R. J., and Tuszynski, M. H. (2008). Efficient retrograde neuronal transduction utilizing self-complementary AAV1. *Mol. Ther.* 16, 296–301. doi: 10.1038/sj.mt.6300367

Hordeaux, J., Wang, Q., Katz, N., Buza, E. L., Bell, P., and Wilson, J. M. (2018). The neurotropic properties of AAV-PHP.B are limited to C57BL/6J mice. *Mol. Ther.* 26, 664–668. doi: 10.1016/j.ymthe.2018.01.018

Hordeaux, J., Yuan, Y., Clark, P. M., Wang, Q., Martino, R. A., Sims, J. J., et al. (2019). The GPI-linked protein LY6A drives AAV-PHP.B transport across the blood-brain barrier. *Mol. Ther.* 27, 912–921. doi: 10.1016/j.ymthe.2019.02.013

Huang, Q., Chan, K. Y., Tobey, I. G., Chan, Y. A., Poterba, T., Boutros, C. L., et al. (2019). Delivering genes across the blood-brain barrier: LY6A, a novel cellular receptor for AAV-PHP.B capsids. *BioRxiv* [Preprint]. doi: 10.1101/538421

Huang, Z. J., Taniguchi, H., He, M., and Kuhlman, S. (2014). Cre-dependent adeno-associated virus preparation and delivery for labeling neurons in the mouse brain. *Cold Spring Harb. Protoc.* 2014, 190–194. doi: 10.1101/pdb.prot080382

Hwang, D. Y., Carlezon, W. A. Jr., Isacson, O., and Kim, K. S. (2001). A high-efficiency synthetic promoter that drives transgene expression selectively in noradrenergic neurons. *Hum. Gene Ther.* 12, 1731–1740. doi: 10.1089/104303401750476230

Jahn, H. M., Kasakow, C. V., Helfer, A., Michely, J., Verkhratsky, A., Maurer, H. H., et al. (2018). Refined protocols of tamoxifen injection for inducible DNA recombination in mouse astroglia. *Sci. Rep.* 8:5931. doi: 10.1038/s41598-018-24085-9

Jahroudi, N., and Lynch, D. C. (1994). Endothelial-cell-specific regulation of von willebrand factor gene expression. *Mol. Cell. Biol.* 14, 999–1008. doi: 10.1128/mcb.14.2.999

Kaplitt, M. G., Leone, P., Samulski, R. J., Xiao, X., Pfaff, D. W., O'Malley, K. L., et al. (1994). Long-term gene expression and phenotypic correction using adeno-associated virus vectors in the mammalian brain. *Nat. Genet.* 8, 148–154. doi: 10.1038/ng1094-148

Kaspar, B. K., Erickson, D., Schaffer, D., Hinh, L., Gage, F. H., and Peterson, D. A. (2002). Targeted retrograde gene delivery for neuronal protection. *Mol. Ther.* 5, 50–56. doi: 10.1006/mthe.2001.0520

Kawashima, T., Okuno, H., and Bito, H. (2014). A new era for functional labeling of neurons: activity-dependent promoters have come of age. *Front. Neural Circuits* 8:37. doi: 10.3389/fncir.2014.00037

Keaveney, M. K., Tseng, H. A., Ta, T. L., Gritton, H. J., Man, H. Y., and Han, X. (2018). A MicroRNA-based gene-targeting tool for virally labeling interneurons in the rodent cortex. *Cell Rep.* 24, 294–303. doi: 10.1016/j.celrep.2018.06.049

Kim, D. W., Uetsuki, T., Kaziro, Y., Yamaguchi, N., and Sugano, S. (1990). Use of the human elongation factor 1α promoter as a versatile and efficient expression system. *Gene* 91, 217–223. doi: 10.1016/0378-1119(90)90091-5

Klein, R. L., Dayton, R. D., Leidenheimer, N. J., Jansen, K., Golde, T. E., and Zweig, R. M. (2006). Efficient neuronal gene transfer with AAV8 leads to neurotoxic levels of tau or green fluorescent proteins. *Front. Cell Dev. Biol.* 13, 517–527. doi: 10.1016/j.ymthe.2005.10.008

Klein, R. L., Dayton, R. D., Tatom, J. B., Henderson, K. M., and Henning, P. P. (2008). AAV8, 9, Rh10, Rh43 vector gene transfer in the rat brain: effects of serotype, promoter and purification method. *Mol. Ther.* 16, 89–96. doi: 10.1038/sj.mt.6300331

Klein, R. L., Meyer, E. M., Peel, A. L., Zolotukhin, S., Meyers, C., Muzyczka, N., et al. (1998). Neuron-specific transduction in the rat septohippocampal or nigrostriatal pathway by recombinant adeno-associated virus vectors. *Gene Ther.* 150, 183–194. doi: 10.1006/exnr.1997.6736

Koh, W., Park, Y. M., Lee, S. E., and Lee, C. J. (2017). AAV-mediated astrocyte-specific gene expression under human *ALDH1L1* promoter in mouse thalamus. *Exp. Neurobiol.* 26, 350–361. doi: 10.5607/en.2017.26.6.350

Kügler, S., Kilic, E., and Bähr, M. (2003). Human synapsin 1 gene promoter confers highly neuron-specific long-term transgene expression from an adenoviral vector in the adult rat brain depending on the transduced area. *Gene Ther.* 10, 337–347. doi: 10.1038/sj.gt.3301905

Lavin, T. K., Jin, L., Lea, N. E., and Wickersham, I. (2019). Monosynaptic tracing success depends critically on helper virus concentrations. *BioRxiv* [Preprint]. doi: 10.1101/736017

Lee, Y., Messing, A., Su, M., and Brenner, M. (2008). GFAP promoter elements required for region-specific and astrocyte-specific expression. *GLIA* 56, 481–493. doi: 10.1002/glia.20622

Leung, J. W. C., Chung, S. S. M., and Chung, S. K. (2009). Endothelial endothelin-1 over-expression using receptor tyrosine kinase tie-1 promoter leads to more severe vascular permeability and blood brain barrier breakdown after transient middle cerebral artery occlusion. *Brain Res.* 1266, 121–129. doi: 10.1016/j.brainres.2009.01.070

Li, S. F., Wang, R. Z., Meng, Q. H., Li, G. L., Hu, G. J., Dou, W. C., et al. (2006). Intra-ventricular infusion of RAAV1-EGFP resulted in transduction in multiple regions of adult rat brain: a comparative study with RAAV2 and RAAV5 vectors. *Brain Res.* 1122, 1–9. doi: 10.1016/j.brainres.2006.09.042

Liu, G., Martins, I. H., Chiorini, J. A., and Davidson, B. L. (2005). Adeno-associated virus type 4 (AAV4) targets ependyma and astrocytes in the subventricular zone and RMS. *Gene Ther.* 12, 1503–1508. doi: 10.1038/sj.gt.3302554

Lo, W. D., Qu, G., Sferra, T. J., Clark, R., Chen, R., and Johnson, P. R. (1999). Adeno-associated virus-mediated gene transfer to the brain: duration and modulation of expression. *Hum. Gene Ther.* 10, 201–213. doi: 10.1089/10430349950018995

Lukashchuk, V., Lewis, K. E., Coldicott, I., Grierson, A. J., and Azzouz, M. (2016). AAV9-mediated central nervous system-targeted gene delivery *via* cisterna magna route in mice. *Mol. Ther. Methods Clin. Dev.* 3:15055. doi: 10.1038/mtm.2015.55

Mandel, R. J., Rendahl, K. G., Spratt, S. K., Snyder, R. O., Cohen, L. K., and Leff, S. E. (1998). Characterization of intrastriatal recombinant adeno-associated virus- mediated gene transfer of human tyrosine hydroxylase and human GTP- cyclohydrolase I in a rat model of Parkinson's disease. *J. Neurosci.* 18, 4271–4284. doi: 10.1523/jneurosci.18-11-04271.1998

Marchiò, S., Sidman, R. L., Arap, W., and Pasqualini, R. (2016). Brain endothelial cell-targeted gene therapy of neurovascular disorders. *EMBO Mol. Med.* 8, 592–594. doi: 10.15252/emmm.201606407

Martino, A. T., Suzuki, M., Markusic, D. M., Zolotukhin, I., Ryals, R. C., Moghimi, B., et al. (2011). The genome of self-complementary adeno-associated viral vectors increases toll-like receptor 9-dependent innate immune responses in the liver. *Blood* 117, 6459–6468. doi: 10.1182/blood-2010-10-314518

Masamizu, Y., Okada, T., Ishibashi, H., Takeda, S., Yuasa, S., and Nakahara, K. (2010). Efficient gene transfer into neurons in monkey brain by adeno-associated virus 8. *Neuroreport* 21, 447–451. doi: 10.1097/wnr.0b013e328338ba00

Masamizu, Y., Okada, T., Kawasaki, K., Ishibashi, H., Yuasa, S., Takeda, S., et al. (2011). Local and retrograde gene transfer into primate neuronal pathways

via adeno-associated virus serotype 8 and 9. *Neuroscience* 193, 249–258. doi: 10.1016/j.neuroscience.2011.06.080

Mastakov, M. Y., Baer, K., Xu, R., Fitzsimons, H., and During, M. J. (2001). Combined injection of RAAV with mannitol enhances gene expression in the rat brain. *Mol. Ther.* 3, 225–232. doi: 10.1006/mthe.2001.0246

McCown, T. J., Xiao, X., Li, J., Breese, G. R., and Samulski, R. J. (1996). Differential and persistent expression patterns of CNS gene transfer by an adeno-associated virus (AAV) vector. *Brain Res.* 713, 99–107. doi: 10.1016/0006-8993(95)01488-8

Mingozzi, F., and High, K. A. (2011). Immune responses to AAV in clinical trials. *Curr. Gene Ther.* 11, 321–330. doi: 10.2174/156652311796150354

Miyanohara, A., Kamizato, K., Juhas, S., Juhasova, J., Navarro, M., Marsala, S., et al. (2016). Potent spinal parenchymal AAV9-mediated gene delivery by subpial injection in adult rats and pigs. *Mol. Ther. Methods Clin. Dev.* 3:16046. doi: 10.1038/mtm.2016.46

Miyazaki, J., Takaki, S., Araki, K., Tashiro, F., Tominaga, A., Takatsu, K., et al. (1989). Expression vector system based on the chicken β-actin promoter directs efficient production of interleukin-5. *Gene* 79, 269–277. doi: 10.1016/0378-1119(89)90209-6

Montiel-Equihua, C. A., Zhang, L., Knight, S., Saadeh, H., Scholz, S., Carmo, M., et al. (2012). The β-globin locus control region in combination with the EF1α short promoter allows enhanced lentiviral vector-mediated erythroid gene expression with conserved multilineage activity. *Mol. Ther.* 20, 1400–1409. doi: 10.1038/mt.2012.50

Morishita, K., Johnson, D. E., and Williams, L. T. (1995). A novel promoter for vascular endothelial growth factor receptor (Flt-1) that confers endothelial-specific gene expression. *J. Biol. Chem.* 270, 27948–27953. doi: 10.1074/jbc.270.46.27948

Murlidharan, G., Corriher, T., Ghashghaei, H. T., and Asokan, A. (2015). Unique glycan signatures regulate adeno-associated virus tropism in the developing brain. *J. Virol.* 89, 3976–3987. doi: 10.1128/jvi.02951-14

Nassi, J. J., Cepko, C. L., Born, R. T., and Beier, K. T. (2015). Neuroanatomy goes viral!. *Front. Neuroanat.* 9:80. doi: 10.3389/fnana.2015.00080

Nathanson, J. L., Jappelli, R., Scheeff, E. D., Manning, G., Obata, K., Brenner, S., et al. (2009a). Short promoters in viral vectors drive selective expression in mammalian inhibitory neurons, but do not restrict activity to specific inhibitory cell-types. *Front. Neural Circuits* 3:19. doi: 10.3389/neuro.04.019.2009

Nathanson, J. L., Yanagawa, Y., Obata, K., and Callaway, E. M. (2009b). Preferential labeling of inhibitory and excitatory cortical neurons by endogenous tropism of adeno-associated virus and lentivirus vectors. *Neurosci.* 161, 441–450. doi: 10.1016/j.neuroscience.2009.03.032

Niwa, H., Yamamura, K., and Miyazaki, J. (1991). Efficient selection for high-expression transfectants with a novel eukaryotic vector. *Gene* 108, 193–199. doi: 10.1016/0378-1119(91)90434-d

Oh, M. S., Hong, S. J., Huh, Y., and Kim, K. S. (2009). Expression of transgenes in midbrain dopamine neurons using the tyrosine hydroxylase promoter. *Gene Ther.* 16, 437–440. doi: 10.1038/gt.2008.148

Ojala, D. S., Sun, S., Santiago-Ortiz, J. L., Shapiro, M. G., Romero, P. A., and Schaffer, D. V. (2018). *in vivo* selection of a computationally designed SCHEMA AAV library yields a novel variant for infection of adult neural stem cells in the SVZ. *Mol. Ther.* 26, 304–319. doi: 10.1016/j.ymthe.2017.09.006

Paterna, J. C., Moccetti, T., Mura, A., Feldon, J., and Büeler, H. (2000). Influence of promoter and WHV post-transcriptional regulatory element on AAV-mediated transgene expression in the rat brain. *Gene Ther.* 7, 1304–1311. doi: 10.1038/sj.gt.3301221

Peel, A. L., Zolotukhin, S., Schrimsher, G. W., Muzyczka, N., and Reier, P. J. (1997). Efficient transduction of green fluorescent protein in spinal cord neurons using adeno-associated virus vectors containing cell type-specific promoters. *Gene Ther.* 4, 16–24. doi: 10.1038/sj.gt.3300358

Pignataro, D., Sucunza, D., Vanrell, L., Lopez-Franco, E., Dopeso-Reyes, I. G., Vales, A., et al. (2017). Adeno-associated viral vectors serotype 8 for cell-specific delivery of therapeutic genes in the central nervous system. *Front. Neuroanat.* 11:2. doi: 10.3389/fnana.2017.00002

Qin, J. Y., Zhang, L., Clift, K. L., Hulur, I., Xiang, A. P., Ren, B. Z., et al. (2010). Systematic comparison of constitutive promoters and the doxycycline-inducible promoter. *PLoS One* 5:e10611. doi: 10.1371/journal.pone.0010611

Reimsnider, S., Manfredsson, F. P., Muzyczka, N., and Mandel, R. J. (2007). Time course of transgene expression after intrastriatal pseudotyped RAAV2/1, RAAV2/2, RAAV2/5, and RAAV2/8 transduction in the rat. *Mol. Ther.* 15, 1504–1511. doi: 10.1038/sj.mt.6300227

Rogers, G. L., Martino, A. T., Aslanidi, G. V., Jayandharan, G. R., Srivastava, A., and Herzog, R. W. (2011). Innate immune responses to AAV vectors. *Front. Microbiol.* 2:194. doi: 10.3389/fmicb.2011.00194

Ruzo, A., Marcó, S., García, M., Villacampa, P., Ribera, A., Ayuso, E., et al. (2012). Correction of pathological accumulation of glycosaminoglycans in central nervous system and peripheral tissues of MPSIIIA mice through systemic AAV9 gene transfer. *Hum. Gene Ther.* 23, 1237–1246. doi: 10.1089/hum.2012.029

Sadakane, O., Masamizu, Y., Watakabe, A., Terada, S. I., Ohtsuka, M., Takaji, M., et al. (2015). Long-term two-photon calcium imaging of neuronal populations with subcellular resolution in adult non-human primates. *Cell Rep.* 13, 1989–1999. doi: 10.1016/j.celrep.2015.10.050

Salegio, E. A., Samaranch, L., Kells, A. P., Mittermeyer, G., San Sebastian, W., Zhou, S., et al. (2013). Axonal transport of adeno-associated viral vectors is serotype-dependent. *Gene Ther.* 20, 348–352. doi: 10.1038/gt.2012.27

Samaranch, L., Salegio, E. A., Sebastian, W. S., Kells, A. P., Bringas, J. R., Forsayeth, J., et al. (2013). Strong cortical and spinal cord transduction after AAV7 and AAV9 delivery into the cerebrospinal fluid of nonhuman primates. *Hum. Gene Ther.* 24, 526–532. doi: 10.1089/hum.2013.005

Samaranch, L., Salegio, E. A., Sebastian, W. S., Kells, A. P., Foust, K. D., Bringas, J. R., et al. (2011). Adeno-associated virus serotype 9 transduction in the central nervous system of nonhuman primates. *Hum. Gene Ther.* 23, 382–389. doi: 10.1089/hum.2011.200

Samaranch, L., Sebastian, W. S., Kells, A. P., Salegio, E. A., Heller, G., Bringas, J. R., et al. (2014). AAV9-mediated expression of a non-self protein in nonhuman primate central nervous system triggers widespread neuroinflammation driven by antigen-presenting cell transduction. *Mol. Ther.* 22, 329–337. doi: 10.1038/mt.2013.266

Scheyltjens, I., Laramée, M. E., Van den Haute, C., Gijsbers, R., Debyser, Z., Baekelandt, V., et al. (2015). Evaluation of the expression pattern of RAAV2/1, 2/5, 2/7, 2/8, and 2/9 serotypes with different promoters in the mouse visual cortex. *J. Comp. Neurol.* 14, 2019–2042. doi: 10.1002/cne.23819

Schultz, B. R., and Chamberlain, J. S. (2008). Recombinant adeno-associated virus transduction and integration. *Mol. Ther.* 16, 1189–1199. doi: 10.1038/mt.2008.103

Schuster, D. J., Dykstra, J. A., Riedl, M. S., Kitto, K. F., Belur, L. R., McIvor, R. S., et al. (2014). Biodistribution of adeno-associated virus serotype 9 (AAV9) vector after intrathecal and intravenous delivery in mouse. *Front. Neuroanat.* 8:42. doi: 10.3389/fnana.2014.00042

Seita, Y., Tsukiyama, T., Azami, T., Kobayashi, K., Iwatani, C., Tsuchiya, H., et al. (2019). Comprehensive evaluation of ubiquitous promoters suitable for the generation of transgenic cynomolgus monkeys. *Biol. Reprod.* 100, 1440–1452. doi: 10.1093/biolre/ioz040

Sondhi, D., Hackett, N. R., Peterson, D. A., Stratton, J., Baad, M., Travis, K. M., et al. (2007). Enhanced survival of the LINCL mouse following CLN2 gene transfer using the Rh.10 Rhesus macaque-derived adeno-associated virus vector. *Mol. Ther.* 15, 481–491. doi: 10.1038/sj.mt.6300049

Stoica, L., Ahmed, S. S., Gao, G., and Sena-Esteves, M. (2013). Gene transfer to the CNS using recombinant adeno-associated virus. *Curr. Protoc. Microbiol.* 14:14D.5. doi: 10.1002/9780471729259.mc14d05s29

Sullivan, J. A., Stanek, L. M., Lukason, M. J., Bu, J., Osmond, S. R., Barry, E. A., et al. (2018). Rationally designed AAV2 and AAVrh8R capsids provide improved transduction in the retina and brain. *Gene Ther.* 25, 205–219. doi: 10.1038/s41434-018-0017-8

Tang, J. C. Y., Rudolph, S., and Cepko, C. L. (2017). Viral delivery of GFP-dependent recombinases to the mouse brain. *Methods Mol. Biol.* 1642, 109–126. doi: 10.1007/978-1-4939-7169-5_8

Taniguchi, H. (2014). Genetic dissection of gabaergic neural circuits in mouse neocortex. *Front. Cell. Neurosci.* 8:8. doi: 10.3389/fncel.2014.00008

Taymans, J. M., Vandenberghe, L. H., Van Den Haute, C., Thiry, I., Deroose, C. M., Mortelmans, L., et al. (2007). Comparative analysis of adeno-associated viral vector serotypes 1, 2, 5, 7 and 8 in mouse brain. *Hum. Gene Ther.* 18, 195–206. doi: 10.1089/hum.2006.178

Tenenbaum, L., Chtarto, A., Lehtonen, E., Velu, T., Brotchi, J., and Levivier, M. (2004). Recombinant AAV-mediated gene delivery to the central nervous system. *J. Gene Med.* 6, S212–S222. doi: 10.1002/jgm.506

Tervo, D. G. R., Hwang, B. Y., Viswanathan, S., Gaj, T., Lavzin, M., Ritola, K. D., et al. (2016). A designer AAV variant permits efficient retrograde access to projection neurons. *Neuron* 92, 372–382. doi: 10.1016/j.neuron.2016.09.021

Thomsen, D. R., Stenberg, R. M., Goins, W. F., and Stinski, M. F. (1984). Promoter-regulatory region of the major immediate early gene of human cytomegalovirus. *Proc. Natl. Acad. Sci. U S A* 81, 659–663. doi: 10.1073/pnas.81.3.659

Tordo, J., O'Leary, C., Antunes, A. S. L. M., Palomar, N., Aldrin-Kirk, P., Basche, M., et al. (2018). A novel adeno-associated virus capsid with enhanced neurotropism corrects a lysosomal transmembrane enzyme deficiency. *Brain* 141, 2014–2031. doi: 10.1093/brain/awy126

Vaughan, A., Vaughan, A., Brumwell, A., and Chapman, H. (2015). Tamoxifen administration for lineage tracing using CreERT2 mice. *Protoc. Exchange*.doi: 10.1038/protex.2015.018

van den Pol, A. N., Acuna-Goycolea, C., Clark, K. R., and Ghosh, P. K. (2004). Physiological properties of hypothalamic mch neurons identified with selective expression of reporter gene after recombinant virus infection. *Neuron* 42, 635–652. doi: 10.1016/s0896-6273(04)00251-x

von Jonquieres, G., Fröhlich, D., Klugmann, C. B., Wen, X., Harasta, A. E., Ramkumar, R., et al. (2016). Recombinant human myelin-associated glycoprotein promoter drives selective AAV-mediated transgene expression in oligodendrocytes. *Front. Mol. Neurosci.* 9:13. doi: 10.3389/fnmol.2016.00013

von Jonquieres, G., Mersmann, N., Klugmann, C. B., Harasta Editha, A., Lutz, B., Teahan, O., et al. (2013). Glial promoter selectivity following AAV-delivery to the immature brain. *PLoS One* 8:e65646. doi: 10.1371/journal.pone.0065646

Watakabe, A., Kato, S., Kobayashi, K., Takaji, M., Nakagami, Y., Sadakane, O., et al. (2012). Visualization of cortical projection neurons with retrograde TET-Off lentiviral vector. *PLoS One* 7:e46157. doi: 10.1371/journal.pone.0046157

Watakabe, A., Ohtsuka, M., Kinoshita, M., Takaji, M., Isa, K., Mizukami, H., et al. (2015). Comparative analyses of adeno-associated viral vector serotypes 1, 2, 5, 8 and 9 in marmoset, mouse and macaque cerebral cortex. *Neurosci. Res.* 93, 144–157. doi: 10.1016/j.neures.2014.09.002

Xie, J., Xie, Q., Zhang, H., Ameres, S. L., Hung, J. H., Su, Q., et al. (2011). MicroRNA-regulated, systemically delivered RAAV9: a step closer to cns-restricted transgene expression. *Mol. Ther.* 19, 526–535. doi: 10.1038/mt.2010.279

Xiong, W., Wu, D. M., Xue, Y., Wang, S. K., Chung, M. J., Ji, X., et al. (2019). AAV cis-regulatory sequences are correlated with ocular toxicity. *Proc. Natl. Acad. Sci. U S A* 116, 5785–5794. doi: 10.1073/pnas.1821000116

Xu, R., Janson, C. G., Mastakov, M., Lawlor, P., Young, D., Mouravlev, A., et al. (2001). Quantitative comparison of expression with adeno-associated virus (AAV-2) brain-specific gene cassettes. *Gene Ther.* 8, 1323–1332. doi: 10.1038/sj.gt.3301529

Yaguchi, M., Ohashi, Y., Tsubota, T., Sato, A., Koyano, K. W., Wang, N., et al. (2013). Characterization of the properties of seven promoters in the motor cortex of rats and monkeys after lentiviral vector-mediated gene transfer. *Hum. Gene Ther. Methods* 24, 333–344. doi: 10.1089/hgtb.2012.238

Yazdan-Shahmorad, A., Tian, N., Kharazia, V., Samaranch, L., Kells, A., Bringas, J., et al. (2018). Widespread optogenetic expression in macaque cortex obtained with MR-guided, convection enhanced delivery (CED) of AAV vector to the thalamus. *J. Neurosci. Methods* 293, 347–358. doi: 10.1016/j.jneumeth.2017.10.009

Ye, L., Allen, W. E., Thompson, K. R., Tian, Q., Hsueh, B., Ramakrishnan, C., et al. (2016). Wiring and molecular features of prefrontal ensembles representing distinct experiences. *Cell* 165, 1776–1788. doi: 10.1016/j.cell.2016.05.010

Zhang, H., Yang, B., Mu, X., Ahmed, S. S., Su, Q., He, R., et al. (2011). Several RAAV vectors efficiently cross the blood-brain barrier and transduce neurons and astrocytes in the neonatal mouse central nervous system. *Mol. Ther.* 19, 1440–1448. doi: 10.1038/mt.2011.98

Zhang, Y., Zheng, Y., Zhang, Y. P., Shields, L. B. E., Hu, X., Yu, P., et al. (2010). Enhanced adenoviral gene delivery to motor and dorsal root ganglion neurons following injection into demyelinated peripheral nerves. *J. Neurosci. Res.* 88, 2374–2384. doi: 10.1002/jnr.22394

Zhu, J., Huang, X., and Yang, Y. (2009). The TLR9-MyD88 pathway is critical for adaptive immune responses to adeno-associated virus gene therapy vectors in mice. *J. Clin. Invest.* 119, 2388–2398. doi: 10.1016/s1525-0016(16)39131-6

Zincarelli, C., Soltys, S., Rengo, G., and Rabinowitz, J. E. (2008). Analysis of AAV serotypes 1-9 mediated gene expression and tropism in mice after systemic injection. *Mol. Ther.* 16, 1073–1080. doi: 10.1038/mt.2008.76

Zingg, B., Chou, X., Zhang, Z., Mesik, L., Liang, F., Tao, H. W., et al. (2017). AAV-mediated anterograde transsynaptic tagging: mapping corticocollicular input-defined neural pathways for defense behaviors. *Neuron* 93, 33–47. doi: 10.1016/j.neuron.2016.11.045

Conflict of Interest: LH, KG, MR, IE, SB, JK, and MF were employed by Addgene, a nonprofit repository that distributes research materials including plasmids and AAV.

The remaining authors declare that the research was conducted in the absence of any commercial or financial relationships that could be construed as a potential conflict of interest.

frontiers in Neuroanatomy

REVIEW
published: 16 June 2020
doi: 10.3389/fnana.2020.00037

Neuromechanisms of SARS-CoV-2: A Review

Marcos F. DosSantos[1,2,3], Sylvie Devalle[4], Veronica Aran[4], Daniela Capra[1,3,4], Natália Roberta Roque[4], Juliana de Mattos Coelho-Aguiar[1], Tânia Cristina Leite de Sampaio e Spohr[4,5], Janice Gonçalves Subilhaga[6], Cláudia Maria Pereira[7], Isabella D'Andrea Meira[8,9,10], Paulo Niemeyer Soares Filho[10] and Vivaldo Moura-Neto[1,3,4,5,10]**

[1] Laboratório de Morfogênese Celular, Instituto de Ciências Biomédicas, Universidade Federal do Rio de Janeiro, Rio de Janeiro, Brazil, [2] Programa de Pós-Graduação em Medicina (Radiologia), Universidade Federal do Rio de Janeiro, Rio de Janeiro, Brazil, [3] Programa de Pós-Graduação em Neurociência Translacional, Instituto Nacional de Neurociência Translacional (INNT-UFRJ), Rio de Janeiro, Brazil, [4] Laboratório de Biomedicina do Cérebro, Instituto Estadual do Cérebro Paulo Niemeyer, Secretaria de Estado de Saúde, Rio de Janeiro, Brazil, [5] Programa de Pós-Graduação em Anatomia Patológica, Hospital Universitário Clementino Fraga Filho, Universidade Federal do Rio de Janeiro, Rio de Janeiro, Brazil, [6] Setor de Pneumologia, Serviço de Clínica Médica, Hospital Federal dos Servidores do Estado, Rio de Janeiro, Brazil, [7] Programa de Pós-Graduação em Biomedicina Translacional e Odontologia Clínica e Experimental, Universidade do Grande Rio (Unigranrio), Duque de Caxias, Brazil, [8] Departamento de Neurologia, Universidade Federal Fluminense, Niterói, Brazil, [9] Programa de Epilepsia do Instituto Estadual do Cérebro Paulo Niemeyer, Secretaria de Estado de Saúde, Rio de Janeiro, Brazil, [10] Instituto Estadual do Cérebro Paulo Niemeyer, Secretaria de Estado de Saúde, Rio de Janeiro, Brazil

Recent studies have suggested the neuroinvasive potential of severe acute respiratory coronavirus 2 (SARS-CoV-2). Notably, neuroinvasiveness might be involved in the pathophysiology of coronavirus disease 2019 (COVID-19). Some studies have demonstrated that synapse-connected routes may enable coronaviruses to access the central nervous system (CNS). However, evidence related to the presence of SARS-CoV-2 in the CNS, its direct impact on the CNS, and the contribution to symptoms suffered, remain sparse. Here, we review the current literature that indicates that SARS-CoV-2 can invade the nervous system. We also describe the neural circuits that are potentially affected by the virus and their possible role in the progress of COVID-19. In addition, we propose several strategies to understand, diagnose, and treat the neurological symptoms of COVID-19.

Keywords: SARS-CoV-2, COVID-19, central nervous system, peripheral nervous system, anosmia, dysgeusia

OPEN ACCESS

Edited by:
Wen-Jie Song,
Kumamoto University Hospital, Japan

Reviewed by:
Ryohei Tomioka,
Kumamoto University, Japan
Hiroyuki Hioki,
Juntendo University, Japan

****Correspondence:***
Marcos F. DosSantos
santosmfh@icb.ufrj.br;
santosmfh@gmail.com
Vivaldo Moura-Neto
vivaldomouraneto@gmail.com

Received: *02 May 2020*
Accepted: *03 June 2020*
Published: *16 June 2020*

Citation:
DosSantos MF, Devalle S, Aran V, Capra D, Roque NR, Coelho-Aguiar JdM, Spohr TCLdS, Subilhaga JG, Pereira CM, D'Andrea Meira I, Niemeyer Soares Filho P and Moura-Neto V (2020) Neuromechanisms of SARS-CoV-2: A Review. Front. Neuroanat. 14:37. doi: 10.3389/fnana.2020.00037

INTRODUCTION

A highly pathogenic coronavirus termed severe acute respiratory syndrome coronavirus 2 (SARS-CoV-2) emerged in December 2019 in Wuhan, China. Since then, it has rapidly spread globally. SARS-CoV-2 causes coronavirus disease 2019 (COVID-19), which can result in rapid and intense respiratory symptoms and lung failure (Dong et al., 2020; Park et al., 2020). Genomic analysis revealed that this virus belongs to the same clade, beta coronaviruses, as severe acute respiratory syndrome coronavirus (SARS-CoV) and Middle East respiratory syndrome coronavirus (MERS-CoV) and that it shares a highly homologous sequence with SARS-CoV (Yu et al., 2020). Due to its high infectivity, the number of people with COVID-19 continues to grow worldwide.

Epidemiological studies have shown that patients with COVID-19 can present a number of symptoms, including a broad range of neurological complications such as headache, ischemic stroke, impaired consciousness, and encephalitis/meningitis (Gautier and Ravussin, 2020;

Giacomelli et al., 2020; Mao et al., 2020; Poyiadji et al., 2020; Wang D. et al., 2020 (**Table 1**). Moreover, the presence of olfactory and taste disorders such as anosmia, hyposmia, ageusia, and dysgeusia in many individuals suggests the involvement of cranial nerves (Gautier and Ravussin, 2020; Giacomelli et al., 2020). Possible involvement of the nervous system (NS) structures, particularly the brainstem, by SARS-CoV-2, has also been suggested (Li Y. C. et al., 2020). According to this hypothesis, which is based on older articles (Andries and Pensaert, 1980; Matsuda et al., 2004; Li et al., 2012, 2013), coronaviruses initially invade peripheral-nerve terminals, and then progress toward the central nervous system (CNS), via synapse-connected routes. This would not be surprising, given the capacity of different viruses (e.g., Herpes Simplex and Herpes Zoster) to migrate via peripheral neurons to either sensory ganglia or to the CNS, where they cause extensive damage (usually after dormancy reactivation) (Oaklander, 2001; Watson and Oaklander, 2002; Dworkin et al., 2008; Dasilva and Dossantos, 2012). Interestingly, a study used electron microscopy to explore the dissemination of the hemagglutinating encephalomyelitis virus (HEV), also a single-stranded RNA beta coronavirus, in the primary motor cortex of infected rats (Li et al., 2013). The results revealed that membranous coating-mediated endo-/exocytosis might be used for the transsynaptic exchanges of coronaviruses. The same study indicated that the transsynaptic pathway could be adapted for larger granular material, including viruses (Li et al., 2013).

Strikingly, coronaviruses have also been reported to cause enteric diseases in both animals and humans (2003; Zhou et al., 2017). Therefore, the involvement of the enteric nervous system (ENS) in the pathophysiology of COVID-19 must also be considered.

This critical review aims to comprehensively evaluate the current literature and examine the available evidence regarding the impacts of COVID-19 on the NS. The possible neural circuits involved in this process and the putative pathophysiological mechanisms will be analyzed. Finally, different approaches to study these phenomena will be proposed.

TABLE 1 | Percentages of patients with COVID-19 that suffered from neurological symptoms, considering the studies included in the current review.

Main neurological symptoms	Percentage (Reference)
Acute cerebrovascular disease	2.8% (Mao et al., 2020)
Acute hemorrhagic necrotizing encephalopathy	Case report (Poyiadji et al., 2020)
Ataxia	0.5% (Mao et al., 2020)
Ageusia	1.7% (Giacomelli et al., 2020)
Ageusia and anosmia	8.5% (Giacomelli et al., 2020)
Ageusia and hyposmia	3.4% (Giacomelli et al., 2020)
Dizziness	9.4% (Wang D. et al., 2020); 16.8 (Mao et al., 2020)
Dysgeusia	8.5% (Giacomelli et al., 2020)
Dysgeusia and anosmia	3.4% (Giacomelli et al., 2020)
Dysgeusia and hyposmia	3.4% (Giacomelli et al., 2020)
Headache	3.4% (Giacomelli et al., 2020); 6.5% (Wang D. et al., 2020); 13.1% (Mao et al., 2020)
Hyposmia	5.1% (4); 5.1% (Mao et al., 2020)
Impaired consciousness	7.5% (Mao et al., 2020)
Ischemic stroke	2.8% (Mao et al., 2020)
Meningitis/Encephalitis	Case report (Moriguchi et al., 2020)
Nerve pain	2.3%
Seizure	0.5% (Mao et al., 2020)
Smell impairment	5.1% (Mao et al., 2020)
Taste impairment	5.6% (Mao et al., 2020)
Vision impairment	1.4% (Mao et al., 2020)
Vomiting	3.6% (Wang D. et al., 2020)

INTERPRETATION OF THE NEUROINVASION RELATED TO SARS-CoV-2 AND THE MAIN NEUROLOGICAL SYMPTOMS ASSOCIATED WITH COVID-19

In a study exploring the main signs and symptoms found in 138 hospitalized patients diagnosed with COVID-19-related pneumonia, all patients reported persistent olfactory and taste disorders (Wang D. et al., 2020). Remarkably, taste alterations were more frequent before hospitalization (91%), whereas after hospitalization, taste and olfactory alterations had equal frequency. The epidemiological heterogeneity related to the type and time-course of these symptoms suggests that COVID-19 might differentially affect individuals according to factors such as gender and age (Giacomelli et al., 2020). In addition, due to its early onset, these taste and olfactory changes provide a useful and straightforward screening opportunity to identify people with COVID-19 and limit viral spread (Gautier and Ravussin, 2020; Giacomelli et al., 2020). Neurological symptoms were also analyzed in a cohort of 214 hospitalized patients diagnosed with COVID-19 (Mao et al., 2020), which found an incidence of anosmia in 5.1% and ageusia in 5.6%. Anosmia has been previously associated with SARS-CoV and other coronaviruses (Hwang, 2006; Vaira et al., 2020). Moreover, it has been proposed that SARS-CoV-2 enters through the olfactory nerve and reaches the brain, in the same manner as SARS-CoV.

It is likely that the mechanisms underlying the taste and olfactory changes in the course of COVID-19 are related to the role played by the angiotensin-converting enzyme-2 (ACE2) receptor (Lu et al., 2020). It has been demonstrated that this receptor is used by SARS-CoV-2 to bind and penetrate human cells (Lu et al., 2020). The wide expression of the ACE2 receptor in the epithelial cells of the oral and nasal mucosa (Xu et al., 2020) suggests that the virus-related damage caused by SARS-CoV-2 in these sites is linked to the effects of the virus on the function of the ACE2 receptor. However, the specific expression of ACE2 through the olfactory pathway in humans and rodents is still debated and has been explored in several studies (Chen R. et al., 2020; Li Y. C. et al., 2020; Natoli et al., 2020; Ueha et al., 2020; Wu Y. et al., 2020). Moreover, it is important to consider the roles of Furin and the transmembrane protease

serine 2 (TMPRSS2) in this process (Ueha et al., 2020). Overall, ACE2 is responsible for the entry of SARS-CoV-2 into cells. This process depends on the binding of the viral spike, glycoprotein, to this cellular receptor. The process also involves cleavage of the viral spike protein by Furin, as well as the occurrence of spike-protein priming by host-cell serine proteases such as the transmembrane protease serine 2 (TMPRSS2), which is localized in the cell membrane and facilitates viral uptake (Li et al., 2003; Coutard et al., 2020; Hoffmann et al., 2020; Lukassen et al., 2020; Matsuyama et al., 2020; Walls et al., 2020; Wu F. et al., 2020). Although there is a lack of evidence regarding the distributions of ACE2, TMPRSS2, and Furin in the different cellular components of the olfactory pathway, the close relationship between smell and the central nervous system (CNS), together with the occurrence of neurological symptoms in patients with COVID-19, alludes to the involvement of the CNS. The possible involvement of the olfactory pathway in the route of SARS-CoV-2 to the CNS has been explored by several authors, who have proposed different mechanisms (Brann et al., 2020; Chen R. et al., 2020; Natoli et al., 2020; Ueha et al., 2020; Wu Y. et al., 2020). Hence, it is crucial to understand the role of the classical sensory pathways that are linked to the cranial nerve functions in COVID-19. Nonetheless, it is also important to determine any alternative routes that SARS-CoV-2 may take to reach the CNS, including those related to the ENS.

SARS-CoV-2 RNA and its viral particle have been found in the feces of patients with COVID-19 (Chen Y. et al., 2020), with sustained viral RNA shedding even after the end of symptoms. These findings suggest the existence of a fecal-oral transmission route (Wölfel et al., 2020). The SARS-CoV and MERS-CoV viruses remain viable in sewage water for a few days and can spread through fecal-oral transmission (Wang et al., 2005; Chan et al., 2011; Van Doremalen et al., 2013). It has been suggested that SARS-CoV-2 is also transmitted through this route (Yeo et al., 2020). In addition, it is possible that binding to ACE2 receptors is also a critical determinant of infectivity that must be considered when analyzing the pathophysiology of COVID-19 (Wrapp et al., 2020; Yeo et al., 2020). The small intestine and colon epithelial cells, in particular the enterocytes, strongly express the ACE2 receptor, displaying even higher expression levels than the lung (Lamers et al., 2020; Liang et al., 2020; Zhou J. et al., 2020). In addition, the same study indicated that the colon neural ganglia also express this receptor. Moreover, viral mRNA has been found in the feces of patients with COVID-19 (Chen Y. et al., 2020; Xiao et al., 2020), suggesting that SARS-CoV-2 may cause not only respiratory but also enteric infection. Therefore, it is equally important to explore the contribution of the ENS to COVID-19. Possible involvement of the ENS and the so-called gut-brain axis is further discussed below.

POSSIBLE MECHANISMS ASSOCIATED WITH SARS-CoV-2 NEUROINVASION

Some evidence suggests that the respiratory effects of COVID-19 might be at least partially associated with the neuroinvasive potential of SARS-CoV-2 (Li Y. C. et al., 2020). As mentioned above, neurological symptoms have been reported in patients with COVID-19 (Wang D. et al., 2020). More importantly, there is strong evidence that rather than being restricted to the respiratory system, coronaviruses also invade the CNS, which could be associated with significant brain damage, different types of neurological diseases, and damage of the medullary cardiorespiratory center which could in turn also affect the respiratory function (Gautier and Ravussin, 2020; Giacomelli et al., 2020; Mao et al., 2020; Poyiadji et al., 2020; Wang D. et al., 2020). Some past studies also indicated the presence of SARS-CoV particles located in brain neurons in samples from infected individuals (Ding et al., 2004; Gu et al., 2005; Li et al., 2016).

Previous experimental models may help to understand the neuromechanisms related to COVID-19. However, caution is essential in evaluating the results of studies that demonstrated the dissemination of SARS-CoV and MERS-CoV to the CNS. Those studies used ACE2 (in the case of SARS-CoV) or DPP4 (in the case of MERS-CoV) transgenic mice, without demonstrating viral spread to the brain of wild-type mice. Therefore, these transgenic models resolve issues related to the infection in wild-type mice by SARS-CoV or MERS-CoV, such as the differences in the structure of mouse and human ACE2 proteins that reduce the tropism of SARS-CoV to mouse tissues (Natoli et al., 2020). A transgenic model was generated to resolve this issue (Netland et al., 2008). In that study, a vector that carried a human ACE2-coding sequence was introduced into wild-type mice (hACE2) under control of the human cytokeratin 18 (K18) promoter (McCray et al., 2007). Upon SARS-CoV infection, the K18-hACE2 transgenic mice showed viral spread through the olfactory pathway, which reached the subcortical and cortical regions (Netland et al., 2008). Some studies performed with transgenic mice showed that both SARS-CoV and MERS-CoV when administered intranasally, may gain access to the brain tissue and rapidly spread toward specific brain areas such as the brainstem and thalamus (Li et al., 2016; Chen Y. et al., 2020). This route of infection could involve the olfactory pathway (Giacomelli et al., 2020). Remarkably, the brainstem, an area that receives the primary afferents of the majority of the cranial nerves and that encloses the medullary cardiorespiratory center, seems to be among the brain regions that are most infected by SARS-CoV and MERS-CoV (McCray et al., 2007; Netland et al., 2008; Li et al., 2016; Li Y. C. et al., 2020). This suggests that infection by SARS-CoV-2 also causes significant changes in many CNS areas, which would probably be reached through routes involving primary afferents of cranial nerves. Nonetheless, the specific route or set of routes by which coronaviruses infect the CNS has not been completely clarified. Lymphatic/hematogenous spread does not seem to be a possibility, especially considering that virtually no viral particle has been detected in the non-neuronal cells of the infected brain areas in cases of SARS-CoV or MERS-CoV (Ding et al., 2004; Gu et al., 2005). This observation also supports the hypothesis that the access of coronaviruses to the CNS would involve peripheral (e.g., cranial) nerves, through synapse-connected neural circuits (Andries and Pensaert, 1980; Matsuda et al., 2004; Li et al., 2012, 2013; Li Y. C. et al., 2020).

POTENTIAL NEURAL CIRCUITS RELATED TO THE MIGRATION OF SARS-CoV-2 FROM THE PERIPHERY TO THE CNS

The olfactory pathway is considered one of the strongest candidate routes for SARS-CoV-2 to reach the CNS. Although the evidence is sparse, the current literature points in this direction. The olfactory pathway starts at the olfactory epithelium localized in the upper part of the nasal cavity, i.e., the olfactory mucosa. Olfactory receptors are small bipolar neurons that contain dendrites emerging from one end of their cell bodies, and axons emerging from the opposite end. The unmyelinated and very thin axons of the olfactory receptors collect into a series of small bundles that cross the holes located in the cribriform plate of the ethmoid bone, to end at the olfactory bulb. These small bundles collectively comprise the olfactory nerve. Unlike other mammalian nerves, the olfactory receptors are replaced throughout life, and new receptors arise from undifferentiated basal cells located in the basal epithelium. This may be important, considering the duration of the olfactory symptoms related to COVID-19. The synapse between the first and second neurons of the olfactory pathway occur at the olfactory bulb on each side, specifically at the olfactory glomeruli (**Figure 1**). Axons of the second-order neurons of this pathway follow a central route into the olfactory tract. The primary central projections of the olfactory bulb are the olfactory nucleus, olfactory tubercle, piriform cortex, amygdala, peri-amygdaloid cortex, insula, and the anterior part of the parahippocampal gyrus (entorhinal cortex) (Nolte, 2009). Of particular interest are the absence of a thalamic relay (although other important connections are established by the olfactory pathway) and the presence of only two neurons in this pathway. However, its cortical targets might be vital in the context of COVID-19. Possible changes in the activity of cortical targets of the olfactory pathway induced by SARS-CoV-2 could, at least in part, explain the neurological symptoms reported by patients with COVID-19 (**Figure 2**). For instance, the corticomedial amygdala is connected to the anterior preoptic and ventromedial nucleus of the hypothalamus. On the other hand, the central nucleus of the amygdala is connected to the lateral part of the hypothalamus (Standring, 2008). The amygdala has two projections to the hypothalamus: the stria terminalis, a long bundle that follows the caudate nucleus, and a shorter pathway, called ventral amygdalofugal. In addition, it is important to remember the olfactory nerve's connections to the hypothalamus, considering the critical role of the hypothalamus in controlling body temperature and its connections to the autonomic nervous system (Paxinos and Mai, 2004). Thus, an infection by SARS-CoV-2 that affects the neurons and synapses along these routes could compromise these essential functions. In addition, taste depends on integration at the frontal lobe of different stimuli that are not only gustatory. Unsurprisingly, the primary olfactory cortex sends information to the frontal lobe via direct projections, or through a relay in the dorsomedial nucleus of the thalamus (Nolte, 2009). All these connections are important to understand the crosstalk between the olfactory pathway and many cortical and subcortical structures, and therefore their potential importance for SARS-CoV-2. Some studies have analyzed the possible involvement of the olfactory pathway in the spread of SARS-CoV-2 from the periphery to the CNS, as well as the contribution of the cells located in the olfactory mucosa to the olfactory disturbances that are frequently found in patients with COVID-19.

By analyzing data from available brain transcriptome databases, one interesting study evaluated the expression of ACE2 in human and mouse brains (Chen R. et al., 2020). This study also scrutinized the expression of ACE2, along with the main structures of the olfactory system. Strikingly, the distribution of ACE2 was similar in both the mouse and human brain. However, high expression of ACE2 was found in the mouse olfactory bulb, whereas in human brains, ACE2 was more highly expressed in the piriform cortex. Although no data were available regarding the expression of ACE2 in the human olfactory bulb, these findings, at least indirectly, support the concept that the invasion of the CNS by SARS-CoV-2 might occur through the olfactory system. It has also been suggested that the unique characteristics of the olfactory nerve, the olfactory bulb, and the other components of the olfactory pathway may help to explain the importance of this route for the dissemination of SARS-CoV or SARS-CoV-2 to the CNS (Natoli et al., 2020). Some unique characteristics of the olfactory pathway include the presence of olfactory receptor cells in the mucosa, in this case, the olfactory epithelium, the presence of only first and second neurons that synapse at the olfactory glomeruli, the ipsilateral central projections, and the absence of a thalamic relay (Nolte, 2009). In addition, high expression of ACE2 in some hypothalamic nuclei was found in the human brain (Chen R. et al., 2020). As already mentioned, the hypothalamus may be indirectly linked to the olfactory pathway. Nonetheless, the specific mechanisms through which SARS-CoV-2 reaches the CNS through the olfactory pathway are still not clear. Interestingly, the same study showed high expression of ACE2 in some important brain areas such as brain ventricles and substantia nigra but also areas directly or indirectly related to the olfactory pathway, including the amygdala, the hippocampus, some hypothalamic nuclei and the frontal cortex (Chen R. et al., 2020). Some of these regions and connections are illustrated in **Figure 2**.

One study suggested that SARS-CoV-2 may adhere to different regions of the respiratory system (e.g., nasal cavity, pharynx, nasopharynx, larynx, and trachea). When the virus adheres to the nasal cavity, it can reach the olfactory epithelium, infect the olfactory neurons located in the olfactory epithelium (**Figure 1**), and then reach the CNS via the olfactory nerve and the related neural circuits (Li Z. et al., 2020). However, other studies have provided more detailed information on SARS-CoV-2 from the olfactory mucosa to the CNS. Through analyses of RNA-seq libraries from the human olfactory neuroepithelium, one study reported the expression of both ACE2 and TMPRSS2 in the olfactory sustentacular cells, microvillar cells, Bowman's glands, and horizontal basal cells (Fodoulian et al., 2020). Another study used *in-situ* hybridization to analyze the expression of *TMPRSS2* mRNA in the olfactory epithelium (Bilinska et al., 2020), which showed that *TMPRSS2* mRNA was present at high levels in sustentacular cells, very

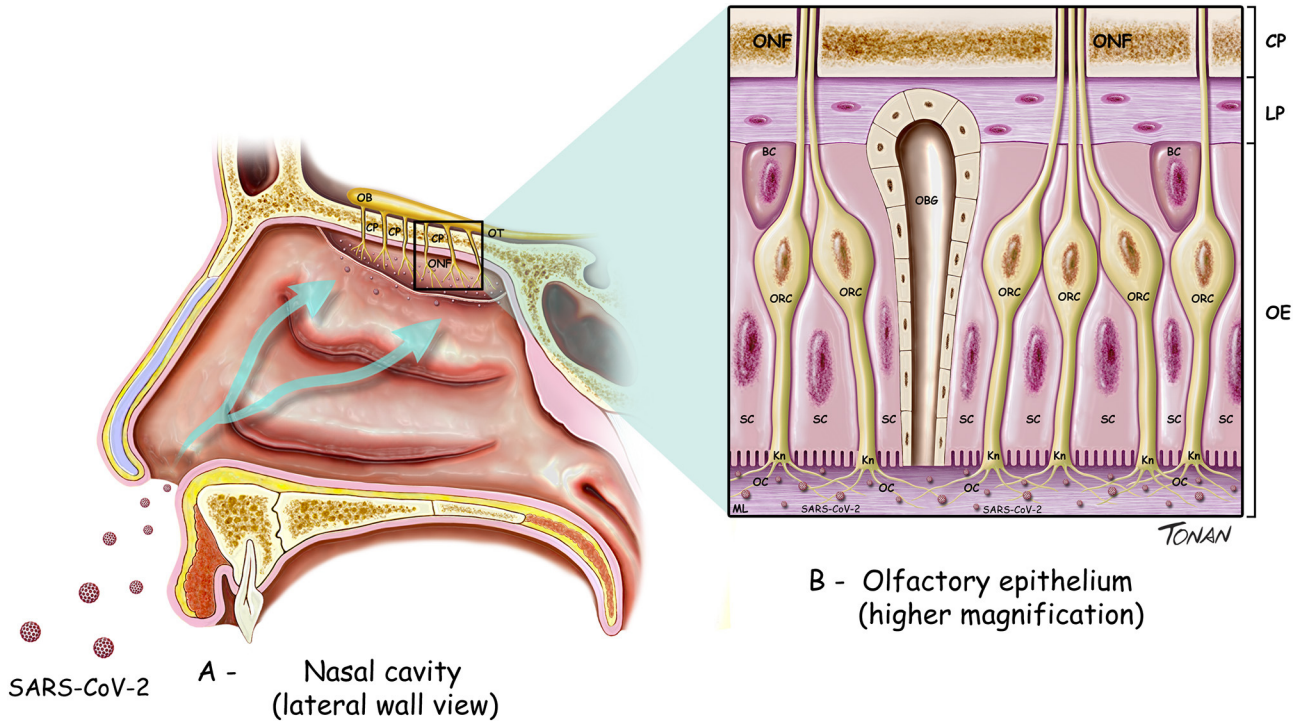

FIGURE 1 | Diagram illustrating the cell types found in the olfactory bulb and part of the olfactory pathway. **(A)** OB, olfactory bulb; OT, olfactory tract; ONF, olfactory nerve fibers; CP, cribiform plate of ethmoid bone. **(B)** ONF, olfactory nerve fibers; CP, cribiform plate of ethmoid bone.; LP, lamina propria; OE, olfactory epithelium; BC, basal cells; SC, supporting (sustentacular) cells; OBG, olfactory Bowman's gland; ORC, olfactory receptor cells; Kn, olfactory Knobs; OC, olfactory cilia.

low (if at all) in mature olfactory receptor neurons, and, at a lower level, in horizontal basal cells. The same study assessed the expression of ACE2 by immunohistochemistry, which confirmed the expression of ACE2 in sustentacular cells, but not in receptor neurons or basal cells (Bilinska et al., 2020). According to Fodoulian et al. (2020), sustentacular cells, rather than other positive cells for ACE2 and TMPRSS2 in the olfactory sensory epithelium, are the prime candidates for the origin of SARS-CoV-2-induced anosmia. Supporting this hypothesis is the rapid development of anosmia triggered by SARS-CoV-2, the high amounts of TMPRSS2 and ACE2 transcripts in sustentacular cells, and the critical role played by sustentacular cells in maintaining the integrity of the olfactory neuroepithelium. When the sustentacular cells are lost, the entire neuroepithelium disintegrates, leading to anosmia. Some examples include transient anosmia related to the effects of some chemical agents that affect sustentacular cells, such as 3-methylindole (Miller and O'bryan, 2003), the antithyroid drug methimazole (Bergström et al., 2003) or nickel sulfate NiSO(4) (Jia et al., 2010). Another study analyzed bulk and single-cell RNA-Seq datasets of humans and mice to determine the cell types in both the olfactory epithelium and the olfactory bulb that express cell-entry molecules related to SARS-CoV-2 infection. Based on the absence of the ACE2 and TMPRSS2 genes in the olfactory sensory neurons as well as in the olfactory bulb, contrasting with their presence in supporting cells, stem cells, and perivascular cells, the authors concluded that anosmia and other olfactory disturbances found in patients with COVID-19 is associated with non-neuronal cells (Brann et al., 2020). Therefore, an alternative mechanism, not involving the direct infection of olfactory neurons, must be considered when interpreting the presence of anosmia in patients with COVID-19. Another study used immunohistochemistry and gene analyses to determine the presence of ACE2, TMPRSS2, and Furin in the respiratory mucosa, olfactory mucosa, and olfactory bulb of both human and mouse tissues (Ueha et al., 2020), which showed that ACE2 was widely expressed in the respiratory mucosa, olfactory mucosa, and olfactory bulb. ACE2, TMPRSS2, and Furin were co-expressed in the respiratory mucosa (e.g., respiratory epithelium and subepithelial glands) and in the olfactory mucosa, particularly in the supporting cells of the olfactory epithelium and Bowman's glands. However, the olfactory receptor neurons of the olfactory mucosa were positive for ACE2 but almost negative for TMPRSS2 and Furin. Olfactory bulb cells strongly expressed ACE2, weakly expressed Furin, and did not express TMPRSS2. The authors of this study concluded that odor transduction can be impaired by neuronal dysfunction, considering the co-expression of ACE2 and TMPRSS2 in the olfactory nerve bundles. Nevertheless, they suggested that it is unlikely that SARS-CoV-2 directly damages the olfactory receptor neurons, since these cells seem to express ACE2, but not TMPRSS2 or Furin. According to the authors, this absence of TMPRSS2 and Furin expression by olfactory receptor neurons could determine an early recovery of anosmia

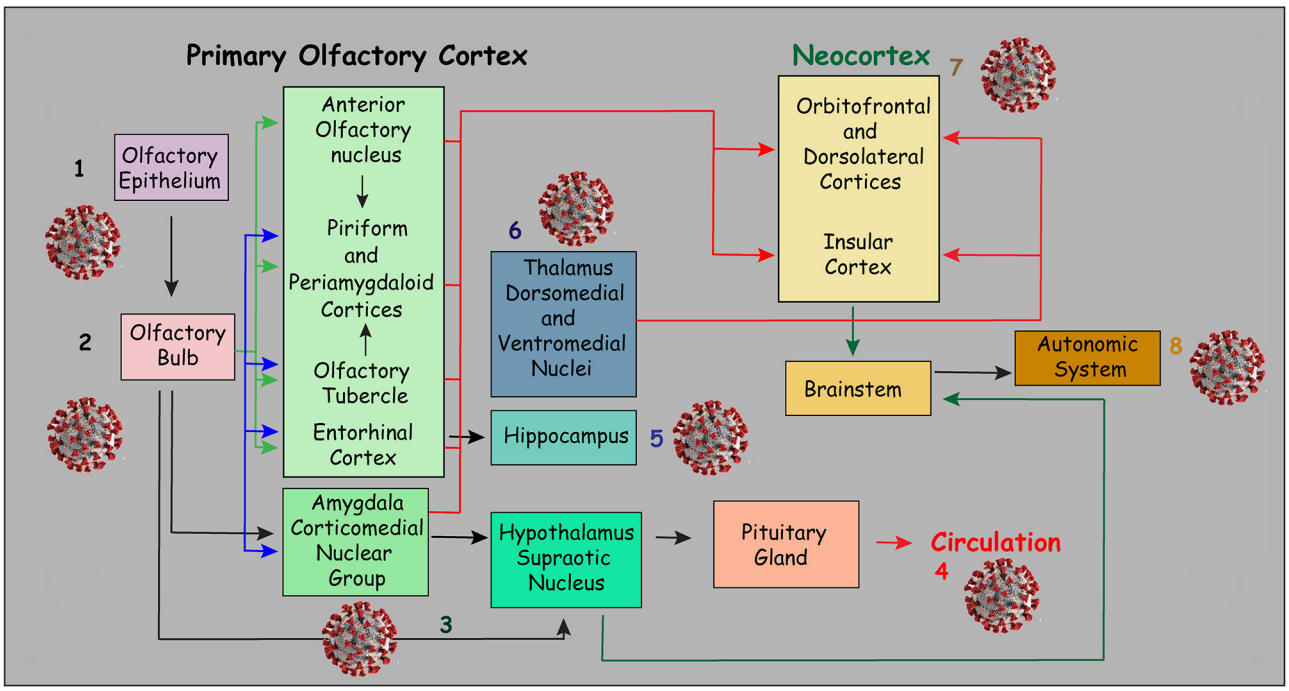

FIGURE 2 | Diagram illustrating the main connections of the primary olfactory cortex. Viral sketches represent the possible symptoms related to the area of impairment: Loss of smell is probably the most evident symptom (1 and 2). However, through direct and indirect connections, the olfactory pathway may be related to several neurologic symptoms. For instance, the connections of the olfactory pathway with the amygdala nuclei may be related to emotional impairment. In addition, other central nervous system changes and neurologic symptoms that may be related to direct or indirect connections of the olfactory pathway are illustrated in this figure. For example, indirect connections to some hypothalamic nuclei, especially the supraoptic nucleus (3) may affect neuroendocrine control, which may, in turn, affect the function of the pituitary gland (4). Moreover, connections to the hippocampus (5) may result in memory impairment. On the other hand, indirect connections to some thalamic nuclei may be associated with sensory and movement impairment (6) while the connections to the frontal and insular cortices (7) may be associated with cognitive impairment. Indirect connections with the brainstem may also result in autonomic nervous system impairment (8). Not surprisingly, the ACE receptor has been found in several of the areas illustrated in this figure (Chen R. et al., 2020). This figure has been adapted from a previous work Devere (2017).

in patients with COVID-19. However, this concept must be further explored.

Conversely, Fodoulian et al. (2020) demonstrated that human horizontal basal cells express ACE2 and TMPRSS2 at low levels. Horizontal basal cells are progenitors that divide throughout adult life and continually replace sensory neurons (Durante et al., 2020). This suggests that olfactory sensory neurons differentiated from infected horizontal basal cells may be infected by SARS-CoV-2, and via a transsynaptic route, this virus migrates through the olfactory bulb to reach the olfactory cortex.

Importantly, not only the olfactory system but also other routes must be considered when exploring the route of entry into the CNS by SARS-CoV-2. For instance, high expression of ACE2 in both the central glial substance and in the cerebrospinal fluid (CSF) has also been found in the human brain (Chen R. et al., 2020). This is important since it provides additional routes that might be potentially used by SARS-CoV-2 to reach the CNS. In addition, the possible contribution of other sensory pathways to this process must be evaluated in detail (Li Z. et al., 2020).

Flavor perception depends on the integrity of the facial, glossopharyngeal, and vagus nerves. Each of these nerves encompasses pseudo-unipolar neurons. The cell bodies of each of these neurons are located within specific peripheral ganglia, as follows: geniculate ganglion (facial nerve), nodose ganglion (vagus nerve), and petrosal ganglion (glossopharyngeal nerve). However, the synapses between the first- and second-order neurons of all these three nerves occur at a single nucleus, the nucleus of the solitary tract (NST), located in the medulla, and are considered to be the main visceral nucleus of the brainstem. From the NST, nerve fibers travel through the ipsilateral central tegmental tract to the medial part of the ventral posteromedial (VPM) nucleus of the thalamus, where a synapse with third-order neurons takes place (Nolte, 2009). Finally, these neurons project to the gustatory cortex, located in the insula and the medial surface of the frontal operculum (Nolte, 2009), which may also be potential CNS targets of SARS-CoV-2. Regarding the possible invasion of brainstem nuclei by SARS-CoV-2, the importance of the NST and the nucleus ambiguous (NA) must be emphasized. The NST receives sensory input from both chemoreceptors and mechanoreceptors in the respiratory tracts. On the other hand, the efferent fibers from the NA and the NST innervate the airway smooth muscles, blood vessels, and glands (Standring, 2008). These neuroanatomical relationships, together with the proximity of the NST and the NA with the medullary cardiorespiratory center, suggest that the death of patients with COVID-19 might be associated with damage to the medullary

cardiorespiratory center. Furthermore, considering a previous finding that the median time from the first symptom to dyspnea is around 5 days, followed by 7 days to hospital admission, and 8 days to intensive care (Wang D. et al., 2020), it has been suggested that the latency period of COVID-19 would be sufficient for the virus to enter and damage the neurons in the cardiorespiratory center, located in the brainstem (Li Y. C. et al., 2020).

On the other hand, the general sensory inputs from the nasal cavity (respiratory mucosa) and oral cavity are carried out by the primary afferents of the trigeminal nerve. Trigeminal neurons are also classified as pseudo-unipolar and have their cell bodies located in the trigeminal (Gasserian) ganglion. In the trigeminal pathway, the synapses between the first- and second-order neurons occur at the trigeminal brainstem sensory nuclear complex (TBSNC) that extends through a large region of the brainstem (Paxinos and Mai, 2004; Standring, 2008; Nolte, 2009). These neurons then project to the VPM nucleus of the thalamus, where synapses occur with neurons that, in turn, project to the primary sensory cortex (S1). All these anatomical descriptions indicate at least four pathways by which SARS-CoV-2 could act at the CNS level. Of particular interest is the proximity between the TBSNC/NST and the cardiorespiratory center, all located in the medulla.

Regarding the ENS, most of its neurons involved in motor function are located within the myenteric plexus, although some primary afferent neurons reside in the submucous plexus. As in all NS involved in sensory-motor control, the ENS includes primary afferents. Enteric neurons receive input from ascending interneurons (which contain opioid peptides) as well as from descending cholinergic neurons (Costa et al., 2000). Considering the several particularities of the ENS (Coelho-Aguiar et al., 2015), the possible role of this system in COVID-19 will be discussed separately.

POTENTIAL CONTRIBUTION OF THE ENS TO SARS-CoV-2 MECHANISMS AND THE COVID-19 GASTROINTESTINAL SYMPTOMS

Gastrointestinal symptoms have been reported in ∼10% of the patients hospitalized and diagnosed with COVID-19, and abdominal pain may also occur (Wang D. et al., 2020). Xiao et al. (2020) found that 53% of 73 hospitalized patients with COVID-19 had viral RNA in their stools. Approximately 23% of these patients still had positive results in their stools, even after their respiratory samples became viral RNA-negative (Xiao et al., 2020). A recent *in-vitro* study of epithelial-cell infection demonstrated that SARS-CoV-2 productively infects human gut enterocytes (Lamers et al., 2020). In this study, human intestinal organoids were readily infected by both SARS-CoV and SARS-CoV-2, as demonstrated by confocal and transmission electron microscopy. After 60 h, SARS-CoV-2 induced the production of a large number of apoptotic cells (Lamers et al., 2020). The same study also showed that mature enterocytes express 300 times more ACE2 (Wan et al., 2020). As previously described, binding to the ACE2 receptor has been considered an important aspect of COVID-19 infectivity. A structural *in silico* analysis that predicts higher effectiveness in the use of SARS-CoV-2 human ACE2 when compared to the 2003 SARS-CoV strain supports this idea (Wan et al., 2020). Furthermore, biophysical and structural evidence demonstrated a higher affinity of SARS-CoV-2 S protein to ACE2 (∼10 to ∼20 fold increase when compared to SARS-CoV S protein) (Wrapp et al., 2020). However, proliferative enterocyte progenitors appeared to be the primary targets of gut infection (Lamers et al., 2020). This finding suggests that even low levels of ACE2 may be sufficient for viral entry, at least in these types of cells (Lamers et al., 2020).

In addition, as shown by an mRNA sequence analysis, SARS-CoV-2 infection causes the expression of a wide range of cytokines and interferon-stimulated genes (ISGs), which are attributed to type I and III interferon responses. Notably, the induction of these genes by SARS-CoV occurred at a much lower level (Lamers et al., 2020). A further study that also used organoids showed, through immunofluorescence, the expression of ACE2 in human intestinal organoids, and also the presence of the TMPRSS2 protein (Zhou J. et al., 2020). Based on the high sequence homology of horseshoe bats to SARS-CoVs, a bat origin of SARS-CoV-2 has been proposed (Zhou P. et al., 2020). This information supported the study of Zhou J. et al. (2020) to establish a model to study the gut cells of bats. With this model, the authors compared human and bat organoids. Enteroids derived from intestinal cells of *Rhinolophus sinicus* bats showed ACE2 and TMPRSS2 proteins similar to the human homologs. In addition, they were susceptible to productive SARS-CoV-2 infection. In the same study, the infectious virus was isolated from the stool of a patient with COVID-19 who had diarrhea (Zhou J. et al., 2020). Altogether these findings strongly suggest that the human intestinal tract serves as an alternative route for SARS-CoV-2 infection.

To fully understand the enteric system's contribution to the pathophysiology of SARS-CoV-2 infection, the importance of the gut-brain axis should be considered. The so-called gut-brain axis is highly important in many disorders that affect the CNS, and several recent studies have shown the relevance of this communication for the clinical manifestation and even for the genesis of numerous diseases (Coelho-Aguiar et al., 2019). This communication would make it possible to stimulate specific centers in the CNS (Coelho-Aguiar et al., 2015). In addition, Parker et al. (2020) showed that viral transmission via neurons from the ENS to the CNS is possible both by anterograde and retrograde pathways and that both routes usually reach the same brain sites. As mentioned above, a classical study showed that when inoculated in the orofacial region of suckling piglets, HEV first reaches the upper airway, lungs, and small intestine (Andries and Pensaert, 1980). Also, during the incubation period, viral antigens were detected by immunofluorescence in some peripheral ganglia, such as the inferior vagal ganglion and the intestinal nervous plexuses of the ENS. After that, the HEV spread to the brainstem and was later also found in other regions of the CNS. Indeed, this virus accessed the spinal cord through a route that uses retrograde motor neuron transport from the gut. Infection was also detected in the intestinal nervous plexuses, and the transmission was demonstrated to

occur through transsynaptic migration of the HEV (Andries and Pensaert, 1980). Based on this, it has been suggested that, upon infection of enterocytes by coronaviruses, ENS cells would also be infected and transmit the virus to the CNS. An alternative possibility is that this virus causes vagal stimulation of the NST, similar to what takes place in infection by other enteric viruses such as the rotavirus. In these cases, after enterocytes are infected, a rotavirus-encoded protein stimulates the secretion of serotonin (5-HT) by the enterochromaffin cells of the gut, which in turn stimulate neurons of the myenteric ganglia and vagal nerves that project to areas of the CNS (Crawford et al., 2017). Therefore, it is tempting to speculate that the vast network that connects the ENS to the CNS (Standring, 2008) may also be involved in SARS-CoV-2 NS infection and may be associated with the gastrointestinal symptoms reported by patients diagnosed with COVID-19 (2003). However, there is little evidence for the specific involvement of ENS cells in COVID-19, and further investigation is needed.

NEURO-IMMUNE ROLE IN COVID-19

The significant lung damage seen in patients with COVID-19 has been, in part, associated with a cytokine dysregulation known as "cytokine release syndrome" or "cytokine storm" (Chen G. et al., 2020; Zhang et al., 2020). This so-called "cytokine storm" takes place when the innate and adaptive immune systems, release aberrant levels of cytokine and other factors in an attempt to control the infection, leading to tissue injury or even acute organ failure (Yang et al., 2010; Brune et al., 2015). Several studies have correlated this inflammatory response to patients critically ill with COVID-19 (Leyva-Grado et al., 2010; Chen N. et al., 2020; Huang et al., 2020; Ruan et al., 2020; Wu C. et al., 2020; Zhou F. et al., 2020). The prevalence of the pro- and anti-inflammatory cytokines interleukin receptor-2 (IL-2R), interleukin-6 (IL-6), tumor necrosis factor α (TNF-α) and IL-10 in severe and moderate cases of COVID-19 has also been studied (Chen G. et al., 2020). Notably, both SARS-CoV and SARS-CoV-2 can encode viral proteins with immunomodulatory activity, modifying the host's interferon response and enabling the activation of a multiprotein complex termed inflammasome (Fung et al., 2020).

The neuro-immune pathway functions bidirectionally, where afferent neurons respond to immune signals at the periphery, and the efferent neurons promote the interaction between the brain and the periphery. This inflammatory reflex has been discussed (Leyva-Grado et al., 2010; Huang et al., 2020), and the neurological aspects of SARS-CoV-2 are emerging. Increased data pointing to the involvement of the CNS in COVID-19 related symptoms led our group to inquire about how the neuro-immune response could modulate host immunity and lung inflammation. Remarkably Leyva-Grado et al. (2010), using an intranasal mouse model of influenza, observed that viral invasion reaching the CNS through the olfactory bulb modulates brain cytokines in the brainstem, which could be related to elevation in the body temperature as well as disease progression. Moreover, it has been previously demonstrated that the transection of the olfactory bulb causes a decrease of TNF-α and IL-1β. The evidence of an exacerbated inflammatory response in severe cases of COVID-19 suggests that patients with olfactory and gustatory dysfunctions have less severe lung function impairments.

One study demonstrated that 45% of patients presented neurological symptoms and had lower lymphocyte counts (Mao et al., 2020). The author also noted that the severely affected subgroup of patients, who presented neurological symptoms, also showed a decrease in lymphocyte count (Mao et al., 2020). This lymphocytopenia seems to be transient (excluding long-term immunosuppression risks) and is probably due to virus-directed destruction of infected cells since the virion was detectable in these cells (Wang X. et al., 2020). Interestingly, lymphocytopenia is being adopted as a severity marker for COVID-19, as described for different groups or subgroups of patients (Leyva-Grado et al., 2010; Chen N. et al., 2020; Liu et al., 2020; Wang D. et al., 2020). Finally, COVID-19 has been associated with a case of the auto-immune disease, Guillain-Barré syndrome, emphasizing the importance of understanding viral-elicited immune responses and their long-term consequences (Virani et al., 2020).

IMPORTANT CONSIDERATIONS AND ADDITIONAL EXPLANATIONS FOR THE NEUROLOGICAL SYMPTOMS RELATED TO COVID-19

An additional explanation for the neurological signs/symptoms related to COVID-19 may be the occurrence of a systemic inflammatory response. Indirect mechanisms, such as hypercoagulability with thrombosis (Yin et al., 2020), due to an inadequate activation pathway of cytokines and the platelet response (Fox et al., 2020), may also occur. Moreover, the existence of axonal peripheral neuropathy and myopathy, probably caused by diffuse vasculitis, was previously identified with SARS-CoV (Tsai et al., 2004). Even though symptoms related to changes in the peripheral nervous system have recently been reported in patients with COVID-19 (Mao et al., 2020), the neuronal impairment related to COVID-19 has not been confirmed. However, it is important to consider the natural course of this disease, which could lead to a mismatch between the clinical, biochemical, and imaging features found during the different stages of COVID-19. For instance, one article reported a case of a young patient diagnosed with COVID-19 who presented meningitis/encephalitis, seizure, and consciousness disturbance, with abnormal findings in brain magnetic resonance imaging (MRI) (Moriguchi et al., 2020). In this case report, COVID-19 was confirmed through polymerase chain reaction (PCR), which was positive for SARS-CoV-2 in the cerebrospinal fluid (CSF), but not in the nasopharyngeal swab (Moriguchi et al., 2020). These findings show that, despite the clinical presentations described, there is still a need for in-depth exploration and identification of the real neurological involvement in COVID-19. In another case report, acute hemorrhagic necrotizing encephalopathy was found in a patient with COVID-19 (Poyiadji et al., 2020). However, a detailed study and proper explanation

for several neurological symptoms found in patients with COVID-19 should be conducted in the future.

STRATEGIES TO STUDY THE NEUROINVASIVE POTENTIAL OF SARS-CoV-2

Some methods might be proposed to study the effects of SARS-CoV-2 on the CNS. Among the challenges is the development of an appropriate animal model of COVID-19. There are structural differences in mouse ACE2 compared to human ACE2 proteins, and the SARS coronaviruses exhibit poor tropism for mouse tissues. Therefore, transgenic models are important tools for studying the course of COVID-19. Evaluation of the pathogenicity of SARS-CoV-2 in hACE2 (human angiotensin-converting enzyme-2) transgenic mice demonstrated only mild disease in these chimeric animals, and an absence of viral growth in wild-type mice, emphasizing the importance of hACE2 for SARS-CoV-2 infection and replication in this animal model (Amanat and Krammer, 2020; Bao et al., 2020). However, as previously found with MERS and SARS-COV, as discussed above, the pattern of the disease found in transgenic mice is different from the pattern in wild-type mice. The development of a genetically tractable mammalian model to mimic human pathogenic phenotypes alongside a genetic control system of both host and hCoV genomes could facilitate the understanding of the relationship between virus/host genetics and the pathogenic outcomes (Cockrell et al., 2018).

Considering microRNAs (miRNAs) as possible therapeutic agents against SARS-CoV-2, a computational study aiming to identify possible interactions between host-cellular miRNAs and viral genes was undertaken (Saçar Demirci and Adan, 2020). This study demonstrated that viral genes involved in mechanisms such as biogenesis, entrance, replication, and infection are possible targets for host-cellular miRNAs (Saçar Demirci and Adan, 2020). However, two aspects of this miRNA-based therapeutic strategy against viruses must be considered: a single nucleotide mutation within the virus target region could disrupt the interaction with the host-cellular miRNAs, resulting in viral evasion; and caution is advised when manipulating the level of host-cell miRNAs, due to the important physiological functions of these molecules. Modulation of miRNA levels could lead to unexpected side effects (Mallick et al., 2009).

Another important question is the degree to which the virus causes damage to neurons in specific brain regions (e.g., medullary cardiorespiratory center). For this purpose, primary cell cultures would be the most feasible approach. Immunohistochemistry will also be important to compare the findings in humans and animals, using a post-mortem analysis. However, this can only be considered when using specific antibodies for SARS-CoV-2. Another more modern approach is the use of organoids differentiated from adult stem cells (ASCs) to study COVID-19. Organoids are three-dimensional structures grown from ASCs, which recapitulate several features of the organ from which the ASCs that give rise to them derive. A recent study showed that enterocytes could be infected by SARS-CoV and SARS-CoV-2 in human small intestinal organoids (hSIOs), demonstrating the feasibility of this method to study the pathophysiological mechanisms related to COVID-19 (Lamers et al., 2020).

Regarding *in-vivo* human studies, diffusion tensor imaging (DTI or DTI-MRI) is a promising and extremely safe neuroimaging tool that could be used to study the pathophysiology of COVID-19. This technique can be easily used to examine the brains of patients with COVID-19, as well as the brains of experimental models infected with human SARS-CoV-2 that develop characteristic human-equivalent symptoms. DT-MRI is considered the only non-invasive method that permits a full analysis of the microstructural organization of CNS tissues *in vivo* (Jones and Leemans, 2011). Overall, with DT-MRI, it is possible to estimate the magnitude and direction of water molecules in the microstructure of the main brain tracts. This allows researchers to evaluate changes in these structures under different conditions. A detailed study of the modifications that occur in the brainstem tracts has been successfully achieved. Hence, DT-MRI would be a robust tool to use to study the changes that occur in the brainstem and cortical tracts due to COVID-19. DTI studies would allow researchers to study the specific tracts that are potentially damaged in patients with COVID-19. For instance, with this method, it is possible to study the majority of the olfactory pathway as well as the entire trigeminal pathway, including not only the trigeminal nerve and its peripheral branches (e.g., ophthalmic, maxillary, and mandibular branches) and the trigeminothalamic tract and its nuclei, including the nucleus caudalis, but also the main sensory nucleus and the mesencephalic nucleus. DTI will also allow researchers to study the NST and the NA, as well as their relationship to the medullary cardiorespiratory center. In addition, changes that may occur in different neural pathways related to COVID-19, especially when comparing the specific tracts of COVID-19 patients with the same tracts of healthy individuals, can be evaluated. All tracts associated with COVID-19 related neuroinvasion and discussed in this review can be evaluated with DTI (Wiegell et al., 2003; Granziera et al., 2006; Lutz et al., 2008; Wilcox et al., 2013), including the olfactory system (Milardi et al., 2017).

Neuroimaging techniques such as DT-MRI seem to be particularly compatible with artificial intelligence (AI) data mining, which could improve the diagnosis and prediction of the risk factors involved in the development of more severe forms of COVID-19. To accelerate research in this area, thus providing more robust scientific evidence to combat COVID-19, the White House, in collaboration with research institutes and technology companies, issued a global call for research on COVID-19 on March 16, 2020 (Alimadadi et al., 2020). AI might be used for research in different areas to develop more rapid diagnostic methods with reasonable accuracy and reduce health professionals' exposure to the virus, reducing contamination risks. This approach could be decisive in expediting and reducing the cost of screening for effective treatments to combat COVID-19, and to increase understanding of its pathogenesis. The

combination of classical experimentation with other technologies is crucial to determine the neuroinvasion potential and related implications of SARS-CoV-2.

CONCLUSIONS

The effects of COVID-19 on the human NS have been inadequately explored. It is essential and urgent to elucidate the degree of NS involvement in COVID-19, as well as determine the neural circuits, if any, that are potentially affected by SARS-CoV-2. The participation of the PNS, especially the cranial nerves and ENS, as well as the CNS and related neural networks impacted by COVID-19, should be confirmed. Moreover, the directionality and time course of the viral spread in the body should be established. The integration of different technologies and fields of research should be encouraged.

AUTHOR CONTRIBUTIONS

MD, DC, and VM-N conceptualized this manuscript. MD, SD, VA, DC, NR, JC-A, TS, JS, CP, ID'A, PN, and VM-N drafted the manuscript. All authors have reviewed and agree with the publication of this manuscript.

FUNDING

This contribution has been supported by the following research agencies of the Brazilian government: FAPERJ (Fundação Carlos Chagas Filho de Amparo à Pesquisa do Estado do Rio de Janeiro), CAPES (Coordenação de Aperfeiçoamento de Pessoal de Nível Superior) and CNPq (Conselho Nacional de Desenvolvimento Científico e Tecnológico). VM-N, TS, SD, VA, NR, ID'A, and PN have been supported by the Associação Mahatma Gandhi.

ACKNOWLEDGMENTS

We thank Rodrigo Tonan for the illustration of **Figure 1**, designed especially for use in this publication, and Janet Reid for the professional English grammar review. We also thank Natália Ferreira, D. D. S., M. S. for her contribution to this paper.

REFERENCES

(2003). WHO issues consensus document on the epidemiology of SARS. *Wkly. Epidemiol. Rec.* 78, 373–375.

Alimadadi, A., Aryal, S., Manandhar, I., Munroe, P. B., Joe, B., and Cheng, X. (2020). Artificial intelligence and machine learning to fight COVID-19. *Physiol. Genomics* 52, 200–202. doi: 10.1152/physiolgenomics.00029.2020

Amanat, F., and Krammer, F. (2020). SARS-CoV-2 vaccines: status report. *Immunity* 52, 583–589. doi: 10.1016/j.immuni.2020.03.007

Andries, K., and Pensaert, M. B. (1980). Immunofluorescence studies on the pathogenesis of hemagglutinating encephalomyelitis virus infection in pigs after oronasal inoculation. *Am. J. Vet. Res.* 41, 1372–1378.

Bao, L., Deng, W., Huang, B., Gao, H., Liu, J., Ren, L., et al. (2020). The pathogenicity of SARS-CoV-2 in hACE2 transgenic mice. *Nature*. doi: 10.1038/s41586-020-2312-y. [Epub ahead of print].

Bergström, U., Giovanetti, A., Piras, E., and Brittebo, E. B. (2003). Methimazole-induced damage in the olfactory mucosa: effects on ultrastructure and glutathione levels. *Toxicol. Pathol.* 31, 379–387. doi: 10.1080/01926230390201101

Bilinska, K., Jakubowska, P., Von Bartheld, C. S., and Butowt, R. (2020). Expression of the SARS-CoV-2 entry proteins, ACE2 and TMPRSS2, in cells of the olfactory epithelium: identification of cell types and trends with age. *ACS Chem. Neurosci.* 11, 1555–1562. doi: 10.1021/acschemneuro.0c00210

Brann, D. H., Tsukahara, T., Weinreb, C., Logan, D. W., and Datta, S. R. (2020). Non-neural expression of SARS-CoV-2 entry genes in the olfactory epithelium suggests mechanisms underlying anosmia in COVID-19 patients. *bioRxiv [Preprint]* doi: 10.1101/2020.03.25.009084

Brune, K., Frank, J., Schwingshackl, A., Finigan, J., and Sidhaye, V. K. (2015). Pulmonary epithelial barrier function: some new players and mechanisms. *Am. J. Physiol. Lung Cell. Mol. Physiol.* 308, L731–L745. doi: 10.1152/ajplung.00309.2014

Chan, K. H., Peiris, J. S., Lam, S. Y., Poon, L. L., Yuen, K. Y., and Seto, W. H. (2011). The effects of temperature and relative humidity on the viability of the SARS coronavirus. *Adv. Virol.* 2011:734690. doi: 10.1155/2011/734690

Chen, G., Wu, D., Guo, W., Cao, Y., Huang, D., Wang, H., et al. (2020). Clinical and immunologic features in severe and moderate Coronavirus Disease 2019. *J. Clin. Invest.* 130, 2620–2629. doi: 10.1101/2020.02.16.20023903

Chen, N., Zhou, M., Dong, X., Qu, J., Gong, F., Han, Y., et al. (2020). Epidemiological and clinical characteristics of 99 cases of 2019 novel coronavirus pneumonia in Wuhan, China: a descriptive study. *Lancet* 395, 507–513. doi: 10.1016/S0140-6736(20)30211-7

Chen, R., Wang, K., Yu, J., Chen, Z., Wen, C., and Xu, Z. (2020). The spatial and cell-type distribution of SARS-CoV-2 receptor ACE2 in human and mouse brain. *bioRxiv [Preprint]* doi: 10.1101/2020.04.07.030650

Chen, Y., Chen, L., Deng, Q., Zhang, G., Wu, K., Ni, L., et al. (2020). The presence of SARS-CoV-2 RNA in feces of COVID-19 patients. *J. Med. Virol.* 92, 833–840. doi: 10.1002/jmv.25825

Cockrell, A. S., Leist, S. R., Douglas, M. G., and Baric, R. S. (2018). Modeling pathogenesis of emergent and pre-emergent human coronaviruses in mice. *Mamm. Genome* 29, 367–383. doi: 10.1007/s00335-018-9760-9

Coelho-Aguiar, J. E. M., Bon-Frauches, A. C., Gomes, A. L., Veríssimo, C. P., Aguiar, D. P., Matias, D., et al. (2015). The enteric glia: identity and functions. *Glia* 63, 921–935. doi: 10.1002/glia.22795

Coelho-Aguiar, J. U. D. M., Veríssimo, C. P., Costa, D. V. D. S., Thomasi, B. B. D. M., Frauches, A. C. B., Ribeiro, F. P., et al. (2019). "The enteric glial network acts in the maintenance of intestinal homeostasis and in intestinal disorders", in *Glia in Health and Disease*, ed T. Spohr (London: IntechOpen), 1–29.

Costa, M., Brookes, S. J., and Hennig, G. W. (2000). Anatomy and physiology of the enteric nervous system. *Gut* 47(Suppl. 4), iv15–iv19; discussion iv26. doi: 10.1136/gut.47.suppl_4.iv15

Coutard, B., Valle, C., De Lamballerie, X., Canard, B., Seidah, N. G., and Decroly, E. (2020). The spike glycoprotein of the new coronavirus 2019-nCoV contains a furin-like cleavage site absent in CoV of the same clade. *Antiviral Res.* 176:104742. doi: 10.1016/j.antiviral.2020.104742

Crawford, S. E., Ramani, S., Tate, J. E., Parashar, U. D., Svensson, L., Hagbom, M., et al. (2017). Rotavirus infection. *Nat. Rev. Dis. Primers* 3:17083. doi: 10.1038/nrdp.2017.83

Dasilva, A. F., and Dossantos, M. F. (2012). The role of sensory fiber demography in trigeminal and postherpetic neuralgias. *J. Dent. Res.* 91, 17–24. doi: 10.1177/0022034511411300

Devere, R. (2017). Disorders of taste and smell. *Continuum* 23, 421–446. doi: 10.1212/CON.0000000000000463

Ding, Y., He, L., Zhang, Q., Huang, Z., Che, X., Hou, J., et al. (2004). Organ distribution of severe acute respiratory syndrome (SARS) associated

coronavirus (SARS-CoV) in SARS patients: implications for pathogenesis and virus transmission pathways. *J. Pathol.* 203, 622–630. doi: 10.1002/path.1560

Dong, E., Du, H., and Gardner, L. (2020). An interactive web-based dashboard to track COVID-19 in real time. *Lancet Infect. Dis.* 20, 533–534. doi: 10.1016/S1473-3099(20)30120-1

Durante, M. A., Kurtenbach, S., Sargi, Z. B., Harbour, J. W., Choi, R., Goss, G. M., et al. (2020). Single-cell analysis of olfactory neurogenesis and differentiation in adult humans. *Nat. Neurosci.* 23, 323–326. doi: 10.1038/s41593-020-0587-9

Dworkin, R. H., Gnann, J. W. Jr., Oaklander, A. L., Raja, S. N., Schmader, K. E., and Whitley, R. J. (2008). Diagnosis and assessment of pain associated with herpes zoster and postherpetic neuralgia. *J. Pain* 9, S37–S44. doi: 10.1016/j.jpain.2007.10.008

Fodoulian, L., Tuberosa, J., Rossier, D., Landis, B. N., Carleton, A., and Rodriguez, I. (2020). SARS-CoV-2 receptor and entry genes are expressed by sustentacular cells in the human olfactory neuroepithelium. *bioRxiv [Preprint]* doi: 10.1101/2020.03.31.013268

Fox, S. E., Akmatbekov, A., Harbert, J. L., Li, G., Quincy Brown, J., and Vander Heide, R. S. (2020). Pulmonary and cardiac pathology in African American patients with COVID-19: an autopsy series from New Orleans. *Lancet Respir. Med.* doi: 10.1016/S2213-2600(20)30243-5. [Epub ahead of print].

Fung, S. Y., Yuen, K. S., Ye, Z. W., Chan, C. P., and Jin, D. Y. (2020). A tug-of-war between severe acute respiratory syndrome coronavirus 2 and host antiviral defence: lessons from other pathogenic viruses. *Emerg. Microbes Infect.* 9, 558–570. doi: 10.1080/22221751.2020.1736644

Gautier, J. F., and Ravussin, Y. (2020). A new symptom of COVID-19: loss of taste and smell. *Obesity* 28:845. doi: 10.1002/oby.22809

Giacomelli, A., Pezzati, L., Conti, F., Bernacchia, D., Siano, M., Oreni, L., et al. (2020). Self-reported olfactory and taste disorders in SARS-CoV-2 patients: a cross-sectional study. *Clin. Infect. Dis.* ciaa330. doi: 10.1093/cid/ciaa330

Granziera, C., Dasilva, A., Snyder, J., Tuch, D., and Hadjikhani, N. (2006). Anatomical alterations of the visual motion processing network in migraine with and without aura. *PLoS Med.* 3:e402. doi: 10.1371/journal.pmed.0030402

Gu, J., Gong, E., Zhang, B., Zheng, J., Gao, Z., Zhong, Y., et al. (2005). Multiple organ infection and the pathogenesis of SARS. *J. Exp. Med.* 202, 415–424. doi: 10.1084/jem.20050828

Hoffmann, M., Kleine-Weber, H., Schroeder, S., Krüger, N., Herrler, T., Erichsen, S., et al. (2020). SARS-CoV-2 cell entry depends on ACE2 and TMPRSS2 and is blocked by a clinically proven protease inhibitor. *Cell* 181, 271–280.e278. doi: 10.1016/j.cell.2020.02.052

Huang, C., Wang, Y., Li, X., Ren, L., Zhao, J., Hu, Y., et al. (2020). Clinical features of patients infected with 2019 novel coronavirus in Wuhan, China. *Lancet* 395, 497–506. doi: 10.1016/S0140-6736(20)30183-5

Hwang, C. S. (2006). Olfactory neuropathy in severe acute respiratory syndrome: report of A case. *Acta Neurol. Taiwan* 15, 26–28.

Jia, C., Roman, C., and Hegg, C. C. (2010). Nickel sulfate induces location-dependent atrophy of mouse olfactory epithelium: protective and proliferative role of purinergic receptor activation. *Toxicol. Sci.* 115, 547–556. doi: 10.1093/toxsci/kfq071

Jones, D. K., and Leemans, A. (2011). Diffusion tensor imaging. *Methods Mol. Biol.* 711, 127–144. doi: 10.1007/978-1-61737-992-5_6

Lamers, M. M., Beumer, J., Van Der Vaart, J., Knoops, K., Puschhof, J., Breugem, T. I., et al. (2020). SARS-CoV-2 productively infects human gut enterocytes. *Science*. eabc1669. doi: 10.1126/science.abc1669

Leyva-Grado, V. H., Churchill, L., Harding, J., and Krueger, J. M. (2010). The olfactory nerve has a role in the body temperature and brain cytokine responses to influenza virus. *Brain Behav. Immun.* 24, 281–288. doi: 10.1016/j.bbi.2009.10.007

Li, K., Wohlford-Lenane, C., Perlman, S., Zhao, J., Jewell, A. K., Reznikov, L. R., et al. (2016). Middle east respiratory syndrome coronavirus causes multiple organ damage and lethal disease in mice transgenic for human dipeptidyl peptidase 4. *J. Infect. Dis.* 213, 712–722. doi: 10.1093/infdis/jiv499

Li, W., Moore, M. J., Vasilieva, N., Sui, J., Wong, S. K., Berne, M. A., et al. (2003). Angiotensin-converting enzyme 2 is a functional receptor for the SARS coronavirus. *Nature* 426, 450–454. doi: 10.1038/nature02145

Li, Y. C., Bai, W. Z., and Hashikawa, T. (2020). The neuroinvasive potential of SARS-CoV2 may play a role in the respiratory failure of COVID-19 patients. *J. Med. Virol*. doi: 10.1002/jmv.25728

Li, Y. C., Bai, W. Z., Hirano, N., Hayashida, T., and Hashikawa, T. (2012). Coronavirus infection of rat dorsal root ganglia: ultrastructural characterization of viral replication, transfer, and the early response of satellite cells. *Virus Res.* 163, 628–635. doi: 10.1016/j.virusres.2011.12.021

Li, Y. C., Bai, W. Z., Hirano, N., Hayashida, T., Taniguchi, T., Sugita, Y., et al. (2013). Neurotropic virus tracing suggests a membranous-coating-mediated mechanism for transsynaptic communication. *J. Comp. Neurol.* 521, 203–212. doi: 10.1002/cne.23171

Li, Z., Liu, T., Yang, N., Han, D., Mi, X., Li, Y., et al. (2020). Neurological manifestations of patients with COVID-19: potential routes of SARS-CoV-2 neuroinvasion from the periphery to the brain. *Front. Med.* 1–9. doi: 10.1007/s11684-020-0786-5

Liang, W., Feng, Z., Rao, S., Xiao, C., Xue, X., Lin, Z., et al. (2020). Diarrhoea may be underestimated: a missing link in 2019 novel coronavirus. *Gut*. 69, 1141–1143. doi: 10.1136/gutjnl-2020-320832

Liu, J., Li, S., Liu, J., Liang, B., Wang, X., Wang, H., et al. (2020). Longitudinal 1209 characteristics of lymphocyte responses and cytokine profiles in the peripheral blood of SARS-CoV-2 infected patients. *EBioMedicine*. 55:102763. doi: 10.1016/j.ebiom.2020.102763

Lu, R., Zhao, X., Li, J., Niu, P., Yang, B., Wu, H., et al. (2020). Genomic characterisation and epidemiology of 2019 novel coronavirus: implications for virus origins and receptor binding. *Lancet* 395, 565–574. doi: 10.1016/S0140-6736(20)30251-8

Lukassen, S., Chua, R. L., Trefzer, T., Kahn, N. C., Schneider, M. A., Muley, T., et al. (2020). SARS-CoV-2 receptor ACE2 and TMPRSS2 are primarily expressed in bronchial transient secretory cells. *EMBO J.* 39:e105114. doi: 10.15252/embj.20105114

Lutz, J., Jäger, L., De Quervain, D., Krauseneck, T., Padberg, F., Wichnalek, M., et al. (2008). White and gray matter abnormalities in the brain of patients with fibromyalgia: a diffusion-tensor and volumetric imaging study. *Arthritis Rheum.* 58, 3960–3969. doi: 10.1002/art.24070

Mallick, B., Ghosh, Z., and Chakrabarti, J. (2009). MicroRNome analysis unravels the molecular basis of SARS infection in bronchoalveolar stem cells. *PLoS ONE*4:e7837. doi: 10.1371/journal.pone.0007837

Mao, L., Jin, H., Wang, M., Hu, Y., Chen, S., He, Q., et al. (2020). Neurologic manifestations of hospitalized patients with coronavirus disease 2019 in Wuhan, China. *JAMA Neurol.* 77, 683–690. doi: 10.1001/jamaneurol.2020.1127

Matsuda, K., Park, C. H., Sunden, Y., Kimura, T., Ochiai, K., Kida, H., et al. (2004). The vagus nerve is one route of transneural invasion for intranasally inoculated influenza a virus in mice. *Vet. Pathol.* 41, 101–107. doi: 10.1354/vp.41-2-101

Matsuyama, S., Nao, N., Shirato, K., Kawase, M., Saito, S., Takayama, I., et al. (2020). Enhanced isolation of SARS-CoV-2 by TMPRSS2-expressing cells. *Proc. Natl. Acad. Sci. U.S.A.* 117, 7001–7003. doi: 10.1073/pnas.2002589117

McCray, P. B., Pewe, L., Wohlford-Lenane, C., Hickey, M., Manzel, L., Shi, L., et al. (2007). Lethal infection of K18-hACE2 mice infected with severe acute respiratory syndrome coronavirus. *J. Virol.* 81, 813–821. doi: 10.1128/JVI.02012-06

Milardi, D., Cacciola, A., Calamuneri, A., Ghilardi, M. F., Caminiti, F., Cascio, F., et al. (2017). The olfactory system revealed: non-invasive mapping by using constrained spherical deconvolution tractography in healthy humans. *Front. Neuroanat.* 11:32. doi: 10.3389/fnana.2017.00032

Miller, M. A., and O'bryan, M. A. (2003). Ultrastructural changes and olfactory deficits during 3-methylindole-induced olfactory mucosal necrosis and repair in mice. *Ultrastruct. Pathol.* 27, 13–21. doi: 10.1080/01913120309944

Moriguchi, T., Harii, N., Goto, J., Harada, D., Sugawara, H., Takamino, J., et al. (2020). A first Case of Meningitis/Encephalitis associated with SARS-Coronavirus-2. *Int. J. Infect. Dis.* 94, 55–58. doi: 10.1016/j.ijid.2020.03.062

Natoli, S., Oliveira, V., Calabresi, P., Maia, L. F., and Pisani, A. (2020). Does SARS-Cov-2 invade the brain? Translational lessons from animal models. *Eur. J. Neurol*. doi: 10.1111/ene.14277. [Epub ahead of print].

Netland, J., Meyerholz, D. K., Moore, S., Cassell, M., and Perlman, S. (2008). Severe acute respiratory syndrome coronavirus infection causes neuronal death in the absence of encephalitis in mice transgenic for human ACE2. *J. Virol.* 82, 7264–7275. doi: 10.1128/JVI.00737-08

Nolte, J. (2009). *The Human Brain: An Introduction to Its Functional Anatomy*. Philadelphia, PA: Mosby/Elsevier.

Oaklander, A. (2001). The density of remaining nerve endings in human skin with and without postherpetic neuralgia after shingles. *Pain* 92, 139–145. doi: 10.1016/S0304-3959(00)00481-4

Park, M., Cook, A. R., Lim, J. T., Sun, Y., and Dickens, B. L. (2020). A systematic review of COVID-19 epidemiology based on current evidence. *J. Clin. Med.* 9, 967. doi: 10.3390/jcm9040967

Parker, C. G., Dailey, M. J., Phillips, H., and Davis, E. A. (2020). Central sensory-motor crosstalk in the neural gut-brain axis. *Auton. Neurosci.* 225:102656. doi: 10.1016/j.autneu.2020.102656

Paxinos, G., and Mai, J. R. K. (2004). *The Human Nervous System*. San Diego, CA: Elsevier Academic Press.

Poyiadji, N., Shahin, G., Noujaim, D., Stone, M., Patel, S., and Griffith, B. (2020). COVID-19-associated acute hemorrhagic necrotizing encephalopathy: CT and MRI features. *Radiology* 201187. doi: 10.1148/radiol.2020201187

Ruan, Q., Yang, K., Wang, W., Jiang, L., and Song, J. (2020). Correction to: Clinical predictors of mortality due to COVID-19 based on an analysis of data of 150 patients from Wuhan, China. *Intensive Care Med.* 46, 1294–1297. doi: 10.1007/s00134-020-06028-z

Saçar Demirci, M. D., and Adan, A. (2020). Computational analysis of microRNA-mediated interactions in SARS-CoV-2 infection. *bioRxiv [Preprint]* doi: 10.1101/2020.03.15.992438

Standring, S. (2008). *Gray's Anatomy: the Anatomical Basis of Clinical Practice, 40th Edn*. Edinburgh: Churchill Livingstone.

Tsai, L. K., Hsieh, S. T., Chao, C. C., Chen, Y. C., Lin, Y. H., Chang, S. C., et al. (2004). Neuromuscular disorders in severe acute respiratory syndrome. *Arch. Neurol.* 61, 1669–1673. doi: 10.1001/archneur.61.11.1669

Ueha, R., Kondo, K., Kagoya, R., Shichino, S., Ueha, S., and Yamasoba, T. (2020). Background mechanisms of olfactory dysfunction in COVID-19: expression of ACE2, TMPRSS2, and Furin in the nose and olfactory bulb in human and mice. *bioRxiv [Preprint]* doi: 10.1101/2020.05.15.097352

Vaira, L. A., Salzano, G., Deiana, G., and De Riu, G. (2020). Anosmia and ageusia: common findings in COVID-19 patients. *Laryngoscope*. 130:1787. doi: 10.1002/lary.28692

Van Doremalen, N., Bushmaker, T., and Munster, V. J. (2013). Stability of Middle East respiratory syndrome coronavirus (MERS-CoV) under different environmental conditions. *Euro Surveill.* 18:20590. doi: 10.2807/1560-7917.ES2013.18.38.20590

Virani, A., Rabold, E., Hanson, T., Haag, A., Elrufay, R., Cheema, T., et al. (2020). Guillain-Barré Syndrome associated with SARS-CoV-2 infection. *IDCases* 20:e00771. doi: 10.1016/j.idcr.2020.e00771

Walls, A. C., Park, Y. J., Tortorici, M. A., Wall, A., Mcguire, A. T., and Veesler, D. (2020). Structure, function, and antigenicity of the SARS-CoV-2 spike glycoprotein. *Cell* 181, 281–292.e286. doi: 10.1016/j.cell.2020.02.058

Wan, Y., Shang, J., Graham, R., Baric, R. S., and Li, F. (2020). Receptor recognition by the novel coronavirus from Wuhan: an analysis based on decade-long structural studies of SARS coronavirus. *J. Virol.* 94:e00127-20. doi: 10.1128/JVI.00127-20

Wang, D., Hu, B., Hu, C., Zhu, F., Liu, X., Zhang, J., et al. (2020). Clinical characteristics of 138 hospitalized patients with 2019 novel coronavirus-infected pneumonia in Wuhan, China. *JAMA*. 323, 1061–1069. doi: 10.1001/jama.2020.1585

Wang, X., Xu, W., Hu, G., Xia, S., Sun, Z., Liu, Z., et al. (2020). SARS-CoV-2 infects T lymphocytes through its spike protein-mediated membrane fusion. *Cell. Mol. Immunol.* 323, 1061–1069. doi: 10.1038/s41423-020-0424-9

Wang, X. W., Li, J., Guo, T., Zhen, B., Kong, Q., Yi, B., et al. (2005). Concentration and detection of SARS coronavirus in sewage from Xiao Tang Shan Hospital and the 309th Hospital of the Chinese People's Liberation Army. *Water Sci. Technol.* 52, 213–221. doi: 10.2166/wst.2005.0266

Watson, C., and Oaklander, A. (2002). Postherpetic neuralgia. *Pain Pract.* 2, 295–307. doi: 10.1046/j.1533-2500.2002.02039.x

Wiegell, M. R., Tuch, D. S., Larsson, H. B., and Wedeen, V. J. (2003). Automatic segmentation of thalamic nuclei from diffusion tensor magnetic resonance imaging. *Neuroimage* 19, 391–401. doi: 10.1016/S1053-8119(03)00044-2

Wilcox, S. L., Gustin, S. M., Eykman, E. N., Fowler, G., Peck, C. C., Murray, G. M., et al. (2013). Trigeminal nerve anatomy in neuropathic and non-neuropathic orofacial pain patients. *J. Pain* 14, 865–872. doi: 10.1016/j.jpain.2013.02.014

Wölfel, R., Corman, V. M., Guggemos, W., Seilmaier, M., Zange, S., Müller, M. A., et al. (2020). Virological assessment of hospitalized patients with COVID-2019. *Nature*. 581, 465–469. doi: 10.1038/s41586-020-2196-x

Wrapp, D., Wang, N., Corbett, K. S., Goldsmith, J. A., Hsieh, C. L., Abiona, O., et al. (2020). Cryo-EM structure of the 2019-nCoV spike in the prefusion conformation. *Science* 367, 1260–1263. doi: 10.1126/science.abb2507

Wu, C., Chen, X., Cai, Y., Xia, J., Zhou, X., Xu, S., et al. (2020). Risk factors associated with acute respiratory distress syndrome and death in patients with coronavirus disease 2019 pneumonia in Wuhan, China. *JAMA Intern Med.* doi: 10.1001/jamainternmed.2020.0994. [Epub ahead of print].

Wu, F., Zhao, S., Yu, B., Chen, Y. M., Wang, W., Song, Z. G., et al. (2020). A new coronavirus associated with human respiratory disease in China. *Nature* 579, 265–269. doi: 10.1038/s41586-020-2008-3

Wu, Y., Xu, X., Chen, Z., Duan, J., Hashimoto, K., Yang, L., et al. (2020). Nervous system involvement after infection with COVID-19 and other coronaviruses. *Brain Behav. Immun.* doi: 10.1016/j.bbi.2020.03.031. [Epub ahead of print].

Xiao, F., Tang, M., Zheng, X., Liu, Y., Li, X., and Shan, H. (2020). Evidence for gastrointestinal infection of SARS-CoV-2. *Gastroenterology*. 158, 1831–1833. doi: 10.1053/j.gastro.2020.02.055

Xu, H., Zhong, L., Deng, J., Peng, J., Dan, H., Zeng, X., et al. (2020). High expression of ACE2 receptor of 2019-nCoV on the epithelial cells of oral mucosa. *Int. J. Oral Sci.* 12:8. doi: 10.1038/s41368-020-0074-x

Yang, G., Hamacher, J., Gorshkov, B., White, R., Sridhar, S., Verin, A., et al. (2010). The dual role of TNF in pulmonary edema. *J. Cardiovasc. Dis. Res.* 1, 29–36. doi: 10.4103/0975-3583.59983

Yeo, C., Kaushal, S., and Yeo, D. (2020). Enteric involvement of coronaviruses: is faecal–oral transmission of SARS-CoV-2 possible? *Lancet Gastroenterol. Hepatol.* 5, 335–337. doi: 10.1016/S2468-1253(20)30048-0

Yin, S., Huang, M., Li, D., and Tang, N. (2020). Difference of coagulation features between severe pneumonia induced by SARS-CoV2 and non-SARS-CoV2. *J. Thromb. Thrombolysis*. doi: 10.1007/s11239-020-02105-8. [Epub ahead of print].

Yu, F., Du, L., Ojcius, D. M., Pan, C., and Jiang, S. (2020). Measures for diagnosing and treating infections by a novel coronavirus responsible for a pneumonia outbreak originating in Wuhan, China. *Microbes Infect.* 22, 74–79. doi: 10.1016/j.micinf.2020.01.003

Zhang, C., Wu, Z., Li, J. W., Zhao, H., and Wang, G. Q. (2020). Cytokine release syndrome in severe COVID-19: interleukin-6 receptor antagonist tocilizumab may be the key to reduce mortality. *Int. J. Antimicrob. Agents* 55:105954. doi: 10.1016/j.ijantimicag.2020.105954

Zhou, F., Yu, T., Du, R., Fan, G., Liu, Y., Liu, Z., et al. (2020). Clinical course and risk factors for mortality of adult inpatients with COVID-19 in Wuhan, China: a retrospective cohort study. *Lancet* 395, 1054–1062. doi: 10.1016/S0140-6736(20)30566-3

Zhou, J., Li, C., Liu, X., Chiu, M. C., Zhao, X., Wang, D., et al. (2020). Infection of bat and human intestinal organoids by SARS-CoV-2. *Nat. Med.* doi: 10.1038/s41591-020-0912-6. [Epub ahead of print].

Zhou, J., Li, C., Zhao, G., Chu, H., Wang, D., Yan, H. H., et al. (2017). Human intestinal tract serves as an alternative infection route for Middle East respiratory syndrome coronavirus. *Sci Adv* 3:eaao4966. doi: 10.1126/sciadv.aao4966

Zhou, P., Yang, X. L., Wang, X. G., Hu, B., Zhang, L., Zhang, W., et al. (2020). A pneumonia outbreak associated with a new coronavirus of probable bat origin. *Nature* 579, 270–273. doi: 10.1038/s41586-020-2012-7

Conflict of Interest: The authors declare that the research was conducted in the absence of any commercial or financial relationships that could be construed as a potential conflict of interest.

frontiers in Neuroanatomy

ORIGINAL RESEARCH
published: 06 October 2020
doi: 10.3389/fnana.2020.596439

Histological Evidence for the Enteric Nervous System and the Choroid Plexus as Alternative Routes of Neuroinvasion by SARS-CoV2

Felix Deffner[1†], Melanie Scharr[1†], Stefanie Klingenstein[2], Moritz Klingenstein[2], Alfio Milazzo[2], Simon Scherer[3], Andreas Wagner[1], Bernhard Hirt[1], Andreas F. Mack[1] and Peter H. Neckel[1*]*

[1] Institute of Clinical Anatomy and Cell Analysis, University of Tübingen, Tübingen, Germany, [2] Institute of Neuroanatomy and Developmental Biology, University of Tübingen, Tübingen, Germany, [3] Department of Pediatric Surgery, University Children's Hospital, Tübingen, Germany

Evidence is mounting that the novel corona virus SARS-CoV2 inflicts neurological symptoms in a subgroup of COVID-19 patients. While plenty of theories on the route of neuroinvasion have been proposed, little histological evidence has been presented supporting any of these hypotheses. Therefore, we carried out immunostainings for ACE2 and TMPRSS2, two proteinases crucial for the entry of SARS-CoV2 into host cells, in the human enteric nervous system (ENS), as well as in the choroid plexus of the lateral ventricles. Both of these sites are important, yet often neglected entry gates to the nervous system. We found that ACE2 and TMPRSS2 are expressed by enteric neurons and glial cells of the small and large intestine, as well as choroid plexus epithelial cells, indicating that these cells meet the molecular requirements for viral entry. Together, our results are fundamental histological evidence substantiating current theories of neuroinvasion by SARS-CoV2.

Keywords: SARS-CoV2, neuro-COVID, neuroinvasion, enteric nervous system, choroid plexus

OPEN ACCESS

Edited by:
Francesco Fornai, University of Pisa, Italy

Reviewed by:
Werend Boesmans, University of Hasselt, Belgium
Tobias Tenenbaum, University of Heidelberg, Germany

***Correspondence:**
Andreas F. Mack
an.mack@uni-tuebingen.de
Peter H. Neckel
peter.neckel@uni-tuebingen.de

† These authors have contributed equally to this work

Received: *19 August 2020*
Accepted: *16 September 2020*
Published: *06 October 2020*

Citation:
Deffner F, Scharr M, Klingenstein S, Klingenstein M, Milazzo A, Scherer S, Wagner A, Hirt B, Mack AF and Neckel PH (2020) Histological Evidence for the Enteric Nervous System and the Choroid Plexus as Alternative Routes of Neuroinvasion by SARS-CoV2. Front. Neuroanat. 14:596439. doi: 10.3389/fnana.2020.596439

INTRODUCTION

Since December 2019, the current COVID-19 pandemic, caused by the severe acute respiratory syndrome coronavirus 2 (SARS-CoV2), led to over 21.2 million reported cases and more than 761,700 deaths around the globe (WHO, 2020). Symptoms primarily involve coughing and dyspnea, but also fever, muscle soreness, acute respiratory distress syndrome, or diarrhea (Sun et al., 2020). While the respiratory symptoms most often are decisive for intensive care measures (Wang et al., 2020), approximately 30% of COVID-19 patients suffer from additional neurological symptoms including anosmia, dysgeusia, headache, fatigue, neuralgia, disorientation, epileptic seizures, pyramidal signs, nausea, or vomiting (Bösel and Berlit, 2020; Leonardi et al., 2020). Therefore, interest sparked in the pathogenesis of these neurological manifestations and more urgently in the routes of neuroinvasion by SARS-CoV2. While the neuroinvasive routes via the olfactory epithelium/olfactory nerve or via the blood-brain barrier have gained much attention, viral transmission via the enteric nervous system (ENS) or the cerebrospinal fluid (CSF), remains poorly investigated.

Recently, the angiotensin I converting enzyme 2 (ACE2) was shown to serve as a cellular receptor on the host cell membrane essential for transmission by SARS-CoV2 (Qiu et al., 2020; Yan et al., 2020; Zhou et al., 2020). The exact mechanisms of virus entry remain fragmentary, but binding of the viral spike protein (S protein) to ACE2 as well as priming of S proteins by the serine protease TMPRSS2 are substantial elements of the process (Hoffmann et al., 2020). Surprisingly, the expression patterns of ACE2 and TMPRSS2, which determine cellular entry routes, have been investigated scarcely in human organs other than the respiratory system (Ziegler et al., 2020). While previous studies found ACE2-mRNA expression in virtually all human organs (Devaux et al., 2020), the corresponding protein expression was much more restricted to epithelia, especially in enterocytes of the small intestine, alveolar epithelial cells of the lungs, vascular endothelial cells, proximal tubular cells, and glomerular epithelium in the kidney, but also, less intense, in smooth muscle cells (Hamming et al., 2004).

Since gastrointestinal symptoms and the presence of virus nucleic acids in the stool of COVID-19 patients have been reported repeatedly (Li Z. et al., 2020; Zhang et al., 2020), Esposito et al. (2020) recently suggested that the ENS could serve as an entry route to the brain. One of the proposed pathways implicate that infected enteric neurons could serve as direct entry to the CNS by passing on the virus via the gut brain axis (e.g., via the vagus nerve or splanchnic nerves). In fact, a comparable mechanism with infection of enteric neurons with successive virus persistence (Brun et al., 2010) as well as neurogenic transmission was previously shown for herpes (Khoury-Hanold et al., 2016) and influenza (Park et al., 2002) viruses. Additionally, Esposito et al. (2020) propose a secondary effect, by which an infected ENS could contribute to and aggravate the cytokine storm elicited by COVID-19. This theory is substantiated by extensive work showing the immunological properties of enteric glial cells (reviewed in detail by Yoo and Mazmanian, 2017). Yet, although other coronaviruses, such as SARS-CoV and MERS-CoV, cause gastrointestinal symptoms as well (Petrosillo et al., 2020), a detailed investigation of the protein expression of ACE2 or TMPRSS2 has not been carried out in the ENS so far.

Various coronaviruses were shown to enter the cerebrospinal fluid (CSF) both in animal experiments and in patients with neurological symptoms (De Felice et al., 2020). In addition, RNA of the SARS-CoV and of the current SARS-CoV2 were detected in the CSF of patients with neurological symptoms (Hung et al., 2003; Moriguchi et al., 2020). Yet, little is known about how these viruses enter the CSF (Cataldi et al., 2020). While most authors proposed a dysfunctional blood–brain barrier (De Felice et al., 2020), the anatomical route via fenestrated capillaries in the circumventricular organs and the choroid plexus, and successively the potential infection of ependymal and plexus epithelium cells has been largely neglected. Moreover, contrary to the exclusively neuronal transmission through the *lamina cribrosa* mentioned above, coronaviruses were also proposed to enter the CSF via the nasal mucosa and subsequently the perineural spaces of the olfactory nerve (Li Z. et al., 2020), thereby allowing for a secondary infection of circumventricular areas. Therefore, it is conceivable that virus particles enter the brain parenchyma at these locations, potentially leading to dysregulation of the water-electrolyte homeostasis in the CSF and brain or even act directly on neuronal functions of circumventricular circuits, such as in the *area postrema*. Both of these mechanisms could explain reported symptoms of dizziness or vomiting in COVID-19 patients. Although similar infection routes are known from other pathogens, no data on the protein expression and localization of ACE2 and TMPRSS2 is available in these areas of the human brain.

In this work, we focused on the protein expression and localization of ACE2 and TMPRSS2 in tissues at the interface between the nervous system and non-neuronal organs and systems. To do so, we carried out immunostainings on paraffin and cryosections of the small and large intestine, choroid plexus, and adjacent brain parenchyma in patient-derived and *post-mortem* material. We report evidence for the expression of ACE2 and TMPRSS2 on protein level in the ENS, choroid plexus epithelium, and the blood brain barrier, which previously only has been presumed based on mRNA data. Thus, our data are constitutive histological evidence for hypothesized alternative routes for neuroinvasion by SARS-CoV-2.

MATERIALS AND METHODS

Patient Specimens

Human gut samples were obtained from nine males and female patients aged 3 months and 8 years who were operated due to imperforate anus, intestinal obstruction syndrome, or rhabdomyosarcoma (**Supplementary Table S1**). All samples were collected after approval of the local ethical committee (Project Nr. 652/2019BO2) and with the consent of the patients' parents.

Post-mortem Specimens

Human choroid plexus was collected from eight cadavers donated to the Institute of Clinical Anatomy and Cell Analysis in Tübingen by female and male volunteers aged between 74 and 94. The body donors gave their informed consent in concert with the declaration of Helsinki to use the cadaver for research purposes. The procedure was approved by the ethics commission at the Medical Department of the University of Tübingen (Project Nr. 237/2007 BO1). Samples were taken within 8 to 19 h *post-mortem* (**Supplementary Table S2**).

Histological Workup

Before embedding, tissue samples were fixated with 4% (w/v) phosphate buffered p-formaldehyde (Applichem, Darmstadt, Germany) overnight and rinsed three times with phosphate-buffered saline (PBS).

For cryoconservation, fixed samples were frozen in isopentane-nitrogen cooled TissueTek® (Sakura, Staufen, Germany) and stored at −80°C until further processing. Before staining, cryosections (15 µm) were dried for 1 h at room temperature, following rehydration with distilled water for 30 min.

For paraffin embedding, fixed tissue samples were dehydrated in an ascending alcohol series, followed by xylene and overnight

infiltration of Paraffin at 60°C. Before staining, paraffin sections (5–10 μm) were dewaxed by xylene and a descending alcohol series and were rinsed once with distilled water. Next, sections were pre-treated with boiled citric acid monohydrate buffer (10 mM, pH 6.0, Merck, Darmstadt, Germany) for 3 min and cooled down at room temperature.

Immunohistochemistry

To prevent unspecific binding of antibodies, samples were blocked for 30 min with PBS containing 4% (v/v) goat serum (Biochrom, Berlin, Germany), 0.1% (v/v) bovine serum albumin (Roth, Karlsruhe, Germany), and 0.1% (v/v) Triton® X-100 (Roth, Karlsruhe, Germany), followed by incubation of primary antibodies (**Supplementary Table S3**) diluted in PBS with 0.1% (v/v) bovine serum albumin and 0.1% (v/v) Triton® X-100 overnight at 4 °C in a humidity chamber. Afterward, samples were washed with PBS three times for 5 to 10 min. The secondary antibody (**Supplementary Table S4**) was diluted in PBS, 0.1% (v/v) Triton X-100, and 0.1% (w/v) BSA and incubated for 60 to 90 min at room temperature. Nuclear staining was carried out with 4′,6-diamidino-2-phenylindole (DAPI) or DRAQ5 solution (200 ng/ml; Roth). After two washing steps with PBS for 5 to 10 min, the samples were washed in distilled water for 5 min, followed by mounting with Kaiser's glycerol gelatine (Merck, Darmstadt, Germany) or Mowiol 4-88 (Roth).

Microscopy

Images were acquired using a Zeiss Axio Imager.Z1 fluorescence microscope (Zeiss, Jena, Germany) with Apotome module, as well as a confocal LSM510 Meta with laser lines at 488, 543, 633 nm for excitation and appropriate filter sets. Images were acquired using ZEN software (Zeiss).

RESULTS

ACE2 and TMPRSS2 in the Human Intestine

Immunoreactivity for ACE2 and TMPRSS2 was detected in various layers and tissues of the intestinal wall (**Figures 1–3**), including the ENS (detailed in the next section). Our stainings confirmed previously reported expression of ACE2 in the epithelial lining of the small and large intestine (**Supplementary Figure S2**). While the expression was especially strong in the brush border of the small intestine, there was also a cytoplasmic staining clearly distinguishable. In addition to previous findings, we found TMPRSS2 expression in the cytoplasm of enteric epithelial cells, both in the small and large intestine. Although we occasionally found a strong fluorescence at the apical cell boundary, we did not detect a clear localization of TMPRSS2 in the microvilli as we did for ACE2 (data not shown).

Furthermore, we found ACE2 expression in smooth muscle cells in the *Tunica muscularis* as well as in the muscular *Tunica media* of arterioles within the intestinal wall. These smooth muscle cells also exhibited a uniform cytoplasmic localization of ACE2 without visible concentration of ACE2 at the plasma membrane. Moreover, we detected TMPRSS2 in the *Tunica muscularis* as well, yet considerably weaker than in the epithelium. Occasionally, endothelial cells of small capillaries especially in the *Tela submucosa* exhibited a uniform, cytoplasmic staining for ACE2. Although the endothelium of larger blood vessels was negative, we found ACE2 staining of the smooth musculature in the *Tunica media* of these vessels. TMPRSS2, however, was not expressed by endothelial cells of the small and large intestine.

ACE2 and TMPRSS2 in the Enteric Nervous System

In addition to the expression pattern in the intestinal epithelium in previous reports, we payed special attention to the localization of ACE2 and TMPRSS2 in the ENS. Interestingly, we found a cytoplasmic expression of ACE2 in the perikarya of enteric neurons as well as glial cells, both in the myenteric and submucous plexus (**Figures 1**, **2**). The fluorescent intensity of neuronal ACE2 was weaker in myenteric neurons than in submucosal nerve cells. Intriguingly, however, the staining of glial cells tended to be stronger in the myenteric ganglia compared to submucosal ganglia. Moreover, the myenteric plexus of the small intestine was stained less intense for ACE2 than the myenteric ganglia of the large intestine. Although the staining of the myenteric ganglia was clearly distinguishable from the surrounding ACE2-positive smooth musculature in all investigated cases, the fluorescent intensity of most neural cells was lower when compared to the intensely stained brush border of the small intestinal enterocytes. Interestingly, we found that enteric neurons exhibited different levels of ACE2 staining intensity (**Supplementary Figure S3**), suggesting that the expression level of ACE2 may vary between neuronal subtypes. It is also noteworthy that we did not detect any staining for ACE2 in the large neuronal fiber bundles outside the ganglia or in the fine neurite network surrounding the mucosal crypts, strongly indicating that ACE2 is not expressed in the dendrites or axons of enteric neurons or extrinsic nerve fibers. Moreover, we did not find any ACE2 expression in glial cells residing in the *Lamina propria mucosae* (type-III enteric glial cells) in the small and large intestine (**Supplementary Figures S4A,B**). In contrast, most extraganglionic enteric glia in the submucosa stained for ACE2 (**Supplementary Figure S4C**), although considerably weaker than type-I and type-II glial cells within the ganglia and the connectives. Interestingly, we also found enteric glial cells making contact to smaller blood vessels with varying ACE2 staining intensities (**Supplementary Figure S4D**). Within the *Tunica muscularis*, type-IV enteric glial cells also expressed ACE2, however, this staining was equally intense as the surrounding tissue (**Supplementary Figures S4E,F**).

We also found TMPRSS2 expression in the ganglia of the myenteric and submucous plexus (**Figure 3**). Both, enteric neurons and glial cells exhibited cytoplasmic staining, partly with marbled patterns or with fluorescent punctae. Intriguingly, the overall fluorescent intensity of enteric ganglia was noticeably

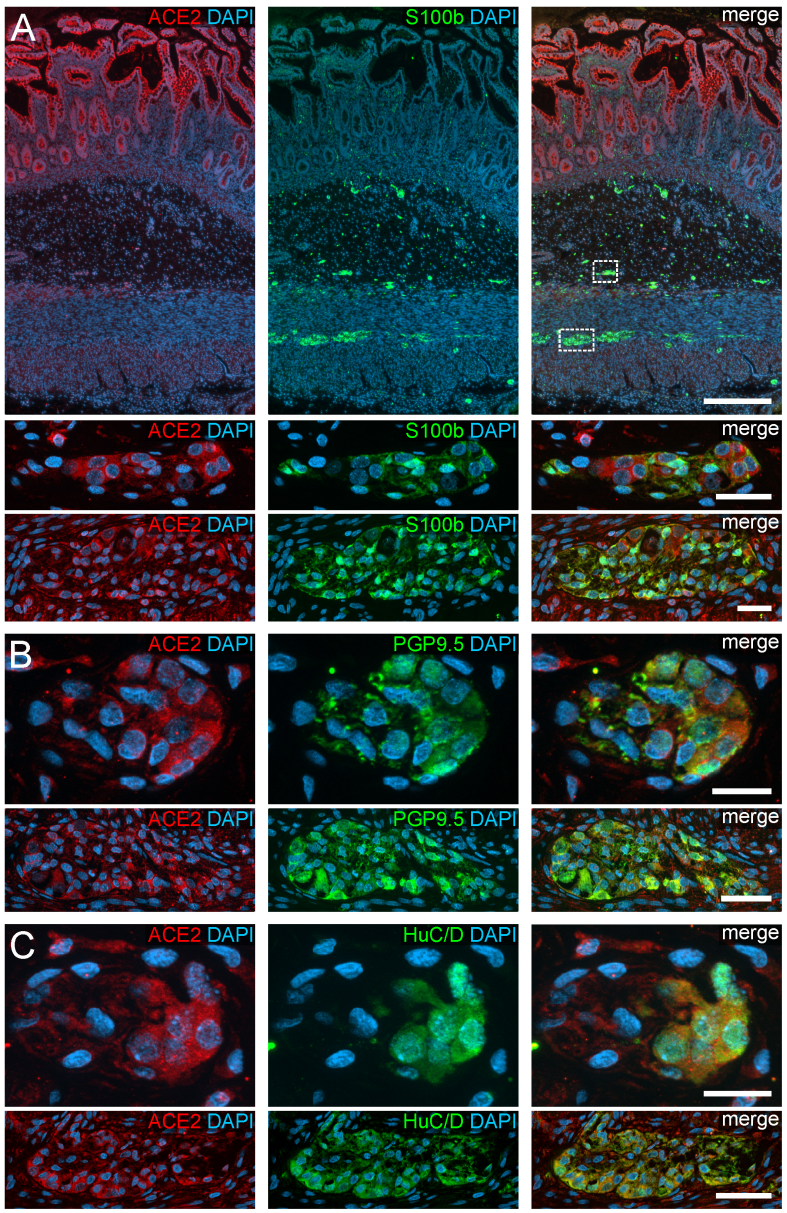

FIGURE 1 | ACE2 expression in the human ENS of the small intestine. **(A)** Overview of the entire gut wall of a small intestinal segment with immunofluorescence stainings for ACE2 (red), the glial marker S100b (green), and with the nuclear marker DAPI (blue). The white rectangles indicate the location of the high power magnification micrographs below showing a representative submucous and myenteric ganglion. **(B,C)** show representative submucous and myenteric ganglia stained for ACE2 (red), DAPI (blue), and the neuronal markers PGP9.5 (**B**, red) or HuC/D (**C**, red). Clearly, a positive staining can be found in enteric neurons and, less intense, in glial cells. The overview is a standard epifluorescence image; details are maximum intensity projections of optical sections by structured illumination. Scale bars: overview 250 μm; details 50 μm.

stronger in the colon compared to the small intestine. Thus, small intestinal myenteric ganglia often stained equally intense as the surrounding smooth muscle tissue (**Figure 3D** and see **Supplementary Figure S1** for negative controls), whereas ganglia in the large intestine exhibited a highly fluorescent TMPRSS2 staining. It is therefore conceivable, that the expression of both proteases differs between the ganglia of different intestinal segments. Moreover, we did not detect a TMPRSS2 signal in the exreganglionic (type-III) glial cells in the Tela submucosa and Lamina propria mucosae (data not shown).

ACE2 and TMPRSS2 in the Human Choroid Plexus

Our staining on post-mortem human choroid plexus revealed an intense protein expression of ACE2 and TMPRSS2 in the vast majority of plexus epithelial cells (**Figure 4**). Both

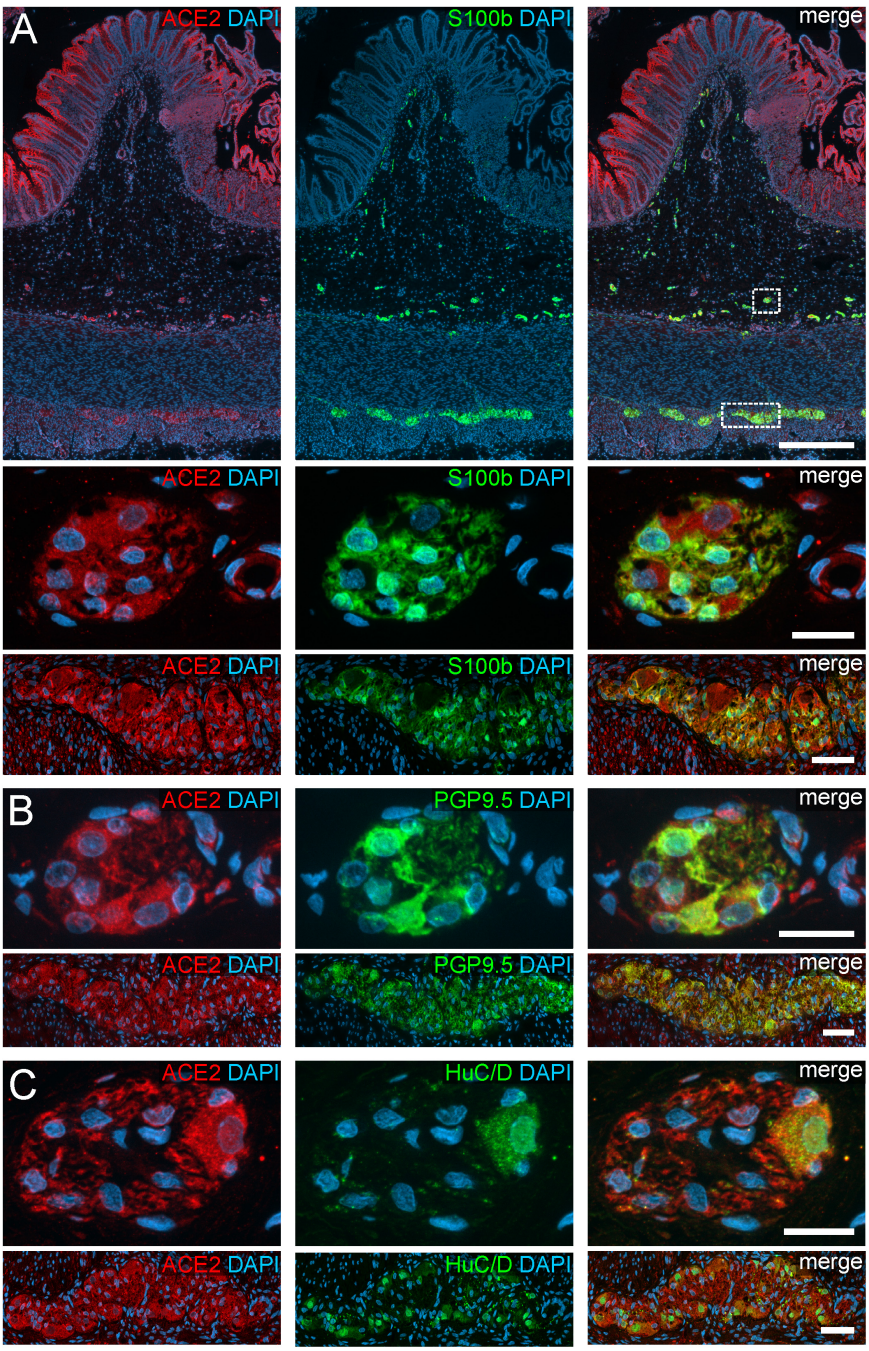

FIGURE 2 | ACE2 expression in the human ENS of the large intestine. **(A)** Overview of the entire gut wall of a colon segment with immunofluorescence stainings for ACE2 (red), the glial marker S100b (green), and with the nuclear marker DAPI (blue). The white rectangles indicate the location of the high power magnification micrographs below showing a representative submucous and myenteric ganglion. **(B,C)** show representative submucous and myenteric ganglia stained for ACE2 (red), DAPI (blue), and the neuronal markers PGP9.5 (**B**, red) or HuC/D (**C**, red). The ACE2 staining can be found in neurons and glial cells and is considerably stronger in the colon compared to the small intestine. The overview is a standard epifluorescence image; details are maximum intensity projections of optical sections by structured illumination. Scale bars: overview 250 μm; details 50 μm.

proteases were localized predominantly in intracellular granules, arguably representing lysosomes or large vesicles. Occasionally, we detected ACE2 immunoreactivity at the apical and/or basolateral cell surface of epithelial cells (**Supplementary Figure S5**). Generally, the staining intensity was heterogeneous, especially in sections stained for TMPRSS2 we found few cells scattered throughout the epithelium with a considerably higher expression throughout the

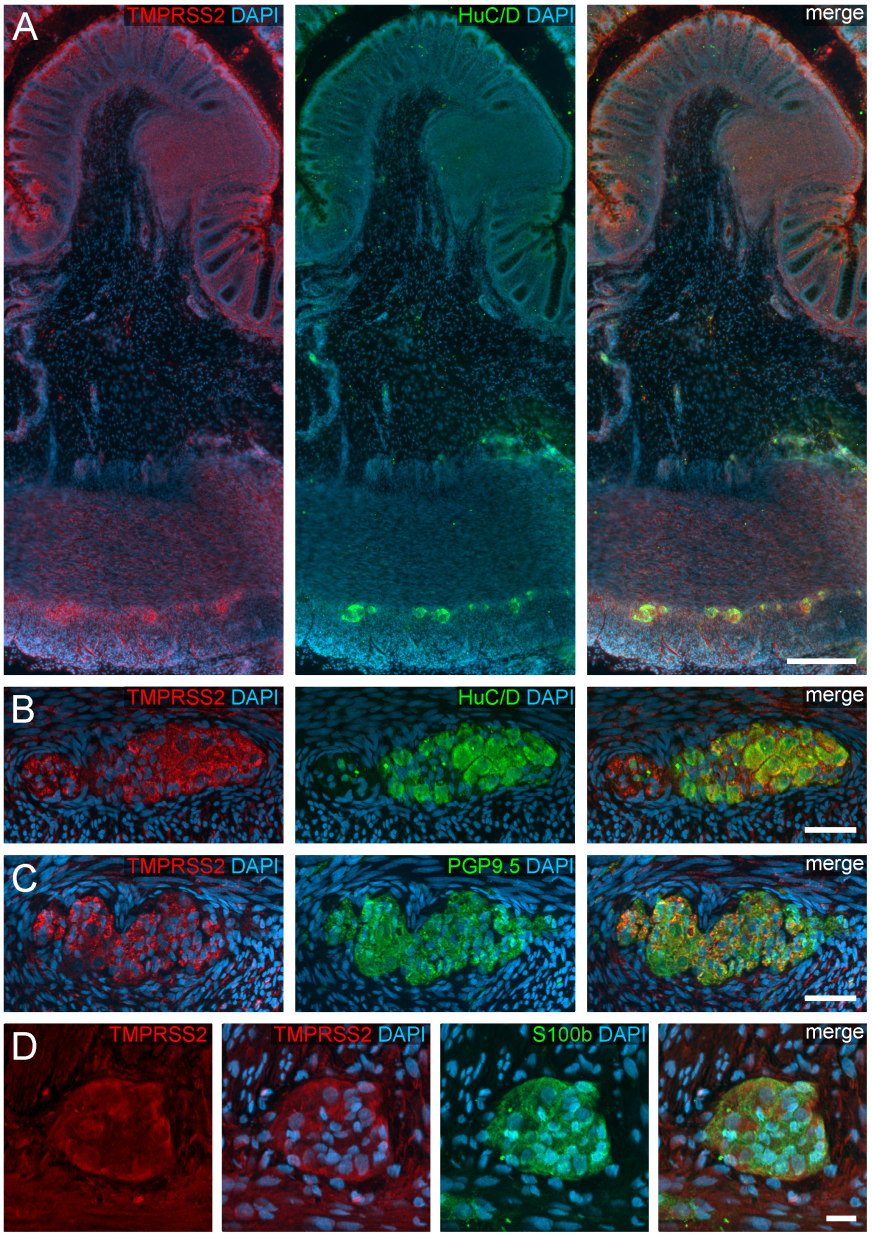

FIGURE 3 | TMPRSS2 expression in the human ENS. **(A)** Overview of the entire gut wall of a colon segment with immunofluorescence stainings for TMPRSS2 (red), the neuronal marker HuC/D (green), and the nuclear marker DAPI (blue). **(B,C)** show representative large intestinal myenteric ganglia stained for TMPRSS2 (red), DAPI (blue), and the neuronal markers HuC/D (**B**, red) or PGP9.5 (**C**, red). **(D)** Representative myenteric ganglion in the small intestine stained for TMPRSS2 (red), the glial marker S100b (green), and the nuclear marker DAPI (blue). Note that TMPRSS2 stainings were markedly stronger in enteric ganglia in the colon **(A–C)** than in the small intestine **(D)**. The overview is a standard epifluorescence image; details are maximum intensity projections of optical sections by structured illumination. Scale bars: **(A)** 250 μm; **(B–D)** 50 μm.

entire cytoplasm when compared to neighboring epithelial cells (**Figure 4C**).

In addition to the plexus epithelium, we investigated attaching and accompanying tissues of the choroid plexus. The *Tela choroidea*, consisting of connective tissue and embedded blood vessels represents the stroma of the choroid plexus and is attached to the brain parenchyma at the so-called *Taenia*. At this *Taenia*, astroglial processes directly abut to the stromal connective tissue of the choroid plexus, and the plexus epithelium connects in a continuous sheet of cells to the ependyma lining the brain ventricles. The astrocytic processes identified by GFAP immunoreactivity showed an evenly distributed cytoplasmic staining for ACE2 that was less intense than in plexus epithelial cells (**Figure 5**). Interestingly, an equally weak ACE2 expression was found also in ependymal cells. Similarly, astrocyte processes were weakly positive for TMPRSS2.

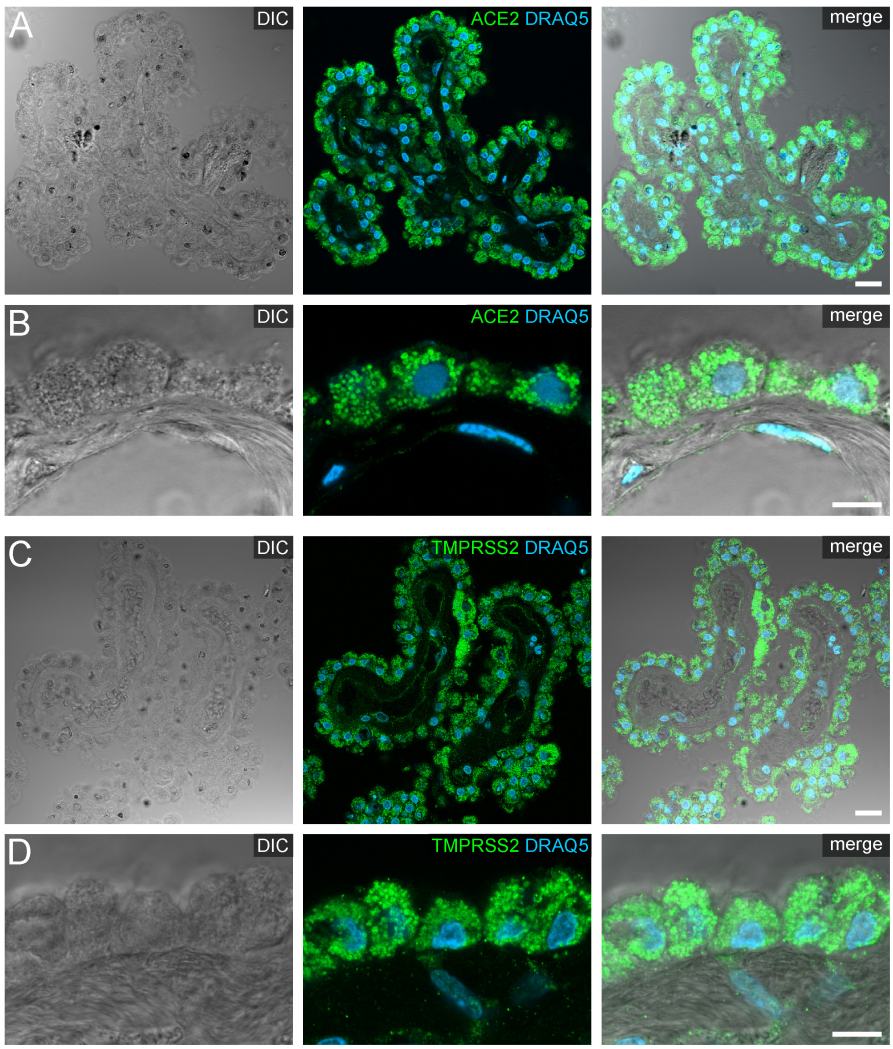

FIGURE 4 | Expression of ACE2 and TMPRSS2 in the human choroid plexus. **(A)** Overview and **(B)** high power images of sections through the human choroid plexus of the lateral ventricle, in a transmitted light DIC image (left), immunostained for ACE2 (green) and the nuclear marker DRAQ5 (blue; middle). **(B)** Shows representative plexus epithelial cells clearly positive for ACE2 (green). **(C)** Overview and **(D)** high power images of sections through the human choroid plexus of the lateral ventricle immunostained for TMPRSS2 (green) and the nuclear marker DRAQ5 (blue; middle). **(D)** Shows that TMPRSS2 has a similar distribution in choroid plexus epithelial as ACE2. All images are single optical sections (pinhole size 1 AU). Scale bars: **(A,C)** 20 μm; **(B,D)** 10 μm.

Ependymal cells, however, were largely devoid of TMPRSS2 immunoreactivity.

Within the brain parenchyma, only a subset of astrocytes were weakly positive for ACE2 and TMPRSS2 (**Supplementary Figure S6**). Occasionally, we detected both proteases located in some astrocytic endfeed at the blood-brain interface in the striatum and cortex. However, it is noteworthy that we were not able to confirm this finding for all capillaries in this brain area.

DISCUSSION

While the respiratory symptoms of COVID-19 are paramount in the treatment and current research, clinical evidence is accumulating that a SARS-CoV2 infection of the nervous system could aggravate the course of disease and arguably plays an important role in systemic disease progression (Li Y. C. et al., 2020; Li Z. et al., 2020). Although plenty of theories have been proposed on how and where corona virus particles could enter the nervous system (Briguglio et al., 2020), there is remarkably little histological and anatomical data available that would support any of these hypothesized routes of virus entry. A few studies have used gene expression analysis tools to identify mRNA expression of ACE2 and/or TMPRSS2 (Devaux et al., 2020; Zhang et al., 2020), yet these results must be interpreted with care since a post-transcriptional regulation of these genes by miRNAs has been reported (Devaux et al., 2020). In our study, we therefore evaluated the protein expression pattern of ACE2 and TMPRSS2, two proteinases involved in the cellular entry mechanism of SARS-CoV2, in

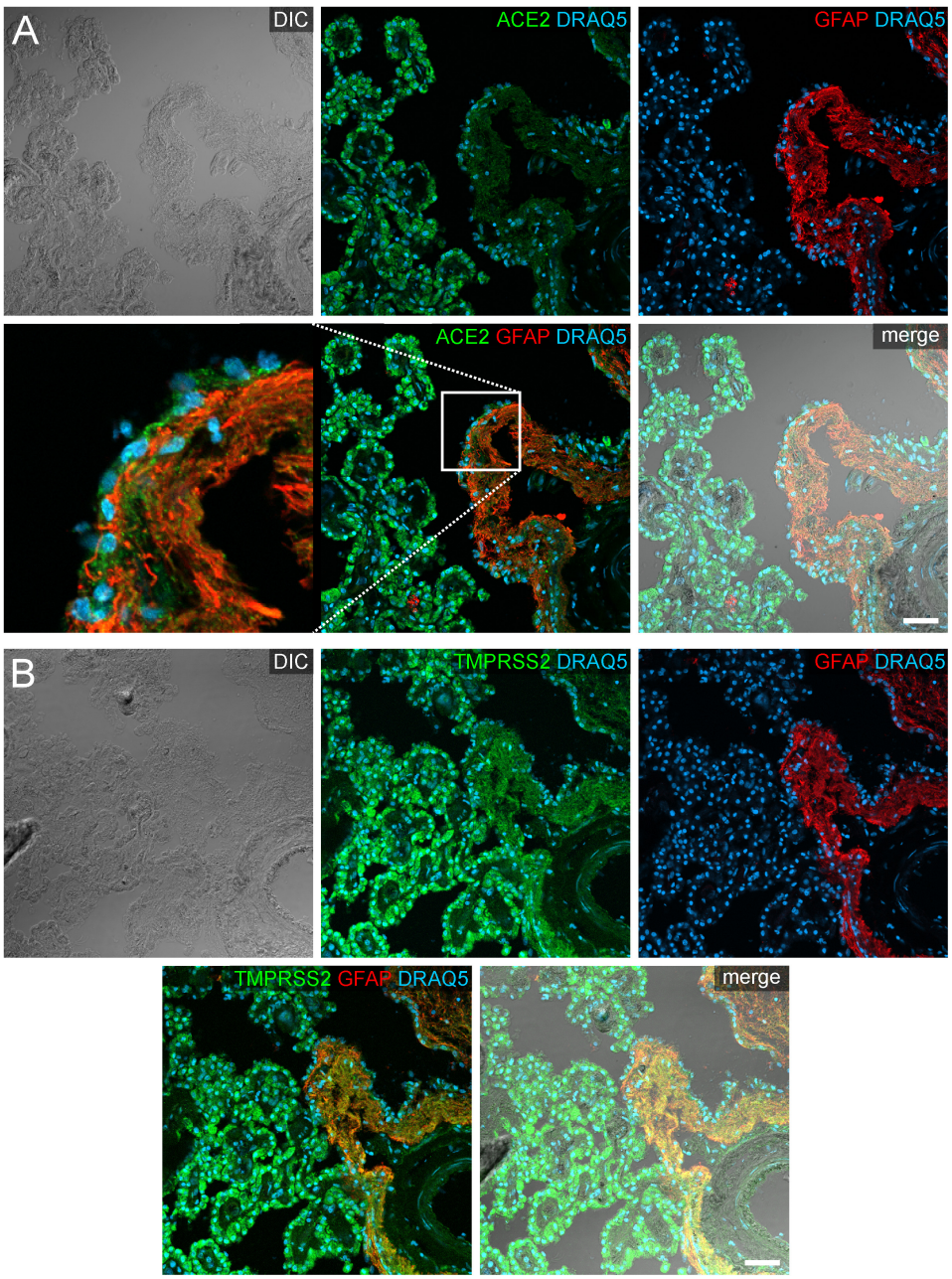

FIGURE 5 | Expression of ACE2 and TMPRSS2 at the *taenia choroidea*. **(A)** Shows a DIC image of the interface between the human choroid plexus of the lateral ventricle and the brain parenchyma (i.e., *taenia choroidea*), as well as stainings for ACE2 (green), the glial marker GFAP (red), and the nuclear marker DRAQ5 (blue). The white rectangle indicates the location of the high power magnification micrograph showing ACE2 expression in ependymal cells at the ventricular surface. The immunoreactivity for ACE2 is much higher in plexus epithelial cells than in ependymal cells or astrocytic processes. **(B)** Shows a corresponding section as a DIC image and with stainings for TMPRSS2 (green), the glial marker GFAP (red), and the nuclear marker DRAQ5 (blue). Compared to the strong staining for TMPRSS2 in the plexus epithelial cells, astrocyte processes are weakly stained. All images are single optical sections (pinhole size 1 AU). Scale bars: 50 μm.

two designated, often neglected, interfaces of the nervous system in the intestine and at the blood-CSF-barrier. Thus, we used small and large intestine resacted from pediatric patients (ranging from 3 months to 8 years and 5 months of age) and *post-mortem* specimens of the choroid plexus of the lateral ventricles.

In general, neuroinvasion can conceivably occur via a neural pathway (i.e., transferring the virus from neuron to neuron) or via body fluids (i.e., hematogenic, lymphogenic, or via the cerebrospinal fluid), as recently reviewed by Li Z. et al. (2020). Thus, an infection of the neuronal network of the ENS and successive transmission of SARS-CoV2 via the vagal, splanchnic,

or spinal nerves into the CNS is therefore a potential route that is currently discussed (Briguglio et al., 2020). Interestingly, similar pathways have been proposed for other viral infections (Park et al., 2002) and for the gut-to-brain transport of misfolded α-synuclein in Parkinson's disease (Holmqvist et al., 2014). Moreover, other corona virus infections, such as SARS or MERS, often exhibit gastrointestinal pathologies (Petrosillo et al., 2020), sometimes even preceding the respiratory symptoms (Mackay and Arden, 2015). Our results substantiate the hypothesis of an ENS-transmitted nervous system entry in that enteric neurons do express ACE2 and TMPRSS2, thereby meeting the histological prerequisites for such an infection. Interestingly, we found differences in the expression level of ACE2 in different enteric neurons, indicating that some neuronal subtypes and their respective networks might be more susceptible to SARS-CoV2 entry than others. This idea is also substantiated by our findings that ACE2 and especially TMPRSS2 expression was considerably stronger in ENS cells of the colon compared to the small intestine. However, we want to point out that ACE2 expression may also vary within one particular neuronal subtype and that immunohistological stainings do not allow precise quantification of protein expression levels. It is up to future research to verify our hypotheses and if applicable to identify more susceptible neuronal subtypes and the potential influence of their infection on the overall enteric function. It is noteworthy, however, that we only found expression of ACE2 and TMPRSS2 in the perikarya, but never in the neurites of the ENS, strongly indicating that an infection would need to take place within the ganglia and that a direct transmission from infected enterocytes to adjacent nerve endings appears unlikely. Moreover, our results were gained from pediatric specimens and future analyses should verify these findings in the ENS of adult and elderly patients.

Additionally, we found ACE2 and TMPRSS2 in glial cells of the ENS. Since enteric glial cells serve various functions, including immune-regulation and antigen presentation (Bassotti et al., 2007; da Silveira et al., 2011), an infection of these cells would potentially compromise a proper immune response, which in turn might contribute to a systemic spread of disease or a cytokine storm. Similar to this indirect effect of an ENS infection, other functions that are critically influenced by the ENS could suffer and cause additional symptoms. Thus, gut motility, intestinal blood flow, or the epithelial barrier could become dysfunctional, in turn hampering important defense mechanisms of the host against COVID-19 and other opportunistic superinfections (Briguglio et al., 2020). Moreover, recent reports link a higher incidence of glucose intolerance to corona virus infections (Chee et al., 2020; Rubino et al., 2020), in which ENS dysfunction arguably does play a role.

We also focused on histological evidence for a neuroinvasion of SARS-CoV2 via the choroid plexus. Viral agents have repeatedly shown to reach the CSF, often using the ensheathing cells of the olfactory nerve as an entry route (reviewed recently by Briguglio et al., 2020). Here, we evaluated the choroid plexus as an alternative route for CSF or brain entry. Since the endothelium of the blood vessels within the *Tela choroidea* are fenestrated, the epithelium of the choroid plexus represents the major element of the blood-CSF barrier (Wolburg and Mack, 2014; Pfeiffer et al., 2017). Indeed, a previous report suggests that ACE2 is expressed by the brush-border of the plexus epithelium; however, these results relied on enzyme activity in the brush border without any further histo-morphological correlation and were performed in sheep (Marshall et al., 2013). Thus, two entry routes into the choroid plexus epithelium appear possible, one apically via the CSF and one via the fenestrated blood vessels. We now found that human plexus epithelial cells express both ACE2 and TMPRSS2 on protein level and therefore are potential targets of a SARS-CoV2 infection. Intriguingly, our results show that both of these proteinases are mainly located in granules within the cytoplasm, with only occasional localization at the apical or basolateral cell surface. As this conceivably would have influence on the efficacy of viral entry, future research needs to elucidate whether a regulatory mechanism exists in order to control a translocation of ACE2 and TMPRSS2 from intracellular vesicle stores to the cell surface. Moreover, Dahm et al. (2016) recently reviewed possible entry mechanism used by viruses crossing the blood-brain-barrier. However, our weak stainings for ACE2 and TMPRSS2 in the brain parenchyma do not provide convincing evidence for this notion. This does not exclude the possibility of an ACE2-independent entry into the brain shuttled by immune cells (Dahm et al., 2016). Additionally, a neuronal transmission of SARS-CoV2 via the olfactory nerve appears unlikely since ACE2 is expressed in the olfactory epithelium by sustentacular cells, but not olfactory receptor neurons (Bilinska et al., 2020; Klingenstein et al., 2020).

It is also noteworthy that although viral nucleic acids have been found in the CSF of COVID-19 patients (Moriguchi et al., 2020), there still is very limited data to estimate the clinical relevance of SARS-CoV2 in the CSF. Just recently, however, Jacob et al. (2020) showed in their pre-publication manuscript that choroid plexus epithelial cells derived from human pluripotent stem cells *in vitro* were highly susceptible to SARS-CoV2 infections adding functional relevance to our morphological findings. Moreover, one should keep in mind that, similar to the ENS, an infection of the plexus epithelium could also have indirect effects on the proper functioning of CSF production as well as on water- and electrolyte homeostasis in the brain. Furthermore, an alternative entry route via the meningeal component of the *Tela choroidea* and a potential persistence of SARS-CoV2 in cells of the nervous system should be considered (Pfeiffer et al., 2017).

Taken together, our data provide fundamental evidence for potential alternative routes for the neuroinvasion of SARS-CoV2. The expression of ACE2 and TMPRSS2 in various cells of the ENS and the choroid plexus will need to be elucidated further in order to identify susceptible subpopulations. Also, the biological function of ACE2 and TMPRSS2 in the ENS and the choroid plexus remains elusive and a more detailed understanding of their physiological role might explain clinical phenomena. We critically want to point out that we did not provide any functional evidence for an actual infection of these cells by SARS-CoV2. Thus, functional transgenic animal models as well as post-mortem examinations of COVID-19 patients with neurological and/or gastroenterological symptoms will provide highly valuable insights.

DATA AVAILABILITY STATEMENT

The raw data supporting the conclusions of this article will be made available by the authors, without undue reservation.

ETHICS STATEMENT

The studies involving human participants were reviewed and approved by Ethik-Kommission an der Medizinischen Fakultät der Eberhard-Karls-Universität und am Universitätsklinikum Tübingen. Written informed consent to participate in this study was provided by the participants' legal guardian/next of kin.

AUTHOR CONTRIBUTIONS

FD and MS: acquisition of data, analysis and interpretation of data, drafting of the manuscript, and critical revision of the manuscript for important intellectual content. SK, MK, and AM: analysis and interpretation of data and critical revision of the manuscript for important intellectual content. SS: acquisition of patient material and critical revision of the manuscript for important intellectual content. AW: acquisition of data and critical revision of the manuscript for important intellectual content. BH: study concept and design, interpretation of data, and critical revision of the manuscript for important intellectual content. AFM and PN: study concept and design, acquisition of data, analysis and interpretation of data, drafting of the manuscript, critical revision of the manuscript for important intellectual content, and study supervision. All authors contributed to the article and approved the submitted version.

FUNDING

The project was supported by a grant from the German Research Foundation (DFG, Grant number: 438504601). FD was supported by the IZKF-Promotionskolleg of the medical faculty of the University of Tübingen. We acknowledge the support by the Deutsche Forschungsgemeinschaft and Open Access Publishing Fund of the University of Tübingen for covering the publication expenses.

ACKNOWLEDGMENTS

We would like to thank Ulrich Mattheus, Karin Seid, and Melina Fischer for technical support and Lothar Just for his helpful comments on the manuscript.

SUPPLEMENTARY MATERIAL

The Supplementary Material for this article can be found online at: https://www.frontiersin.org/articles/10.3389/fnana.2020.596439/full#supplementary-material

FIGURE S1 | Negative controls for antibody stainings. **(A,B)** Overviews of transversal sections of the human colon of two different patients treated with both secondary antibodies as a negative control and the nuclear stain DAPI (blue) for better orientation. The white rectangles indicate the location of the high power magnification micrographs on the right. Arrowheads point at enteric neurons in the submucous and myenteric plexus. **(C,D)** Overviews of sections through the human choroid plexus treated with secondary antibodies as a negative control and the nuclear stain DRAQ5 (blue) for better orientation. The microscope settings were the same as for the single channel stainings in **Figure 4C** and for double stainings in **Figure 5D**. **(A,B)** Are standard epifluorescence images; **(C,D)** are single optical sections (pinhole size 1 AU). Scale bars: **(A,B)** 500 μm; **(C,D)** 50 μm.

FIGURE S2 | ACE2 expression in the intestinal epithelium. Overviews of the *Tunica muscosa* of the human small intestine **(A)** and colon **(B)** stained for ACE2 (red) and the nuclear stain DAPI (blue). The white rectangles indicate the location of the respective high power magnification insets. Especially the brush border of the small intestine exhibits a highly intense staining. All images are maximum intensity projections of optical slices by structured illumination. Scale bars: overviews 100 μm; insets 20 μm.

FIGURE S3 | Variable expression levels of ACE2 in submucosal enteric neurons. **(A,B)** show maximum intensity projections of representative submucous ganglia of the human small intestine stained for ACE2 (red) and the nuclear stain DAPI (blue). Arrows point to enteric neurons with a weak expression of ACE2, arrowheads point to neurons with a highly intense ACE2 staining. Scale bars: 20 μm.

FIGURE S4 | ACE2 expression in extraganglionic enteric glial cells. Shows type-III enteric glial cells (S100b in green) in the *Lamina propria mucosae* of the small **(A)** and large **(B)** intestine, not exhibiting any ACE2 immunoreactivity (red). **(C,D)** Depict extraganglionic glial cells in the *Tela submucosa*, most of which express ACE2. In **(D)**, enteric glial cells in close contact to blood vessels are shown, with ACE2 expressed especially by smooth muscle cells of the *Tunica media* and the glial cells, however, with varying intensity. **(E,F)** show type-IV enteric glial cells within the smooth musculature of the Tunica muscularis in the small **(E)** and large **(F)** intestine. ACE2 is expressed in these cell with the same intensity as in the surrounding muscle tissue. All images are maximum intensity projection of optical sections by structured illumination. Scale bars: 20 μm.

FIGURE S5 | Differential subcellular localization of ACE2 in epithelial cells of the human choroid plexus. **(A)** Shows a DIC image of epithelial cells of the human choroid plexus. In **(B)** immunostainings for ACE2 (green) reveal two types of subcellular localization of the protease: in intracellular vesicles (arrow) or at the cell surface (arrowheads). Shown is a single optical section (pinhole size 1 AU). **(C)** The image is the merged image. Scale bars: 10 μm.

FIGURE S6 | ACE2 and TMPRSS2 expression at the blood-brain barrier in the human striatum. **(A)** Shows a section of the human striatum immunostained for ACE2 (green) and GFAP (red). ACE2 can be detected in some astrocytic cell processes and occasionally surrounding vessels. In **(B)** immunostainings for TMPRSS2 (green) and GFAP (red) are depicted. TMPRSS2 is expressed in some astrocytic endfeed at the blood–brain interface. The asterisk indicates the lumen of a capillary. All images are single optical sections (pinhole size 1 AU). Scale bars: 20 μm.

REFERENCES

Bassotti, G., Villanacci, V., Antonelli, E., Morelli, A., and Salerni, B. (2007). Enteric glial cells: new players in gastrointestinal motility? *Lab Invest.* 87, 628–632. doi: 10.1038/labinvest.3700564

Bilinska, K., Jakubowska, P., Von Bartheld, C. S., and Butowt, R. (2020). Expression of the SARS-CoV-2 entry proteins, ACE2 and TMPRSS2, in cells of the olfactory epithelium: identification of cell types and trends with age. *ACS Chem. Neurosci.* 11, 1555–1562. doi: 10.1021/acschemneuro.0c00210

Bösel, J., and Berlit, P. (2020). Neurological effects of COVID-19. *DGNeurologie* 3, 277–284. doi: 10.1007/s42451-020-00191-9.)

Briguglio, M., Bona, A., Porta, M., Dell'Osso, B., Pregliasco, F. E., and Banfi, G. (2020). Disentangling the hypothesis of host dysosmia and SARS-CoV-2: the bait symptom that hides neglected neurophysiological routes. *Front. Physiol.* 11:671.

Brun, P., Giron, M. C., Zoppellaro, C., Bin, A., Porzionato, A., De Caro, R., et al. (2010). Herpes simplex virus type 1 infection of the rat enteric nervous system evokes small-bowel neuromuscular abnormalities. *Gastroenterology* 138, 1790–1801. doi: 10.1053/j.gastro.2010.01.036

Cataldi, M., Pignataro, G., and Taglialatela, M. (2020). Neurobiology of coronaviruses: potential relevance for COVID-19. *Neurobiol. Dis.* 143:105007. doi: 10.1016/j.nbd.2020.105007

Chee, Y. J., Ng, S. J. H., and Yeoh, E. (2020). Diabetic ketoacidosis precipitated by Covid-19 in a patient with newly diagnosed diabetes mellitus. *Diabetes. Res. Clin. Pract.* 164:108166. doi: 10.1016/j.diabres.2020.108166

da Silveira, A. B., de Oliveira, E. C., Neto, S. G., Luquetti, A. O., Fujiwara, R. T., Oliveira, R. C., et al. (2011). Enteroglial cells act as antigen-presenting cells in chagasic megacolon. *Hum. Pathol.* 42, 522–532.

Dahm, T., Rudolph, H., Schwerk, C., Schroten, H., and Tenenbaum, T. (2016). Neuroinvasion and inflammation in viral central nervous system infections. *Mediators Inflamm.* 2016:8562805.

De Felice, F. G., Tovar-Moll, F., Moll, J., Munoz, D. P., and Ferreira, S. T. (2020). Severe acute respiratory syndrome coronavirus 2 (SARS-CoV-2) and the central nervous system. *Trends Neurosci.* 43, 355–357.

Devaux, C. A., Rolain, J. M., and Raoult, D. (2020). ACE2 receptor polymorphism: susceptibility to SARS-CoV-2, hypertension, multi-organ failure, and COVID-19 disease outcome. *J. Microbiol. Immunol. Infect.* 53, 425–435. doi: 10.1016/j.jmii.2020.04.015

Esposito, G., Pesce, M., Seguella, L., Sanseverino, W., Lu, J., and Sarnelli, G. (2020). Can the enteric nervous system be an alternative entrance door in SARS-CoV2 neuroinvasion? *Brain Behav. Immun.* 87, 93–94. doi: 10.1016/j.bbi.2020.04.060

Hamming, I., Timens, W., Bulthuis, M. L., Lely, A. T., Navis, G., and van Goor, H. (2004). Tissue distribution of ACE2 protein, the functional receptor for SARS coronavirus. A first step in understanding SARS pathogenesis. *J. Pathol.* 203, 631–637. doi: 10.1002/path.1570

Hoffmann, M., Kleine-Weber, H., Schroeder, S., Kruger, N., Herrler, T., Erichsen, S., et al. (2020). SARS-CoV-2 cell entry depends on ACE2 and TMPRSS2 and is blocked by a clinically proven protease inhibitor. *Cell* 181, 271.e8–280.e8.

Holmqvist, S., Chutna, O., Bousset, L., Aldrin-Kirk, P., Li, W., Björklund, T., et al. (2014). Direct evidence of Parkinson pathology spread from the gastrointestinal tract to the brain in rats. *Acta Neuropathol.* 128, 805–820. doi: 10.1007/s00401-014-1343-6

Hung, E. C., Chim, S. S., Chan, P. K., Tong, Y. K., Ng, E. K., Chiu, R. W., et al. (2003). Detection of SARS coronavirus RNA in the cerebrospinal fluid of a patient with severe acute respiratory syndrome. *Clin. Chem.* 49, 2108–2109.

Jacob, F., Pather, S. R., Huang, W.-K., Wong, S. Z. H., Zhou, H., Zhang, F., et al. (2020). Human pluripotent stem cell-derived neural cells and brain organoids reveal SARS-CoV-2 Neurotropism. *bioRxiv* [Preprint]. doi: 10.1101/2020.07.28.225151

Khoury-Hanold, W., Yordy, B., Kong, P., Kong, Y., Ge, W., Szigeti-Buck, K., et al. (2016). Viral spread to enteric neurons links genital HSV-1 infection to toxic megacolon and lethality. *Cell Host Microbe* 19, 788–799. doi: 10.1016/j.chom.2016.05.008

Klingenstein, M., Klingenstein, S., Neckel, P. H., Mack, A. F., Wagner, A., Kleger, A., et al. (2020). Evidence of SARS-CoV2 entry protein ACE2 in the human nose and olfactory bulb. *bioRxiv* [Preprint].

Leonardi, M., Padovani, A., and McArthur, J. C. (2020). Neurological manifestations associated with COVID-19: a review and a call for action. *J. Neurol.* 267, 1573–1576. doi: 10.1007/s00415-020-09896-z

Li, Y. C., Bai, W. Z., and Hashikawa, T. (2020). The neuroinvasive potential of SARS-CoV2 may play a role in the respiratory failure of COVID-19 patients. *J. Med. Virol.* 92, 552–555. doi: 10.1002/jmv.25728

Li, Z., Liu, T., Yang, N., Han, D., Mi, X., Li, Y., et al. (2020). Neurological manifestations of patients with COVID-19: potential routes of SARS-CoV-2 neuroinvasion from the periphery to the brain. *Front. Med.* 1–9. doi: 10.1007/s11684-020-0786-5

Mackay, I. M., and Arden, K. E. (2015). MERS coronavirus: diagnostics, epidemiology and transmission. *Virol. J.* 12:222.

Marshall, A. C., Shaltout, H. A., Pirro, N. T., Rose, J. C., Diz, D. I., and Chappell, M. C. (2013). Antenatal betamethasone exposure is associated with lower ANG-(1-7) and increased ACE in the CSF of adult sheep. *Am. J. Physiol. Regul. Integr. Comp. Physiol.* 305, R679–R688.

Moriguchi, T., Harii, N., Goto, J., Harada, D., Sugawara, H., Takamino, J., et al. (2020). A first case of meningitis/encephalitis associated with SARS-Coronavirus-2. *Int. J. Infect. Dis.* 94, 55–58.

Park, C. H., Ishinaka, M., Takada, A., Kida, H., Kimura, T., Ochiai, K., et al. (2002). The invasion routes of neurovirulent A/Hong Kong/483/97 (H5N1) influenza virus into the central nervous system after respiratory infection in mice. *Arch. Virol.* 147, 1425–1436. doi: 10.1007/s00705-001-0750-x

Petrosillo, N., Viceconte, G., Ergonul, O., Ippolito, G., and Petersen, E. (2020). COVID-19, SARS and MERS: are they closely related? *Clin. Microbiol. Infect.* 26, 729–734. doi: 10.1016/j.cmi.2020.03.026

Pfeiffer, F., Mack, A. F., and Wolburg, H. (2017). "Topological aspects of the blood–brain and blood–cerebrospinal fluid barriers and their relevance in inflammation," in *The Blood Brain Barrier and Inflammation*, eds R. Lyck and G. Enzmann (Cham: Springer International Publishing), 23–48. doi: 10.1007/978-3-319-45514-3_2

Qiu, Y., Zhao, Y. B., Wang, Q., Li, J. Y., Zhou, Z. J., Liao, C. H., et al. (2020). Predicting the angiotensin converting enzyme 2 (ACE2) utilizing capability as the receptor of SARS-CoV-2. *Microbes Infect.* 22, 221–225. doi: 10.1016/j.micinf.2020.03.003

Rubino, F., Amiel, S. A., Zimmet, P., Alberti, G., Bornstein, S., Eckel, R. H., et al. (2020). New-Onset Diabetes in Covid-19. *N. Engl. J. Med.* 383, 789–790.

Sun, P., Qie, S., Liu, Z., Ren, J., Li, K., and Xi, J. (2020). Clinical characteristics of hospitalized patients with SARS-CoV-2 infection: a single arm meta-analysis. *J. Med. Virol.* 92, 612–617. doi: 10.1002/jmv.25735

Wang, D., Hu, B., Hu, C., Zhu, F., Liu, X., Zhang, J., et al. (2020). Clinical characteristics of 138 hospitalized patients with 2019 novel coronavirus-infected pneumonia in wuhan, China. *JAMA* 323, 1061–1069. doi: 10.1001/jama.2020.1585

WHO (2020). *Coronavirus Disease (COVID-19) Situation Report – 209*. Geneva: World Health Organization.

Wolburg, H., and Mack, A. F. (2014). Comment on the topology of mammalian blood–cerebrospinal fluid barrier. *Neurol. Psychiatry Brain Res.* 20, 70–72. doi: 10.1016/j.npbr.2014.10.004

Yan, R., Zhang, Y., Li, Y., Xia, L., Guo, Y., and Zhou, Q. (2020). Structural basis for the recognition of SARS-CoV-2 by full-length human ACE2. *Science* 367, 1444–1448. doi: 10.1126/science.abb2762

Yoo, B. B., and Mazmanian, S. K. (2017). The enteric network: interactions between the immune and nervous systems of the gut. *Immunity* 46, 910–926. doi: 10.1016/j.immuni.2017.05.011

Zhang, H., Kang, Z., Gong, H., Xu, D., Wang, J., Li, Z., et al. (2020). Digestive system is a potential route of COVID-19: an analysis of single-cell coexpression pattern of key proteins in viral entry process. *Gut* 69, 1010–1018. doi: 10.1136/gutjnl-2020-320953

Zhou, P., Yang, X. L., Wang, X. G., Hu, B., Zhang, L., Zhang, W., et al. (2020). A pneumonia outbreak associated with a new coronavirus of probable bat origin. *Nature* 579, 270–273. doi: 10.1038/s41586-020-2012-7

Ziegler, C. G. K., Allon, S. J., Nyquist, S. K., Mbano, I. M., Miao, V. N., Tzouanas, C. N., et al. (2020). SARS-CoV-2 receptor ACE2 is an interferon-stimulated gene in human airway epithelial cells and is detected in specific cell subsets across tissues. *Cell* 181, 1016.e19–1035.e19.

Conflict of Interest: The authors declare that the research was conducted in the absence of any commercial or financial relationships that could be construed as a potential conflict of interest.

Advantages of publishing in Frontiers

OPEN ACCESS
Articles are free to read for greatest visibility and readership

FAST PUBLICATION
Around 90 days from submission to decision

HIGH QUALITY PEER-REVIEW
Rigorous, collaborative, and constructive peer-review

TRANSPARENT PEER-REVIEW
Editors and reviewers acknowledged by name on published articles

Frontiers
Avenue du Tribunal-Fédéral 34
1005 Lausanne | Switzerland

Visit us: www.frontiersin.org
Contact us: frontiersin.org/about/contact

REPRODUCIBILITY OF RESEARCH
Support open data and methods to enhance research reproducibility

DIGITAL PUBLISHING
Articles designed for optimal readership across devices

FOLLOW US
@frontiersin

IMPACT METRICS
Advanced article metrics track visibility across digital media

EXTENSIVE PROMOTION
Marketing and promotion of impactful research

LOOP RESEARCH NETWORK
Our network increases your article's readership